DEVELOPMENT OF TRANSIENT ATTENUATED TOTAL REFLECTANCE SPECTROSCOPY AND INVESTIGATION OF PHOTOINDUCED KINETICS IN THIN FILMS

by

Anne M. Simon

A Dissertation Submitted to the Faculty of the

DEPARTMENT OF CHEMISTRY AND BIOCHEMISTRY

In Partial Fulfillment of the Requirements
For the Degree of

DOCTOR OF PHILOSOPHY
WITH A MAJOR IN CHEMISTRY

In the Graduate College

THE UNIVERSITY OF ARIZONA

2012

THE UNIVERSITY OF ARIZONA
GRADUATE COLLEGE

As members of the Dissertation Committee, we certify that we have read the dissertation

prepared by Anne M. Simon

entitled DEVELOPMENT OF TRANSIENT ATTENUATED TOTAL REFLECTANCE SPECTROSCOPY AND INVESTIGATION OF PHOTOINDUCED KINETICS IN THIN FILMS

and recommend that it be accepted as fulfilling the dissertation requirement for the

Degree of Doctor of Philosophy

_____Date: 9/19/12
Dr. S. Scott Saavedra

_____Date: 9/19/12
Dr. Jeanne Pemberton

_____Date: 9/19/12
Dr. Neal R. Armstrong

_____Date: 9/19/12
Dr. Douglas Loy

_____Date: 9/19/12
Dr. Pamela Vandiver

Final approval and acceptance of this dissertation is contingent upon the candidate's submission of the final copies of the dissertation to the Graduate College.

I hereby certify that I have read this dissertation prepared under my direction and recommend that it be accepted as fulfilling the dissertation requirement.

_____ Date: 9/19/12
Dissertation Director: Dr. S. Scott Saavedra

STATEMENT BY AUTHOR

This dissertation has been submitted in partial fulfillment of requirements for an advanced degree at the University of Arizona and is deposited in the University Library to be made available to borrowers under rules of the Library.

Brief quotations from this dissertation are allowable without special permission, provided that accurate acknowledgment of source is made. Requests for permission for extended quotation from or reproduction of this manuscript in whole or in part may be granted by the head of the major department or the Dean of the Graduate College when in his or her judgment the proposed use of the material is in the interests of scholarship. In all other instances, however, permission must be obtained from the author.

SIGNED: Anne M. Simon

ACKNOWLEDGEMENTS

S. Scott Saavedra: Thank you for taking me into your group and guiding my research. Your effort and dedication is unyielding and I am grateful for the example you set daily in pursuit of scientific answers.

Jeanne Pemberton, Neal Armstrong, Douglas Loy and Pamela Vandiver: Thank you for your guidance through these years in graduate school. I am also grateful for the opportunity to lead the Energy Science Group and participate in the EFRC.

Saavedra Research Group: Hsiaochu, Boying, Han, Kristina, Anthony, Sean, Nicole, Zeynep, James, Saliya and Ian. I was truly lucky to get to know each of you. I appreciate the daily conversations, laughter and constant support.

Mom and Dad: Your encouragement and belief in my abilities gave me the confidence to pursue seemingly insurmountable goals.

Pam, Jon, Susan and friends: Thank you for helping me to keep everything in perspective. I am glad you are on my side.

Most of all, John: I cannot imagine going through this process without your love and support. You have made every moment of this journey a happier one. I look forward to our next great adventure.

TABLE OF CONTENTS

LIST OF FIGURES

LIST OF TABLES

ABSTRACT

The efficiency of photoconversion systems such as organic photovoltaic cells and photocatalytic water-splitting cells is largely governed by the interfacial charge transfer processes. Understanding the structure-function relationship, specifically at the molecular thin film/transparent conducting oxide interface will allow for engineering these interfaces to promote charge transfer and reduce the rate of charge recombination. Important factors that are hypothesized to influence charge transfer are morphology, chemical characteristics, electronic properties and molecular orientation. As molecules are bound to a transparent conducting oxide or incorporated into a thin film, the local solid-state molecular environment greatly influences the excited state properties of the molecule. Pathways for quenching, radiative and nonradiative decay drastically limit the excited state lifetimes.

In order to investigate the photoinduced kinetics of thin films and at interfaces a instrument was developed coupling transient absorbance spectroscopy to attenuated total reflectance spectroscopy. The photoinduced kinetics of a thin film of bacteriorhodopsin was used to evaluate the instrument performance, and it was determined that 1% of a close-packed monolayer could be detected with this geometry.

The properties of a molecular thin film/transparent conducting oxide were investigated by tethering zinc porphyrin to ITO. The electrochemical properties were influenced by the functional group of the binding moiety. To improve our understanding of how the solid state molecular environment affects excited states lifetimes, zinc

porphyrins were incorporated into mono- and multilayer thin films and measured with transient ATR spectroscopy.

Finally, multilayer films related to photocatalytic water-splitting were investigated with the incorporation of inorganic nanosheets. The nanosheets helped to create a stratified assembly for multilayer films, spatially segregating electron donor (palladium porphyrin) and electron acceptor (poly(viologen)) molecules. The role of the nanosheets in the electron transfer between the donor and acceptor was studied by monitoring the triplet state lifetimes of a palladium porphyrin with transient ATR spectroscopy.

1. INTRODUCTION

1.1 Solar Cells

The human population consumes about 15 terawatts (TW = 10^{12} W) of energy every year.[1] As the population continues to grow, along with urbanization of third-world countries and industrialized nations, the demand for energy will increase at a staggering rate. According to the US Energy Information Administration, non-renewable sources make up 83% of the US Energy portfolio.[2] This heavy reliance on fossil fuels is unsustainable as well as detrimental to the environment. Hoffert outlined the major implications in regards to CO_2 emissions from utilizing carbon based sources to meet the growing energy demands.[3] He stated that in order to avoid catastrophic planetary changes, 10 TW of carbon neutral energy must be added to the global energy portfolio by 2050.[4] To meet this challenge, cost-effective, efficient and sustainable sources need to be researched and developed. One of the major thrusts towards this goal is with solar energy conversion. Solar power irradiates the Earth with one hundred and twenty thousand TW of power per year, harvesting this energy for a single day would supply the planet with power for one year.[1, 5]

Conversion of solar energy to electricity was first documented in 1839 by Becquerel with the use of liquid electrolytes.[6] The most prevalent solar cells today are still based on the work of Chapin from 1954, where a silicon based solid state p-n junction cell demonstrated an efficiency of 6%.[7] Although single crystal silicon cells or 'Generation I' cells have the highest efficiencies of close to 30% and are the most

prevalent on the commercial market, they are plagued with the high cost of silicon purification.[8] 'Generation II' cells emerged to address the manufacturing cost and improve the power conversion efficiency.[9] These cells utilize other inorganic semiconductor materials that are more highly absorbing than crystalline silicon. Some of the materials include cadmium telluride (CdTe), copper indium gallium selenide (CIGS), and amorphous silicon (A-Si). Although CIGS cells have achieved efficiencies of close to 20% in the laboratory,[10] they have not replaced single crystal silicon on the marketplace.

Organics based solar cells are known as 'Generation III' cells and have been researched for more than the past two decades. The first single hetero-junction solar cell was reported by Tang in 1986 with a power conversion efficiency of 1%.[11] Unlike single crystal silicon cells, organic solar cells can be processed from solution and deposited on large flexible substrates. The energy consumption during the manufacturing process of these cells can be minimal, since solution processing requires close to ambient temperatures.[12] Successful development of organic solar cells will help to make solar energy a viable and affordable option, moving the global energy portfolio towards sustainable and low carbon emission sources.

There are several technologies that fall under the 'Generation III' category, such as bulk inorganic or multijunction solar cells, colloidal quantum dot solar cells, organic photovoltaic cells (OPVs) and dye-sensitized solar cells (DSSCs).[12] For the purpose of this research, the latter two technologies will be discussed in detail, although the topics will be of interest to the entire organics based solar cell community.

1.1.1 Organic Photovolatics

Organic photovoltaics (OPVs) have the potential to significantly contribute to the renewable energy portfolio due to advantages of using earth-abundant materials and low cost of production. Recently reports have shown power generation current efficiencies from 8-9%,[13-14] which has resulted from development of new materials and molecular architectures along with the advancement of the fundamental science framework to enable rational design of devices.[15]

The general architecture of the OPV is similar to that reported by Tang[11]. It consists of two organic light absorbing layers, one with electron-accepting properties (A, e.g. fullerene) and the other with electron-donating properties (D, e.g. copper phthalocyanine) sandwiched between two electrodes. The highest occupied and lowest unoccupied molecular orbitals (HOMO, LUMO) are the important electronic properties of these semiconducting donor and acceptor molecules. One electrode is transparent, usually a metal oxide such as indium tin oxide (ITO), and the opposite electrode has a work function to promote current flow through the device. An important property of the electrodes is their work function, defined as the energy difference between the Fermi level (E_F) and vacuum.[16] A general electronic structure for an organic semiconductor-metal interface is shown in Figure 1.1. This schematic illustrates the alignment of the energy levels as the organic semiconductor comes into contact with the metal or metal oxide electrode. The energy shift between the vacuum levels (E_{vac}) is a result of the interface dipole barrier and represented by (Δ).

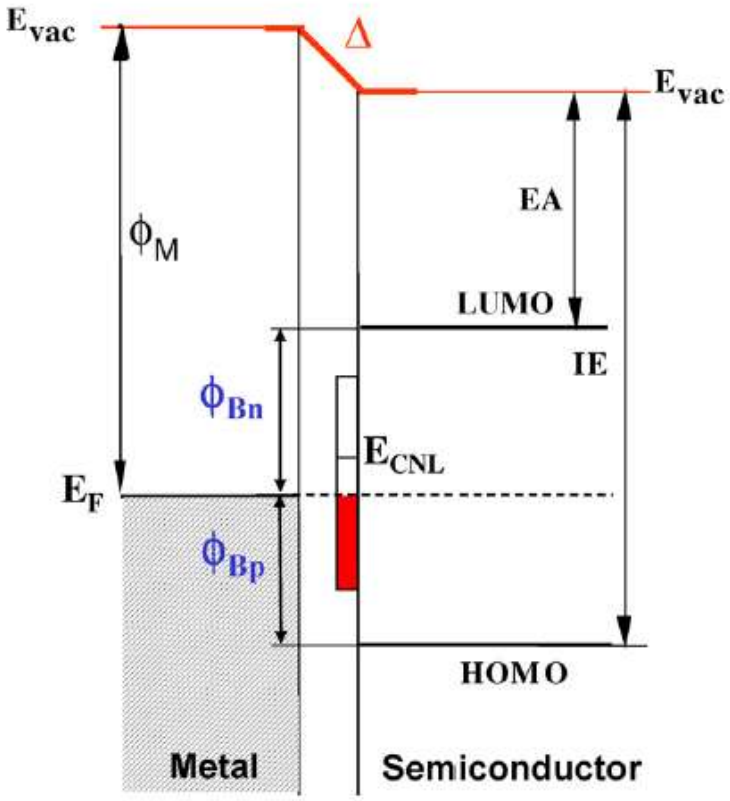

Figure 1.1 General electronic structure of organic semiconductor-metal interface. The important properties of the metal are the Fermi energy (E_F) and the work function of the electrode (Φ_M) = the work function of the electrode. The organic semiconductor properties are electron affinity (EA) and the ionization energy (IE). Each material has its vacuum energy level (E_{vac}) and at the semiconductor-metal interface the vacuum shift as a result of the interface dipole is represented as Δ. The energy of the charge neutral species is denoted as E_{CNL}, while the electron and hole injection barriers are Φ_{Bn} and Φ_{Bp}, respectively. Reprinted from ref 16. Used from with permission from Elsevier.

The photoconversion process of an OPV is shown in Figure 1.2 and can be described in a four-step mechanism. The first step (1) is the absorption of a photon by the donor molecule, generating a localized excited state. The charge neutral excited state is an electron-hole pair or exciton which is bound by a Coulomb binding energy of ~1eV. This localization of the exciton is the main difference between organic and inorganic semiconductors where, for example, the binding energy of an exciton formed in a silicon crystal is <0.1 eV.[15, 17] A key molecular requirement for (1) is a high molar absorptivity covering a broad range of the solar spectrum.

After an exciton in the donor material is created, it diffuses to the donor-acceptor interface, denoted as step two (2). This diffusion is limited by the distance the exciton lifetime and its diffusion rate which is approximately <~10 nm in polymers.[12] At the donor-acceptor (D-A) interface, the energy offset of the LUMO levels drives step three (3): exciton dissociation or charge separation. A competing process to (3) is charge recombination. The charges are now located on separate molecules and migrate towards the respective electrodes. Step four (4) is the electron and hole migration and collection of charges at the interface.[17] Charge carrier mobility should be high in order to move charges rapidly from the D-A interface. The charge collection at the molecule-electrode interface must also happen rapidly and if possible with charge selectivity to improve the harvesting of specific charges (either holes or electrons).[18]

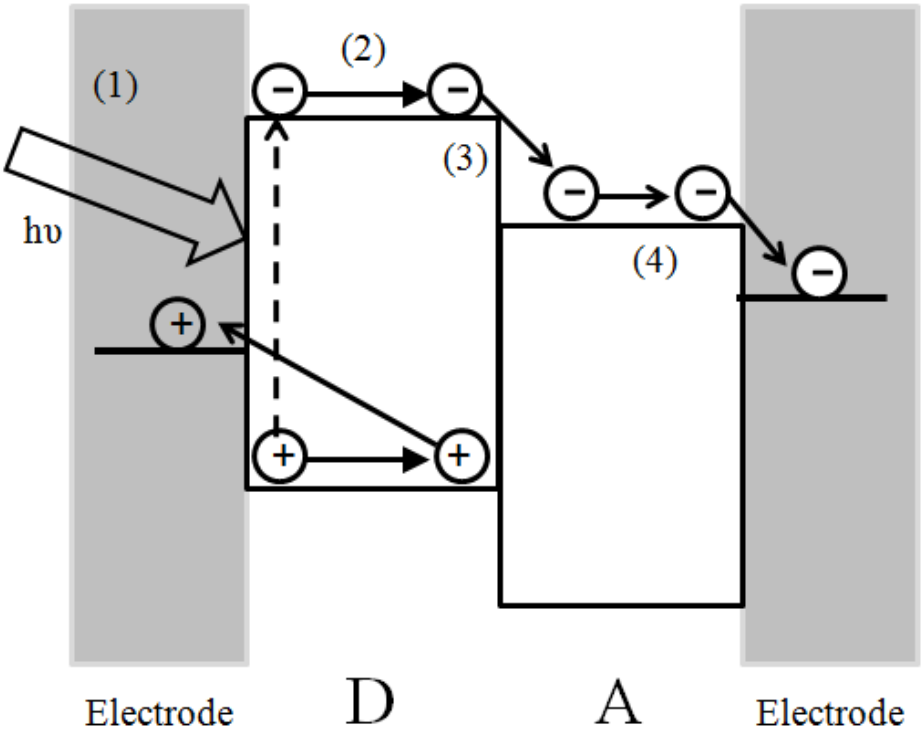

Figure 1.2 Schematic for the four step process in OPV photoconversion. The donor material is denoted as D, while the acceptor material is denoted as A. Step (1) is the absorption of a photon by the donor material and creation of an exciton. The exciton diffuses to the D-A interface in (2), where it dissociates into free electrons and holes (3). The charges migrate to the respective electrodes where they are collected (4).

These processes highlight the complexity of the OPV architecture and the challenge to improve the efficiencies at each interface throughout the cell. The overall efficiency of the OPV (η_{IQE}) can thus be broken down into the product of the efficiencies of the individual events as shown in Equation 1.1 where the first step is absorption of photons (η_A), followed by exciton diffusion (η_{ED}), then charge separation (η_{CS}), ending with charge collection (η_{CC}).

$$\eta_{IQE} = \eta_A \text{ x } \eta_{ED} \text{ x } \eta_{CS} \text{ x } \eta_{CC} \quad (1.1)$$

The power conversion efficiency (η) shown in Equation 1.2 is the common metric for solar cells, describing the output electrical power per unit of incident electromagnetic radiation applied (I_S).[12, 17] The experimental short-circuit current density (J_{SC}) and open circuit voltage (V_{OC}) are measured under illumination of the solar cell. The theoretical V_{OC} is defined by the offset between the HOMO of the donor and LUMO of the acceptor. The experimentally determined V_{OC} is generally smaller than the theoretical V_{OC} due to charge recombination reactions competing with forward electron transfer. The fill factor (FF) is the ratio between the maximum power (P_{max}) from the illuminated device and the theoretical power defined by the product of J_{SC} and V_{OC}.

$$\eta = \text{FF x } \frac{J_{SC}V_{OC}}{I_S} \quad (1.2)$$

There are several strategies that have proved critical to improvement of OPV efficiency, including development of low optical band gap materials to cover the broad solar spectrum. Another research avenue is increasing the HOMO of donor and decreasing the LUMO of the acceptor to increase the V_{OC}. Others have investigated controlling the D-A microstructure to decrease exciton diffusion distances, moving away

from the planar heterojunction cell as first documented by Tang[11], and towards bulk heterojunction platforms. Finally, studies have also focused on interlayers at the electrode-molecular interface in order to increase the metal oxide conductivity, match electrode work functions to the molecular semiconductors and to increase the degree of charge selectivity at the electrode.[15, 18]

1.1.2 Dye-Sensitized Solar Cells

The main difference between OPVs and dye-sensitized solar cells (DSSCs) is that the OPV solid-state architecture forms heterojunctions between materials to separate the exciton into two charge carriers, while the DSSC utilizes a nanocrystalline semiconductor and liquid electrolyte to separate and transfer charges. DSSCs were first introduced by O'Regan and Grätzel in 1991[19] and for the past twenty years strides have been made to improve stability and photoconversion efficiency. Research labs have demonstrated efficiencies of 11% for single junction DSSCs with conventional materials[20] and as high as 12.3% with unconventional materials.[21] As with OPVs, controlling the many interfaces within DSSC devices is paramount to advancing this technology.[1]

A schematic of a DSSC is shown in Figure 1.3. There are typically five major components of a DSSC: a transparent electrode, a nanocrystalline semiconductor film, a sensitizer dye adsorbed to the semiconductor film, an electrolyte with a redox mediator and a counter electrode. The transparent electrode is usually a conductive metal oxide. The semiconductor film is typically nanocrystalline TiO_2 due to its low cost, large band

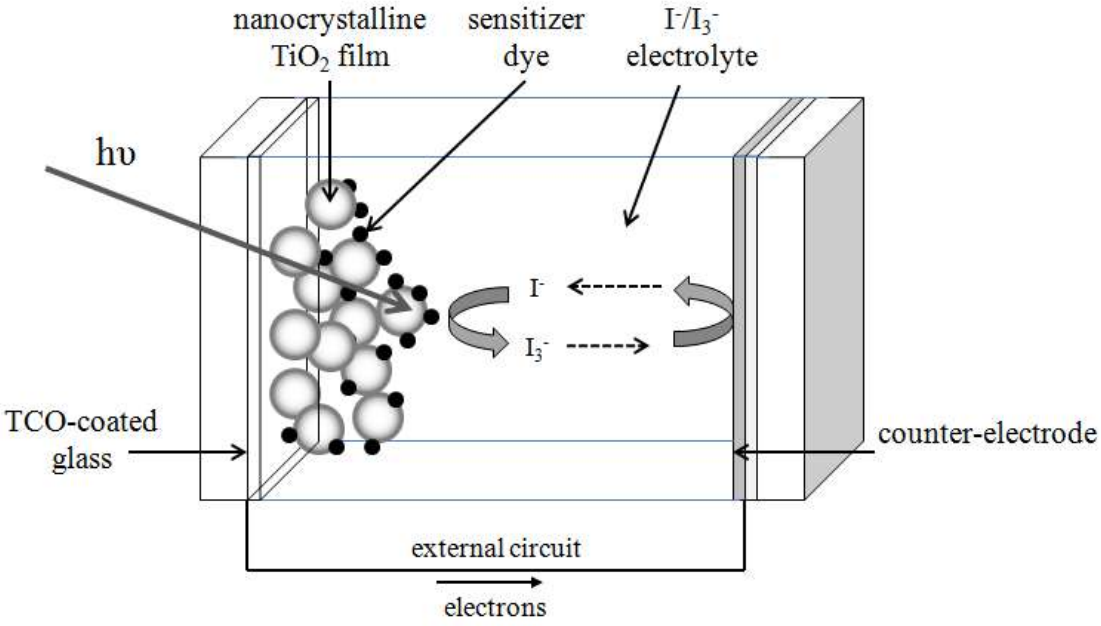

Figure 1.3 Schematic of a dye sensitized solar cell (DSSC). Light is absorbed by the sensitizer adsorbed to the nanocrystalline TiO_2 film. The electron is injected into the TiO_2 and transported to the transparent conductive oxide (TCO) electrode where the charge is collected. The photooxidized dye is regenerated by the iodine (I^-). The triiodine (I_3^-) diffuses to the counter electrode where it is reduced back to I^-.

gap and high surface area to allow for a large quantity of dye adsorption. The common sensitizers used in DSSCs are ruthenium (Ru) complexes and the redox couple is triiodide/iodine (I_3^-/ I^-),[22-23] although successful investigations in the past 2 years have focused on a $Co^{(II/III)}$tris(bipyridyl) redox complexes[21, 24] in conjunction with an array of dye sensitizers that do not contain ruthenium.[25]

The process for photoconversion is diagramed in Figure 1.4 and begins with the sensitizer absorbing light followed by injecting its excited state electron into the conduction band (CB) of the semiconductor, generating the oxidized form of the dye. This is denoted as S^+ although the oxidized species are not necessarily positively charged. The electrons flow through the nanocrystalline semiconductor to the back electrode contact. This first step is referred to as 'injection'. The 'regeneration' step is the donation of an electron from the redox couple to the oxidized dye molecule, recovering the ground state of the dye. The oxidized form of the redox couple diffuses toward the counter electrode where it is converted back to the reduced form. The electrical circuit is completed by the electron migration through the external load.[22]

The major requirements for the dye molecule are a high molar absorptivity, a LUMO that aligns with the nanocrystalline semiconductor to allow for electron injection and a HOMO that aligns with the redox couple to promote regeneration. Ideally, the dye forms monolayers on the nanocrystalline semiconductor, eliminating the need for exciton diffusion and diminishing the nonradiative quenching often encountered with multilayer films. The high surface area of the nanocrystalline semiconductor is critical as it increases the dye adsorption, enhancing the interaction with light through the cell.[22]

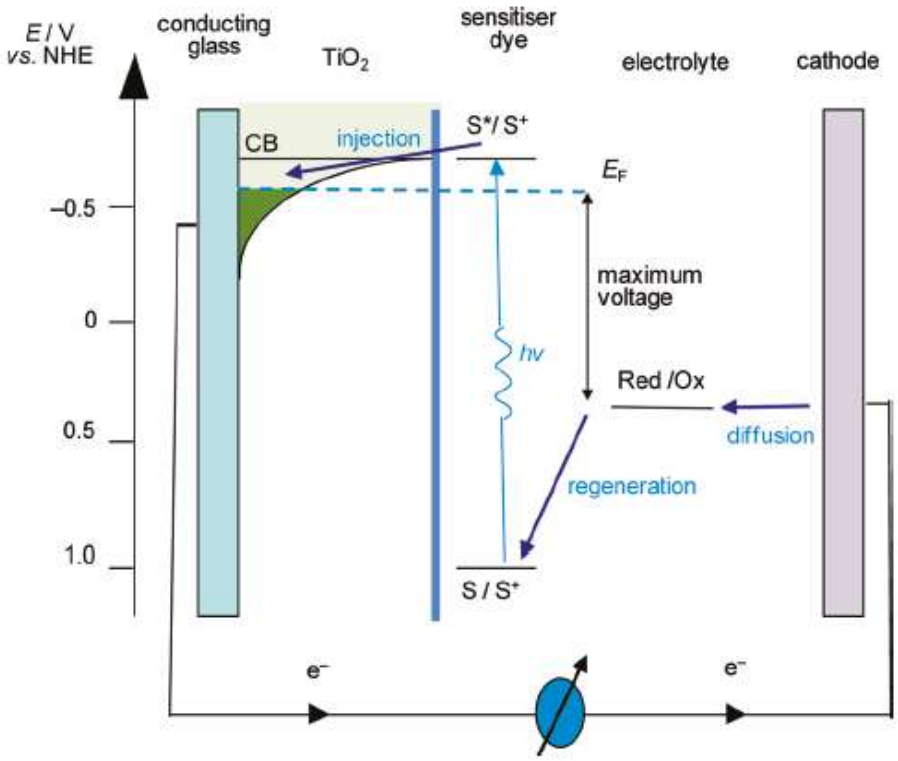

Figure 1.4 Photoconversion energy diagram for a typical DSSC. Reprinted from ref 22. Used by permission of the American Chemical Society.

Finally, the redox couple, in addition to energetic alignment with the dye molecule to regenerate the dye ground state, ideally should not accept electrons from the nanocrystalline semiconductor. The oxidized iodide mediator, I_3^-, fits this criterion.

In addition to the solar cell efficiencies (η) determined by Equation 1.2, another important metric to evaluate the sensitizer dye is the incident monochromatic photon-to-current conversion efficiency (IPCE).[23, 26] Equation 1.3 shows this relationship as the ratio between the number of electrons generated in the external circuit per incident photons as a function of wavelength. This efficiency can also be written as the product of the LHE(λ) or the light harvesting efficiency at a specific wavelength, the quantum yield for injection (φ_{inj}) and the efficiency of collection of electrons (η_{coll}). This relationship highlights the importance of the transferring of charges at metal oxide-molecule interface.[23]

$$IPCE(\lambda) = \frac{Photocurrent\ density}{Wavelength \times Photo\ flux} \tag{1.3}$$

$$= LHE(\lambda) \times \varphi_{inj} \times \eta_{coll}$$

As with OPVs, an approach to improving DSSC efficiency has been development of dye sensitizers that absorb from the visible to the near-IR to closely match the solar spectrum. Another research focus has been to replace the iodide mediator in order to increase the voltage of the DSSCs. Recently, efficiencies exceeding 12% have been accomplished with cobalt redox complexes in combination with a new design of sensitizers which covalently bind an electron donor moiety (ie. diarylamine) with an electron acceptor (ie. ethylnylbenzoic acid) through a π bridge (ie. zinc porphyrin), referred to as a D-π-A molecule.[21] In addition to synthesizing molecules with optimal

HOMO and LUMO levels to achieve the highest possible voltage, the research is focused towards the fundamental understanding of interfaces to promote forward electron transfer and to prevent competing charge recombination reactions. As with OPVs, the control over the complex and abundant DSSC interfaces is critical to moving the organics based solar devices towards commercially competitive efficiencies.

The research described herein is aimed at understating the properties which contribute to efficient charge transfer at the molecular thin film-electrode interface of an OPV. DSSC studies have focused much attention on optimizing charge injection efficiencies at the dye sensitizer – nanocrystalline metal oxide interface. The chemical questions addressed are pertinent to the molecular thin film-electrode interface and therefore relevant discussions of DSSC challenges will be presented.

1.2 Structure – Charge Transfer Relationship

Unlike solar cells made of inorganic materials where charge carriers are spontaneously generated after light absorption, organic based solar cells bring together materials and molecules in multilayer structures to convert sunlight to energy. The interfaces between these layers are essential to the efficiency of the cell because they dictate the efficiency of electron and hole separation, migration and collection at the electrodes. Researchers have outlined the optimal operation of each molecule and interface in these devices. The requirements highlight the shortcomings of current materials, but have led to fundamental investigations of what parameters at these

interfaces play a role in improving charge separation, charge transfer and overall solar cell efficiency.

In order to understand the how to optimize the device performance, it is necessary to evaluate the current knowledge of the thermodynamic and kinetic nature of the charge transfer processes at the interfaces. These principles have guided further research strategies to control these interfacial properties and device efficiency.

1.2.1 Charge Separation

As described previously, all organic based solar cells have the significant step of separating the Coulombically bound exciton into free charge carriers, (electrons and holes). In OPVs, this charge separation happens at the molecular D-A interface, and in DSSCs the dye sensitizer injects electrons into the nanocrystalline semiconductor film. In order to transfer this charge there needs to be an energy offset between the LUMO of the light absorbing molecule and the LUMO of the electron accepting molecule or the conduction band of the semiconductor.

The exciton dissociation process in OPVs is not fully understood. An energetic scheme of this process is given in Figure 1.5.[12] The working description is that it is a two step process involving a transition from the exciton state to a charge transfer state (CT), where the hole sits on the HOMO level of the donor molecule and the electron is on the LUMO level of the acceptor molecule. There are in close proximity and strongly Coulombically bound, thus the CT state is lowest in energy. From the CT state, the charges either recombine to reform the ground state or dissociate into free charge carriers

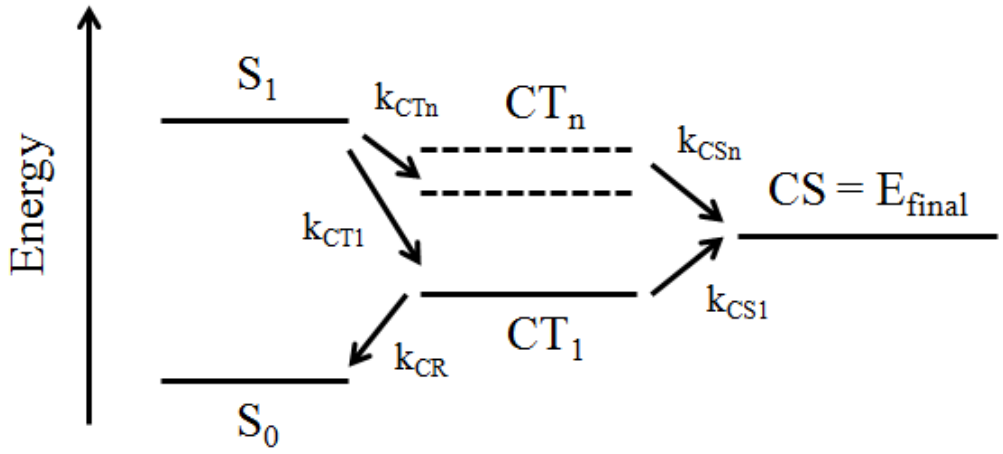

Figure 1.5 Energetic scheme of exciton dissociation. S_0 is the ground state and S_1 is the singlet excited state. The charge transfer states where the hole is on the donor molecule and the electron is on the acceptor molecule are shown as CT_n as the higher-energy state and CT_1 as the lowest energy charge transfer state. The charge separated state (CS) describes the free hole in the donor layer and the free electron in the acceptor layer. The competing charge transfer rates are denoted as k_i.

denoted as the charge separated state (CS). The energy level of the free charges is then defined by the HOMO of the donor and the LUMO of the acceptor.[12, 27] According to this scheme, the rates of charge separation must be faster than the rates of charge recombination as well as radiative and nonradiative decays to achieve exciton dissociation. Control over the electric field at these interfaces, by manipulating of the charge carrier concentration in the acceptor material, has been shown to play an important role in formation of the charge separated state.[28]

The dye sensitizers in DSSCs are covalently bound to the nanocrystalline semiconductor film in monolayers usually through a carboxylate or phosphonate group. The forward charge transfer process or electron injection into the nanocrystalline semiconductor film competes with radiative and nonradiative decay of the dye as well as quenching. Determining the conduction band of mesoporous TiO_2 is complex. The protonation of the TiO_2, as with most oxides, is dependent on the proton activity in the surrounding medium. The changes in surface charge cause a Nernstian dependence on effective pH, thus shifting the surface potential by 60 mV per pH unit when in aqueous media.[29] Surface charge is associated with conduction and valence band bending in bulk metal oxides. However, in the case of mesoporous TiO_2, the nanoparticles are too small to support band bending under electron depletion, therefore the whole conduction band shifts as a result.[22] This can significantly affect the charge injection at the dye sensitizer-semiconductor interface. Since many DSSCs are operated in organic solvents, the determination of conduction band edges is more complex. The concentration of ions,

mainly small cations such as lithium, can change the conduction band potential of TiO_2 up to 1 V.[30]

Electron injection efficiency is not solely dependent on the absolute kinetics of the charge injection process, rather it is the combination of the injection kinetics and the decay of the excited state to ground.[22] Fast electron injection requires strong electronic coupling between the LUMO of the dye sensitizer and the metal oxide conduction band, as well as a large density of states energetically accessible in the TiO_2. In model systems, electron injection occurs in ~100 picoseconds,[5] where typical singlet excited state lifetimes of dye sensitizers can vary greatly, from picoseconds to nanoseconds. Organic dyes such as coumarin and porphyrins which do not include a heavy metal center, have singlet state lifetimes of ~100 picoseconds to a few nanoseconds, and intersystem crossing (ISC) from the singlet to the triplet excited state happens in nanoseconds. In contrast, heavy metal containing compounds such as ruthenium complexes have very fast ISC on the order of <100 fs, and therefore are usually considered as triplet sensitizers. The triplet decays in these species on the order of tens to hundreds of nanoseconds.[22] Although triplet states are longer lived compared to singlet states, ranging from nanoseconds to milliseconds, they are less energetic and transfer to the TiO_2 may not be possible.

In addition to radiative and nonradiative decay, quenching pathways are another type of competing processes to charge injection. Dye aggregation on the semiconductor film has been demonstrated to enhance quenching[31] as well as increase the probability of reduction of the excited dye state by the oxidized redox couple in the electrolyte.[32]

Scientists have used these criteria to study and optimize the D-A interface as well as the dye sensitizer-metal oxide interface to promote fast and efficient charge separation and charge injection, respectively. The nature of these interfaces is complex and therefore the fundamental understanding is still evolving. There is not one optimal set of molecules to use in the devices. Rather, as one molecule shows promising results the established relationship between the structure of the interface and efficient charge transfer will help engineer the other components to achieve a device with high performance.

1.2.2 Charge Regeneration

DSSCs differ from OPVs in that they include an electrolyte solution containing a redox couple that regenerates the ground state of the dye sensitizer. This is also referred to as a charge separation step in that it moves the charges in the cell further from one another. As with the initial charge injection from the dye sensitizer into the semiconducting film, there needs to be an energy offset to thermodynamically drive the regeneration process. This is the energy difference between the midpoint reduction potential of the redox couple and the HOMO of the dye sensitizer. The efficiency of this step is evaluated by the rate of rereduction of the photooxidized dye by the redox couple in comparison to the rate of charge recombination between the photooxidized dye and the nanocrystalline semiconductor.[22]

The most commonly used redox couple is the triiodide/iodine couple due to the energy alignment with common dye sensitizers and the fact that it does not readily accept

electrons from the TiO_2 semiconductor film. The rate of regeneration is on the order of ~1 μsec,[22] therefore it can compete with the charge recombination between the dye and the semiconductor which is on the order of microseconds to milliseconds. The mechanism of charge transfer between I^- and the dye is not fully understood, with data suggesting schemes as either first or second order. Some factors influencing the rate of charge regeneration are the concentration of the redox couple[33] as well as the viscosity of the solvent.[34] The kinetics of the regeneration reaction have also been shown to depend on cations from the iodide salt that adsorb onto the TiO_2 surface. When smaller cations, such as Li^+ and Mg^{2+}, are incorporated into the DSSCs, as compared to bulkier TBA^+ ions, faster regeneration rates are achieved.[35]

It is imperative to investigate the structure-function relationship at the dye-redox couple interface, as well as the competitive nanocrystalline semiconductor film-redox couple interface, in order to intelligently engineer efficient charge transfer and inhibit charge recombination at these junctions, respectively.

1.2.3 Charge Collection

The final step in photoconversion is the collection of charges at the electrode contacts. The charge transfer at the electrode-molecule interface in OPVs is critical for the efficiency of the device, although the nature of the process is also not well understood. The common transparent conducting oxide used in OPVs is indium tin oxide (ITO) because of its good conductivity ($1 \times 10^4\ \Omega^{-1}\ cm^{-1}$), high transparency in the visible region (90%) and adhesion to substrates, such as glass or flexible substrates.[36] ITO, like

other contacts used in OPVs, is heterogeneous in both ohmicity and composition. Coupling these contacts to active materials with low charge mobilities proves detrimental for OPV performance.

In addition, ITO and other metal oxides are hydrophilic in nature rendering them chemically incompatible with the active layers which are typically non-polar organic materials.[18, 37] Controlling the surface energy and wettability of the electrodes in addition to tuning the work functions has spurred research in electrode modification. ITO has been modified with self assembled monolayers (SAMs),[38] chemisorbed small molecules such as carboxylic acids, phosphonic acids and thiols,[37, 39] as well as conductive polymers such as poly(3.4-diethoxy-thiophene):poly(styrene-sulfonate) (PEDOT/PSS)[40] to tune the electrode-molecule interface and overall showed improved device performance.[17]

As with the other charge transfer processes in the OPV, the charge collection is in competition with processes such as charge recombination and annihilation pathways. The kinetics at each of the electrodes, one collecting electrons and the other collecting holes, should match each another for optimal device efficiency. Interlayers are materials that have been used to modify the electrode surface in order to improve OPV efficiency. Some interlayers include doped small molecules, conductive polymers such as PEDOT/PSS or metal oxides.[18] Interlayers are important to improving the chemical composition of the electrodes, but an additional approach is including a degree of charge selectivity in order to increase the rate of charge harvesting at the interfaces.[18] Some metal oxides such as TiO_2 and ZnO are potential interlayer materials for OPVs to act as electron collection interlayers.

The charge collection in a DSSC is based on a diffusive process at both contacts. The oxidized redox couple must diffuse through a solution to the electrode to be rereduced. The viscosity and concentration of the electrolyte solution play a role in the rate of electron transfer to the photooxidized dye sensitizer, and rate of converting the oxidized redox couple to the reduced form.[21]

After the electron is injected into the nanocrystalline TiO_2 film, it must diffuse through the mesoporous network towards the transparent conductive oxide. The efficiency of charge collection is high when the charge transport through the TiO_2 occurs at a faster rate than the recombination of the injected electron with the photooxidized dye. The transport of charges through the TiO_2 is greatly influenced by sub-bandgap states which can trap electrons. Raising the Fermi level of the TiO_2 towards the conduction band/ fills the trap sites and allows for faster transport through the network to the electrode contact.[22, 41]

Like the other processes and interfaces in OPVs and DSSCs, charge collection with these complex materials is also not well understood. Properties at these interfaces have and continue to be investigated in order to better define the role of the molecular structure in the charge transfer kinetics. In both of these complex, multilayer devices, the efficiency of each interface is defined as the ability to promote forward charge transfer before the competing charge recombination or quenching reactions occur. The energetic alignment only is one piece of this equation. The other is the nature of the two unique materials forming an interface where the electronic coupling, among other properties,

dictate the rates of charge transfer. Therefore it is crucial to understand the fundamental nature of these interfaces in order to engineer the most efficient devices.

1.3 Strategies to Control the Interfaces

Due to the complex nature of solar cells, the efficiencies rely heavily on the individual charge transfer events at the variety of interfaces. It is clear that although molecules and electrodes demonstrate certain properties as individual species, in solution for example, creating a solid-state heterogeneous device with these same molecules does guarantee an efficient device. Scientists have developed strategies to control important interfacial properties such as the morphology,[42] chemical nature,[39, 43] electronic properties[16] and molecular orientation[44] to promote efficient charge transfer and to hinder charge recombination. As will be evident in the following examples, the charge transfer processes at the interfaces are not well understood. Therefore it is essential to conduct fundamental studies and be mindful of measurement and experimental limitations. The important parameters regarding charge transfer must then be optimized in order to produce an efficient organic based solar cell.

1.3.1 Morphology

Morphology plays a key role in the structure of the OPV and DSSC devices. The morphology can influence how molecular orbitals align and determine the electronic properties at surfaces. Controlling the morphology sheds light on ways to improve

device efficiency when considered in conjunction with the other factors influencing the structure-charge transfer relationship.

In an OPV, upon photoexcitation of the donor molecule and creation of the exciton, diffusion towards the D-A interface is limited by the lifetime of the exciton. A diffusion distance of 10 nm is typical before decay occurs.[1] The planar heterojunction geometry is not ideal for these diffusion lengths, as a common donor species such as copper-phthalocyanine (CuPc) would only have a light absorption efficiency of 14% or 26% for a single or double pass device, respectively. The optimal light absorption efficiency to balance the exciton diffusion is 86%-95%.[12] Today the highest efficiency OPVs are achieved by mixing the semiconducting donor and acceptors to form a bulk heterojunction (BHJ). The first demonstration of this adaption was in 1991 by Yokoyama and co-workers via codeposition of two molecular materials.[45] In 1995 the Heeger research group made mixed donor and acceptor blends to deposit attaining efficiencies of 2.9%.[42]

In a BHJ, the interpenetration of the donor and acceptor molecular blends creates a large D-A interface to ensure short exciton diffusion distances and as a result, exciton dissociation has a high quantum yield. The morphology of the molecular domains, defining the interface between the donor and acceptor materials, plays an important role in exciton dissociation but also in electron and hole transport away from the interface to prevent charge recombination. With molecular modeling, assigning exciton diffusion lengths from 10-20 nm, it was determined that for the best OPV performance, the optimal domain size in the phase separated morphology should be less than 50 nm.[46] In another

study that investigated the phase segregation, varying the thicknesses of mixed donor and acceptor molecules showed that finer BHJ morphology obtained in the thicker films resulted in a greater degree of charge separation between the species. This study took into account the exciton quenching via the electrodes which does not result in electrical current.[47]

The phase separation and crystallinity of the active layers of the BHJs are important for charge separation and charge transport towards the electrodes. So in addition to the requirements that the D-A interface must have an offset between the LUMO levels to allow for exciton dissociation, the D-A interface must have a morphology to ensure short exciton diffusion distances and rapid charge migration to the electrodes.[12]

The nanocrystalline semiconductor films in DSSCs, typically TiO_2, have been used from the onset to create a high surface area platform for adsorption of the dye sensitizers and to create a continuous network for charge transport to the electrode contact.[19] As described in Section 1.2.1, the properties of the nanocrystalline metal oxide do not mirror behavior of a bulk metal oxide film in regards to surface charges causing changes in the conduction band of the semiconductor. Galoppini and co-workers have recently investigated TiO_2 nanotube arrays (NTAs) as an alternative morphology to the nanocrystalline films.[48] Zinc porphyrins were tethered to the inner diameter of the nanotubes and the incident photon-to-current efficiencies (IPCE) were measured. The IPCE values compared favorably to literature values of the best performing DSSCs with nanocrystalline films. It is hypothesized that the vectorial injection of electrons is more

efficient pathway to the electrode contact, as a result of the controlled NTA morphology. The photoelectrochemical performance was also assessed as a function of inner nanotube diameter. The largest diameter of 120 nm was found to perform better than the ~55 nm and ~70 nm diameter nanotubes and has been attributed partially to better accessibility for the triiodide/iodine redox couple to regenerate the oxidized dye molecules.[48]

These examples of controlling the morphology demonstrate that it has a direct impact on the charge separation, transport and collection in organic solar cells. More investigations are needed to build the entire picture of the structure-charge transfer relationship and work towards increased solar cell efficiencies.

1.3.2 Chemical Nature

It is well known that the chemical properties of OPV and DSSC interfaces play a role in efficient charge transfer and charge collection. Strong electronic coupling is necessary between molecules for charge transfer to occur, and this coupling is dictated by overlapping of molecular orbitals. The chemical nature of the D-A and the electrode-molecule interface also affect the compatibility of the components, which has proven to be important in BHJ OPVs. Strong intermolecular interactions such as dipole-dipole and Van der Waals interactions between the electrode and molecular films are important for long term stability and coupling at the interfaces.[39] It is important to control these properties to promote forward transfer of charges in devices.

As previously discussed, ITO is the typical transparent conducting oxide most frequently used in OPVs, despite chemical incompatibility with most non-polar organic

active materials. The surface of ITO, like other metal oxides, is hydrophilic with exposed polar oxo and hydroxyl groups.[43] Hotchkiss *et al.* investigated surface modifications with a series of phosphonic acid functionalized small molecules (fluorinated benzyl) to control the wettability and tune the ITO work function by adjusting the molecular surface dipole.[39] An adsorbed molecule with the negative pole directed outwards resulted in an increase in the local work function, where a negative pole pointing inward showed a decrease in the local work function of ITO. The work function was effectively tuned by ~1.2 eV depending on the molecule used, which matched well with the theoretical calculations. The surface energy of ITO was lowered from 56 and 71 mJ/m^2 (detergent and oxygen plasma cleaned, respectively) with this family of small molecules to relatively similar energies (35-38 mJ/m^2). This demonstrated that the work function can be quasi-independently tuned from the surface energy.[39] This adjustment of the interfacial properties may have a significant impact on the chemical and thermodynamic aspects of interfacial charge transfer.

The charge injection process in DSSCs is relies on the energy level alignment of the dye sensitizer and the nanocrystalline semiconductor film, and is in competition with the excited state decay and quenching reactions. Typically, aggregation of dye sensitizers is avoided due to increased probability for quenching,[31] but research by Watson and co-workers has demonstrated with chalcogenorhodamine dyes that H-aggregation leads to increases in light harvesting efficiencies and electron injection yields.[44] The adsorption of the dyes to the surface of the nanocrystalline TiO_2 was through a carboxylated thienyl group which controlled the molecular orientation of the molecules on the surface.

Although the more studies need to be conducted to investigate these results, they hypothesized that the 2-to-3 fold charge injection yield may arise from the excited state charge migration through the monolayers of H-aggregated dyes to find localized TiO_2 hot spots. Another possibility could be the higher-energy excited states of the H-aggregated dyes or a possible increased charge-separated state lifetime to compete with the charge recombination reactions.[44] These studies highlight the utilization of control over molecular orientation to control the extent of dye aggregation on the surface. Both of these properties have direct impacts on the charge transfer process at this interface.

In DSSCs, the dye sensitizers are covalently bound to the nanocrystalline semiconducting metal oxides typically through either a carboxylate or phosphonate group. It has been demonstrated that a delocalization of the dye's LUMO orbital over the carboxylate anchoring group helps to promote electron injection into the metal oxide.[19, 49] Although the phosphonate group has shown the most stability in aqueous electrolytes,[50] the carboxylate group is the most widely used and demonstrated the highest DSSC efficiencies.[21, 26] Willig and co-workers found time constants of 13 and 28 fs for electron transfer when studying carboxylate and phosphonate anchoring groups, respectively.[51]

Another factor that has been shown to affect the charge injection rate is the conjugation of a spacer between the dye and the anchor group. One study demonstrated that with a -CH2-CH2- spacer between the perylene sensitizer and the carboxylate tethering group, the charge injection time constant slowed to 57 fs, where without the spacer or with an unsaturated spacer –CH=CH-, the electron injection time constant was 13 fs.[52] Other systematic studies have shown that the increase spacer length of

unconjugated linker groups, positioned between the dye and the anchor group decrease the injection rate due to the greater through space tunneling distance between the dye and the semiconductor film.[53] A new approach to DSSC sensitizers is to employ a covalently bound D –π- A to incorporate hydrogen bonding to increase electron injection at the metal oxide interface.[54]

The chemical nature of these interfaces impacts the charge transfer because it influences the overlap of molecular orbitals, surface energies and ultimately the energy alignment and rates of charge transfer. The complexity of the interfaces, molecules and materials within these devices requires attention to the fundamental principles in order to engineer efficient solar cells.

1.3.3 Electronic Properties

The electronic nature of the electrodes and interfaces in OPVs and DSSCs are important to the charge transfer events. The energy alignment between all the materials and molecules in the OPV and DSSC must be suited to move electrons in one direction to achieve a photocurrent. This is evident in the energy level diagrams in Figures 1.2 and 1.4. As discussed previously, the HOMO and LUMO levels of the semiconducting molecules and the work functions of the electrodes can be determined as individually, but this often does not reflect the behavior as solid-state multilayer films are formed.

For OPVs, simple theoretical predictions for ideal solar cell behavior often assume that the electrode contacts are homogeneous and ohmic over a large area. In practice, the heterogeneity both in ohmicity and composition of typical electrodes (ITO

for example) in an OPV platform result in higher degrees of charge recombination and overall decreased efficiencies.[55] The ideal process for any photovoltaic platform is that the rate of electron collection at one electrode matches the rate of hole collection at the opposite electrode. Interlayers between the electrode-molecular interface could offer the benefits of compositional and electrically control to improve charge harvesting. Depending on the electronic nature, the interlayers have the potential to provide thermodynamic and kinetic charge selectivity at these critical interfaces.[18]

In section 1.3.2 the surface modification of ITO had an impact on the surface energy, thus the wettability of the electrode but it also served to tune the work function.[39] This demonstrates how closely tied these properties are to one another. A change in the chemical nature of the interface also affects the electronic structure.

This charge selectivity as discussed for OPVs already plays a major role in DSSCs, utilizing nanocrystalline semiconducting films such as TiO_2 and ZnO for electron collection.[23] The large bandgaps of these materials align with the dye sensitizer and have demonstrated relatively insufficient alignment to donate to or accept electrons from the I_3^-/I^- redox couple. In order to increase the V_{OC}, DSSC research is moving towards replacing I_3^-/I^- with a redox couple with a more positive midpoint potential (E^0), such as $Co^{(II/III)}$tris(bipyridyl).[21, 25] The energetic alignment between this redox couple and the semiconductor increase the possibility for charge recombination, therefore it has been proposed that a future strategy would be adding an insulating layer to the TiO_2 to diminish the charge transfer at this interface.[25]

1.3.4 Molecular Orientation

The molecular orientation of molecules at the metal oxide interface has already been described to play a role in the aggregation of dye sensitizer molecules on TiO_2, leading to increased charge injection rates.[44] Other scientists have recognized that the distance between the molecule and the metal oxide, as determined by molecular orientation is an important factor in controlling the through space electron transfer.

As previously discussed, Galoppini and co-workers investigated TiO_2 nanotube arrays (NTAs) to investigate a different morphology of the semiconductor film, but they also examined the dye sensitizer binding, aggregation and molecular orientation on the IPCE. They used a series of zinc-(tetraphenyl)porphyrins with carboxylic acid anchor groups positioned at different carbon bonds of the phenyl ring to control the adsorbed molecular orientation. The porphyrins that gave the best photocurrent conversion were designed to adsorb to the TiO_2 NTAs in a 'spider-like' fashion, with porphyrin ring in-plane to the metal oxide surface.[48] The increased IPCE is not fully understood, except with the conclusion that molecular orientation plays a role in efficient charge transfer.

Charge transfer rates of a zinc phthalocyanine bound to ITO as a function of orientation and aggregation were studied by Lin *et.al.*[37] The monolayers were formed on ITO via a phosphonic acid group and contained aggregated and monomeric populations with a distribution of molecular orientations. Electrochemical and spectroelectrochemical measurements demonstrated that the aggregated species exhibited faster charge transfer rates as compared to the monomeric species, largely in part to the lower reorganization energy needed for electron transfer of the aggregate to the ITO.

Potential-modulated attenuated total reflection allowed for orientation-dependent charge transfer to be measured, showing that the in-plane aggregates had a 3-fold faster transfer rate than the upright aggregates.[37] The ITO heterogeneity plays a role in the distance of the macrocycle of the molecule to the ITO. The through space electron tunneling distance of the in-plane aggregate to the ITO was deemed shorter as compared to the upright aggregate, which resulted in a faster charge transfer rate.

These studies help to examine the key properties associated with efficient charge transfer. Researchers have controlled many aspects of the interfaces in order to understand how these will affect solar cell efficiency.

1.4 Photoinduced Kinetics

Scientists have aimed to control the properties at these critical interfaces in order to study the effects on the charge transfer and the solar cell efficiency. Photoconversion is initiated by the absorption of a photon to promote an electron to an excited state. This excited state may thermally decay or ISC to a triplet state. If the circumstances are favorable, this high energy electron can move downhill in energy to occupy a lower lying energy level of a different molecule or material. This thermodynamic process continues until the electron is extracted or it decays back to the energy level of the ground state. The movement of charges through the network of molecules creates a series of transient species. In order to understand the predominant path of the charge takes through these molecules and materials it is necessary to monitor the existence and lifetimes of the short-lived, transient species. As evident through the studies described, properties such as

morphology, molecular orientation, chemical and electronic nature impact the charge transfer pathways, although the mechanisms are not fully understood. Therefore, it is necessary to measure the transient species that result from photoinduced excitation as a function of these properties.

1.4.1 Transient Absorbance Spectroscopy

In OPVs and DSSCs the forward charge transfer and competing pathways occur on the order of femto- to milliseconds.[12, 22] An ultrafast measurement technique is required to monitor the migration of charges through the materials as well as the formation of new species. Transient absorbance spectroscopy can be utilized to measure these transient states.

Transient absorbance spectroscopy involves two sources of light, an excitation and monitoring source. The excitation beam is a short, high energy laser pulse and dictates the fastest time scale that can be detected. For example, a 5-7 nanosecond pulse width allows for decay times of tens of nanoseconds to be measured. Typically, multiple transient absorbance experiments are conducted at once and signals are averaged. In this case, the repetition rate of the laser controls the slowest time scale that can be measured. The individual transient experiment must be concluded before the next laser pulse arrives to the sample. A laser with a 10 Hz repetition rate can take measure transient signals out to 100 milliseconds. The monitoring beam can be either a steady state source or a probe pulse. The steady state monitoring source is focused on for the purpose of describing of

the transient absorbance principles. The probe pulse is used in ultrafast transient absorbance instruments (~100 fs time resolution) and discussed in Appendix B.

The excitation laser pulse is absorbed by a fraction of molecules in the ground state and promoted to an electronically excited state. If the excited states or transient states have energetically allowed transitions, these species can absorb light from the monitoring source. An energy level schematic of this process is shown in Figure 1.6. The intensity of the monitoring beam is much weaker than the excitation source, so the excited state population is not appreciably affected by the absorption of the monitoring source.

The absorbance of the monitoring source is detected as a function of time. The transient curves are reported as a difference absorbance, denoted as ΔA, as a function of time at a single wavelength of light. Another way to present the transient data is with a difference absorbance spectrum, with ΔA as a function of wavelength at a given delay time between the excitation and the monitoring beam.

There are several states that contribute to the ΔA spectrum. The first is the ground state bleach, which appears as a negative ΔA. When the excitation source interacts with the molecules, a significant fraction is promoted to the excited state, depleting the ground state. If the ground state becomes repopulated through the course of the experiment, the transient curve as a function of time is referred to as a recovery curve. The second potential contribution is the excited state absorption or a charge transfer product which is a positive ΔA in the spectrum. The ΔA as a function of time can appear as an increase of

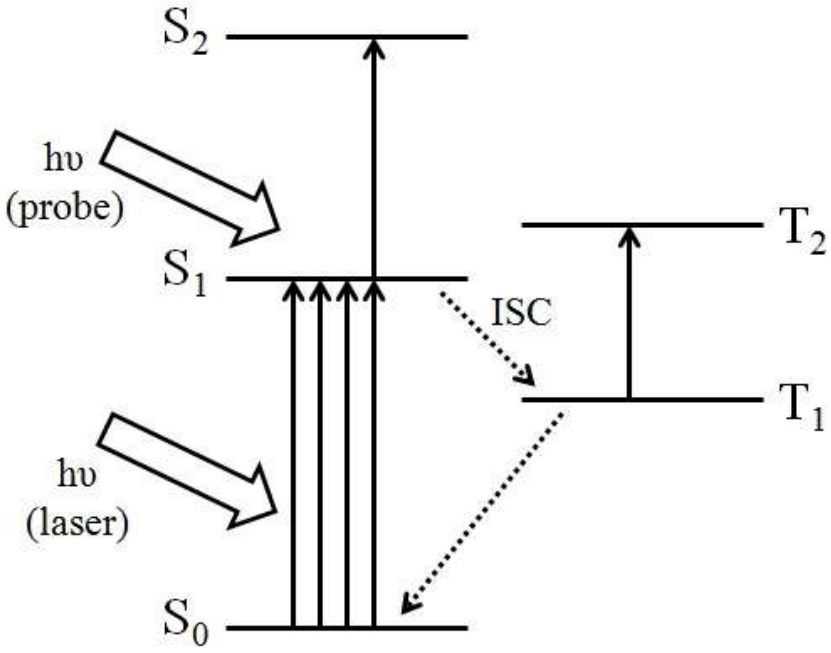

Figure 1.6 Schematic of transient absorbance energetic diagram. The singlet ground state is denoted as S_0. The laser light promotes a large fraction of molecule to the singlet excited state (S_1) where they can intersystem cross (ISC) to the triplet excited state (T_1) or reside in the S_1 state. The light from the probe source is absorbed by the populated S_1 or T_1 state where it is promoted to S_2 and T_2 electronic energy levels. The excited states can then decay back to repopulate S_0.

ΔA as the transient state is populated followed by a decrease which is associated with the decay of the excited state or charge transfer product.

Typical transient absorbance measurements are conducted in a transmission geometry. The pathlength of light or the sample concentration can be increased in order to increase the sensitivity of the experiments. Scientists studying DSSCs adsorb dye to nanocrystalline metal oxides materials to study dye sensitizer injection and recombination kinetics.[5] Although a monolayer of dye is adsorbed to the nanocrystalline metal oxide, these experiments are unable to access specific interfacial properties of the molecular film such as molecular orientation. The planar electrode contacts in OPVs pose different challenges, since the molecules in the cell are in the solid-state. Charge transfer at the molecular thin film/TCO interface is hypothesized to be controlled by the properties such as molecular orientation, morphology, chemical environment and electrochemical contact between the monolayer of molecules in contact with the TCO. An interface sensitive technique must be employed in order to study the molecular thin film/TCO interface relevant to the OPV geometry. In this research, an instrument was developed coupling transient absorbance spectroscopy (TAS) to attenuated total reflectance (ATR) spectroscopy in order to improve our understanding of the structure-function relationship at the molecular thin film/TCO interface.

1.4.2 Total Internal Reflection

Attenuated total reflection (ATR) spectroscopies are used understand the properties at interfaces.[56] ATR is based on the total internal reflection phenomenon

which occurs when light passes from a high refractive index material (η_1) to a lower refractive index material (η_2) at an incidence angle that is equal to or greater than the critical angle. The critical angle (θ_C) is defined by Snell's law shown in equation 1.4.

$$\eta_1 \sin \theta_C = \eta_2 \sin 90° \quad (1.4)$$

The ATR geometry is shown in Figure 1.7 where light is coupled into the internal reflection element (IRE) with a prism and at each reflection at the substrate/medium interface, an evanescent field extends into the medium with an exponential decay. The depth of penetration into the medium is defined in equation 1.5 and is dependent on the angle of internal reflection (θ_i), the indices of refraction of the IRE (η_1) and medium (η_2) and the wavelength of light (λ).[57]

$$d_p = (\lambda/4\pi\eta_2)[\sin^2\theta-(\eta_1/\eta_2)^2]^{-1/2} \quad (1.5)$$

Due to the evanescent decay, ATR spectroscopy is highly surface sensitive, as molecules closer to the surface attenuate the light to a greater extent than those in further into the bulk, beyond the evanescent field.

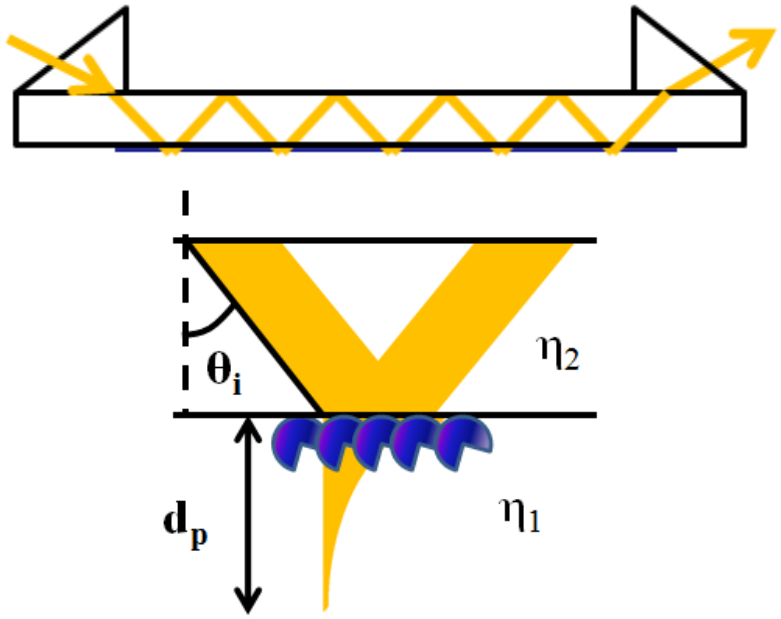

Figure 1.7 Schematic of the ATR geometry and the evanescent field. Light is coupled into and out of the internal reflection element (IRE) via prisms. The internal reflection angle is denoted at θ_i, the indices of refraction of the IRE and the medium are η_2 and η_1, respectively. The depth of penetration is denoted as d_p.

1.5 Overview of Experiments

The research described in this dissertation investigates the properties that contribute to efficient charge transfer at interfaces. The measurements of the kinetics specifically at the interfaces required the design and evaluation of an innovative instrument, coupling transient absorbance spectroscopy to the ATR geometry. The most sensitive measurements of this type to date were achieved by measuring the photoinduced kinetics of submonolayer films of bacteriorhodopsin (Chapter 2).

The molecular thin film/TCO interface was studied with zinc porphyrin molecules tethered to ITO (Chapter 3). The electrochemical, molecular orientation and surface coverage properties for zinc porphyrin adsorbed to ITO through a carboxylic acid and phosphonic acid group were characterized. These data indicate significant aggregation of the zinc porphyrin on the ITO. The inability to monitor charge transfer kinetics at the zinc porphyrin-ITO interface, even when presumably controlling the driving force with applied potential, led to the hypothesis that the excited state kinetics of zinc porphyrin were altered as a result of its local molecular environment. Monolayer and multilayer thin films of zinc porphyrin were investigated in order to understand the effects of the solid-state composition on the excited state lifetimes. The zinc porphyrin aggregation possibly affects the triplet state decay, intersystem crossing efficiency, and the potential for interporphyrin electron and energy transfer. Overall, zinc porphyrin was found to be more susceptible to quenching as a result of aggregation as compared to palladium porphyrin.

Photoinduced charge and energy transfer are also important in other photoconversion processes such as water-splitting. As with OPVs and DSSCs, the forward charge transfer competes with the decay and recombination pathways. One strategy to control the charge transfer at the interfaces is to create an organized molecular assembly where the electron transfer path is well-defined. Inorganic nanosheets are a unique material utilized in recent years in multilayer films which can control intermolecular distances as well as participate in the electron transfer process.[58-59] The role of the nanosheets in the charge transfer process between an electron donor (palladium porphyrin) and electron acceptor (poly(viologen)) on a planar geometry was investigated. The incorporation of nanosheets without the electron acceptor led to stabilization of the porphyrin triplet state. Although concrete evidence was not achieved for charge transfer, when the 'active' nanosheets were treated to presumably align their band energy between the band energies of the electron donor and acceptor, significant quenching of the palladium porphyrin triplet state was observed, suggesting nanosheet participation in charge transfer. The complexity of these molecular solid-state films, i.e. their chemical properties and intermolecular interactions, highlight the importance of gaining a fundamental understanding of their effects on photoexcited state and charge transfer processes. (Chapter 4).

2. MEASURING PHOTOCHEMICAL KINETICS IN SUBMONOLAYER FILMS OF BACTERIORHODOPSIN AND EVALUATION OF TRANSIENT ATR INSTRUMENT PERFORMANCE

2.1 Introduction

As discussed in Chapter 1 a major goal of this research is to develop an analytical tool to understand the reaction kinetics of molecular thin films. Transient absorbance spectroscopy (TAS) combined with attenuated total reflectance (ATR) spectroscopy in a multiple reflection planar waveguide geometry is an effective strategy to increase the optical pathlength of the thin film absorbance measurements. As a first step, the performance of the instrument was evaluated using a thin film composed of purple membrane (PM) fragments containing bacteriorhodopsin deposited onto PDAC, a positively charged polymer.

2.2 Transient Absorbance / ATR Instrumental Set-up

2.2.1 Instrumental Diagram

The design of the TAS/ATR instrument is illustrated in Figure 2.1. It was constructed in part from selected components of a commercially available waveguide spectrometer (SIS-5000, System Instruments, Japan) and a TAS instrument (Proteus, Ultrafast Systems). The pump source is a Nd:YAG pulsed laser (Continuum) at 532 nm, with a pulse width of 5-7 ns at 10 Hz. The probe beam is a Xe lamp (Newport) coupled to a

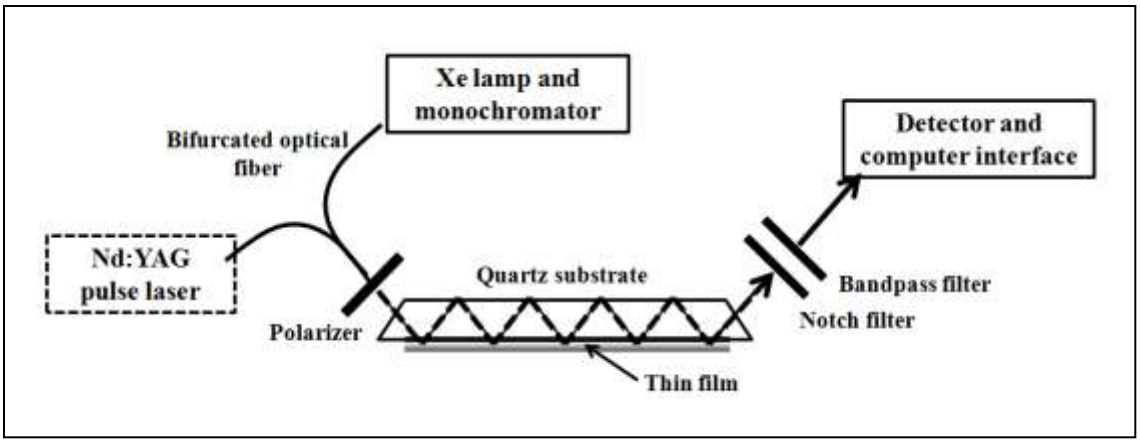

Figure 2.1 Schematic showing major optical components of the TAS/ATR instrument.

monochromator. Focusing optics are used to couple the pump and probe beams into a bifurcated optical fiber bundle where the common output is directed through a polarizer and into the end face of the planar waveguide. The polarizer is used to select transverse electric (TE) or transverse magnetic (TM) polarized light. The waveguide substrate is a 200 μm thick quartz slide with the end faces polished at an internal angle of 60° (Systems Instruments, Japan).

A second optical fiber collects the light exiting the waveguide and directs it to a Si photodiode detector. A 532 nm notch filter attenuates the excitation pulse along with a bandpass filter with a transmission maximum at the monitoring wavelength. The detector output signal is amplified with a variable gain current amplifier (FEMTO) and recorded on a digital oscilloscope on which multiple traces are accumulated for signal averaging. The resulting kinetic trace is converted to a difference absorbance through the Proteus software and the curve is fit with the program Surface Xplorer (Ultrafast Systems).

The planar waveguide is mounted on the x-y stage of the SIS-5000 spectrometer. The launch and collection optical fibers are mounted on goniometers in the spectrometer, which allows the launch and collection angles between the optical fibers and the waveguide to be adjusted independently. The SIS-5000 is also equipped with an internal Xe lamp and CCD detector that allow steady-state ATR spectra to be measured independent of the TAS portion of the instrument. The components of the transient ATR instrument are labeled in the picture in Figure 2.2.

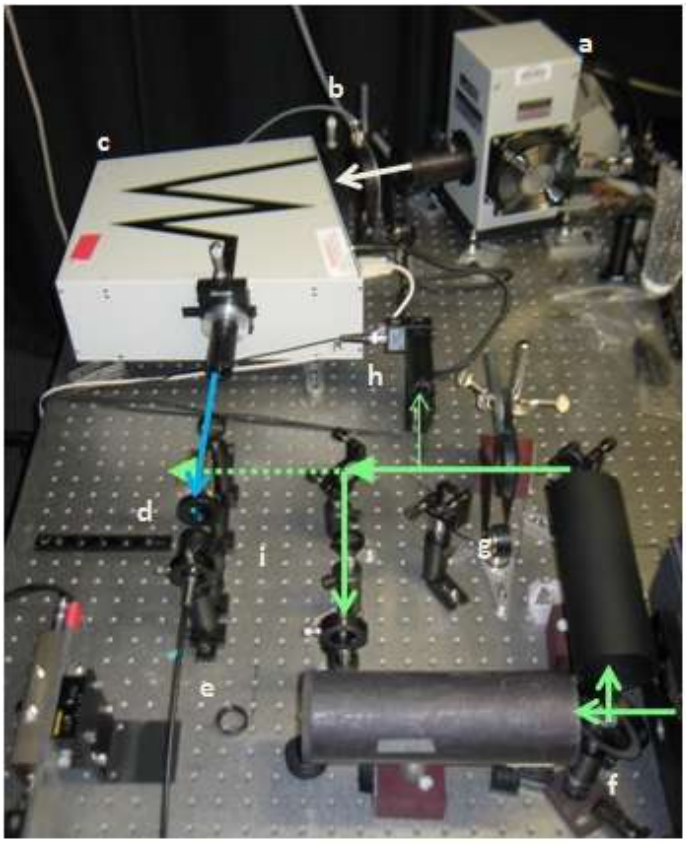

a. 150 W Xe lamp
b. Shutter
c. Monochromator
d. Focusing optics
e. Bifurcated optical fiber bundle
f. Nd:YAG laser and beamsplitter
g. Shutter
h. Diode for timing
i. Focusing optics for ATR experiment

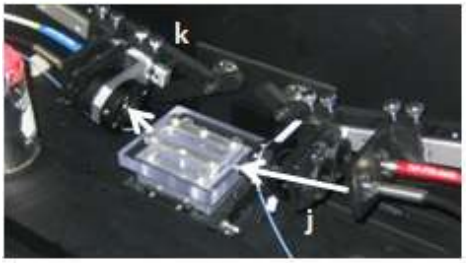

j. Light input for ATR element: optical fiber connection and polarizer on goniometer
k. Light output for ATR element: Notch and bandpass filter on goniometer

l. Diode detector
m. Variable gain current amplifier

Figure 2.2 Transient ATR (Proteus) bench and components.

2.2.2 Design of the Flowcell

A custom fabricated flow cell allows solutions in contact with the upper surface of the waveguide to be exchanged. A diagram of the flow cell is outlined in Figure 2.3. The design of the flow cell had to account for lack of translation in the z direction in the SIS-5000 spectrophotometer. Other considerations were exposing the polished edges of the quartz slides and obtaining a long interaction path of the film with the waveguide. A picture of the flow cell mounted in the SIS-5000 spectrophotometer is shown in Figure 2.4.

2.3 Experimental

2.3.1 Purification of Purple Membrane Fragments

PM fragments were isolated from Halobacterium salinarium (ATCC #29341) using standard procedures.[60] The freeze-dried bacteria were suspended in a cassin medium (4.3 M NaCl, 83 mM $MgSO_4$, 27 mM KCl, 10 mM trisodium citrate, 10 g/L Oxoid Bacteriological L-37 or Bacto-Peptone, Difco Technical Grade peptone). The bacteria was divided into aliquots containing 0.5 mg of bacteria and stored at -80°C. The growth medium is also the cassin medium. The medium was autoclaved and set up in a paraffin bath at 40°C. An aliquot of the bacteria was added to the medium and stirred with a stir bar. A white light shined directly on the culture, and was set on a timer for 12-hour on/off cycles.

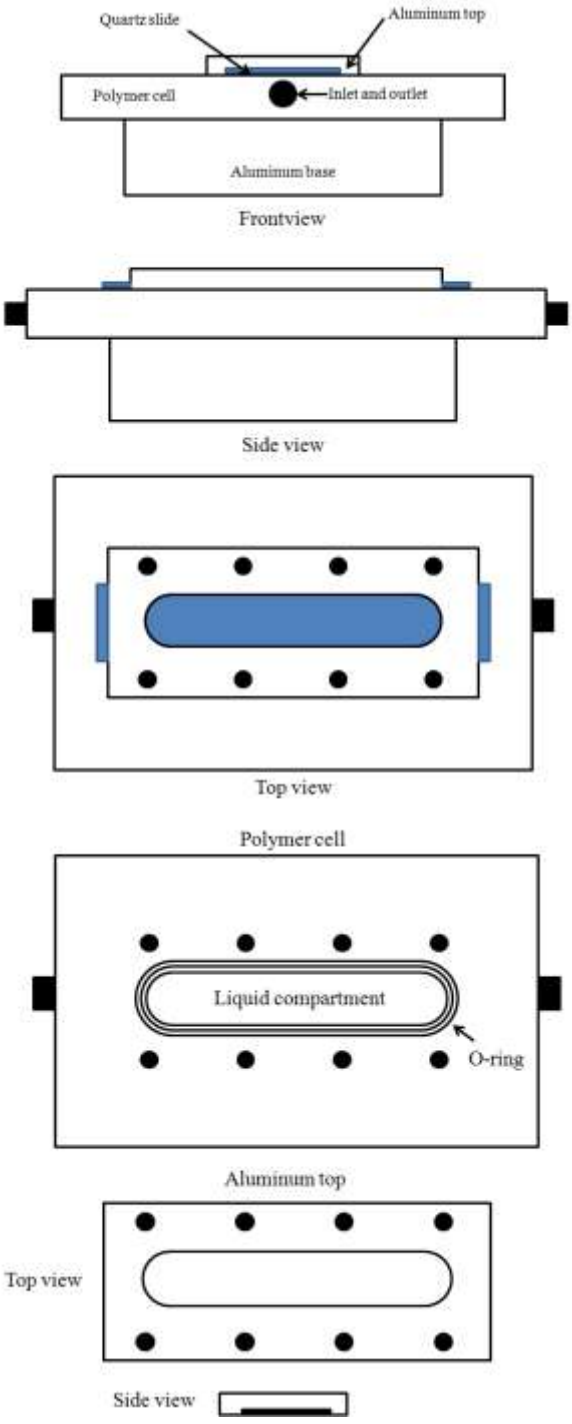

Figure 2.3 Diagram of flowcell for SIS-5000 spectrophotometer.

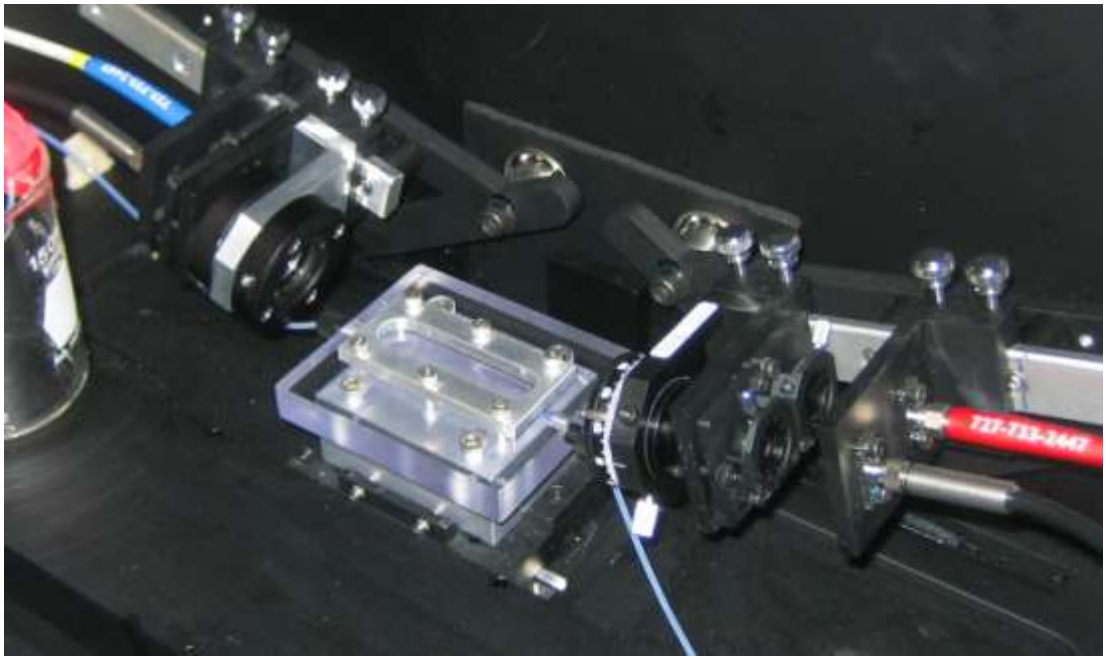

Figure 2.4 Custom fabricated flowcell mounted in the SIS-5000 spectrophotometer.

The growth of the bacteria and protein was monitored by transferring aliquots of the culture into a cuvet and measuring the absorbance with a UV-Vis spectrophotometer (SI Photonics) at the wavelengths of 660 nm and 560 nm, respectively. The grown culture itself appears pink in color. The bacterial culture was grown for 2 weeks, at which point a 1 mL aliquot was added to a new flask of medium to start another culture. The bacteria cells were harvested by centrifugation for 15 min at 13,000 g at 4°C. The cells were suspended in a basal salt solution (cassin medium without peptone) and 600 units of DNase (Sigma #D5025) were added. The cells were lysed by dialyzing (6-8,000 MWCO membrane) overnight against 0.1 M NaCl at 4°C. The red lysates were washed by centrifugation at 40,000 g for 40 min at 4°C, after which the red supernatant was decanted and the reddish purple sediment was suspended in 0.1 M NaCl. This was repeated for a total of 3 centrifugations.

The supernatant at the end of this process appeared colorless. The sediment was then suspended in nanopure water and washed in this same fashion another 3 times, discarding the supernatant and suspending the sediment. The final sediment was suspended in a small volume of nanopure water and layered over a sucrose gradient (30%-50%). The sucrose gradients were centrifuged for 17 hours at 100,000 g at 4°C. Figure 2.5 shows an example of one of the tubes after the centrifugation. The large purple band in the middle has the highest amount of pure protein at the buoyant density of 1.18g/cm^3, so this was collected first. A smaller purple band at a higher density was sometimes present. This band was also collected but kept separate from the other protein.

Figure 2.5 Band of purple membrane fragments after sucrose gradient centrifugation.

The protein bands were collected into separate centrifuge tubes and the sucrose was diluted by adding nanopure water and centrifuging at 50,000 g for 30 min. The clear supernatant was poured off and the purple membrane (PM) fragments were suspended in nanopure water and diluted/centrifuged for a total of 4 times. After the final centrifugation, the PM fragments were suspended in 50 mM HEPES buffer, pH 8.0.

UV-Vis spectroscopy was used to determine the purity and concentration of the PM fragments. The ratio of 280/560 nm gave a value for purity around 2.0. A UV-Vis spectrum of the purple membrane fragments is shown in Figure 2.6. The concentration was determined using the molar absorptivity of bacteriorhodopsin of 63,000 $M^{-1}cm^{-1}$ at 563 nm[61] and the molecular mass 26 kD. The protein concentration used for the experiments was 0.5 mg/mL.

2.3.2 Background to Layer by Layer (LbL) Assembly

Electrostatic layer by layer assembly is a convenient method to create multilayer films with directional control. This method was first developed by Decher and Hong in 1991.[62] The polyanions and polycations are sequentially adsorbed to a substrate and allow for small, charged molecules to adhere to the substrate surface. One challenge is that when depositing linear polyelectrolytes, the layers mix and the molecular boundaries are described as "fuzzy".[63]

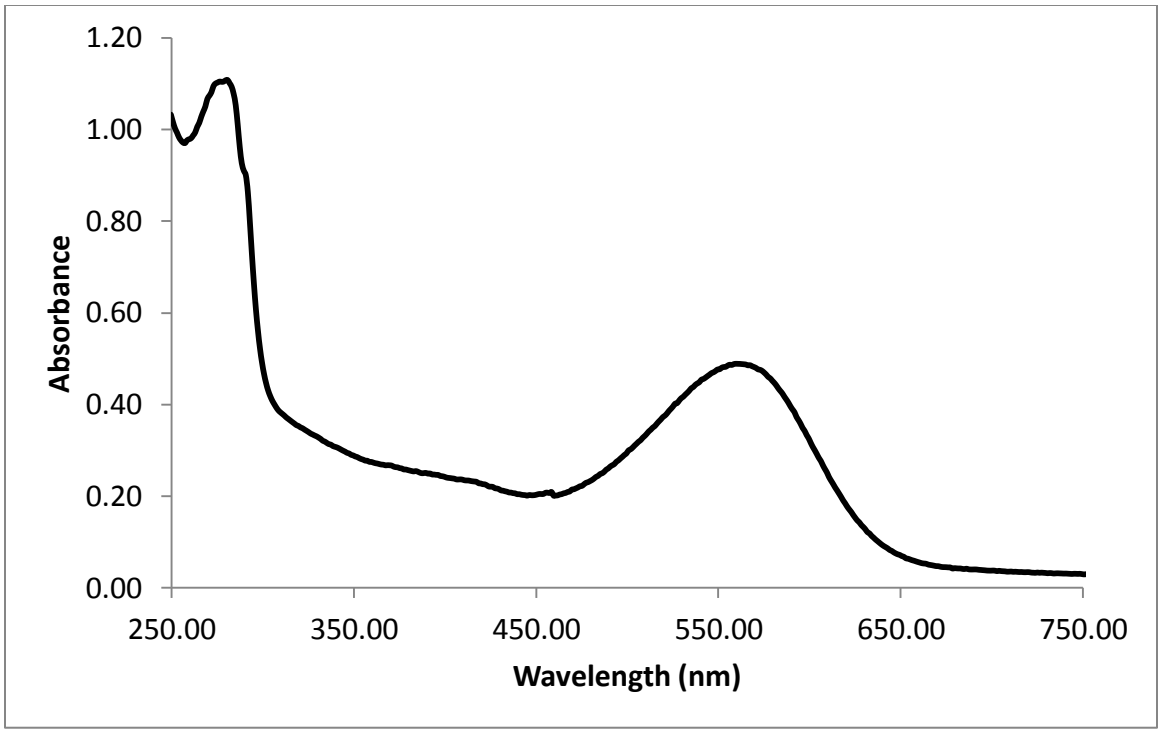

Figure 2.6 An example UV-Vis spectrum of PM fragments after purification. The ratio of the absorbance of 280/560 is used to determine the purity. This ratio represents the protein purity, and generally has a value close to 2.0.

2.3.2a Film Preparation by Electrostatic Layer by Layer Deposition

The quartz waveguides were cleaned with 2% Micro90® cleaning solution (International Products Corporation), rinsed with water (Barnstead Nanopure system, 18 MΩ•cm resistivity), soaked in piranha (7:3, sulfuric acid: 30% hydrogen peroxide) for 15 minutes, rinsed with water and dried under a N_2 stream. The slides were cleaned immediately prior to use. A 2 mg/mL solution of the positively charged polyelectrolyte, poly(diallyldimethylammonium chloride) (PDAC, Sigma Aldrich, average MW 200,000-350,000 g/mol, dissolved in water) was prepared in 50 mM phosphate buffer, pH 6.8, 0.5 M NaCl. The cleaned waveguide was exposed to the PDAC solution for 5 minutes, then thoroughly rinsed with water and dried with a stream of N_2. The flow cell was assembled and filled with 50 mM HEPES buffer, pH 8.0. A reference spectrum was acquired before injecting PM fragments (0.5 mg/mL) into the flow cell. After incubation for 30 minutes, the flow cell was then rinsed with 50 mM HEPES buffer pH 8.0, generating the adsorbed PM film. The electrostatic layer by layer film is depicted in Figure 2.7.

2.3.3 Steady State ATR

Due to the low signal quality of the CCD in the SIS-5000 instrument, the spectra were acquired on the separate CCD camera (Andor) that was connected to a monochromator (Newport).

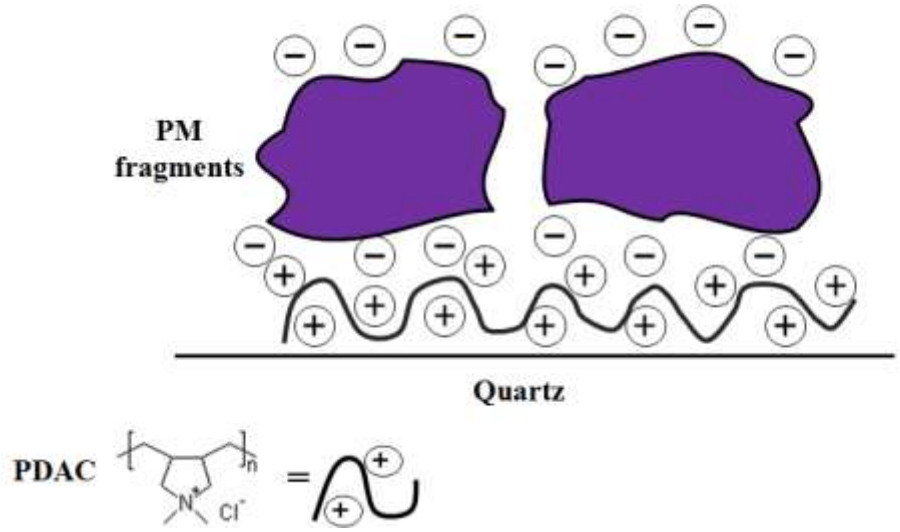

Figure 2.7 Illustration of electrostatic layer by layer deposition of PDAC/PM fragments on quartz substrate.

2.3.4 Transient Spectroscopy (ATR and Solution)

The operation of the Proteus transient absorbance instrument is described in Appendix A. The solution and ATR transient experiments conducted here utilized a 410 nm bandpass filter immediately before coupling into the photodiode. This is illustrated as position k in Figure 2.2. The variable amplifier was set to high speed setting with gains of 10^4 and 10^8 for the solution and ATR experiments, respectively.

2.3.5 Ellipsometry

A silicon wafer with aluminum backing was cleaned in the same fashion as the quartz waveguides, and then a PDAC/PM fragment film was deposited as described above. After deposition of the PM fragments, the film was rinsed with 50 mM HEPES buffer pH 8.0 and blown dry with a stream of N_2. Measurements were taken on the cleaned wafer and after application of each adsorbed layer using a Sentech Instruments GmbH ellipsometer at 632.8 nm and an incident angle of 70 degrees. Three measurements were acquired and averaged in different locations on the wafer. To estimate film thickness, the following real (*n*) and imaginary (*k*) indices of refraction were used: (1.46, 0), (1.375, 0), and (1.52, 0.004) for the silicon, PDAC and PM fragments, respectively. The real index of refraction for a PM film was determined by Ormos et al.[64] The *k* value was calculated using $\varepsilon = 10{,}000\ M^{-1}cm^{-1}$ for the ground state of bacteriorhodopsin at 632.8 nm.

2.4 Results and Discussion

2.4.1 Molecular Orientation

PM fragment films were formed by electrostatic adsorption to a positively charged polymer (PDAC) as described by Li et al.[65] A single adsorption cycle was used to create films of relatively low bR surface coverage. Representative steady-state ATR spectra measured in TE and TM polarizations are shown in Figure 2.8 and exhibit a dichroic response, indicative of an anisotropic orientation distribution of retinal chromophores in the PM film.

The dichroic ratio obtained from these spectra was used to calculate the mean tilt angle of the retinal absorption dipoles in the PM film, as described in previous papers.[66-67]

The mean tilt angle (θ_μ) of the absorption dipole of the retinal in PM fragment films is defined relative to the surface normal. θ_μ was determined from the measured dichroic ratio (ρ) at 563 nm as described in previous papers.[66-67] For a linear absorption dipole, the dichroic ratio (ρ) is related to θ_μ by[68-69]

$$\rho = \frac{A_{f,\,TE}}{A_{f,\,TM}} = \frac{E_y^2}{E_x^2 + 2E_z^2(\cot^2\theta_\mu)} \qquad (2.1)$$

where $A_{f,TE}$ and $A_{f,TM}$ are the absorbances of the film in TE and TM polarizations, respectively. Expressions for E_x^2, E_y^2, and E_z^2, the electric field intensities along the x-,

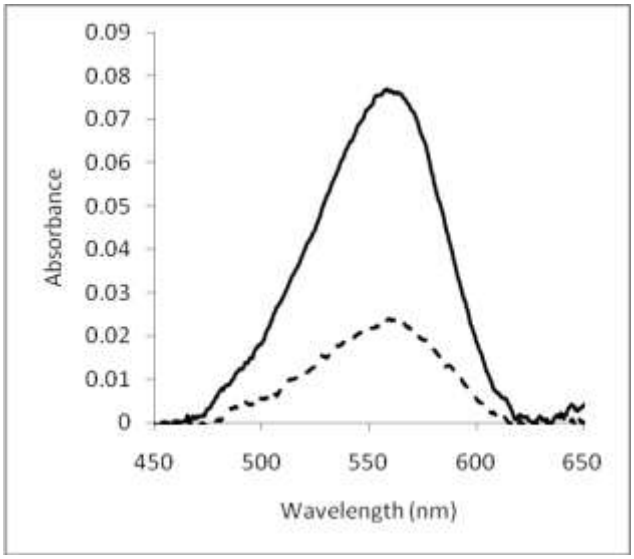

Figure 2.8 Steady-state ATR spectra of a PM film adsorbed to a PDAC film in TE (solid line) and TM (dashed line) polarizations.

y-, and z-axes, respectively, are shown in Equation 2.2a-c and are given in Lee and Saavedra.[66] The thin film approximation was used in order to solve for the electric field intensities (E_x, E_y and E_z), with values of 1.339 (HEPES buffer) for n_1 and 1.46 (quartz) for n_2.

$$E_x^2 = \frac{4\cos^2\beta\left(\sin^2\beta - \left(\frac{n_1}{n_2}\right)^2\right)}{\left(1-\left(\frac{n_1}{n_2}\right)^2\right)\left(1+\left(\frac{n_1}{n_2}\right)^2\sin^2\beta - \left(\frac{n_1}{n_2}\right)^2\right)} \quad (2.2a)$$

$$E_y^2 = \frac{4\cos^2\beta}{1-\left(\frac{n_1}{n_2}\right)^2} \quad (2.2b)$$

$$E_z^2 = \frac{4\cos^2\beta\sin^2\beta}{\left(1-\left(\frac{n_1}{n_2}\right)^2\right)\left(1+\left(\frac{n_1}{n_2}\right)^2\sin^2\beta - \left(\frac{n_1}{n_2}\right)^2\right)} \quad (2.2c)$$

The calculation yielded a mean tilt angle of 68° from the surface normal. This result agrees well with crystallography[70] and polarized FTIR difference spectroscopy[71] from which retinal tilt angles of 68.5° and 69°, respectively, from surface normal to the PM plane were determined.

2.4.2 Surface Coverage

The retinal surface coverage in these films was estimated using two approaches based on the ATR spectroscopy and ellipsometry. In the planar waveguide ATR configuration, the absorbance of a thin film (A_f) is given by[57, 66]

$$A_f = N(I_e/I_i)\,\varepsilon_f\,\Gamma \quad (2.3)$$

where where N is the number of total internal reflections that interact with the sample on the waveguide surface, I_e/I_i is the interfacial transmitted intensity per unit incident beam intensity, ε_f is the molar absorptivity of the chromophore in the thin film, and Γ is the surface coverage. A experimental value for $N(I_e/I_i)$ was obtained by first measuring the bulk evanescent pathlength (L_b) of the ATR instrument,

$$L_b = N(I_e/I_i)d_p \qquad (2.4)$$

where d_p is the depth of penetration.

2.4.2a Determination of Experimental Bulk Evanescent Pathlength

In the planar waveguide ATR configuration, the absorbance of a bulk-dissolved chromophore (A_b) is given by[57, 66]

$$A_b = N(I_e/I_i)d_p\varepsilon_b C_b \qquad (2.5)$$

where N is the number of total internal reflections that interacts with the sample on the waveguide surface, $\varepsilon_b C_b$ is the product of the molar absorptivity and the concentration of the chromophore, d_p is the depth of penetration, and I_e/I_i is the interfacial transmitted intensity per unit incident beam intensity. The bulk evanescent pathlength (L_b) is

$$L_b = N(I_e/I_i)d_p \qquad (2.6)$$

and is commonly expressed as evanescent pathength per unit distance of beam propagation in the plane of the waveguide, with units of μm/cm. Expressions for d_p and for I_e/I_i in both transverse electric (TE) and transverse magnetic (TM) polarizations for a two-phase system composed of two optically transparent media are given in the references.[57, 66, 72] In the expressions, n_1 and n_2 are the refractive indices of the bulk solvent and the waveguide substrate, respectively, β is the angle of total internal reflection, and λ is the wavelength.

The experimental L_b values were determined by measuring the ATR spectra of a series of solutions of bromophenol blue dissolved in phosphate buffer. When dissolved in aqueous buffer, this chromophore does not adsorb to quartz and thus the concentration-distance profile is constant throughout the evanescent volume.[73]

The following parameters were used in these experiments as well as those involving PM fragment films :

β = 73°

n_1 (phosphate buffer) = 1.335

n_2 (quartz) = 1.46

waveguide thickness = 0.2 mm

interaction length along waveguide sampled by the totally reflected beam = 4.9 cm

Example spectra and calibration plots are shown in Figure 2.9. Dividing the slope of each line in Figure 2.9B by ε_b for bromophenol blue (72,500 $M^{-1}cm^{-1}$ at 590 nm) yields

$N(I_e/I_i)d_p$, which is the experimental value of L_b. In TM and TE polarizations, L_b = 16.4 μm and 13.9 μm, respectively. L_b values can also be expressed as evanescent pathength per unit distance of beam propagation in the plane of the waveguide, which are 3.3 μm/cm and 2.8 μm/cm, respectively. Dividing L_b by d_p at 590 nm (0.115 μm; calculated using the expression given in the references[57, 66, 72]) yields values for $N(I_e/I_i)$ of 143 and 121, respectively.

2.4.2b Steady state ATR

Using the mean L_b value (15.2 μm) and dividing by d_p (0.115 μm) yields $N(I_e/I_i)$ = 132. Using ε_f = 63,000 $M^{-1}cm^{-1}$ for the molar absorptivity of retinal and taking A_f to be 0.05 (see TE- and TM-polarized spectra in Figure 2.5), the retinal Γ is calculated to be 6 $pmol/cm^2$ from Eq 2.2.

2.4.2c Ellipsometry

To perform ellipsometry, PDAC/PM films were formed under identical conditions on oxidized silicon wafers. The measured PM film thickness was 9.9 ± 0.9 nm (*n*=3). The thickness of PM is reported to be 4.5-5 nm,[74] so the films formed here have an approximate thickness of two membranes which is consistent with results from previous work.[61] The structure of a PM fragment is a 2-dimensional hexagonal lattice in which the unit cell is a trimer of bR molecules, the unit cell dimension is 6 nm, and each bR

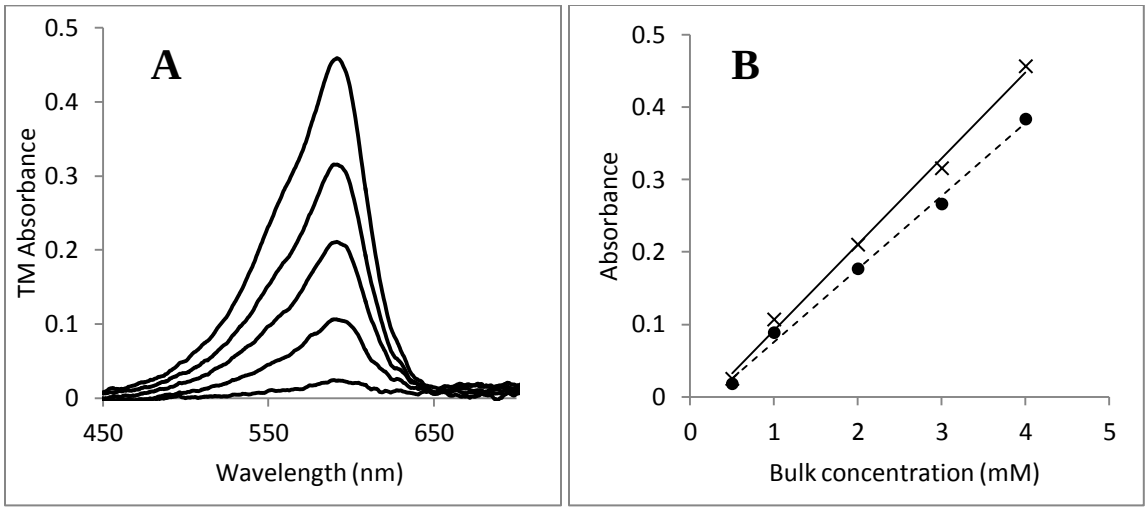

Figure 2.9 (A) TM-polarized ATR spectra of bromophenol blue in 100 mM phosphate buffer, pH 7. (B) Absorbance at the wavelength of maximum absorbance (590 nm) in TM (—) and TE (- - -) polarizations.

contains one retinal chromophore.[75] The bR trimer therefore has a projected surface area of 31 nm^2 and a close-packed, two-layer film of PM fragments is calculated to have a retinal Γ of 32 $pmol/cm^2$.

Considering the ellipsometry and the ATR spectral data in tandem, the retinal Γ is in the range of 6 – 32 $pmol/cm^2$. This range is about a factor of 10 lower than that of a close-packed monolayer of a small chromophore, which is about 200 $pmol/cm^2$. The discrepancy between the surface coverages obtained by ATR spectroscopy and ellipsometry is not surprising given the assumptions and uncertainties inherent in these methods. For example: *i*) It is assumed that the molar absorptivity of suspended PM fragments is an accurate estimate of ε_f, which in turn implies that the chromphore orientation distribution in the film is isotropic (whereas Figure 2.5 shows that it is anisotropic) and that the molar absorptivity is not altered by adsorption to PDAC. *ii*) It is assumed that incident beam is collimated which produces a uniform angle of total reflection (θ_i) in the waveguide. Thus at a given wavelength, a single value is calculated for d_p. In practice, the incident beam is focused with a lens which produces a range of internal reflection angles and a distribution of d_p values, and thus a range of optical pathlengths. *iii*) The Γ value calculated using ellipsometry relies on the assumption that the packing density of bR in the film is equivalent to that in the crystal structure of PM. The packing density in an adsorbed film of PM fragments will certainly be less (so Γ must be < 32 $pmol/ cm^2$). Furthermore, there is some uncertainty in the values used for the refractive indices of the PDAC and PM layers, and possible effects from film surface roughness (which was not measured here) on the ellipsometric thickness were ignored.

2.4.3 Transient ATR

The photocycle of bacteriorhodopsin has been well-studied.[76-77] Upon absorption of a photon, bR decays through a series of intermediates including a relatively long-lived metastable state (M-state) which has a maximum absorbance at 410 nm. Here the lifetime of the M-state was examined using TAS/ATR, pumping the sample at 532 nm which is close to the ground state absorbance of bR at 563 nm and using a probe beam centered at 410 nm. A typical decay curve obtained using TE polarization is shown in Figure 2.10A. All decay curves were satisfactorily fit to a first order exponential. The decay lifetime of the M-state of bR in PDAC/PM films was determined to be 4.4 ± 0.5 ms (n=5). The TAS instrument can also be operated in the transmission geometry and applied to dissolved samples, with the pump beam traversing the cuvet perpendicular to the probe beam. This arrangement was used to measure decay curves of 0.5 mg/mL PM fragments suspended in 50 mM HEPES buffer pH 8.0 (Figure 2.10B). A M-state lifetime of 4.0 ± 0.7 ms (n=2) was obtained which agrees well with published data.[78] These results show that the decay kinetics of the M-state are unaffected by adsorption of PM on PDAC which indicates that the chemical environments of the retinal in suspended and adsorbed PM fragments are very similar. Immobilization of proteins on solid substrates without perturbing their structure and activity has been a focus of considerable research efforts (see refs [79-81] for recent reviews) because protein films are the functional component in affinity-based separations, biosensors, and several other biotechnologies. In contrast to our results, previous studies on dried, 90-layer PDAC/PM films found that the

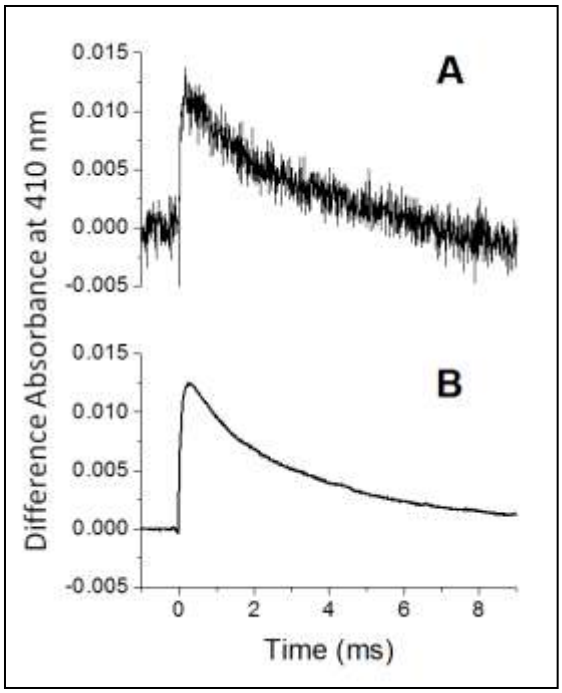

Figure 2.10 Transient absorbance decay of the M-state measured at 410 nm after excitation at 532 nm at time = 0. (A) PDAC/PM film measured in the ATR geometry on a quartz waveguide in TE polarization. (B) 0.5 mg/mL PM fragments suspended in 50 mM HEPES buffer, pH 8.0 and measured in a transmission geometry.

M-state decay kinetics were altered from native bR.[82] Multi-exponential decays and much longer M-state lifetimes were observed which were attributed to the effects of dehydration on the protein structure.

2.4.4 Fraction of Retinal Photoexcited in PM films

The energy of the 532 nm pump laser launched into the waveguide is about 20 μJ/pulse. The fraction of PM in the film excited by the laser pulse is calculated using the difference absorbance value at 410 nm immediately after the pulse ($\Delta A_{410\ nm} = 0.013$). The M-state molar absorptivity at 409 nm is 48,800 $M^{-1}cm^{-1}$.[83] Using equation 2.2 and a polarization-averaged value of 132 for $N(I_e/I_i)$, the surface coverage of M-state is calculated to be 2 pmol/cm^2. This surface coverage is approximately 1% of a close-packed monolayer of a small chromophore and about 0.3 of the retinal surface coverage (assumed to be 6 pmol/cm^2 based on $A_f \approx 0.05$). Thus it is estimated that photoexcitation converted ca. 30% of retinal to the M-state.

2.5 Quantitative Comparison to Literature Values

Returning to the single PDAC/PM bilayers examined here, the sensitivity of the TAS measurement on these films is now compared to other TAS/ATR studies of low surface coverage films. One parameter that can be used for comparison is $\varepsilon_f \Gamma$, the unitless product of the molar absorptivity (at the pump wavelength) and the chromophore surface coverage. Numeric values for chromophore surface coverage, however, generally have not been reported in the TAS/ATR literature. A survey of this literature produced

the following estimates: *i*) Ryan et al.[84] made measurements on films of eosin (ε = 89,500 $M^{-1}cm^{-1}$ at 532 nm[85]) adsorbed to TiO_2. Although the surface coverage was not measured, monolayer coverage was assumed based on the appearance of a plateau in the adsorption isotherm. Assuming a surface area of 70 $Å^2$ per adsorbed molecule, this corresponds to a surface coverage of ca. 200 pmol/cm^2, and therefore $\varepsilon_f \Gamma = 1.8 \times 10^{-2}$. *ii*) Lemmetyinen and coworkers performed TAS/ATR on two monolayers of a porphyrin-fullerene dyad;[86] the surface density in each layer was 0.25 molecule/nm^2 which equates to Γ = 83 pmol/cm^2. Using ε = 195,000 $M^{-1}cm^{-1}$ at 428 nm,[86] $\varepsilon_f \Gamma = 1.6 \times 10^{-2}$. *iii*) Nagamura and coworkers spin-coated polymer films doped with chromophores onto waveguides fabricated by ion-exchange. In Figure 1 of their paper on TAS/ATR studies of tetraphenylporphinesulfonic acid (TPPS) films,[87] the absorbance of the highest energy Q band is 1.2×10^{-3}. Using ε = 16,500 $M^{-1}cm^{-1}$ at 515 nm,[88] Γ is estimated to be 73 pmol/cm^2. At 532 nm, ε_f is estimated to be 7000 $M^{-1}cm^{-1}$ so $\varepsilon_f \Gamma = 5.1 \times 10^{-4}$. *iv*) In a subsequent paper, Nagamura and coworkers examined 30 nm thick films composed of 9% spiropyran dispersed in poly(styrene) and poly(methyl methacrylate).[89] A composite waveguide was used, consisting of a K^+-doped guiding layer overcoated with a sputtered TiO_2 film. Figure 10 in that paper shows the absorbance spectrum of a 1200 nm thick film. Based on that spectrum and ε = 11,200 $M^{-1}cm^{-1}$ at 355 nm,[90] a surface coverage of 670 pmol/cm^2 is estimated for a 30 nm thick film, from which $\varepsilon_f \Gamma = 7.5 \times 10^{-4}$ is calculated.

To compare the literature $\varepsilon_f \Gamma$ values to the TAS measurements on PM films reported herein, the spectral value used for bR surface coverage (6 pmol/cm^2).

Consistency dictates this choice because the literature $\varepsilon_f \Gamma$ values were also calculated using spectral data. At 532 nm, ε_f = 54,000 $M^{-1}cm^{-1}$ for bR and thus $\varepsilon_f \Gamma = 3.2 \times 10^{-4}$. This value is slightly less than that estimated for Nagamura's most sensitive experiment,[87] and about 50-fold less than the values estimated from the data of Ryan et al.[84] and Lemmetyinen and coworkers.[86] On the basis of this comparison, it can be concluded that the TAS/ATR measurements described herein represent the most sensitive reported to date. Equally important is that the ATR element in our instrument is a 200 μm thick, multimode waveguide that is simpler to fabricate than a composite, ion-exchange waveguide. Collinear coupling of the pump and probe beams to the waveguide through optical fibers is also simpler than aligning the pump beam normal to the waveguide plane and launching the probe beam into the waveguide using a prism coupler.[89] Finally, it is recognized that additional parameters could be considered in this sensitivity comparison, such as the fraction of chromophores excited by the pump pulse, the molar absorptivity of the excited state species, the physical characteristics of the waveguide (e.g., $N(I_e/I_i)$, and the bandwidth of the measurement. However information about these parameters is generally lacking in the TAS/ATR literature which precludes us from making a more complete comparison. To enable these comparisons to be made in the future, as well as the feasibility of a proposed TAS/ATR measurement to be quantitatively assessed, all of these parameters are stated herein for our instrument and thin film samples.

2.6 Instrument Sensitivity

Although TAS/ATR measurements on PDAC/PM films were feasible in TE polarization, decay curves could not be measured in TM polarization because the absorbance was too low (see Figure 2.5), which is a consequence of the predominately in-plane orientation of the retinal absorption dipole. This demonstrates the importance of matching the polarization of the pump and probe beams in a TAS/ATR experiment. As for all TAS experiments, a significant fraction of chromophores must be excited by the pump pulse to enable measurement of the subsequent relaxation process, and chromophore orientation relative to the polarization of the pump and probe beams is clearly an important factor. Under the experimental conditions used here, the surface coverage of retinal that was excited in TE polarization by the 532 nm pump pulse is calculated to be 2 pmol/cm^2. In other words, the surface coverage of the M-state that produced the transient signal shown in Figure 2.10A was about 1% of a close-packed monolayer of a small molecule. A comparison cannot be offered of this value to published studies because the TAS/ATR literature generally does not provide sufficient information to allow the surface coverage of excited state species to be calculated.

2.7 Conclusions

Polarized waveguide ATR has been combined with and pump-probe spectroscopy in a relatively simple instrumental arrangement to probe molecular orientation and photochemical kinetics in a weakly absorbing molecular film with a surface coverage of ca. 0.1 monolayer. Here a reaction that decays on the ms timescale was examined as a

test case but studies of much faster reactions are certainly feasible and will be a focus of future studies. The temporal resolution of the first generation instrument described here, about 5 ns, is dictated by the pulse width of the pump laser. The sensitivity to low $\varepsilon_f \Gamma$ could be further improved by using a much thinner waveguide which would increase the evanescent pathlength.[91-92] Other configurations for ATR spectroscopy, such as evanescent wave cavity ring-down spectroscopy,[93] are also extremely sensitive and should be useful when combined with TAS. Finally, it is noted that electroactive waveguide ATR spectroscopy has been implemented using both multimode and single-mode waveguides.[73, 94-95] TAS could be combined with electroactive waveguide techniques to characterize the kinetics of charge transfer processes in thin molecular films on transparent conducting oxides, which is an important process in organic and dye-sensitized solar cells.

3. INVESTIGATIONS OF THE MOLECULAR THIN FILM/TRANSPARENT CONDUCTING OXIDE INTERFACE AND PROPERTIES CONTRIBUTING TO THE OBSERVATION OF CHARGE TRANSFER KINETICS

3.1 Introduction

As discussed in detail in Chapter 1, the organic photovoltaic (OPV) device efficiency is the product of the efficiencies of the individual migration and charge transfer processes. Understanding the structure-function relationship, specifically at the molecular thin film/transparent conducting oxide (TCO) interface will allow for engineering these interfaces to enhance charge transfer events and reduce the rate of charge recombination. As a result, the efficiency of an OPV will improve. Important parameters which describe the structure-function relationship include chemical properties of the TCOs,[18] the attachment chemistry of the molecular film to the TCO, the orientation of molecules on the surface[37, 96] and the surface coverage.

In addition to the factors described here, there are other chemical questions which arise regarding the local molecular environment of the thin film and how that environment affects the excited state band edges and lifetimes. This pertains to molecules bound to a TCO, but also molecules in close association with nearby functional groups and charged species. This chapter addresses the properties that are hypothesized to influence the charge transfer kinetics at the molecular thin film/TCO interface. In addition, studies herein explore other properties, such as the local molecular environment of the solid-state film, which are hypothesized to significantly affect the

excited state characteristics, such as quantum yield and lifetimes. These studies aim to improve our understanding of optimal characteristics of the molecular thin film/TCO interface in order to increase charge transfer efficiency and overall performance of the OPV.

3.1.1 Background to Porphyrins

Absorption of light and efficient charge transfer are key aspects to OPV and DSSC performance. Porphyrins have been thoroughly studied as light harvesting agents due to their high molar absorptivities and ability to undergo electron transfer reactions. Advancement in synthesis of porphyrins has contributed a library of design possibilities, including functional groups attachment to metal oxides[48, 97] and supramolecular structures.[98] Porphyrins have a large π-electron system (macrocycle), a possible metal atom in the center, axial ligands, and intrinsic space over the porphyrin ring for axial ligands and substituents. The porphyrin properties affect the electronic structure of the molecule, as well as singlet and triplet excited state energy levels and their lifetimes.[98]

Aggregated porphyrins are known to have different excited state behavior as compared to non-aggregated porphyrins, for example decreased excited state lifetimes.[99-100] There are solvent effects for many of these porphyrins as well, as a function of pH or solvent polarity. The excited state behavior of porphyrins in solution cannot be extrapolated to its behavior adsorbed to a surface or in close proximity to a solvent-free network of molecules.[48, 101] Porphyrin molecules tethered to a metal oxide and incorporated into mono- and multilayer films were researched in order to better

understand the properties contributing to efficient charge transfer at the molecular thin film/TCO interface.

3.1.2 Background to Zinc Porphyrin-Indium Tin Oxide (ITO) Interface

The molecular thin film/TCO interface investigated was zinc porphyrin adsorbed to indium tin oxide (ITO). Zinc porphyrins have been thoroughly studied, especially as dye sensitizers adsorbed to nanocrystalline semiconducting electrodes in DSSCs.[48, 102-103] They have high molar absorptivities at wavelengths in the visible light region and long lived triplet states (~0.65 – 1.4 ms).[97] They also exhibit little to no aggregation in concentrated solutions.[104]

Indium tin oxide (ITO) is a transparent conducting oxide that also has been vastly researched.[36, 40] ITO is indium oxide doped with tin and as a result, highly conductive (1 x 10^4 Ω^{-1} cm^{-1}). It is 90% transparent in the visible region and it can be deposited on a variety of substrates.[36] ITO is heterogeneous in ohmicity and composition, and as a result scientists have investigated ways to improve its performance in OPVs.[40]

The band energy diagram for this interface is shown in Figure 3.1A. The values for the zinc porphyrin energy levels are based on solution electrochemical studies of zinc(II)-5,10,15,20-tetra(carboxyphenyl)porphyrin (ZnTCPP).[102] The Fermi energy shown for ITO varies depending on cleaning and pretreatment conditions.[105] The photoexcitation and possible reaction mechanisms for ZnTCPP tethered to ITO are shown in Figure 3.1B. The zinc porphyrin absorbs visible light and populates the singlet excited state. It can intersystem cross to form the triplet excited state, transfer an electron

A

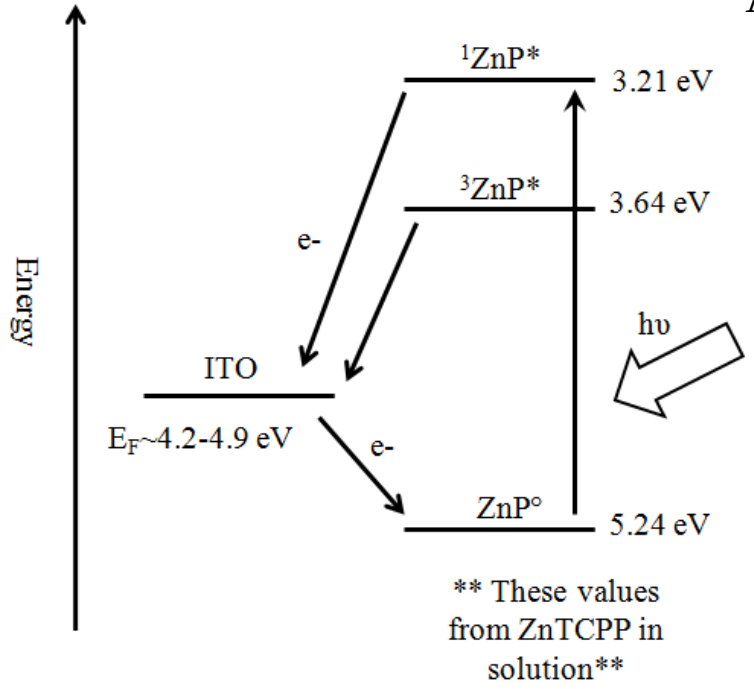

B

1) $ZnP + h\nu \rightarrow {}^1ZnP^*$
2) ${}^1ZnP^* \rightarrow {}^3ZnP^*$
3) ${}^1ZnP^* + ITO \rightarrow ZnP^{\cdot+} + ITO^{\cdot-}$
4) ${}^3ZnP^* + ITO \rightarrow ZnP^{\cdot+} + ITO^{\cdot-}$
5) $ZnP^{\cdot+} + ITO^{\cdot-} \rightarrow ZnP + ITO$

Figure 3.1 (A) Band diagram for the zinc porphyrin (ZnP) – indium tin oxide (ITO) interface. E_F is the Fermi energy for ITO; it varies depending on surface treatments and cleaning. The energy levels for ZnP are the values from solution electrochemistry of ZnTCPP.[106] Values vs. NHE were converted to vacuum by 4.44 eV.[107]
(B) Photoexcitation of ZnP and potential reactions after photoexcitation of zinc porphyrin.

to the ITO, or decay back to the ground state. The triplet state can either decay back to the ground state or transfer an electron to the ITO. Finally, if a charge has been transferred to the ITO and it has not been extracted by closing the electrochemical circuit, it can recombine with the oxidized porphyrin to repopulate the ground state.

In this chapter electrochemical studies with zinc porphyrins adsorbed to ITO address if the oxidation potential values assigned from solution electrochemical studies are appropriate estimations or if a more accurate energy level diagram must be developed. Steady state ATR spectroscopy was used to characterize properties such as molecular orientation and surface coverage that are hypothesized to influence charge transfer and excited states kinetics. Spectroelectrochemical ATR spectroscopy identified the cation radical absorbance spectra of the zinc porphyrins so these species could be monitored with transient absorbance spectroscopy.

As demonstrated in Chapter 2, transient ATR spectroscopy provides molecular and photoinduced kinetic information about weakly absorbing thin films on a waveguide surface. Since ITO is a conductive semiconductor, transient ATR spectroscopy was conducted at open circuit and under potential control, as a way to control the driving force of the charge transfer kinetics.[108] In order to address the local molecular environmental role in the excited state characteristics, zinc porphyrins in the presence of charged polymer solutions and thin films were also investigated.

3.2 Instrumental Set-up

3.2.1 Steady State ATR Spectroscopy

The steady state ATR measurements were made on a custom built ATR instrument described elsewhere.[73] Briefly, white light from a 10 W tungsten-halogen lamp (International Light Technologies) was focused into an optical fiber, collimated by a lens and spatial filter, passed through a polarizing lens and prism-coupled (BK-7 right angle prisms, Edmund Optics) into the internal reflection element (IRE). The IRE was an indium tin oxide (ITO) coated glass slide (Colorado Concepts Coating, LLC). The light was totally internally reflected down the waveguide and out-coupled via another prism, where it was focused into the end of an optical fiber and directed into a monochromator (Newport MS260i) and CCD camera (Andor iDus420A). Spectroelectrochemical ATR measurements were conducted using this custom instrument and a flowcell that accommodated a Ag/Ag+ (10 mM $AgNO_3$, 0.1 M tetrabutylammoniumperchlorate (TBAP), acetonitrile) non-aqueous reference electrode (Bioanalytical Systems, Inc.) (RE), a platinum wire counter electrode (CE) and a transparent conducting oxide as the working electrode (WE), described in detail elsewhere.[73] The electrochemical ATR cell was held at a potential via an EG&G Princeton Applied Research Model 263A potentiostat/galvanostat.

3.2.2 Transient Absorbance Spectroscopy

The diagram of the Proteus transient absorbance instrument is found in Figure 2.1. Solution transient experiments were set up with the excitation and monitoring beams perpendicular to one another. After passing through the sample, the monitoring beam was focused into an optical fiber connected to the Si-photodiode (Newport). The ultrafast transient instrument, Eos/Helios (Ultrafast Systems, Inc.) is described in Appendix B.

The transient ATR experiments in this chapter used prism coupling to totally internally reflect light down the IRE as opposed to polished quartz slides described in Chapter 2. A custom flow cell was designed to match the requirements of the commercial waveguide spectrometer (SIS-5000). The translational stage of the SIS-5000 only moves along the x and y axes, thus the z-axis was fixed at the optimal height for prism coupling. The cell is diagramed in Figure 3.2. Potential controlled TAS/ATR measurements were conducted using a pseudo reference electrode (anodized silver wire), a platinum counter electrode and the transparent conducting oxide as the working electrode, controlled by a potentiostat (EG&G Princeton Applied Research Model 263A).

3.3 Experimental

3.3.1 Preparation of ITO Substrates

The indium tin oxide (ITO) coated glass substrates used in these studies were obtained either from Colorado Concept Coating Limited (CC) or sputtered by Ajaya Sigdel at the

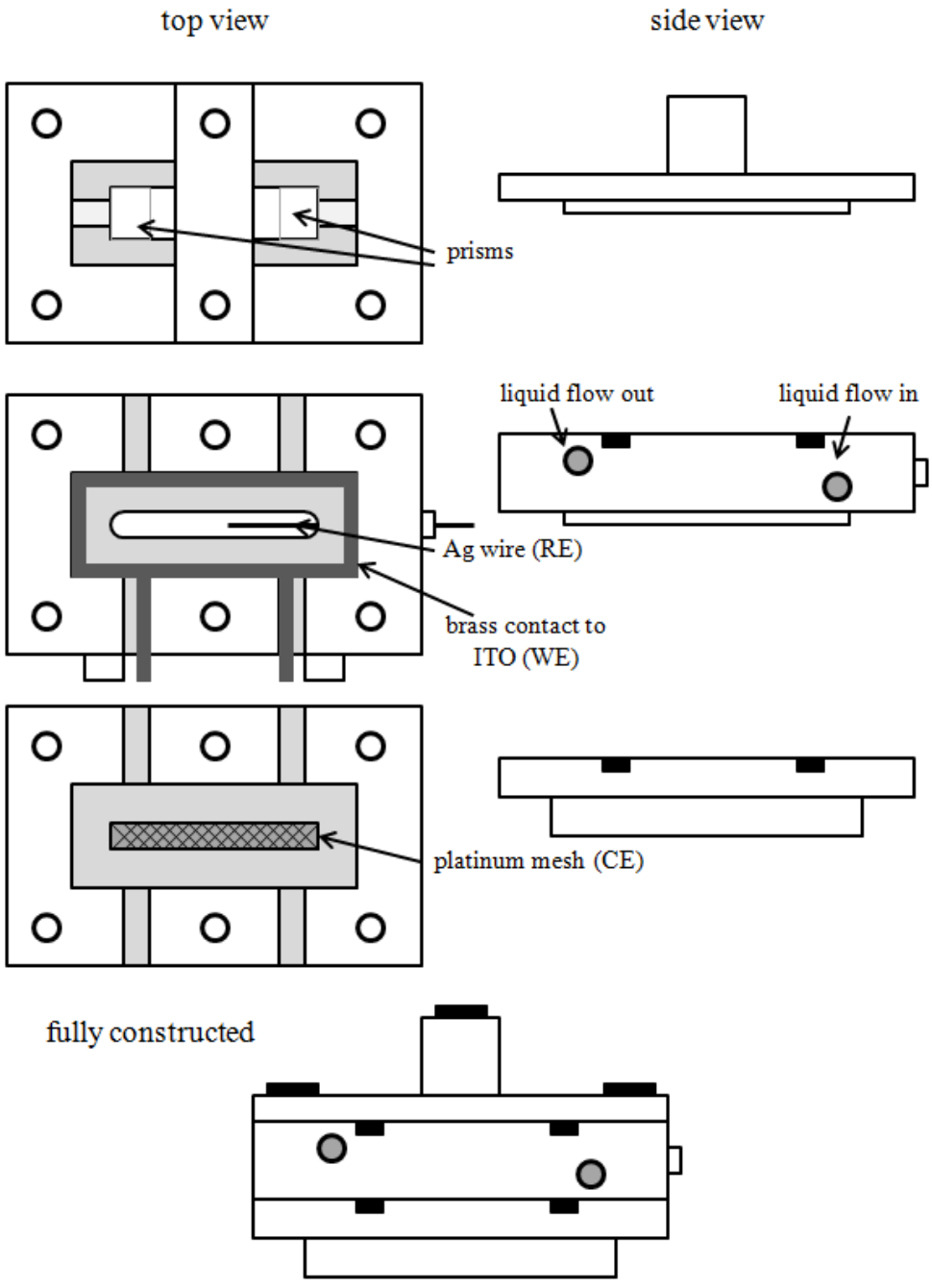

Figure 3.2 Diagram of Delrin ATR flowcell for the SIS-5000 waveguide spectrophotometer for prism coupling and potential control with ITO as the working electrode, anodized silver wire as the pseudo-reference electrode and platinum mesh as the counter electrode.

Department of Energy National Renewable Energy Laboratory (NREL). The CC and NREL ITO both had thicknesses of ~100 nm and a sheet resistance of ca. 13 Ω/ □. Ajaya Sigdel from NREL measured the NREL ITO thickness with ellipsometry, the sheet resistance using a 4-point probe and the crystallinity with X-ray diffraction (XRD).

The ITO coated glass (CC) was cut into ¾" x ¾" pieces for cyclic voltammetry and 1" x 3" slides for ATR experiments. The ITO was prepared for film depositions by cleaning with a 1% Alconox solution for 1 minute, then sonicating for 15 minutes each in a dilute Triton X-100 solution, water (Barnstead nanopure, measured resistivity = 18.3 MΩ•cm), and ethanol. The slides were stored in ethanol prior to use. Immediately prior to film deposition, the slides were air plasma cleaned (Harrick model PDC-3XG) for 15 minutes at 30 W.

3.3.2 Zinc Porphyrins

Zinc porphyrins have been widely studied for their dye sensitizer properties in dye sensitized solar cells.[102, 109] They have a long lived triplet state lifetime, (0.65 – 1.4 ms) and have demonstrated little to no aggregation in concentrated solutions.[97] Zinc porphyrins used in these experiments were chosen for their functional groups to covalently bind to the ITO. The chemical structures for the zinc(II)-5,10,15,20-tetra(carboxyphenyl)porphyrin (ZnTCPP) (Frontier Scientific) and zinc(II)-5,10,15,20-tetra(phosphonylmethylphenyl)porphyrin (ZnPA) (Frontier Scientific) are shown in Figure 3.3A and B. A schematic of the possible binding chemistries of carboxylic acid to a TiO_2 surface, used as a representative example of a metal oxide is shown in Figure

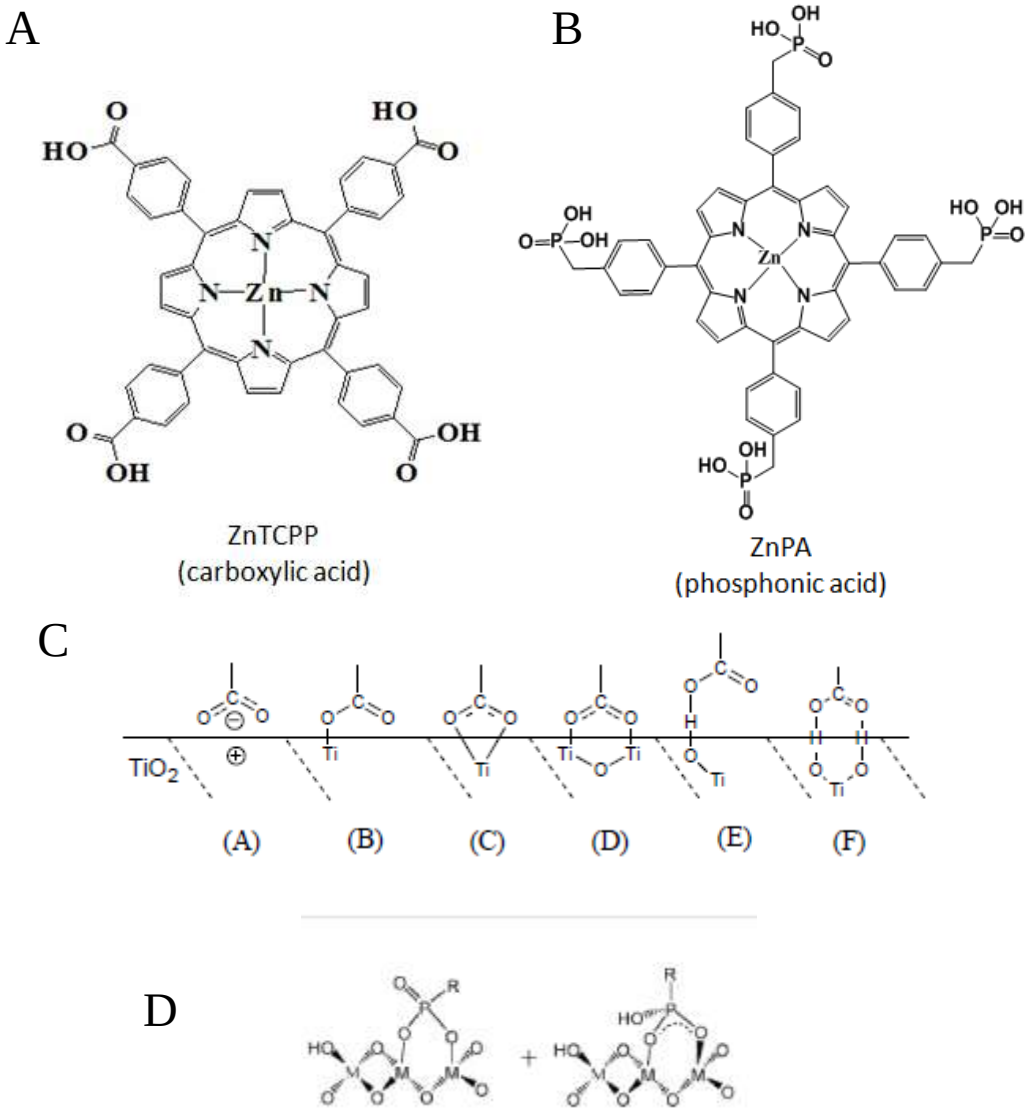

Figure 3.3 (A) Molecular structure of zinc(II) meso-tetra(4-carboxyphenyl)porphyrin (ZnTCPP). (B) Molecular structure of zinc(II) meso-tetra(4-phosphorylmethylphenyl)porphyrin (ZnPA). (C) Potential binding chemistries of carboxylic acid to TiO_2. Ti in this figure can also represent another metal. Reprinted from ref. 104. Used by permission of the American Chemical Society. (D) Potential binding chemistries of phosphonic acid to a metal oxide. Reprinted from ref. 43. Used by permission of Elsevier.

3.3C.[104] A schematic of possible binding chemistries of phosphonic acid to a metal oxide surface is shown in Figure 3.3D.[43] The solution absorbance spectra for 5 μM ZnTCPP in EtOH and 1 μM ZnPA in 10 mM MES buffer (pH 5.5) are shown in Figure 3.4. The molar absorptivities of ZnTCPP at the Soret band (420 nm) and the Q-bands (556 nm and 594 nm) are 160,000 $M^{-1}cm^{-1}$, 11,500 $M^{-1}cm^{-1}$ and 6,400 $M^{-1}cm^{-1}$, respectively.[97] The molar absorptivities of ZnPA bands were determined experimentally, with the Soret band (422 nm) and Q-bands (557 nm and 598 nm) at 289,000 $M^{-1}cm^{-1}$, 11,300 $M^{-1}cm^{-1}$ and 7,200 $M^{-1}cm^{-1}$, respectively.

3.3.3 Cyclic Voltammetry

Cyclic voltammetry was conducted using a standard 3-electrode cell, with a Ag/Ag+ (10 mM $AgNO_3$, 0.24 M TBAP, acetonitrile) non-aqueous reference electrode (Bioanalytical Systems, Inc.), a gold coated slide as the counter electrode and ITO coated glass (Colorado Concepts Coating, LLC) as the working electrode. The teflon electrochemical cell had a working electrode area of 0.785 cm^2. The electrochemical measurements were performed in 0.24 M tetrabutylammoniumperchlorate (TBAP) in acetonitrile (ACN) with a CH420A potentiostat (CH Instruments, Inc.). The scan rate for the thin film cyclic voltammograms (CVs) was 25 mV/sec.

3.3.4 Solution Transient Absorbance

The Proteus transient instrument (Ultrafast Systems, Inc.) is described in detail in Chapter 2 and Appendix A. The zinc porphyrin solutions contained in a 1 cm x 1 cm

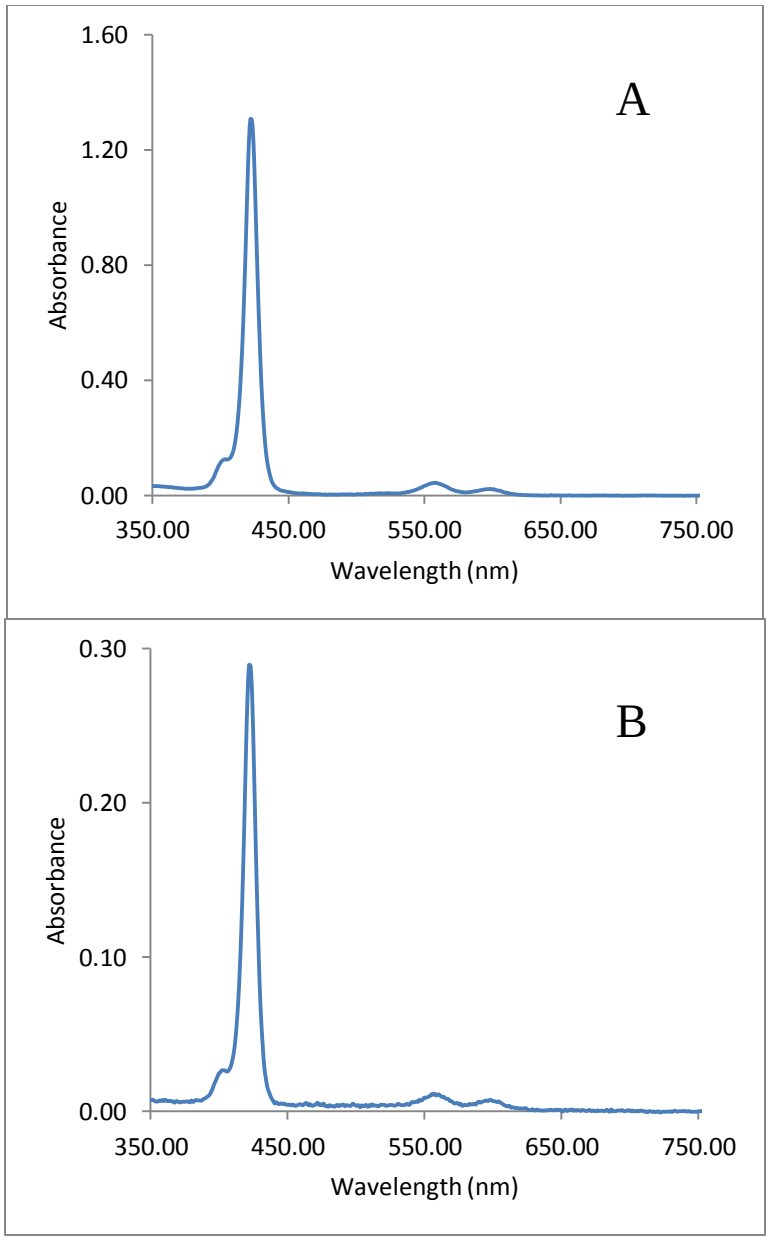

Figure 3.4 Solution UV-Vis absorbance spectra for (A) 5 μM ZnTCPP in EtOH and (B) 1 μM ZnPA in 10 mM MES buffer (pH 5.5).

quartz cuvet were purged with argon gas, sealed and introduced into the Proteus instrument. Decay curves at single wavelengths were obtained after excitation at 532 nm with the Nd:YAG laser (Continuum) or at ~560 nm with the dye laser (Continuum).

The Eos/Helios transient instrument (Ultrafast Systems, Inc.) is described in Appendix B. Briefly, the solutions were in a 2 mm pathlength quartz cuvet with a stir bar and purged with argon gas prior to excitation. The wavelength of excitation of 532 nm was selected for interaction with the Q-band as well as to match the Nd:YAG laser in the Proteus experiments. The white light continuum source and the CCD camera allowed for collection of the difference absorbance spectrum for the transient species.

3.4 Results and Discussion: Zinc Porphyrins on ITO

3.4.1 Electrochemical Results

When investigating the molecular thin film/TCO interface, the values for the energy levels must be determined accurately in order to understand the charge transfer kinetics. These electrochemical thin film experiments were conducted to determine the oxidation potentials of ZnTCPP and ZnPA bound to ITO and evaluate the role of the binding functional group. If the thin film oxidation potentials differ from the solution zinc porphyrin oxidation potentials then the estimated band energy diagram in Figure 3.1 must be adjusted.

ZnTCPP was dissolved in ethanol at 25 μM and adsorbed to ITO for 30 minutes at room temperature. ZnPA was dissolved in 10 mM MES buffer (pH 5.5) at 25 μM and

adsorbed to ITO for 30 minutes at room temperature. The excess porphyrin was rinsed away with acetonitrile (ACN) and the film was blown dry under a stream of N_2. The films were sealed in the 3-electrode electrochemical cell.

CV scans were conducted from 0.0 to +0.65 V vs. Ag/Ag+, with 0.24 M TBAP/ACN as the electrolyte solution and a scan rate of 25 mV/sec. The background-subtracted CV of ZnTCPP adsorbed to ITO and background CV are shown in Figure 3.5. The diffusion controlled electrochemistry of ZnTCPP is well known.[97] ZnTCPP undergoes a two electron oxidation, where the first oxidation at 0.8 V vs. NHE (0.4 V vs. Ag/Ag+) is reversible and the second oxidation at 1.06 V vs. NHE (0.66 V vs. Ag/Ag+) is irreversible.[97, 106] Assuming the CV contains only contributions from the first oxidation, the mid-point potential ($E^{0\prime}$) was determined to be 0.51 V vs. Ag/Ag+. This value is more positive than that for the diffusion controlled situation and therefore the film is more difficult to oxidize. Due to electrostatic repulsion, it is energetically unfavorable to introduce a positive charge on a molecule with an adjacent positive charge. The electroactive surface coverage was determined to be 140 pmol/cm^2 by integrating under the anodic curve and assuming a one electron transfer. This value corresponds to ~0.4 closed-packed monolayers of ZnTCPP molecules adsorbed in the edge-on orientation with a projected surface area of 50 Å^2/molecule.[108] If the ZnTCPP molecules were parallel to the ITO surface the projected surface area would be 360 Å^2/molecule, this surface coverage would correspond to ~3 closed-packed monolayers.[108]

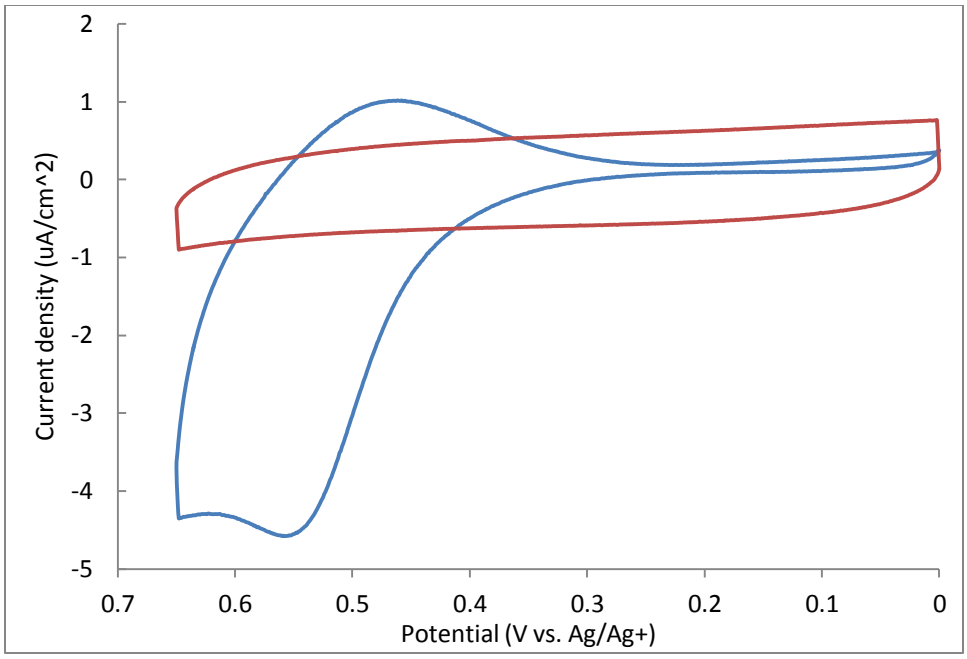

Figure 3.5 Thin film cyclic voltammogram of ZnTCPP on ITO (blue) and background (red) showing the first oxidation. Solvent was 0.24 M TBAP/ACN and scan rate was 25 mV/sec.

The background-subtracted CV of ZnPA adsorbed to ITO and background CV are shown in Figure 3.6. The oxidation and reduction peaks are not well resolved. There is some indication of two oxidation steps, but it is difficult to determine the mid-point potentials. The first oxidation peak appears to occur between +0.3 and +0.4 V vs. Ag/Ag+ and the second between +0.5 and +0.6 V vs. Ag/Ag+. The first oxidation potential is less positive than the ZnTCPP film, which suggests that the ZnPA film is easier to oxidize. The non-faradaic background is too large to allow the electroactive surface coverage to be determined. The diffusion controlled electrochemistry of ZnPA is not published and was unable to be experimentally determined. The oxidation and reduction peaks could not be resolved and the redox potentials could not be determined due to large non-faradaic backgrounds with diffusion controlled ZnPA experiments.

3.4.2 Potential Controlled ATR Spectroscopy

In Figure 3.1B the photoinduced reactions at the zinc porphyrin/ITO interface were described. After the photoexcited porphyrin presumably injects an electron into the ITO, the resulting film will be the oxidized porphyrin species. It is important to know the spectra of the oxidized zinc porphyrin in order to identify the absorbance bands that are monitored during the transient absorbance experiments. Steady state ATR spectroscopy was coupled to electrochemistry to obtain the spectra of the oxidized porphyrin film. In addition, the mid-point potentials were determined with this technique without interference from non-faradaic current seen with the CVs.

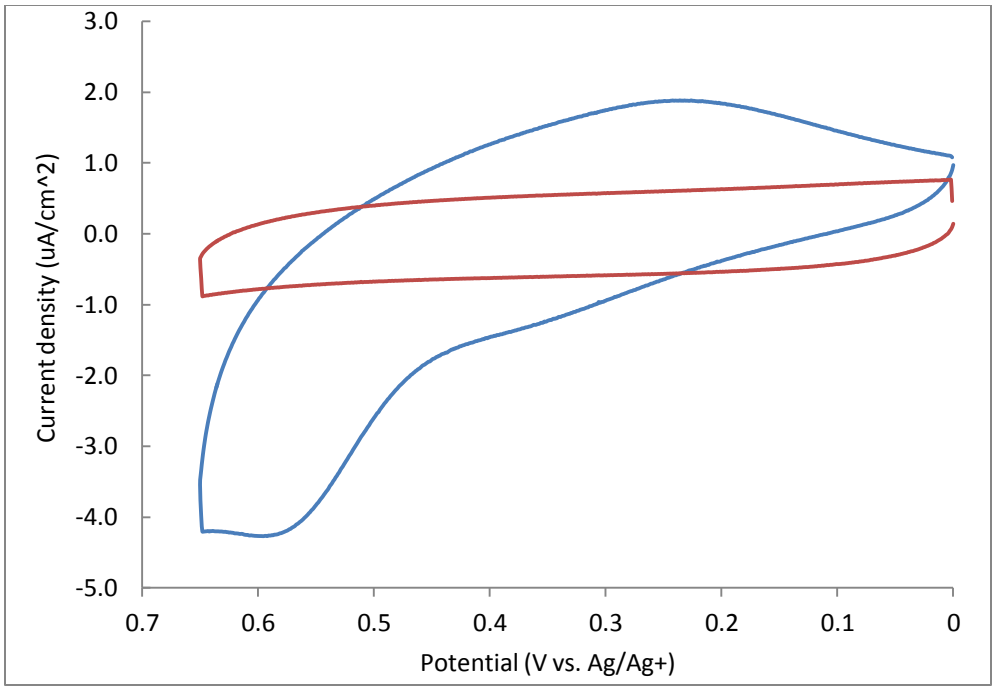

Figure 3.6 Thin film cyclic voltammogram of ZnPA on ITO (blue) and background (red) showing the first oxidation and possibly the second oxidation. Solvent was 0.24 M TBAP/ACN and the scan rate was 25 mV/sec.

The ITO was prepared as described in Section 3.3.1 and the ATR flowcell was assembled. A blank was obtained with 0.1 M tetrabutylammonium perchlorate in acetonitrile (TBAP/ACN) in contact with the ITO coated slide. 25 μM ZnTCPP in ethanol or 25 μM ZnPA in 10 mM MES buffer (pH 5.5) was injected into the flowcell and allowed to adsorb for 30 minutes. The cell was rinsed with 10 mL of 0.1 M TBAP/ACN and spectra of the resulting porphyrin film were collected for both TE and TM polarizations. De-oxygenated 0.1 M TBAP/ACN continuously flowed through the ATR cell as positive potentials were applied. The potential of the film was held for 30 seconds before acquiring a spectrum.

The ATR spectra in both TE and TM polarizations of the ZnTCPP film on ITO at open circuit are shown in Figure 3.7A. The Soret band is broadened as compared to the solution sample in Figure 3.4A, where the solution Soret:Q-band ratio is 29 and the thin film ratio is 5-6. The broadening of the Soret band is indicative of aggregation.[100]

The absorbance of the ZnTCPP Soret band maximum, 425 nm for TE and 410 nm for TM, as a function of applied potential, normalized to the value at V_{OC} (open circuit potential) is shown in Figure 3.7B. The mid-point potential ($E^{0\prime}$) of the oxidative bleaching agrees with the mid-point potential from the CV results of ~0.5 V vs. Ag/Ag+.

The TE and TM absorbance spectra of the oxidized ZnTCPP film as a function of applied potential are shown in Figure 3.7C and 3.7D. The spectra represent the radical cation species of ZnTCPP and agree with spectra in the literature of zinc porphyrin radical cations.[106, 110] As compared to the film at open circuit, there is a decrease in the

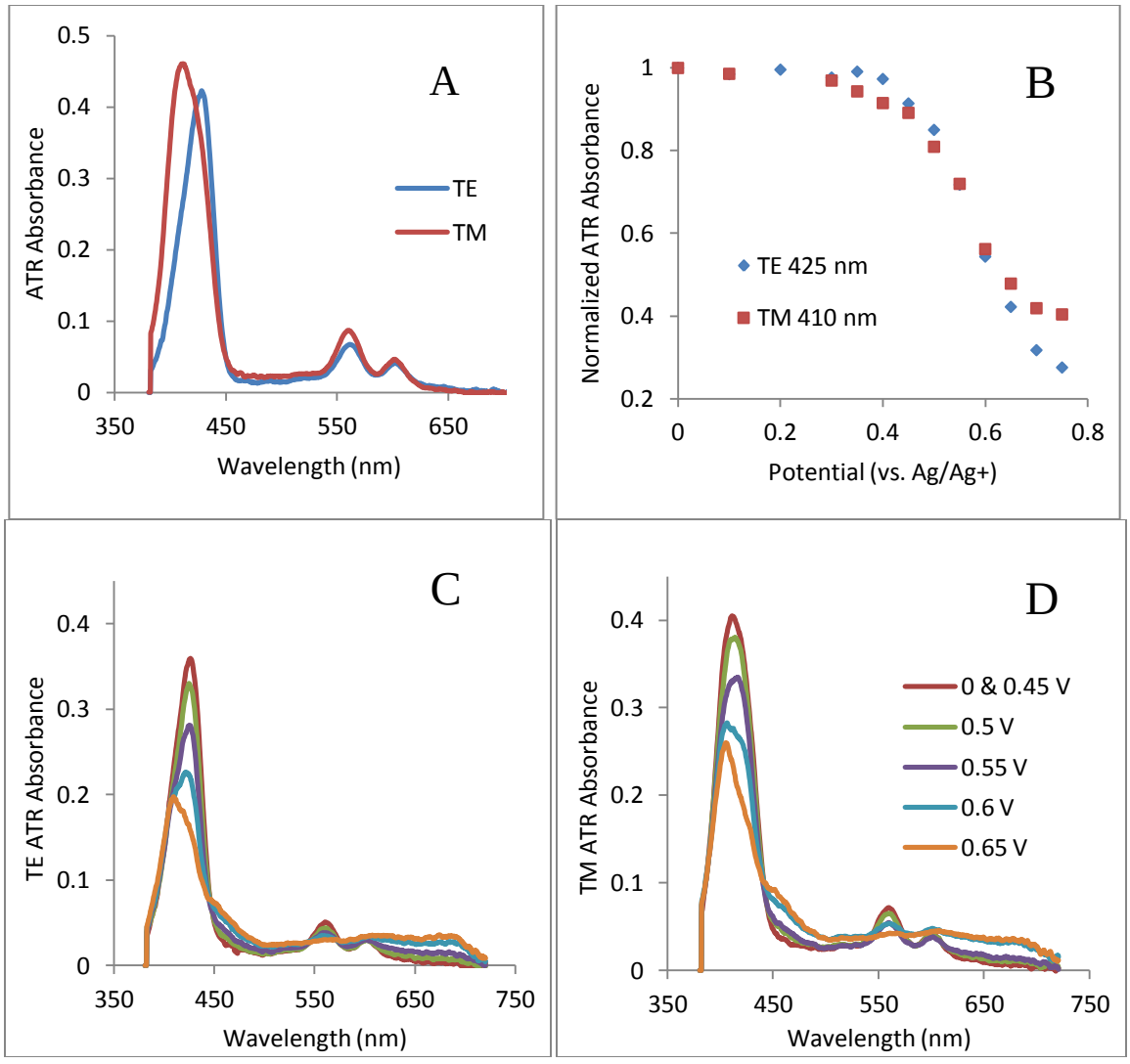

Figure 3.7 (A) ATR spectra of ZnTCPP on ITO at open circuit, TE and TM. (B) Normalized absorbance vs. potential (V vs. Ag/Ag+) for TE at 425 nm and TM at 410 nm. (C) Potential controlled ATR spectra, TE. (D) Potential controlled ATR spectra, TM. Legend in (D) applies to (C).

Soret band absorbance and an increase of absorbance at wavelengths around 650 nm, with increasing potential.

The ATR absorbance spectra for ZnPA adsorbed to ITO in both TE and TM polarizations are shown in Figure 3.8A. As with the ZnTCPP films, there is broadening of the Soret band, suggesting aggregation.[48] The ratio of Soret band:Q-band for the solution sample in Figure 3.4B was 26 while the ratio for the ATR films was ~5. The normalized absorbance at the Soret band as a function of applied potential is presented in Figure 3.8B. The spectra were evaluated at 430 nm and 407 nm for TE and TM polarizations, respectively. Although an exact mid-point potential cannot be extracted from this data, the oxidative bleaching occurs around +0.45 V vs. Ag/Ag+. This is slightly less than the mid-point potential found for thin films of ZnTCPP on ITO.

The potential controlled ATR spectra of ZnPA adsorbed to ITO are shown in Figure 3.8C and 3.8D for TE and TM polarizations, respectively. The shape of these spectra is similar to the oxidized ZnTCPP films and other oxidized zinc porphyrins in literature.[106, 110] The ZnPA oxidized film also shows a decrease of the Soret band absorbance and an increase around 650 nm. The increased absorbance at 650 nm is much larger compared to the ZnTCPP oxidized film. The reason for this difference in molar absorptivity of the oxidized species is unclear.

The ZnTCPP and ZnPA oxidized spectra are important when looking for absorbance changes as a result of charge transfer. The band diagram in the zinc porphyrin film coupled to ITO, as depicted in Figure 3.1, shows the energy level

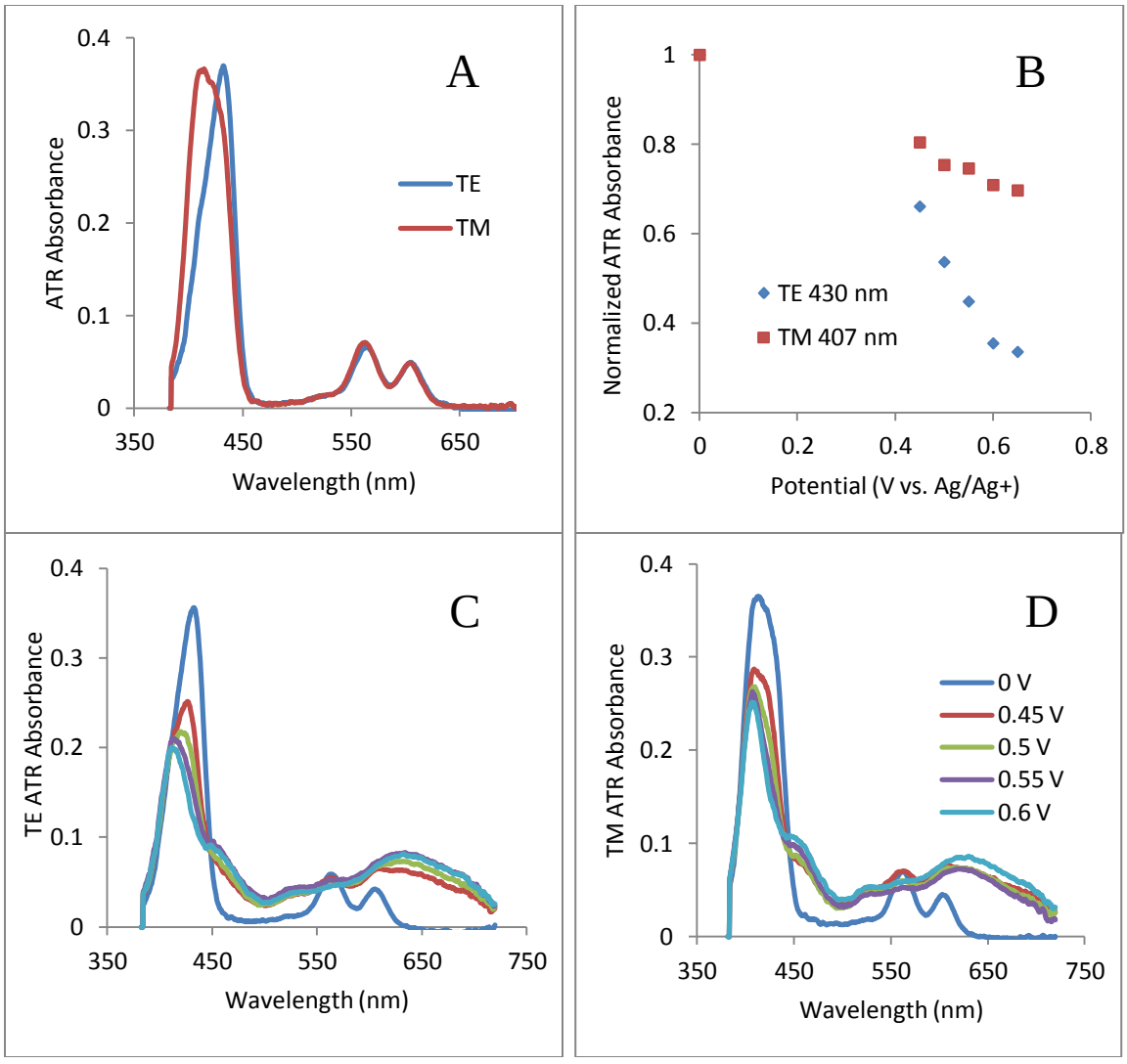

Figure 3.8 (A) ATR spectra of ZnTCPP on ITO at open circuit, TE and TM. (B) Normalized absorbance vs. potential (V vs. Ag/Ag+) for TE at 430 nm and TM at 407 nm. (C) Potential controlled ATR spectra, TE. (D) Potential controlled ATR spectra, TM. Legend in (D) applies to (C).

alignment to favor charge injection of the photoexcited porphyrin into the ITO. The radical cation of the zinc porphyrin is the resulting species which has the absorbance profile in Figures 3.7C, 3.7D, 3.8C and 3.8D.

The spectroelectrochemical experiments have provided more confidence in the oxidation values of the zinc porphyrins bound to ITO obtained from the cyclic voltammetry experiments. It can be concluded from these experiments that the oxidation potentials from diffusion controlled electrochemical experiments do not accurately represent the oxidation potentials and thus the energy level alignments of thin molecular films.

In the case of ZnTCPP, the adsorbed film was more difficult to oxidize than the dissolved sample. Studies of redox reactions of ferrocene monolayers immobilized on gold electrodes have demonstrated positive shifts of oxidation-reduction potentials as compared to the corresponding dissolved ferrocene.[111] Creagar and co-workers explained that variations of solvation effects of the counterion between molecules immobilized at the electrode surface and those in the bulk solution lead to a shift in redox potential.[111] Further studies where the ferrocene groups were buried in the monolayer exhibited strong shifts to positive potentials as compared to ferrocene groups that were more 'exposed' to the electrolyte solution.[112] The reason for the positive shift in the redox potential of the ZnTCPP film as compared to the bulk solution is likely due to the inability of counterions to sterically access the redox centers in the closed-packed zinc porphyrin film and screen the positive charges.

A revised band diagram is presented in Figure 3.9 with the adjusted potentials as determined by cyclic voltammetry and potential controlled ATR spectroscopy. The values of the triplet state energy levels for ZnTCPP and ZnPA films were assumed to be fixed relative to the energy of the ground and singlet excited states. The corrected energy alignment decreases the energy needed to transfer an electron from the zinc porphyrin film to the ITO as compared to the solution sample. In addition, the energy offset between the Fermi energy of the ITO and the zinc porphyrin films also increases the driving force for recombination. Determining accurate energy level alignments is essential to understanding the charge transfer kinetics at the molecular film-TCO interface.

3.4.3 Molecular Orientation

Another property of the molecular thin film that is hypothesized to influence the photoinduced charge transfer kinetics is the molecular orientation.[96, 103, 113] As described in detail in Chapter 1, Lin, et al. correlated molecular orientation with electron transfer in zinc phthalocyanine molecules tethered to ITO. The aggregated in-plane population demonstrated a 3-fold faster electron transfer rate than the upright aggregates.[37] The orientation of the zinc porphyrins on ITO has a potential to affect the charge transfer kinetics. Therefore, it is important to characterize the orientation.

The steady-state ATR spectra in Figure 3.7A and 3.8A were used to determine the mean tilt angle of the ensemble of zinc porphyrins adsorbed to ITO. Due to the excessive

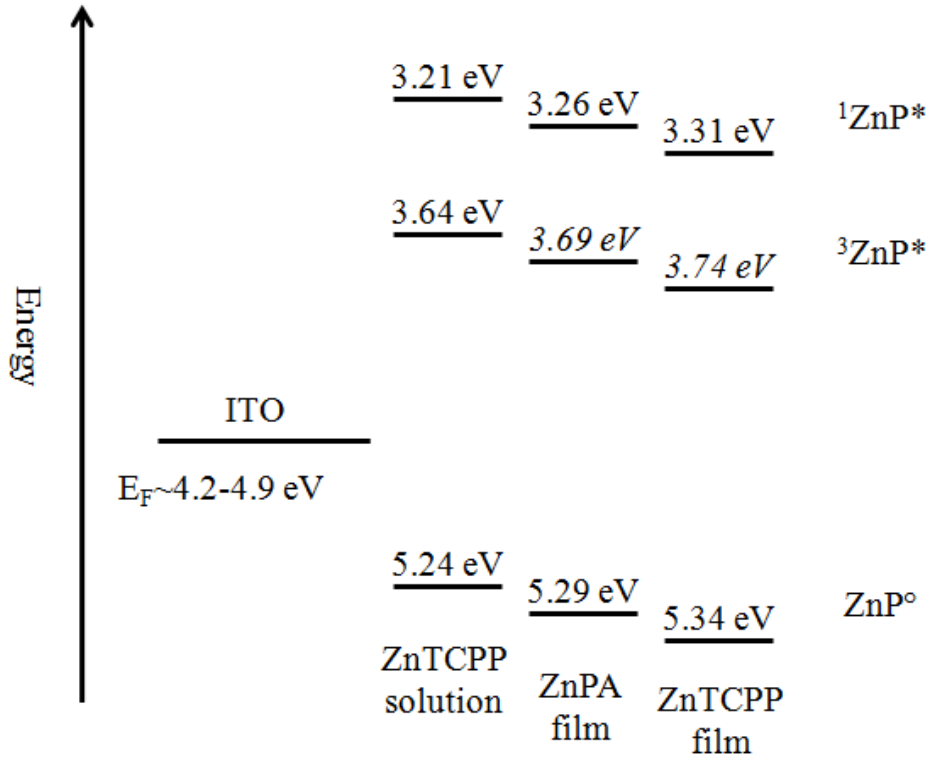

Figure 3.9 Revised band diagram of ZnP-ITO interface. Values for triplet state energy levels of ZnPA and ZnTCPP films (in italics) were assumed to have a fixed relative energy to the ground and excited state energy levels. Energy levels were converted from NHE to vacuum by 4.44 eV.[107]

broadening of the Soret band, the absorbance at the first Q-band was used to quantify the mean tilt angle.

The dichroic ratio (ρ) is related to the mean tilt angle (θ_μ) by Equation 3.1 for circular dipoles. Expressions for the electric field intensities E_x^2, E_y^2, and E_z^2 are provided in Lee and Saavedra and are shown in Equation 2.2.[67] A diagram of the direction of the electric fields is shown in Figure 3.10A. The absorbance of the film in TM and TE are denoted as $A_{f,TM}$ and $A_{f,TE}$, respectively. N_{TM} and N_{TE} are the number of total internal reflections in the TM and TE polarizations and were calculated from the internal reflection angle (β) and the interaction length along the waveguide by the totally reflected beam. The thin film and two-phase approximations were used in these calculations, ignoring contributions from the 100 nm thick ITO.

$$\rho = \frac{A_{f,TM}}{A_{f,TE}} = N_{TM}\left[E_x^2 + \frac{2E_z^2\cos^2\theta_\mu}{1+\sin^2\theta_\mu}\right]\left[N_{TE}E_y^2\right]^{-1} \qquad (3.1)$$

The steady state ATR experiments of ZnTCPP and ZnPA on ITO used the following parameters:

Internal reflection angle, β = 72° (ZnTCPP) and 71° (ZnPA)

n_1 (acetonitrile) = 1.34

n_2 (glass) = 1.51

waveguide thickness = 1.0 mm

interaction length along waveguide sampled by the totally reflected beam = 4.2 cm

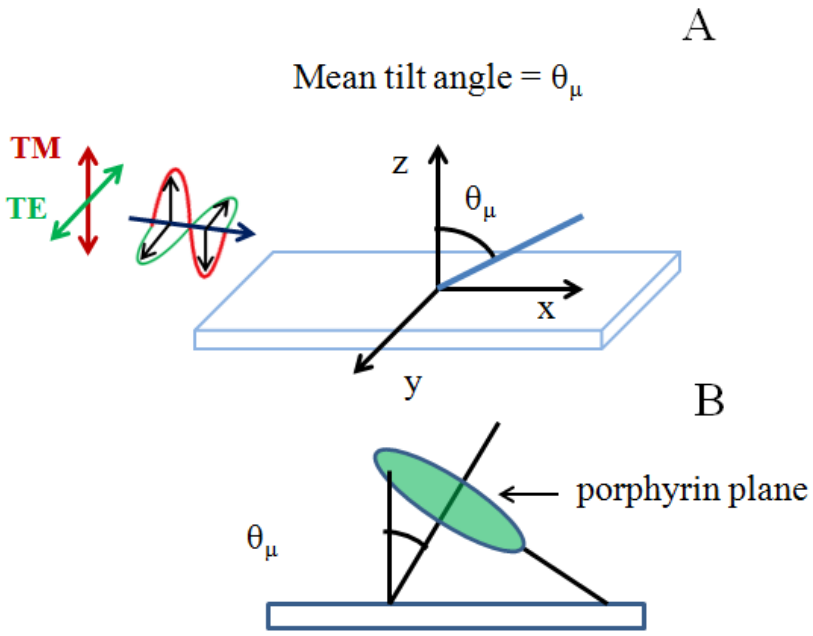

Figure 3.10 (A) A diagram of the electric field vectors in relation to the place of the waveguide. (B) A schematic of the mean tilt angle between the molecular plane normal and the normal to the surface plane of the ITO.

The calculated θ_μ describes the mean tilt angle between the molecular plane normal and the normal to the ITO surface plane. A schematic of this geometry is shown in Figure 3.10B. ZnTCPP on ITO was found to be 34°, while ZnPA on ITO was found to be 39°. These values assume a uniformly tilted ensemble of molecules in these thin films and not a distribution of angles. The θ_μ was not anticipated to be similar between these two molecules, since the ZnPA structure has an additional methyl group as compared to ZnTCPP. The θ_μ for both ZnTCPP and ZnPA suggest that no more than two functional groups for each porphyrin molecule are bound to the ITO; if 3-4 groups were bound a significantly smaller θ_μ would have been measured indicating a predominantly in-plane orientation with the ITO surface.

The stability of the film on the ITO surface is dominated by the binding between the carboxylic acid and phosphonic acid to the ITO. The indication of aggregation from the broadening of the Soret band in Figures 3.7A and 3.8A also support the conclusion that the ensemble of molecules is not in-plane. If the molecules were mostly in-plane, a second molecule to form an aggregate with the bound porphyrin would be further in distance from the ITO surface, not allowing for covalent binding with the ITO. The aggregation is initially dominated by the intermolecular interactions such as π-π or Van der Waals interactions, which are not as stable as the covalent binding between the functional groups and ITO.

As discussed previously, the orientation of molecules at the molecular thin film/TCO interface play a role in the charge transfer efficiency. It can control the electron tunneling distance from the molecule to the TCO.[37] The molecular orientation

can also impact the aggregation of molecules at the surface, which can affect the photoinduced excited states of the molecules.[99-100]

3.4.4 Surface Coverage

The surface coverage of the porphyrins on ITO was determined using steady state ATR spectroscopy. The equations to determine the evanescent intensity vs. the incident intensity (I_e/I_i) for TE and TM polarizations are shown in equations 3.2a-b.[57]

$$\frac{I_e}{I_i}_{TE} = \left(\frac{n_1}{n_2}\right)\left(\frac{4\cos\beta}{1-\left(\frac{n_1}{n_2}\right)^2}\right) \quad (3.2a)$$

$$\frac{I_e}{I_i}_{TM} = \left(\frac{I_e}{I_i}_{TE}\right)\left[\frac{2\sin^2\beta-\left(\frac{n_1}{n_2}\right)^2}{\left(1+\left(\frac{n_1}{n_2}\right)^2\right)\sin^2\beta-\left(\frac{n_1}{n_2}\right)^2}\right] \quad (3.2b)$$

The values of I_e/I_i for the ZnTCPP ATR experiments were 5.1 and 6.3 for TE and TM, respectively. ATR experiments with the adsorption of ZnPA had I_e/I_i values of 5.4 and 6.6 for TE and TM, respectively. As discussed previously, the thin film and a two-phase approximation were used when determining the surface coverage. The isotropic molar absorptivities for the first Q-band, 11,500 $M^{-1}cm^{-1}$ (ZnTCPP) and 11,300 M-1cm^{-1} (ZnPA), were used in equation 2.3 along with the calculated I_e/I_i values to determine the surface coverage.

The surface coverage for ZnTCPP adsorbed to ITO was determined to be 340 pmol/cm^2. The surface coverage of ZnPA on ITO was determined to be 290 pmol/cm^2.

These values are reasonable, as they are equivalent to ~1.0 and 0.9 for ZnTCPP and ZnPA, respectively, of a closed-packed monolayer (ML) if the molecules are oriented in an edge-on geometry with a projected area of 50 $Å^2$/molecule.[108] If the molecules were predominantly oriented in-plane to the ITO surface, with a projected surface area of 360 $Å^2$/molecule,[108] it would equate to ~7.0 and 6.3 ML for ZnTCPP and ZnPA, respectively. As concluded from the mean tilt angle calculations, it is evident that the molecules are not oriented in-plane to the ITO surface.

The value of 140 pmol/cm^2 found from the thin film CV of ZnTCPP on ITO reflects the electroactive surface coverage. This is less than 50% of the coverage determined from the ATR spectrum. For both molecules, the CVs exhibited a large non-faradaic current, so this could have introduced some error in the calculation. The thin film molar absorptivity of the ZnTCPP and ZnPA molecules are not known, therefore the molar absorptivity of the isotropic solution was used to calculate the surface coverage. This discrepancy may also introduce some error into the surface coverage values that were determined.

The optimal degree of surface coverage to improve charge transfer from the thin molecular film to ITO is not fully understood. The broadening of the Soret band in the ATR spectra suggests that the porphyrin aggregates upon adsorption to the ITO.[48] The surface coverage and effects due to the local molecular environment, such as aggregation or presence of other functional groups, will likely have a strong effect on the excited state characteristics and thus the charge transfer kinetics at the molecular thin film/TCO interface.[99-100]

3.4.5 Solution Transient Absorbance of ZnTCPP and ZnPA

The previous experiments helped define the band energy diagrams by finding the oxidation potentials of ZnTCPP and ZnPA adsorbed to ITO. In addition, the spectroelectrochemical studies provided ATR spectra of the oxidized porphyrin thin film, a transient species that would result from charge transfer into ITO. The porphyrin triplet state is another transient species that can play a role in the charge transfer and reveals information about the excited state porphyrin behavior.[104] Zinc porphyrins in solution have an intersystem crossing quantum yield (Q_{ISC}) between ~0.75 – 0.9,[97, 114] so it is likely the triplet species will participate in charge transfer to the ITO. Triplet state absorbance spectra and transient decay curves were obtained for both ZnTCPP and ZnPA using the EOS instrument (Ultrafast Systems, Inc.).

The difference spectrum for 100 μM ZnTCPP in EtOH at a delay time of 0.1 μsec is shown in Figure 3.11A. The excitation pump laser was 532 nm. The transient decay curve was evaluated at 460 nm, where the difference absorbance spectrum had the largest change. The transient decay curve is shown in Figure 3.11B and was fit to a first order exponential of 0.89 μsec. The difference absorbance spectrum for 100 μM ZnPA in 10 mM MES buffer (pH 5.5) at a delay time of 0.1 μsec is shown in Figure 3.12A. The transient decay curve at 460 nm is shown in Figure 3.12B and was fit to a first order exponential with a lifetime of 3.1 μsec. These transient decays correspond to the triplet state decay lifetimes for the porphyrins.[97]

The triplet lifetimes for both zinc porphyrin samples are significantly shorter than the reported lifetimes of purged zinc porphyrin solutions, where deoxygenated solutions

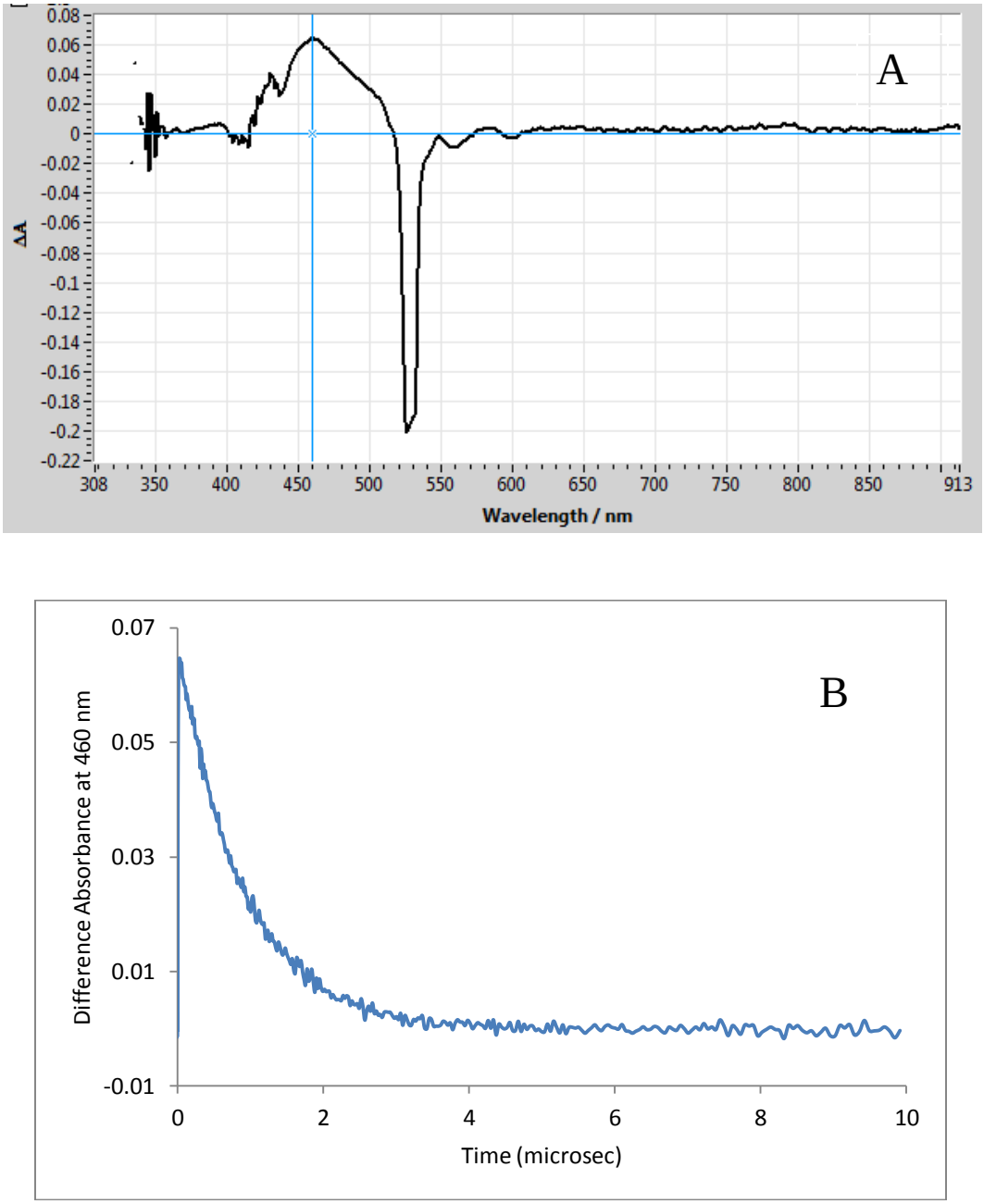

Figure 3.11 (A) Solution transient difference absorbance spectrum of 100 μM ZnTCPP in EtOH at a delay time of 0.1 μsec. (B) Transient decay curve at 460 nm. The excitation pump wavelength was 532 nm.

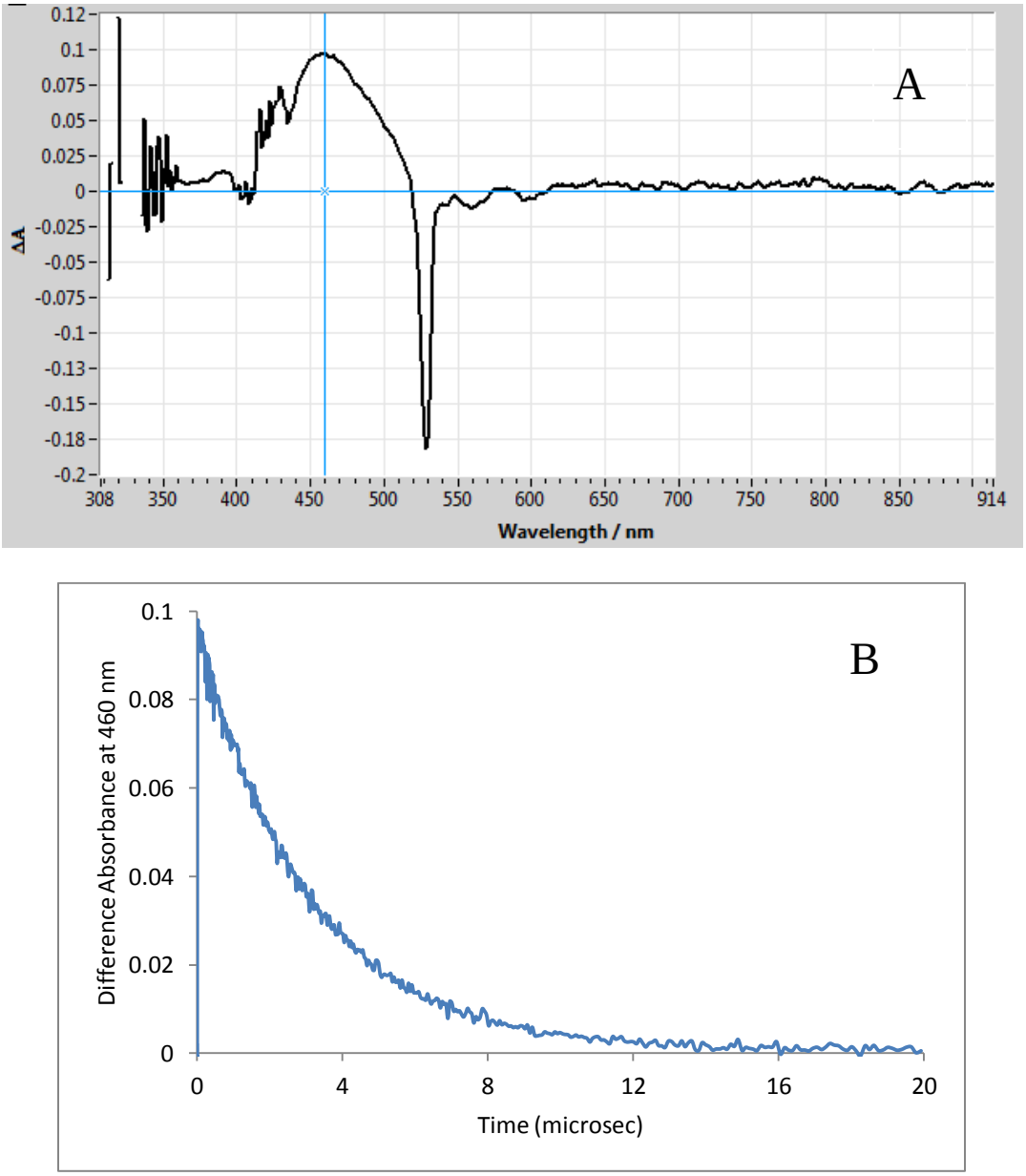

Figure 3.12 (A) Solution transient difference absorbance spectrum of 100 μM ZnPA in 10 mM MES buffer (pH 5.5) at a delay time of 0.1 μsec. (B) Transient decay curve at 460 nm. The excitation pump wavelength was 532 nm.

at room temperature have a lifetime range of 0.65 – 1.4 ms.[97] When zinc porphyrin solutions are aerated, triplet lifetimes are reduced to <200 nsec.[114] Although the solutions in this study were purged with argon prior to placing them in the instrument, it was not possible to keep the solutions completely de-oxygenated throughout the entire pump-probe experiment.

The transient decay of 25 μM ZnTCPP in EtOH was measured using the Proteus instrument. The Proteus instrument accommodates a 10 mm pathlength cuvet where a 2 mm cuvet is used in the EOS instrument. As a result the concentration was lowered to account for this change. The excitation was at 532 nm and the monitoring beam was at a wavelength of 480 nm. The band pass filter available for the Proteus transient experiment was at 480 nm, which was sufficient to monitor the triplet state. The transient decay curve is shown in Figure 3.13. The triplet state lifetime was not successfully fit to a first order exponential, thus an additional component was added. The lifetimes of the triplet state were determined to be 0.23 and 1.2 ms with weighing factors of 0.77 and 0.23, respectively. The triplet lifetime of ZnTCPP in water has been measured and fit with a single exponential with a value of 1.3 ms.[97] The longer lived component of ZnTCPP in EtOH matches closely to the literature value. The shorter lifetime could be a result of inadequate de-oxygenation of the sample. It is also possible that the solvation of ZnTCPP by EtOH as opposed to water affects the triplet state lifetime. Studies of triplet state lifetimes of ZnTPP and ZnTSPP have shown a significant difference in triplet state lifetimes as a function of solvent. In dichloromethane, zinc(II)tetraphenyl porphyrin ZnTPP has a triplet decay of 583 μsec, where as in pyridine the triplet decay is shortened

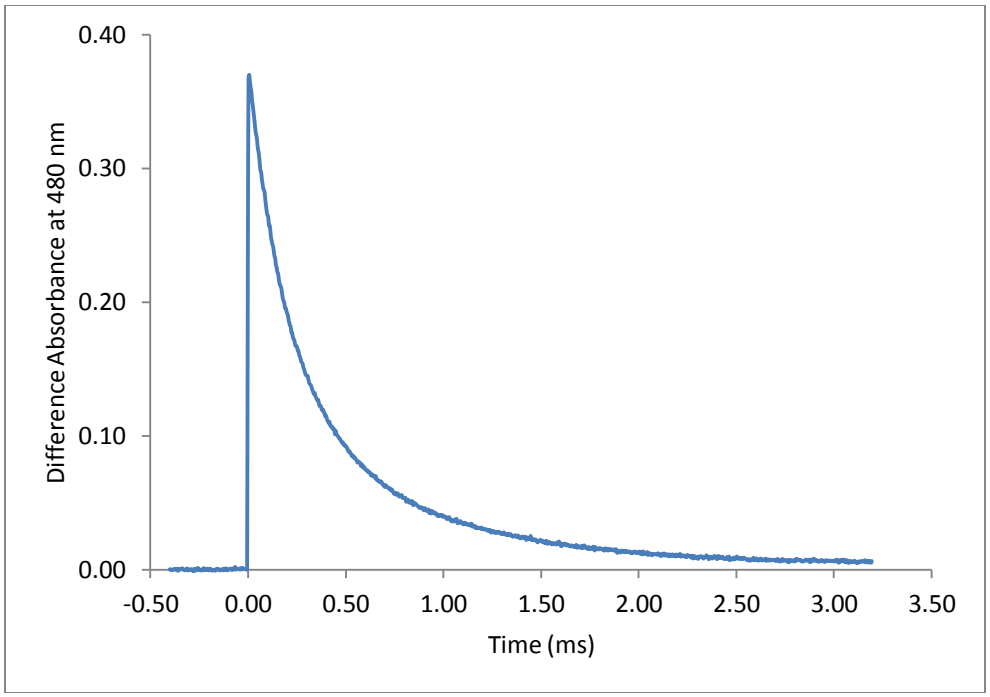

Figure 3.13 Transient decay curve of ZnTCPP in EtOH measured using the Proteus instrument with excitation at 532 nm and monitoring at 480 nm, representing the triplet state decay.

to 200 μsec.[115] Zinc(II)tetrakis(4-sulfonatophenyl) porphyrin (ZnTSPP) in water has a triplet lifetime of 1.4 ms[97] where in methanol it is decreased to 785 μsec.[115] The dielectric constants of water, methanol and ethanol are of 80.1, 33, and 24.3, respectively. In addition, ethanol also has an organic component that could interact with the porphyrin to cause triplet annihilation.

The charge transfer efficiency between a molecular thin film and TCO is influenced by the excited state lifetime of the molecule. The solvation of the molecule, whether by a solution or a polymer network, will have a large impact on the charge transfer. Therefore, these properties must be considered when designing OPVs.

3.4.6 Transient ATR Spectroscopy

As described in detail in Chapter 1, the overall efficiency of an OPV is dictated by the efficiencies of the charge transfer and migration processes. Charge transfer at the molecular thin film/TCO interface is hypothesized to be influenced by factors such as the attachment chemistries, molecular orientation and the local molecular environment. The final charge collection step is dictated by a small fraction of molecules in the donor layer, a single monolayer or less, at the donor layer/TCO interface. Transient ATR spectroscopy has the sensitivity to probe photoinduced kinetics in submonolayer films and the potential to determine charge transfer and recombination kinetics at these critical interfaces.

3.4.6a Sensitivity Considerations

In Chapter 2 the optical sensitivity considerations for conducting a transient ATR experiment were thoroughly discussed. An appreciable amount of the excitation beam must be absorbed by the ground state molecules to promote a significant fraction of molecules to the excited state. The term presented in Chapter 2 to compare sensitivity between films was the product of the molar absorptivity at the excitation wavelength and the molecular surface coverage ($\varepsilon_f\Gamma$). The value that was determined for the PM fragments was 3.2×10^{-4}. The other term that should be considered is the number of total internal reflections (N). The transient ATR experiments in Chapter 2 utilized 200 μm thick quartz slides to achieve 39 total internal reflections. Another important factor not included in the sensitivity comparison is the molar absorptivity of the excited state. The M-state of the PM fragments has a molar absorptivity of 48,800 $M^{-1}cm^{-1}$.[83]

The product of the ZnTCPP surface coverage of 340 $pmol/cm^2$ and the molar absorptivity at the excitation wavelength ($\varepsilon_{532\ nm}$ = 1,500 $M^{-1}cm^{-1}$) is 5.1×10^{-4}. This value is comparable to the value found for the PM fragments, but it neglects the contributions from the total internal reflections and the molar absorptivity of the excited state. An estimated molar absorptivity of the oxidized ZnTCPP film can be determined from the ATR absorbance spectra at open circuit and under potential control in Figure 3.7A and 3.7C as shown in equation 3.3: $A_{TE,\ 560\ nm}$ is the absorbance at open circuit of the Q-band, $\varepsilon_{560\ nm}$ is the molar absorptivity of the Q-band, $A_{TE,\ 650nm}$ is the absorbance of the oxidized film at 676 nm, and $\varepsilon_{676\ nm}$ is its molar absorptivity.

$$A_{TE,\ 560\ nm}/A_{TE,\ 676\ nm} = \varepsilon_{560nm}/\varepsilon_{676nm} \qquad (3.3)$$

The molar absorptivity for the 1st Q-band at 560 nm is 11,500 $M^{-1}cm^{-1}$,[97] and its absorbance value is 0.07 a.u. for TE polarization. The absorbance of the oxidized ZnTCPP film at 676 nm was 0.033. Therefore, the molar absorptivity can be estimated to be ~ 5,500 $M^{-1}cm^{-1}$.

Thin films of ZnTCPP were prepared on ITO coated glass slides (CC) and were suitable for the electrochemical and steady state absorbance measurements. The ITO coated glass slides in the steady state ATR experiments had 7 total internal reflections. In order to attain a more comparable sensitivity for transient ATR with ZnTCPP, ITO coated coverslips with a thickness of 150 μm were obtained from NREL and used in these experiments. These coverslips afforded 42 total internal reflections using the prism coupling geometry. The revised relationship in order to determine feasibility of the transient ATR experiments is shown in equation 3.4. The sensitivity is the product of the molar absorptivity at the excitation wavelength (ε_f), molecular surface coverage (Γ), number of total internal reflections (N) and molar absorptivity of the transient state (ε_{ts}).

$$\text{sensitivity} = \varepsilon_f \times \Gamma \times N \times \varepsilon_{ts} \qquad (3.4)$$

The value of sensitivity for the transient ATR experiment conducted on PM films is ~610, where as the value for the transient ATR measurement proposed with an excitation at 532 nm is ~120. Although the detection limit of the transient ATR instrument has not been determined, this value may be too low to observe a transient signal from the oxidized porphyrin film.

To increase the sensitivity, the Nd:YAG laser was connected to a dye laser attachment, as described in Appendix A, to allow for excitation ~ 560 nm, where $\varepsilon_{560\ nm}$ =

11,500 $M^{-1}cm^{-1}$.[97] This increased the sensitivity value to ~900, which is higher than ~610, the value found for the successful transient ATR experiments described in Chapter 2.

Films of ZnTCPP and ZnPA were prepared on ITO coated slides (CC) and ITO coated coverslips (NREL) as described for the electrochemical experiments. The films were prepared outside of the cell and then secured into the Delrin ATR cell. Argon-purged acetonitrile flowed through the cell for the duration of the experiments. The difference absorbance was undetectable at 430, 480, and 676 nm for ZnTCPP or ZnPA adsorbed to either the ITO coated glass slides or the ITO coated coverslips. When a transient ATR experiment was conducted with an ITO coated coverslip with porphyrin adsorbed, there was very little light throughput between 400 and 430 nm, indicating that the Soret band absorbance exceeded the stray light limit of the instrument.

Thin molecular films of zinc porphyrin were adsorbed to ITO in order to measure charge transfer kinetics as a function of properties such as molecular orientation, binding chemistries and surface coverage. The energy diagram for charge transfer and photoinduced reactions were outlined in Figure 3.3. The energy diagram was then adjusted, shown in Figure 3.9, after measuring the ZnTCPP and ZnPA thin film mid-point potentials. Since ITO is highly conductive, it is likely that fast charge injection occurs from the photoexcited zinc porphyrin to the ITO, followed by rapid recombination. These charge transfer steps could all be happening on a time scale that is too fast for the transient ATR instrument to measure.

The time resolution of the Proteus transient instrument is based on the pulse width of the laser (5-7 ns). However, the incorporation of the optical elements in the instrument causes significant light loss. To account for this, the signal from the photodiode is current amplified (variable gain) which adjusts the time resolution of a transient ATR experiment from 700 ns to 300 μsec, depending on the gain. In these experiments a gain setting with amplification of 10^8 is used, which corresponds to a detector rise time of 1.8 μsec. Therefore, if the charge transfer and recombination events are occurring faster than ~3 μsec, the transient ATR instrument will not be able to record signal on the timescales necessary to measure the events.

3.4.6b Potential Controlled Transient ATR

It is hypothesized that at open circuit, the forward and backward charge transfer between the zinc porphyrins and ITO occurs on time scales that are too fast to be measured with the Proteus instrument. One way to alter the kinetics of charge transfer and recombination reactions is to decrease the driving force for charge recombination by holding the electrode at positive potentials. These types of experiments were conducted by other researchers with dye sensitizers on semiconducting nanocrystalline electrodes.[108] Gervaldo et al. prepared an ITO electrode with a mesoporous tin oxide (SnO) film on to which they deposited zinc porphyrin. By transient absorbance spectroscopy they measured the ground state recovery of the porphyrin, as a result of charge recombination. They did not provide the lifetimes for the potential controlled measurements, but by estimation there is a long lived component that decays ~3-fold slower for the films held

at 200 mV (vs. Ag/AgCl) as compared to the films held at -300 mV (vs. Ag/AgCl). The longer lived transient species could be monitored beyond 15 μsec in this experiment.

The strategy for observation of charge transfer at the zinc porphyrin – ITO interface is to decrease the driving force for recombination by holding the ITO at positive potentials. Another strategy is to decrease the driving force for charge injection by holding the ITO at negative potentials. In the latter situation, a triplet state decay could possibly be measured.

Thin films of ZnTCPP were prepared on ITO coated slides and coverslips, and secured into the Delrin ATR cell. Argon-purged 0.1 M TBAP/ACN flowed through the cell for the duration of the experiments. Since the film was constructed outside of the cell, there was no blank acquired to obtain absorbance spectra. Intensity spectra as a function of applied potential were measured to verify that electrochemical contact was made with the thin film. Figure 3.14A shows the negative difference intensity spectra ratioed to the 400 mV spectrum as a function of applied potential (vs. Ag wire). Figure 3.14B is the intensity at 420 nm as a function of applied potential. These spectra are similar to the oxidative bleaching spectra attained from potential controlled steady state ATR in Figure 3.7B. The mid-point potential is around +1 V vs. Ag wire, establishing the reference point between the anodized Ag wire reference electrode and the Ag/Ag+ non-aqueous reference electrode, where Ag/Ag+ is +0.5 V vs. Ag wire.

The film was held at a potential for 30 seconds prior to conducting the transient ATR experiment. As with the open circuit experiments, the species monitored were the triplet state at 480 nm, the cation radical at 676 nm and when there was sufficient light

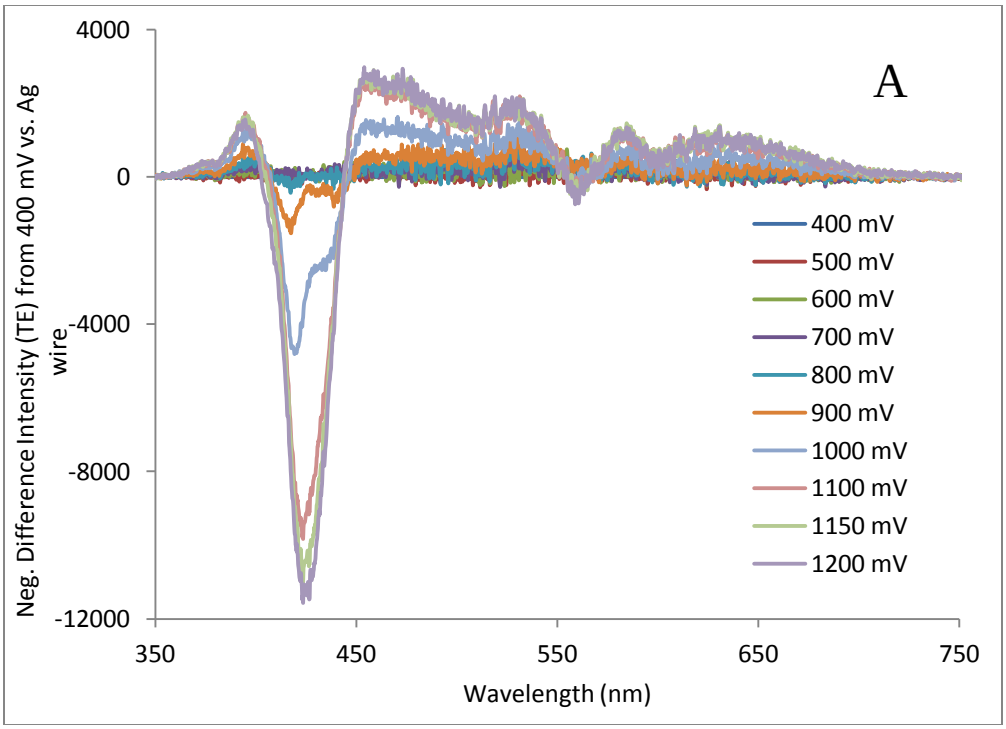

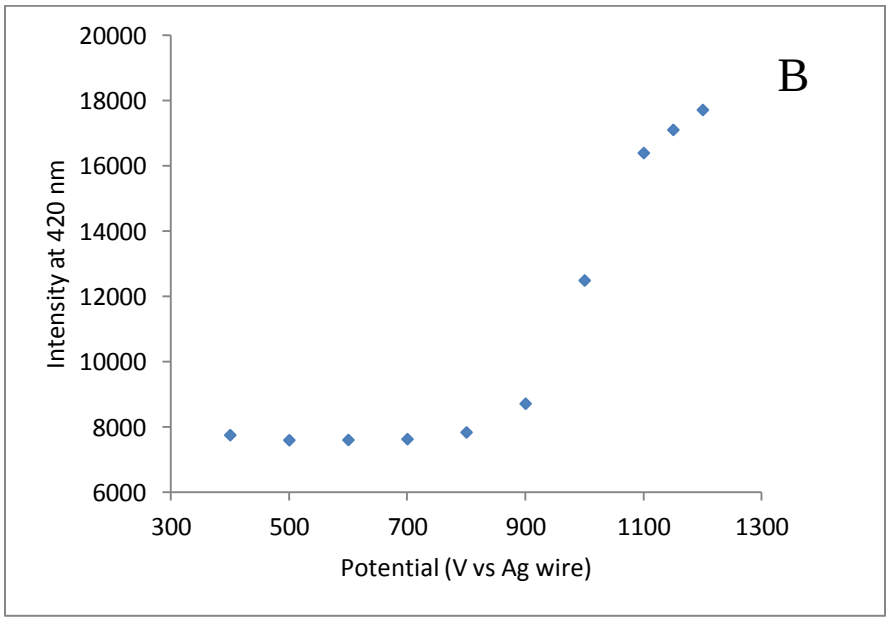

Figure 3.14 (A) Potential controlled difference spectra from 400 mV-1200 mV, vs. Ag wire of ZnTCPP on ITO in Delrin ATR cell. Spectra were ratioed to the 400 mV spectrum. (B) Absolute intensity as a function of potential (vs. Ag wire) for ZnTCPP adsorbed to ITO.

throughput, utilizing an ITO coated slide, the ground state recovery of the Soret band at 420 and 430 nm. According to the energy level diagram in Figure 3.9, it would be expected that as the ITO electrode is held at increasingly positive potentials, approaching the mid-point potential of ZnTCPP, the driving force for recombination would be small.[108] However, transient decay curves were not observed above the noise for any of these wavelengths at applied potentials of + 500, 600, 700, 800, 900, 1000 mV, vs. Ag wire. The other hypothesis was addressed by holding ITO at a negative potential; so that the driving force for triplet state charge injection would decrease. Transient decay curves were not observed at 430, 480, or 676 nm at the following applied potentials: -700, -800, -900, -1000 mV, vs. Ag wire. These experiments were also attempted with ZnPA tethered to ITO with comparable results.

There are several possibilities for not observing transient decay curves at the zinc porphyrin – ITO interface with the transient ATR instrument. The first that was addressed is the excitation efficiency in regards to the surface coverage and sensitivity of the instrument. Section 3.4.6a outlines the details of the sensitivity argument. It can be concluded that zinc porphyrin is sufficiently photoexcited and that the instrument is sensitive enough to measure transients with a molar absorptivity of ~5,500 $M^{-1}cm^{-1}$. The second possibility is that charge transfer and recombination between zinc porphyrin and ITO is happening on a fast timescale which is not within the time resolution of the Proteus instrument. A strategy to slow down the reaction was implemented. By holding ITO at positive and negative potentials, it was hypothesized that the driving force was decreased and therefore the kinetics of charge injection and recombination slowed.[108] It

is possible that the kinetics were altered, but were still too fast for the time resolution of the instrument.

Another way to slow down the kinetics is to decrease the temperature. ZnTPP in methylene chloride at 77K is known to have a triplet state lifetime of 26 ms.[98] Another strategy to investigate the zinc porphyrin-ITO interface could be to adsorb zinc porphyrin to ITO nanoparticles and measuring them in solution in a cuvet. The light loss through the optics in the ATR geometry drastically limits the time resolution of the measurement and utilizing nanoparticles would allow for nanosecond lifetimes to be measured. The disadvantage of this approach is losing the ability to apply a potential to the ITO and measure charge transfer as a function of molecular orientation.

In addition to these hypotheses for inability to measure transients at the zinc porphyrin – ITO interface, there are many other chemical questions that arise from these experiments. The behavior and chemical nature of non-aggregated porphyrin solution samples cannot necessarily be extrapolated to porphyrins adsorbed to a conducting metal oxide. The ATR spectra in Figures 3.7A and 3.8A suggest that aggregation of the porphyrin occurs on the surface, in addition, there may also be local molecular environment effects resulting in significant alterations of the excited state behavior. The zinc porphyrin molecular thin film must be further studied to understand the chemical influences on the photoinduced excited states, which directly affect the kinetics of charge transfer to a metal oxide, for example.

3.5 Results and Discussion: Zinc Porphyrin Mono- and Multilayers on Glass

Efficient charge transfer at the molecular thin film – TCO interface is important for performance of OPVs. Properties such as molecular orientation,[37] energy alignment[55] and chemical nature are hypothesized to influence charge transfer. It is necessary that the excited state lifetimes of the donor species are sufficiently long to promote charge transfer and resist decay and recombination pathways. The excited state lifetimes of the molecule at the molecular thin film – TCO interface are not well understood. In order to improve our knowledge about the kinetics at the molecular thin film – TCO interface, zinc porphyrins were tethered to ITO and electrochemical and optical properties were investigated. It is clear from the electrochemical results that zinc porphyrins bound to ITO behave differently than zinc porphyrins in solution.[106] This is highlighted in the energy level diagram in Figure 3.9. Transient ATR experiments were conducted to study the charge transfer at the zinc porphyrin – ITO interface, at open circuit and at positive and negative potentials. Transient decays were not observed for these systems and a thorough explanation is given in Section 3.4.6.

It is therefore hypothesized that a key aspect to charge transfer is how the local chemical environment influences the excited state lifetimes. When adsorbed to a surface, the porphyrin experiences the attraction or repulsion of the surface charge. As the porphyrin aggregates or forms strong intermolecular interactions with other species, new pathways for excited state decay are introduced.[99] Mono- and multilayer thin films of zinc porphyrin were prepared and studied on inert glass as opposed to ITO in order to

probe how the local molecular environments will specifically influence the excited state lifetimes.

3.5.1 Solution Transient Absorbance of Zinc Porphyrins and Charged Polymers

Films were prepared using electrostatic layer by layer (LbL) deposition, a convenient method to form thin films[62], as described in Chapter 2. The LbL method utilizes charged molecules and polymers to form multilayer films. Prior to studying zinc porphyrins incorporated into films with charged polymers, transient absorbance studies were done to evaluate how the photoinduced reactions of dissolved porphyrins were affected by the presence and absence of charged polymers. These experiments served as controls for the mono- and multilayer film experiments.

The polymers used for these studies were positively charged poly(allylamine hydrochloride) (PAH) (Sigma) and negatively charged poly(sodium 4-styrenesulfonate) (PSS) (Sigma). The polymers were dissolved in water (HPLC grade), and the concentrations calculated by the molecular weight of the monomeric unit, 93.5 g/mol and 206 g/mol, for PAH and PSS, respectively. Due to its compatibility with the aqueous LbL assembly method, ZnPA was the focus of these experiments.

3.5.1a ZnPA with PAH

Solution samples of ZnPA combined with the charged polymers were studied as controls for the thin film experiments. The solution sample results are discussed in this section and in Section 3.5.1b. UV-Vis absorbance spectra for 10 μM ZnPA in MES

buffer (pH 5.5) (ZnPA) and 10 μM ZnPA + 5 mM PAH in MES buffer (pH 5.5) (ZnPA-PAH) are shown in Figure 3.15. At a pH of 5.5, there is a single negative charge on each of the phosphonic acid groups on the porphyrin because the pKa values of the phosphonic acids groups are 3 and 8.[116] The broadening of the Soret band and red shift of the Q-bands suggest an aggregated species when the negatively charged ZnPA was combined with PAH. The Soret band:Q-band ratios were 29 and 13 for the ZnPA and ZnPA-PAH solutions, respectively. PAH does not absorb in the visible region, so there were no bands interfering with ZnPA in the absorbance spectra.

All of the solution transient experiments were conducted on the Proteus transient instrument in the 1 cm x 1 cm quartz cuvet. The samples were excited with ~560 nm from the dye laser pumped by the Nd:YAG. The excitation and the monitoring beam were aligned perpendicular to one another. Transient absorbance curves were measured before and after purging with argon. The triplet state was monitored at 480 nm and the ground state recovery was monitored at 430 nm for all of the solution experiments.

The transient decay and recovery curve for unpurged 10 μM ZnPA in 10 mM MES buffer (pH 5.5) (ZnPA) is shown in Figure 3.16A. The triplet decay at 480 nm and the ground state recovery at 430 nm were both fit to first order exponentials with lifetimes of 3.7 μsec and 4.2 μsec, respectively. These values are also reported in Table 3.1. Figure 3.16B shows the transient decay and recovery for argon purged 10 μM ZnPA, also measured at 480 nm and 430 nm, respectively. These curves were also fit to first order exponentials with triplet state lifetime of 20 μsec and the ground state recovery lifetime of 19 μsec, as reported in Table 3.1.

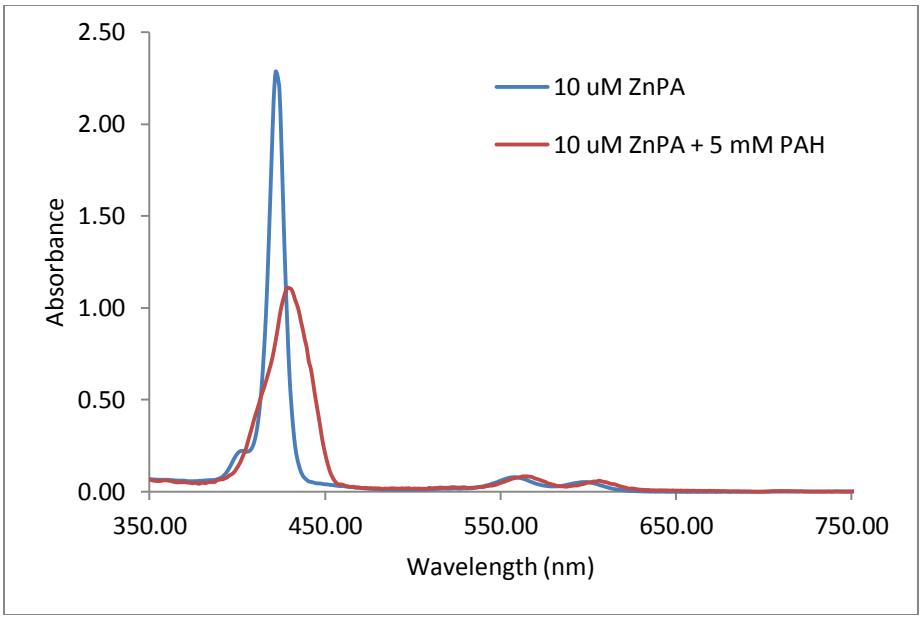

Figure 3.15 UV-Vis absorbance spectra of 10 μM ZnPA (blue) and 10 μM ZnPA + 5 mM PAH (red) in MES buffer.

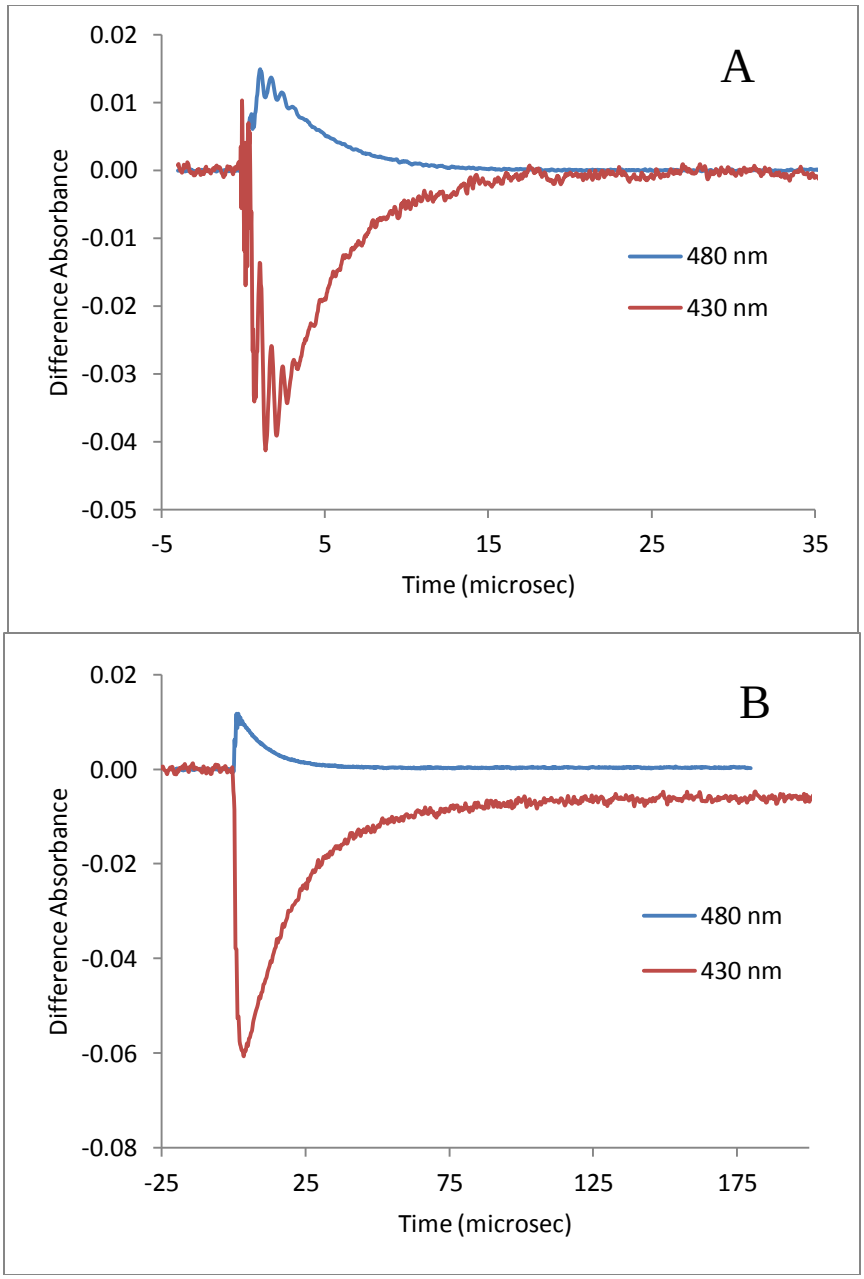

Figure 3.16 Transient decay and recovery curves of 10 μM ZnPA in 10 mM MES buffer (pH 5.5): (A) unpurged at 480 nm (blue) and 430 nm (red) and (B) argon purged at 480 nm (blue) and 430 nm (red).

Table 3.1 Transient absorbance lifetimes and weighing factors for ZnPA solution and multilayer films.

Sample		λ	Lifetime	Weighing factors
10 μM ZnPA, 10 mM MES buffer (ZnPA)	unpurged	480 nm	3.7 μsec	1.0
		430 nm	4.2 μsec	1.0
	argon purged	480 nm	20 μsec	1.0
		430 nm	19 μsec	1.0
10 μM ZnPA + 5 mM PAH, 10 mM MES buffer (ZnPA-PAH)	unpurged	480 nm	3.3 μsec, 15 μsec	0.3, 0.7
		430 nm	6.5 μsec, 20 μsec	0.47, 0.53
	argon purged	480 nm	400 μsec, 1.2 ms	0.13, 0.8, (0.07)
		430 nm	400 μsec, 1.4 ms	0.19, 0.8, (0.01)
12 μM ZnPA + 500 μM PSS, 10 mM MES buffer (ZnPA-PSS)	unpurged	480 nm	3.5 μsec	1.0
		430 nm	4.5 μsec	1.0
	argon purged	480 nm	27 μsec	1.0
		430 nm	28 μsec	1.0
12 μM ZnPA + 500 μM PSS + 5 mM PAH, 10 mM MES buffer (ZnPA-PSS-PAH)	unpurged	480 nm	20 μsec, 125 μsec	0.3, 0.7
		430 nm	N/A	N/A
	argon purged	480 nm	83 μsec, 570 μsec	0.39, 0.61
		420 nm	81 μsec, 570 μsec	0.43, 0.57
*glass/PAH/$(ZnPA/PAH)_{100}$	argon purged	430 nm	6 μsec, 430 μsec	0.64, 0.36

*UV-Vis absorbance spectrum suggests demetallation of ZnPA.

The values of triplet decay and ground state recovery are comparable to each other for both the unpurged and argon purged samples. The fit to first order exponentials reflect the excited state species decay pathway via intersystem crossing to the triplet state and decay to the ground state. As expected, since the porphyrin excited states are sensitive to oxygen, purging with argon yields longer lived excited state species. These values are not as long lived as the typical zinc porphyrins in solution,[97-98] where triplet state lifetimes are in the hundreds of microseconds and milliseconds.[97] While the solvent effects on the excited state lifetimes of ZnPA have not been thoroughly investigated, it is known that porphyrins such as zinc(II)tetrakis(4-sulfonatophenyl) porphyrin (ZnTSPP), tend to dimerize even at modest concentrations of electrolyte.[117] Kadish, et al recently studied zinc porphyrin with diethoxyphosphoryl ($P(O)(OEt)_2$) groups in the *para*-position of the phenyl ring.[118] They noted that the $P(O)(OEt)_2$ can bind to the Zn(II) ion of another porphyrin in solution (most likely via the P=O⋯Zn) and the aggregation was both solvent and concentration dependent. At a 10^{-4} M concentration of this zinc porphyrin, there was only a 20% decrease from the linear Beer's law molar absorptivity, with almost no apparent Soret band broadening.[118] From the UV-Vis absorbance of 10 μM ZnPA, it is difficult to determine if weak aggregation is occurring. Since aggregation is known to quench the triplet excited state,[99-100] this is another possibility for a decreased triplet state lifetime as compared to zinc porphyrins in the literature.[97]

The transient absorbance decay and recovery curves for 10 μM ZnPA + 5 mM PAH in MES buffer (pH 5.5) (ZnPA-PAH) are shown in Figure 3.17. First order

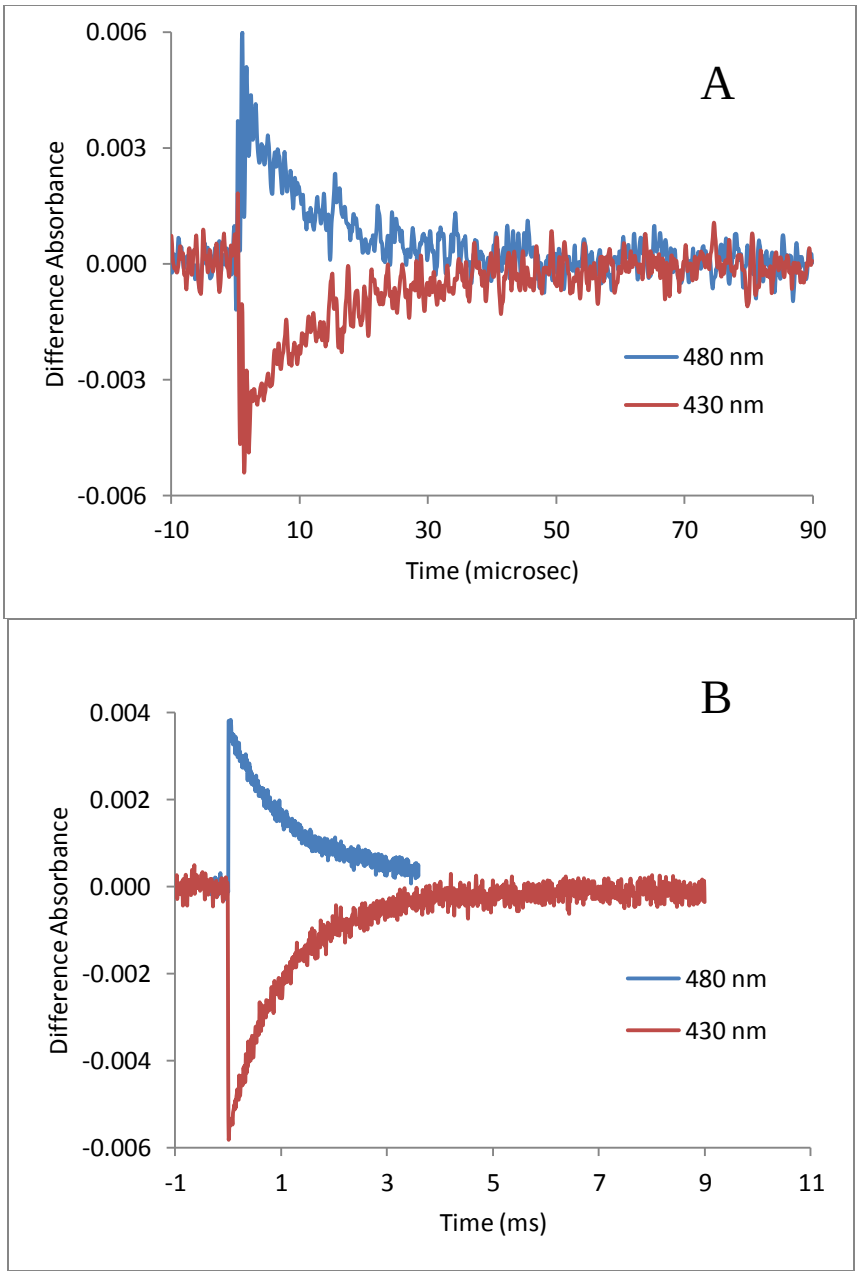

Figure 3.17 Transient decay and recovery curves of 10 μM ZnPA + 5 mM PAH in 10 mM MES buffer (pH 5.5): (A) unpurged at 480 nm (blue) and 430 nm (red) and (B) argon purged at 480 nm (blue) and 430 nm (red).

exponentials did not adequately fit both of the unpurged and argon purged decay and recovery curves, so 2nd order exponentials were used as reported in Table 3.1. The unpurged triplet state had lifetimes of 3.3 μsec and 15 μsec with weighing factors of 0.3 and 0.7, respectively. The ground state recovery curve for the unpurged solution was fit with lifetimes of 6.5 μsec and 20 μsec with weighing factors of 0.47 and 0.53. After argon purging, the lifetimes were also fit to 2nd order exponentials. Compared to the unpurged samples, the triplet state lifetimes were significantly extended to 400 μsec and 1.2 ms with weighing factors of 0.13 and 0.8, respectively. For the decay curve at 480 nm a third component, referred to an 'infinite' component was included in the fit, since the absorbance did not reach the pre-excitation value. This component had a weighing factor of 0.07. The ground state recovery had lifetimes of 400 μsec and 1.4 ms with weighing factors of 0.19 and 0.8, respectively. The absorbance at 430 nm also did not completely recover, so a third 'infinite' component was applied with a weighing factor of 0.01. The triplet state decay and the ground state recovery lifetimes agree, showing that triplet formation and decay to the ground state is the predominant relaxation pathway.

Longer triplet and ground state recovery lifetimes when the samples were argon purged was expected. It is not clear why, in the presence of the positively charged PAH, the lifetimes are significantly longer for both the unpurged and argon purged samples as well as including a 2nd component in the fit. From the UV-Vis absorbance spectra, the broadening of the Soret band although indicative of aggregation, could also represent the close association of the ZnPA with the PAH.[101, 119] It is likely that there are strong electrostatic interactions since these molecules are oppositely charged.

One hypothesis is if ZnPA in MES buffer is prone to weak aggregation, then this aggregation provides a rapid triplet state decay pathway, with only slight effects from oxygen quenching. This explains the slight increase in lifetimes of the triplet state from 3.7 μsec to 20 μsec after argon-purging. If the studies on the zinc porphyrin with $(P(O)(OEt)_2$ groups[118] can be applied to ZnPA, the interaction of the Zn(II) ion with the phosphonic acid group would appear as J-aggregates, where the center metal of one porphyrin aligns with the phosphonic acid groups on another porphyrin.

When PAH is introduced into the solution, the electrostatic interaction between the positive charge on the amine and the negative charge on the phosphonic acid group dominates and the weak self-aggregation of the ZnPA is disrupted. The broadening in the Soret band of the ZnPA-PAH absorbance spectrum is indicative of electronic coupling, from the interaction between the amine group and the porphyrin as well as porphyrin aggregation seen with other electrostatic porphyrin polymer systems.[110] Prior to argon-purging the ZnPA+PAH solution, the triplet state was quenched by oxygen in solution with a lifetime of 3.3 μsec and 15 μsec. After argon-purging the decay significantly increased in lifetime to 400 μsec and 1.2 ms. The longer lived lifetime is comparable to zinc porphyrin lifetimes reported in literature.[97-98]

More studies should be conducted to determine if ZnPA will behave differently in a lower concentration of MES buffer and in solutions of varying pH. The aggregation can be determined by examining the Beer's law linearity. As discussed previously, weakly aggregated solutions may only have a ~20% decrease from Beer's law linearity,[118] but even slight aggregation may affect triplet decay pathways. The zinc

porphyrin with $(P(O)(OEt)_2$ groups was characterized with crystallography and electrochemistry in the presence of a triphenylphosphine oxide. From these studies, Kadish et al. was able to determine the binding of the phosphoryl group to the Zn(II) ion.[118] These methods could potentially be employed for ZnPA as well.

3.5.1b ZnPA with PAH and PSS

The films of ZnPA on glass that were studied also contained the negatively charged polymer PSS, so it was necessary to conduct control experiments on solutions of the ZnPA with PSS, as well as solutions of all three components: ZnPA, PAH and PSS. UV-Vis absorbance spectra were obtained for 12 μM ZnPA + 500 μM PSS in 10 mM MES buffer (pH 5.5) denoted (ZnPA-PSS) and 12 μM ZnPA + 500 μM PSS + 5 mM PAH in 10 mM MES buffer (pH 5.5) denoted (ZnPA-PSS-PAH), and are shown in Figure 3.18. 10 μM ZnPA in 10 mM MES buffer (pH 5.5) is shown in Figure 3.18 as a reference. The spectrum of ZnPA-PSS sample does not exhibit shifts in the peak absorbance wavelength of the Soret band or the Q-bands as compared to the ZnPA alone. However, the ZnPA-PSS absorbance spectrum has a slight shoulder around 445 nm which is not present in the ZnPA absorbance spectrum. The ZnPA-PSS-PAH solution has a broadened Soret band, and red shift of the Soret band and Q-bands maxima. This spectrum is similar in shape to the ZnPA-PAH sample, but the broadening is less severe with the addition of PSS. This is clear by comparing the Soret band absorbance maxima, 1.2 a.u. and 1.7 a.u. for the ZnPA-PAH and ZnPA-PSS-PAH samples, respectively.

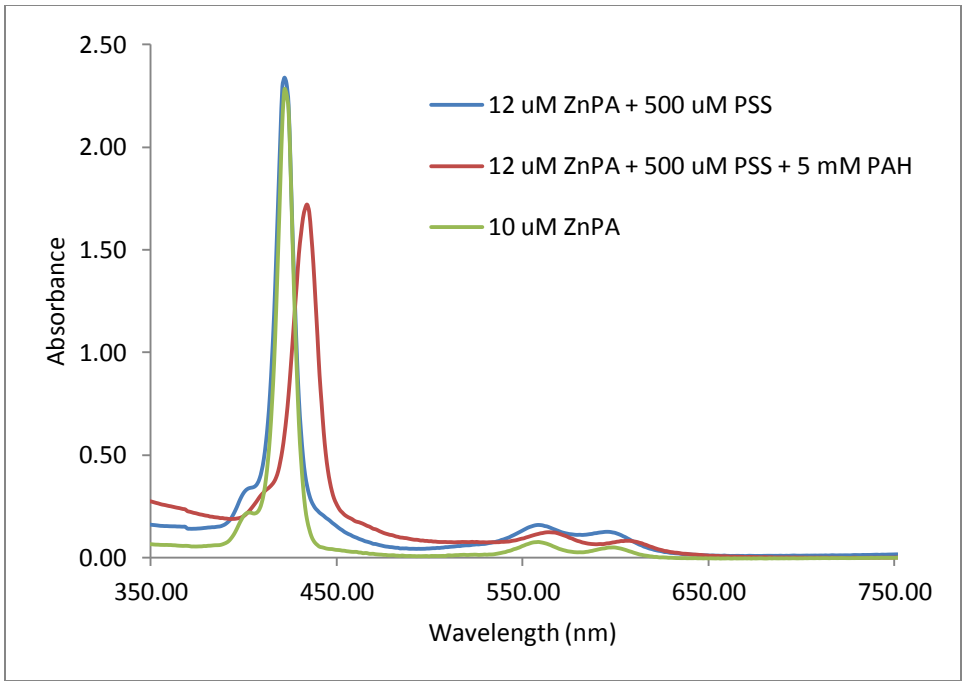

Figure 3.18 UV-Vis absorbance spectra of 12 μM ZnPA + 500 μM PSS (blue); 12 μM ZnPA + 500 μM PSS + 5 mM PAH (red); 10 μM ZnPA in MES buffer (green).

Transient absorbance experiments were performed on the ZnPA-PSS solution and the decay and recovery curves are shown in Figure 3.19. The unpurged and argon purged samples were fit to first order exponentials and are reported in Table 3.1. The triplet decay and ground state recovery curves for the unpurged sample were fit to lifetimes of 3.5 μsec and 4.5 μsec, respectively. These values are comparable to the unpurged ZnPA solution. After argon purging the decay and recovery curves were fit to lifetimes of 27 μsec and 28 μsec, respectively. These lifetimes are longer than those of the unpurged samples, and slightly longer than those of the ZnPA argon purged solution, but they still are less than those reported for other zinc porphyrins, which are from 650 μsec – 1.4 ms.[97]

ZnPA and PSS are both negatively charged, so there is most likely little interaction between the molecules, as shown with other porphyrin and like-charged polymers.[101] The additional negative charges from the PSS may change the solvation of the ZnPA slightly altering the triplet decay kinetics. Although the hypothesis is supported that the dominant triplet decay pathway is from a potentially weakly aggregated ZnPA solution and not oxygen quenching.

Transient decay and recovery curves for the ZnPA-PSS-PAH sample are shown in Figure 3.20. First order exponentials did not adequately fit the curves, so they were fit with 2nd order exponentials and are listed in Table 3.1. Only the triplet state decay at 480 nm for unpurged ZnPA-PSS-PAH was fit, since the noise was extremely high for the recovery curve at 430 nm. The lifetimes were 20 μsec and 125 μsec with weighing factors of 0.3 and 0.7, respectively. The triplet state decay curve for argon purged ZnPA-

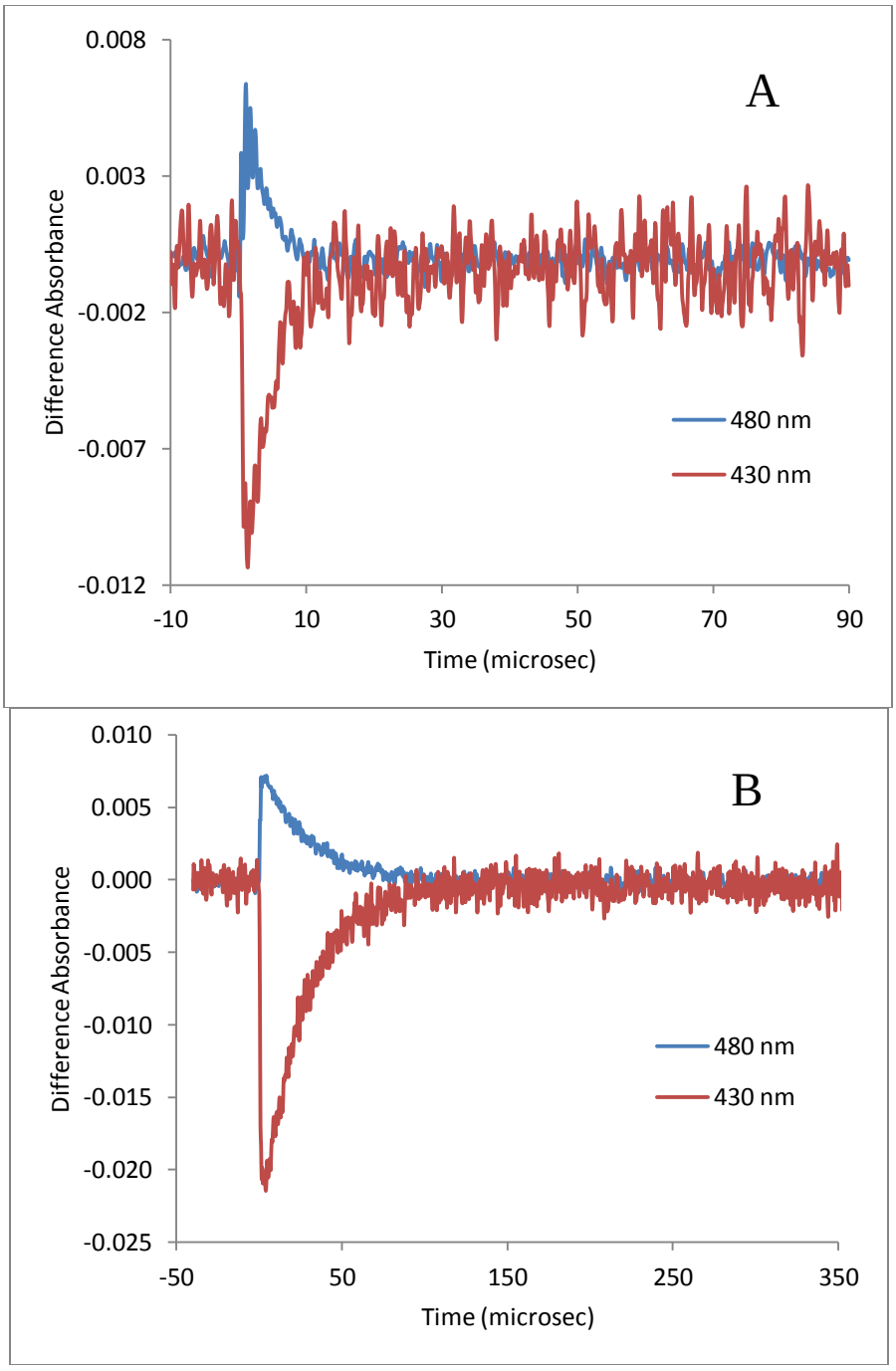

Figure 3.19 Transient decay and recovery curves of 12 μM ZnPA + 500 μM PSS in 10 mM MES buffer (pH 5.5): (A) unpurged at 480 nm (blue) and 430 nm (red) and (B) argon purged at 480 nm (blue) and 430 nm (red).

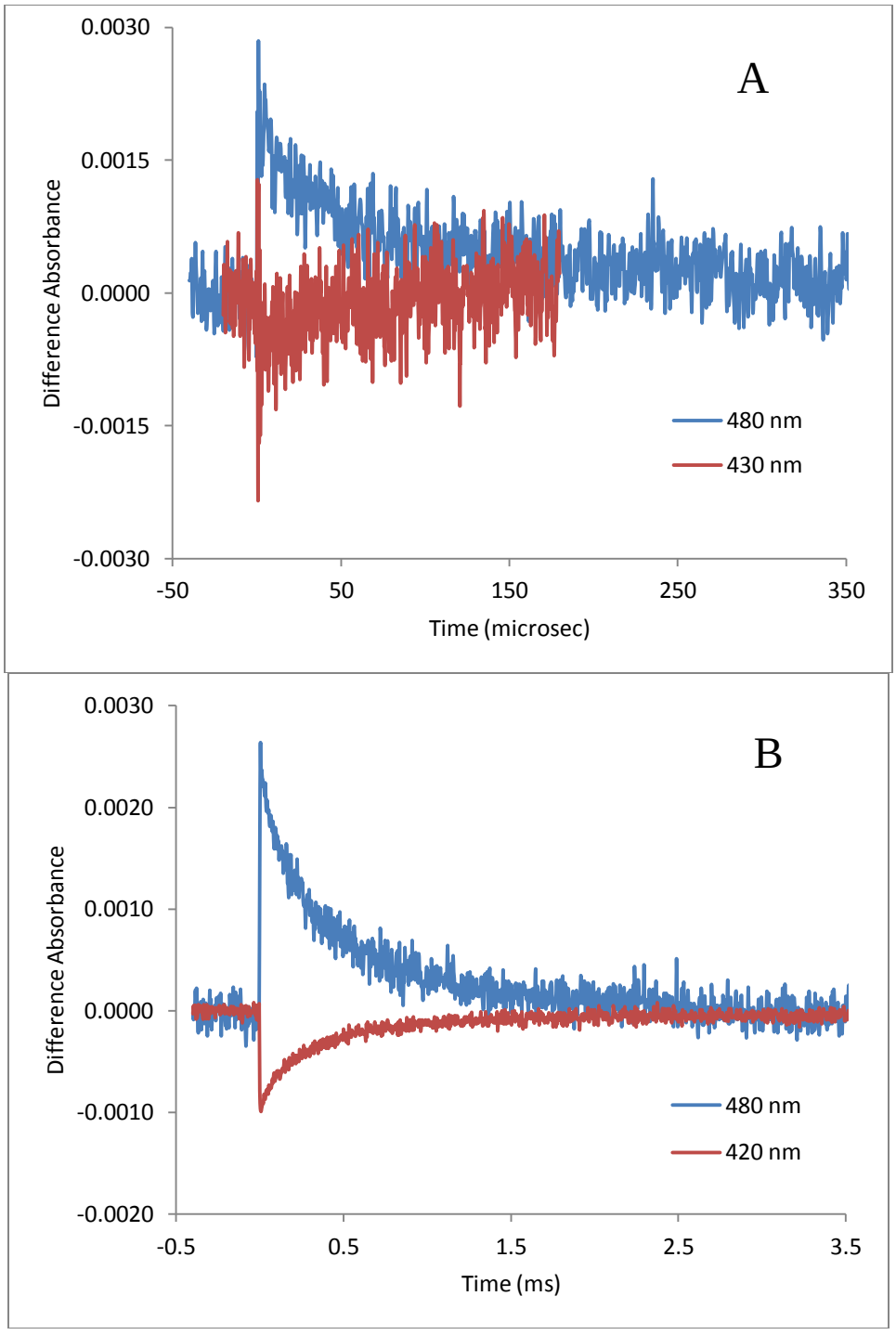

Figure 3.20 Transient decay and recovery curves of 12 μM ZnPA + 500 μM PSS + 5 mM PAH in 10 mM MES buffer (pH 5.5): (A) unpurged at 480 nm (blue) and 430 nm (red) and (B) argon purged at 480 nm (blue) and 420 nm (red).

PSS-PAH was fit to lifetimes of 83 μsec and 570 μsec with weighing factors of 0.39 and 0.61, respectively. The transient recovery curves at 430 nm were extremely noisy, so the ground state recovery was monitored at 420 nm for the argon purged sample. The recovery curve was fit to lifetimes of 81 μsec and 570 μsec with weighing factors of 0.43 and 0.57, respectively. The argon purging successfully extended the triplet state lifetimes, although they are not as long lived as the argon-purged ZnPA-PAH samples.

The triplet decay and the recovery curves have the same lifetime fit for the argon-purged ZnPA-PSS-PAH solution, which indicates that the excited state proceeds through intersystem crossing to the triplet state which decays via two different pathways back to the ground state. The introduction of PAH to the ZnPA-PSS sample clearly disrupts, to some extent, the weakly aggregated ZnPA. In all of these solutions there is a balance of intermolecular interactions that are affecting the triplet state lifetimes. When ZnPA is in MES buffer or with PSS the dominant interaction is hypothesized to be between the phosphoryl group and the zinc (II) ion to form aggregates. Those interactions are disrupted by the electrostatic interactions between oppositely charged molecules. The effects need to be further studied to determine if the interactions are dominated by the charges or if the specific functional groups play a role.

As with the ZnPA-PAH solutions, the transient results from the ZnPA-PSS-PAH samples lead to more questions about the stability of the excited states in these complex environments. From the results presented in Table 3.1 the triplet state lifetime lengthens as the degree of aggregation increases: ZnPA-PAH>ZnPA-PSS-PAH>ZnPA-PSS = ZnPA. The ZnPA-PSS solution has comparable triplet decay lifetime to the ZnPA

sample. Clearly, different molecular environments with these solution experiments yielded alterations in the triplet decay lifetime of zinc porphyrin. In an OPV, the efficiency of the device is dictated by the charge transfer and migration processes at the interfaces. The electron transfer at a molecular thin film/TCO interface is strongly influenced by the lifetimes of the excited states. If the local molecular environment is dominated by chemical interactions which promote a rapid excited state decay, the charge transfer efficiency is impaired.

3.5.2 Layer by Layer Films of Zinc Porphyrins and Charged Polymers

The previous investigations established an understanding of the photoexcited behavior of ZnPA in the presence of the charged polymers, PAH and PSS, in solution. The interaction hypothesized to dominate the local molecular environment of the porphyrin is self-aggregation, which is disrupted by addition of the positively charged PAH. The electrostatic environment, in this case, contributed to longer lived triplet states as compared to ZnPA in MES buffer.

Multilayer films containing ZnPA were prepared so that sensitivity was not a limiting factor, and the excited state lifetimes were probed. Although the films have a moderate degree of complexity, these investigations are important to evaluate how the photoinduced excited state lifetimes and eventually charge transfer kinetics are affected by the local, molecular environment.

The films were constructed with electrostatic LbL self-assembly. Borosilicate glass coverslips (VWR) were cleaned in piranha (7:3, sulfuric acid: 30% hydrogen

peroxide) for 10 minutes. They were then rinsed thoroughly in nanopure water and immediately immersed for at least one hour in the positively charged solution, 10 mM PAH in water (pH adjusted to 8.7 with HCl). The coverslips were then rinsed in water (HPLC grade) and immersed in either 10 μM ZnPA in 10 mM MES buffer (pH 5.5) (ZnPA) or 10 μM ZnPA + 500 μM PSS in 10 MES buffer (pH 5.5) (ZnPA-PSS) for 10 minutes. The film was then rinsed in water (HPLC grade) and immersed in 10 mM PAH for 10 minutes. The multilayer films were made by successive immersions in oppositely charged solutions in this fashion until ~25 bilayers (ZnPA/PAH) or (ZnPA-PSS/PAH) were formed. These depositions were done on both sides of the coverslip so the total number of bilayers formed was twice this value, ~50 bilayers. After the final PAH layer, the film was rinsed with water and blown dry under a stream of N_2.

The sample glass/PAH/$(ZnPA/PAH)_{50}$ was cut into several pieces with a diamond glass cutter and 2 pieces were inserted into a 1 cm pathlength cuvet. The cuvet was filled with water and purged with argon. A transmission UV-Vis absorbance spectrum was obtained of the ~100 bilayers on glass and is shown in Figure 3.21A. The ratio between the Soret band maximum at 434 nm and the first Q-band at 565 nm is 11.5, which is close to the ratio for the ZnPA-PAH solution sample, 13. Another point to note is the presence of another Q band around 635 nm. Due to the D_{4h} symmetry of the zinc porphyrin, there should only be two Q-bands. Demetallated porphyrins such as H_2TCPP have four Q-bands, measured at 518 nm, 556 nm, 596 nm and 635 nm.[97] Although only 3 Q-bands are apparent in the spectrum, it is possibly that a fourth is concealed under the light scattering background. These data suggest that a fraction of the porphyrin in the film is

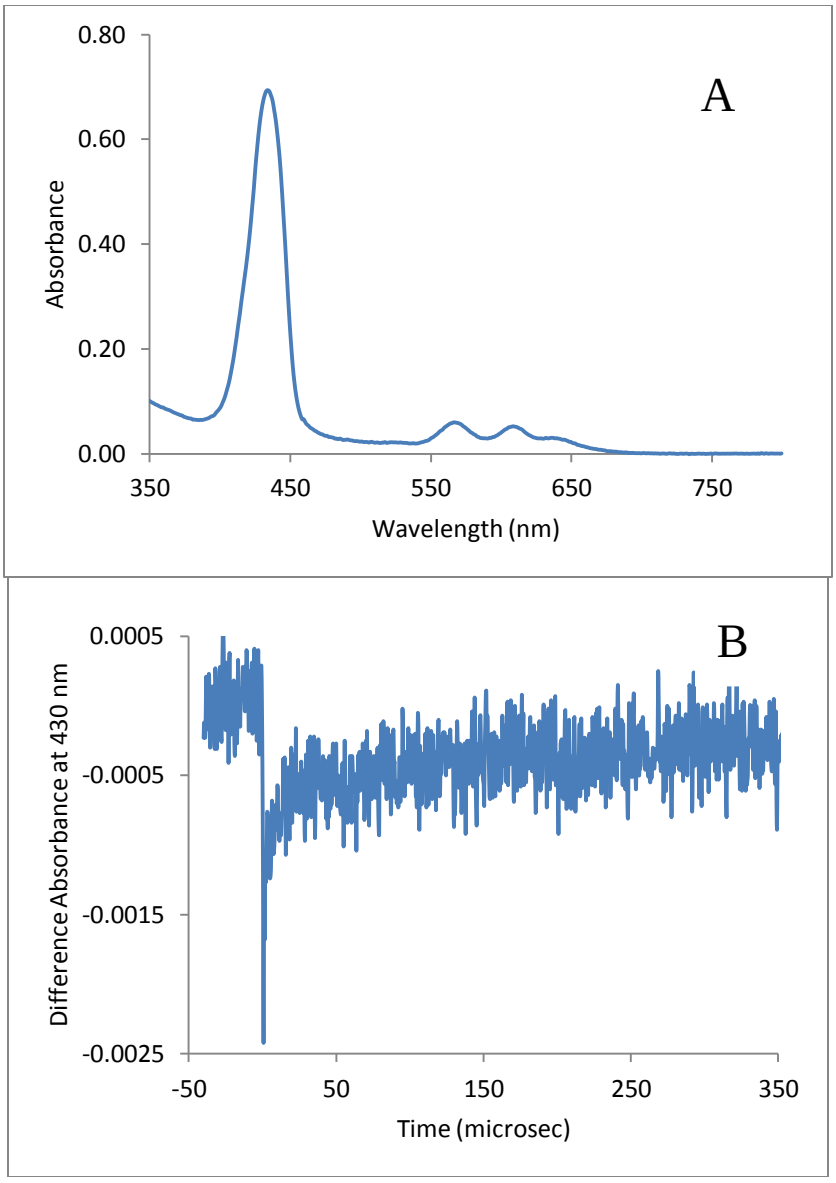

Figure 3.21 (A) UV-Vis absorbance spectrum of glass/PAH/(ZnPA/PAH)$_{100.}$ (B) Transmission transient absorbance curve of glass/PAH/(ZnPA/PAH)$_{100}$.

demetallated. In general, demetallated porphyrins have shorter triplet state lifetimes as compared to zinc porphyrins, ranging from 100 μsec – 1.5 ms.

The cuvet was set up in the Proteus transmission transient absorbance instrument and the glass/PAH/$(ZnPA/PAH)_{100}$ film was excited by the light from the Nd:YAG coupled to the dye laser with a wavelength of ~560 nm. The species monitored were the triplet state at 480 nm and the ground state at 430 nm. The transient recovery curve at 430 nm is shown in Figure 3.21B. A first order exponential did not adequately fit the recovery curve, so it was fit to a 2^{nd} order exponential. The lifetimes were 6 μsec and 430 μsec with weighing factors of 0.64 and 0.36, respectively. The signal to noise at 480 nm was too low to measure a triplet decay lifetime. The longer lifetime component of 430 μsec for the recovery curve is shorter than the longest values for the solution experiments. It is hypothesized that as the films were being formed, ZnPA was able to deposit on the PAH, maintaining a portion of its weak self-aggregation. As the films were constructed, the PAH disrupted the majority of these interactions and therefore the ZnPA self-aggregation did not dominate the excited state kinetics. It is also likely that during the deposition process, the porphyrin was demetallated and therefore a comparison cannot be made between the solution and multilayer films.

Multilayer films were also prepared with co-deposited ZnPA-PSS, and transmission transient absorbance experiments were performed, but there was no signal above the noise for either the triplet state decay or the ground state recovery. As with the glass/PAH/$(ZnPA/PAH)_{100}$ film, the glass/PAH/$(ZnPA\text{-}PSS/PAH)_{100}$ film also showed a third Q-band that suggested demetallation of the porphyrin had occurred.

In order to eliminate the additional population of demetallated ZnPA that was evidenced with the thick films, thinner films were prepared for transient ATR spectroscopy using slight alterations to the process described previously. ZnPA and ZnPA-PSS were only deposited on a single side of the glass coverslip by balancing the coverslip on a watch-glass so that one side was facing up. The porphyrin solution was applied dropwise so that it spread over the entire face of the coverslip. The coverslip was covered with a glass water bath container to prevent significant evaporation of the ZnPA or ZnPA-PSS solution in contact with the coverslip. Only 1-4 bilayers were deposited for the transient ATR experiments. UV-Vis absorbance spectra of these films did not show additional Q-bands, suggesting that the zinc porphyrin was not demetallated in these samples as shown in Figure 3.22.

The films were secured in the Delrin cell and BK-7 right angle prisms placed on the coverslip with index matching fluid (n=1.51). Transient ATR experiments were conducted while flowing argon purged water (HPLC grade) through the Delrin flowcell. The films were excited with the light from the Nd:YAG laser coupled to the dye laser at a wavelength of ~560 nm. As with the zinc porphyrin films on ITO, the high molar absorptivity of the Soret band resulted in the instrument reaching the stray light limit between 400-430 nm. Therefore, only the triplet state at 480 nm was monitored. There was no signal measured above the noise for any of these samples with transient ATR spectroscopy. The chemical explanation for immeasurable triplet state yields is unclear. It was hypothesized that the weakly aggregated ZnPA in MES buffer had presented a

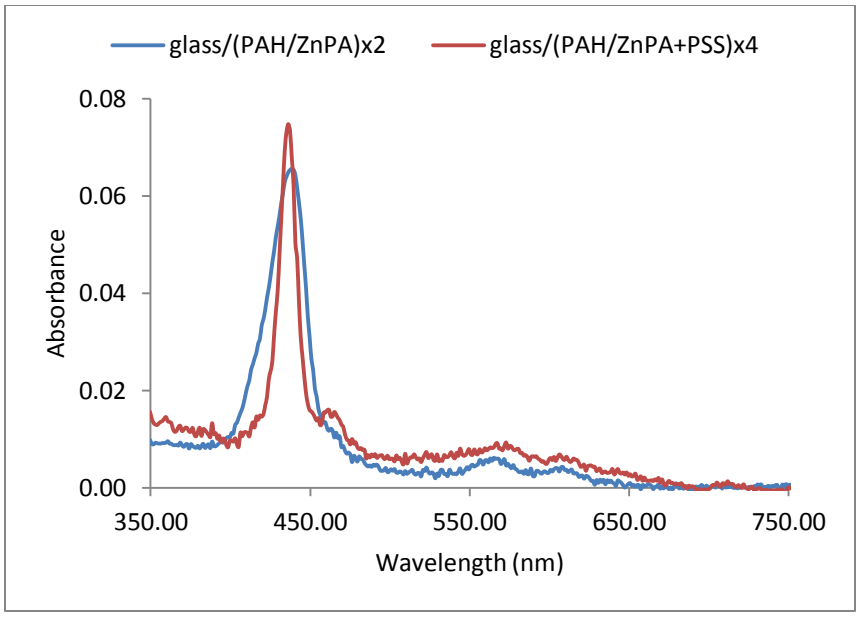

Figure 3.22 UV-Vis absorbance spectra of: glass/$(PAH/ZnPA)_2$ (blue) and glass/$(PAH/ZnPA+PSS)_4$ (red).

rapid triplet state decay pathway. Larger aggregated ZnPA populations could be forming in the multilayer films and as a result the triplet is rapidly quenched.

The inability to measure the transient states in the zinc porphyrin films could be due to self-exchange (electron transfer) or self-transfer (energy transfer). Photosynthetic organisms utilize electron and energy transfer to efficiently convert sunlight to energy. Research groups have used this paradigm as a model to construct artificial reaction centers and in turn studied interporphyrin electron and energy transfer.[120-124]

Porphyrins are well suited for electron transfer because of their highly conjugated π systems and they have minimal structural change as a result of uptake or release of an electron. The metal center, the porphyrin ligands and the non-planar distortion of the porphyrin skeleton all play a role in the efficiency of heterogeneous and homogeneous electron transfer.[125] According to Marcus theory, the rate of electron transfer includes a reorganization component.[126] Cross reactions of metalloporphyrins with outer-sphere oxidizing or reducing agents can be extrapolated using the Marcus cross relation to estimate the reorganization energy and rate constants for self-exchange reactions of metalloporphryins.[125, 127] $Fe^{2+/3+}$ and $Co^{2+/3+}$ metal-centered porphyrins were found to have relatively slow electron self-exchange rates with rate constants of $10^{7} – 10^{8}$ M^{-1} s^{-1} and $10^{-3} – 10^{4}$ M^{-1} s^{-1}, respectively. The relatively large inner-sphere reorganization energies were hypothesized to cause these slow electron transfer rates, which is expected for metal centers participating in the electron transfer.[128] In comparison, porphyrin-centered redox reactions (between the metalloporphyrin and the π-cation radical) of Cu(II) and Zn(II) complexes of 5,10,15,20-tetraphenelporphryin (TPP) are more highly

reactive because of the smaller inner-sphere reorganization energies. The self-exchange rate constants between the parent porphyrin and its cation radical were determined to be 10^{10} M^{-1} s^{-1} and 10^{11} M^{-1} s^{-1} for the Cu(TPP) and Zn(TPP), respectively.[125] Aoki and co-workers evaluated the self-exchange rate constants between the parent porphyrin and the π-cation radical for planar and highly distorted Cu(II) and Zn(II) porphyrin complexes. The highly distorted porphyrins exhibited slower self-exchange reactions, with rate constants of $10^4 – 10^6$ M^{-1} s^{-1}. This was attributed to the large reorganization energy needed to transfer an electron from the parent complex to the highly deformed π-cation radical.[125] The zinc porphyrin molecules in the thins film studied herein are similar to Zn(TPP) studied by Aoki *et al*. The absorbance data collected suggest significant aggregation of the zinc porphyrin molecules in the films. Although the reorganization energy is not known for ZnTCPP and ZnPA tethered to ITO, rapid homogeneous electron transfer is likely to occur upon photoexcitation. Therefore it is possible that an appreciable fraction of the excited state species may not be present in the optical path to be monitored. Ultimately, the limiting factor in this case is the timescale of the Proteus transient ATR instrument (~3 μsec).

Energy transfer is also possible in these closed-packed zinc porphyrin films. Singlet-singlet Förster energy transfer occurs from an excited donor molecule to an acceptor molecule through resonant coupling of the transition dipoles.[121] This process is non-radiative and highly dependent on the intermolecular distance. The key factors include quantum yield of the donor molecule, spectral overlap of the donor and acceptor molecules, directional relationship of the transition dipoles, refractive index of the

medium, and distance between chromophores. Förster energy transfer can occur over distances of ~1-10 nm.[129-130] Overlap of π orbitals as indicated by the aggregation of zinc porphyrin molecules may also promote singlet-singlet or triplet-triplet Dexter energy transfer.[130] Dexter energy transfer requires the overlap of wavefunctions or the electron clouds and is considered short-range energy transfer, because it occurs over distances of ~1 nm or less. Dexter energy transfer has an exponential relationship to chromophore distance.[130]

Kroeze *et al.* investigated self-organizing porphyrin films (~50 nm thick) on TiO_2 and the nature of exciton diffusion or energy transfer through these films in order to improve the incident-photon-to-charge-separation efficiency (IPCSE).[131] Films of a free-base tetra-*para*-octylphenyl porphyrin, upon annealing, presumably achieved a lamellar phase consisting of ordered stacks of porphyrin molecules on TiO_2, with an edge-on/perpendicular orientation to the surface. They concluded that the unannealed and therefore randomly distributed porphyrin films gave a 10% IPCSE, as a result of both singlet and triplet excited state injection into the TiO_2 as well as triplet state Dexter energy transfer through the film at distances of at least 9.6 nm.[131] The annealed and thus ordered films presumably disabled the triplet-triplet energy transfer because the distances between the lamellae stacks increased as compared to the unannealed films and overall gave an IPCSE of 1%. Kroeze and co-workers concluded that singlet electron transfer of the porphyrin layer directly adjacent to the TiO_2 was the dominant contribution to the IPCSE with the annealed films.[131] As with interporphyrin electron transfer, it is possible that Förster and even Dexter energy transfer is happening efficiently in the ZnPA and

ZnTCPP thin films. On microsecond timescales, the current limit of the Proteus transient ATR instrument, an appreciable fraction of the excited state may diffuse prior to the monitoring.

3.5.3 Films with ZnTSPP

The nature of the immeasurable yields of the triplet state for ZnPA incorporated into the LbL films with PAH and PSS is not fully understood. In addition, the ZnPA excited state behavior in solution is not completely established, specifically the effects of pH, electrostatic charges and different functional groups. Therefore, the chemical question arose regarding the role of the phosphonic acid functional group and its effect on the ZnPA photoinduced excited states. It was hypothesized that there is an interaction between the phosphoryl group and the Zn(II) ion to cause weakly aggregated species in solution which resulted in rapid triplet state decay lifetimes. In order to study if the susceptibility of the zinc porphyrin to its local molecular environment lies within the nature of the phosphonic acid functional group or is a property of the zinc metal center, the analogous zinc porphyrin, zinc(II)tetrakis(4-sulfonatophenyl) porphyrin (ZnTSPP) (Frontier Scientific) was investigated. Investigations involving palladium(II)tetrakis(4-sulfonatophenyl) porphyrin (PdTSPP) along with PAH and PSS are discussed in detail in Chapter 4. LbL films were constructed using PdTSPP and the triplet state lifetimes were measured, with lifetimes on the order of hundreds of microseconds, using transient ATR spectroscopy.

The structure of ZnTSPP is shown in Figure 3.23A. The UV-Vis absorbance spectrum of 1 μM ZnTSPP in water (HPLC grade) is shown in Figure 3.23B. LbL films were prepared as described previously, depositing ZnTSPP and ZnTSPP-PSS on a single side of the PAH coated glass coverslip. The films were set up in the Delrin flowcell and argon was blown over the cell throughout the transient experiments. This was the procedure used in studies with PdTSPP thin films. In separate experiments the films were excited at both ~560 nm and 532 nm. The triplet state was monitored at 480 nm and there was no appreciable signal above the noise for any of these films. As with the other porphyrin samples on coverslips, the wavelength range of 400-430 nm had reached the stray light level of the instrument due to the strongly absorbing Soret band.

From these investigations, it is likely that the zinc metal centered porphyrin is exceptionally susceptible to its local molecular environment as compared to the palladium metal centered porphyrin. In solution, the intersystem crossing quantum efficiency (Q_{ISC}) for PdTSPP is 1.0, while for ZnTSPP it is 0.84[97]. The metal center has a strong interaction with the porphyrin macrocycle, which is evident in the differences between the electronic states shown in the UV-Vis absorbance spectra. The differences can arise with the valence state of the metal, in this case Pd and Zn are diamagnetic.[114] The heavy-atom effect is one factor that controls the nature of the metal interaction with the porphyrin ring and as a result the excited state lifetimes. Pd with an atomic number of 46, is heavier than Zn with an atomic number of 30. Pd porphyrins have very short singlet state lifetimes, but exhibit a higher Q_{ISC} as compared to zinc porphyrins.[97-98, 114]

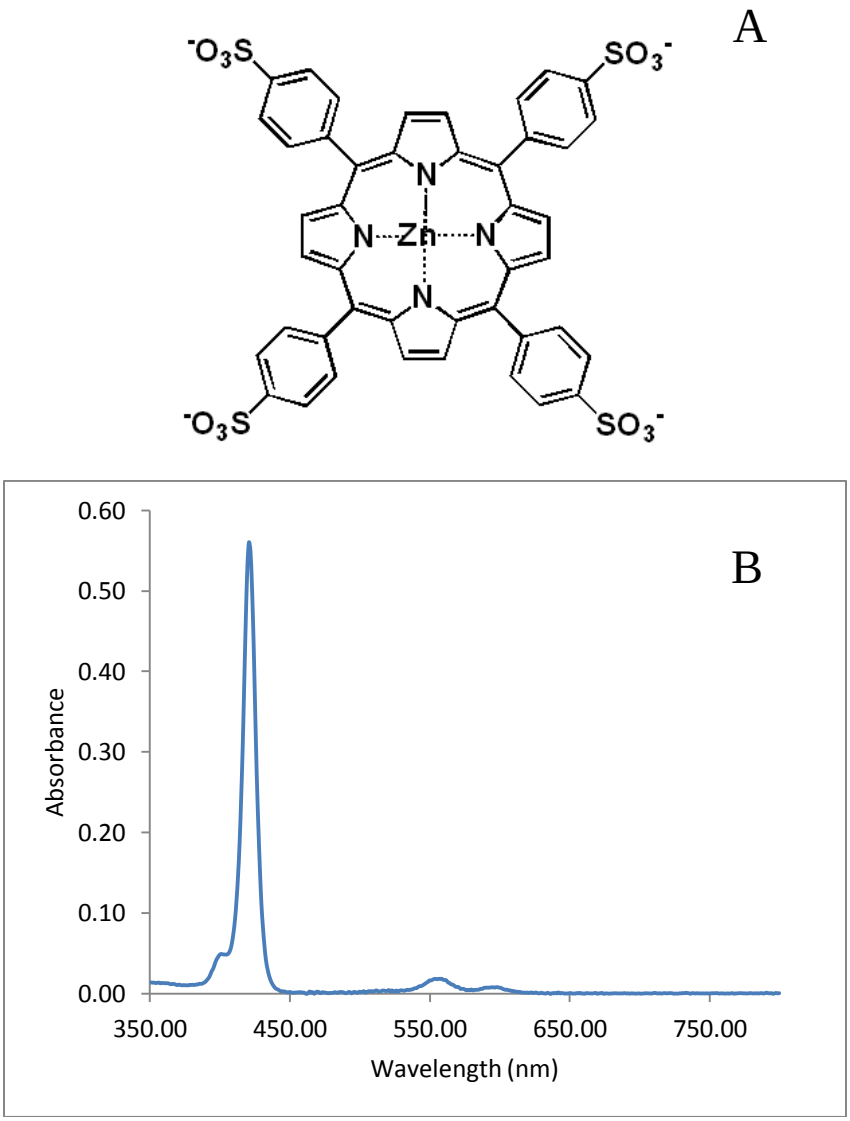

Figure 3.23 (A) Molecular structure of zinc(II)tetrakis(4-sulfonatophenyl) porphyrin (ZnTSPP) and (B) UV-Vis absorbance of 1 μM ZnTSPP in water.

One hypothesis is that the aggregated zinc porphyrins experience quenching of the singlet state and do not convert to the triplet state. Since the Pd porphyrins have a higher Q_{ISC}, the triplet state is formed, even when aggregated. Another possibility is that energy transfer occurs with the Zn porphyrins and does not occur with Pd porphyrins. Therefore the excited states in the film have diffused out of the monitoring path before converting to the triplet state or decaying to the ground state. Since the Pd porphyrin Q_{ISC} is extremely efficient, the triplet state is created and Förster energy transfer is forbidden.

In addition to the chemical nature of local molecular environment, the intrinsic properties of the molecule used in the OPV systems is extremely important for creation and lifetime of excited state species which inherently affects the charge transfer efficiency at interfaces.

3.6 Conclusions

This study investigated the properties at the interface between zinc porphyrin and ITO in order to further our understanding about the factors which affect charge transfer. The examination of the electrochemistry and spectroelectrochemistry results of ZnTCPP and ZnPA tethered to ITO show that the binding chemistries contribute to the energy level alignment at this interface. Comparing redox potentials for ZnTCPP thin films on ITO and dissolved ZnTCPP demonstrated that it was more difficult to oxidize the ZnTCPP thin films. This was attributed to the limited access of the counterions to access the redox center of the ZnTCPP in a closed-packed monolayer.

The molecular orientation and surface coverage were also hypothesized to influence charge transfer. The mean tilt angle for ZnTCPP and ZnPA adsorbed to ITO was 34° and 39°, respectively. The surface coverages corresponded to ~1.0 and 0.9 ML for ZnTCPP and ZnPA, respectively if the molecules were oriented in an edge on geometry. These findings, in addition to broadening of the Soret band in the ATR spectra indicate significant aggregation of the Zn porphyrin films.

The excited state lifetimes and charge transfer kinetics could not be measured at the Zn porphyrin/ITO interface. There are several possibilities:

1) The Zn porphyrin was not sufficiently excited by the excitation source. Calculations in regards to the sensitivity evaluated the molar absorptivities of the excited state species at the excitation wavelength and the transient state, the number of total internal reflections and the molecular surface coverage. After comparing the values with those found from the study in Chapter 2, it was determined that the experiment was feasible.
2) Charge transfer reaction was happening, but on timescales too fast for the transient ATR instrument (3 μsec). Experiments were conducted which aimed to decrease the driving force for recombination as well as decrease the driving force for charge transfer. These may have been successful in altering the charge transfer kinetics, but the reaction may still have been too fast to monitor
3) Local molecular environment significantly affected the excited state lifetimes of the Zn porphyrin. Thus, decay to the ground state occurred before charge

transfer could occur. The main components hypothesized to influence this behavior are the Zn porphyrin aggregation and the adsorption to ITO.

ZnPA was further studied in order to understand how the local molecular environment affects the excited state lifetimes. Control experiments with ZnPA in solution with charged polymers, PAH and PSS, established different molecular environments and demonstrated unique triplet state lifetimes. The results established that the triplet state lifetime of ZnPA lengthened as the degree of aggregation increased. Multilayer films were prepared on glass $(PAH/ZnPA)_{100}$ and experiments were conducted in a transmission geometry to readdress the sensitivity considerations. The ground state recovery of Zn porphyrin in these high surface coverage films confirmed that instrument sensitivity was not an issue. The triplet state was not observed and an additional microenvironment attributed to porphyrin demetallation led to more studies with transient ATR spectroscopy.

The transient ATR experiments of ZnPA incorporated into charged polymer films showed no observable evidence of demetallation. The transients for the ground state recovery at the Soret band were not able to be measured due to the stray light limit of the instrument. The triplet state was not detected which is comparable to the multilayer films. Several possibilities for the inability to measure the triplet state include the effects of the molecular environment contributing to rapid triplet decay or a decrease in intersystem crossing efficiency. Another possibility is within the Zn porphyrin closed-packed films that interporphyrin electron and/or energy transfer is occurring. If long

range electron or energy transfer is efficient, the excited states of the porphyrin molecules may no longer exist within the optical monitoring path.

Finally, a comparison was made between ZnTSPP and PdTSPP incorporated into solid-state LbL films. The sensitivity of the instrument was sufficient for Pd porphyrin thin films and thus should be for the Zn porphyrin thin films as well. It was hypothesized that the singlet state of Zn porphyrin is highly susceptible to quenching in these aggregated species, where Pd porphyrin is not. The Q_{ISC} for PdTSPP is 1.0 as compared to ~0.84 for ZnTSPP, which may allow for Zn interporphyrin electron or singlet-singlet energy transfer. The nature of the chemical interactions and local molecular environment are essential for long lived excited states and efficiency of charge transfer at interfaces.

4. TRANSIENT ATR INVESTIGATION OF LAMELLAR POLYANION/POLYCATION THIN FILMS TOWARDS UNDERSTANDING ELECTRON AND ENERGY TRANSFER

4.1 Introduction

In addition to OPVs, other photoconversion systems such as artificial photosynthesis and water-splitting are of interest to many researchers and pose similar challenges. Fujishima and Honda demonstrated the first example of water-splitting using a TiO_2 photoanode in 1972.[132] Scientists have been interested in the production of solar fuels and there have been many recent reviews providing a thorough discussion about water-splitting.[133-134] Hydrogen is the most abundant element on Earth and a fuel that can be used directly in combustion engines or combined with CO_2 to form other long chain carbon fuels. The most common method of hydrogen production is steam reforming, utilizing fossil fuels as the resource and with byproducts such as carbon monoxide and CO_2.[135] Currently, expensive photovoltaic cells are used in hydrogen production via electrolysis, so there is much to be gained by improving the efficiency of this technology.

The key challenge facing scientists is that photocatalysis of water is a thermodynamically uphill process. Water-splitting is similar to the processes in organic photovoltaic cells described in detail in previous chapters. Light absorption results in the formation of charge separated states between the donor and acceptor systems. Electrons must flow in the forward direction so water is oxidized to O_2 on one side of the cell and is

reduced to H_2 on the opposite side. An energy level diagram of this process is shown in Figure 4.1.

As with OPVs, the kinetics of charge transfer at the following interfaces is vital to the overall efficiency of the water-splitting reaction: water molecule-dye, dye - semiconductor, and semiconductor-H^+. Often the charge recombination steps are fast and the multi-electron charge transfer needed for the water oxidation and reduction reactions are slow.[133-134]

Researchers are investigating many areas to improve the solar conversion efficiency at a low cost, including synthesis of new catalysts, studying different semiconductors, etc.[133] This chapter focuses on the organization of molecules into assemblies, which promote long-lived charge separated states as reviewed by Youngblood et al.[136] This work was a continuation of research conducted in the Mallouk group at Penn State and done in collaboration with John Swierk, a graduate student in the Mallouk group.

4.1.1 Background to Water-splitting

Water-splitting is technically possible with visible and near infrared light because the energy difference between the reduction of H_2O to H_2 and oxidation of H_2O to O_2 is 1.23 eV.[137] Bolton and co-workers studied the thermodynamics of water and determined that 12% of incident solar energy could be stored as hydrogen after accounting for reasonable losses of energy transfer at the interfaces.[137] He did not, however, account for quantum yields below 100%. For the past several decades, scientists have not been able

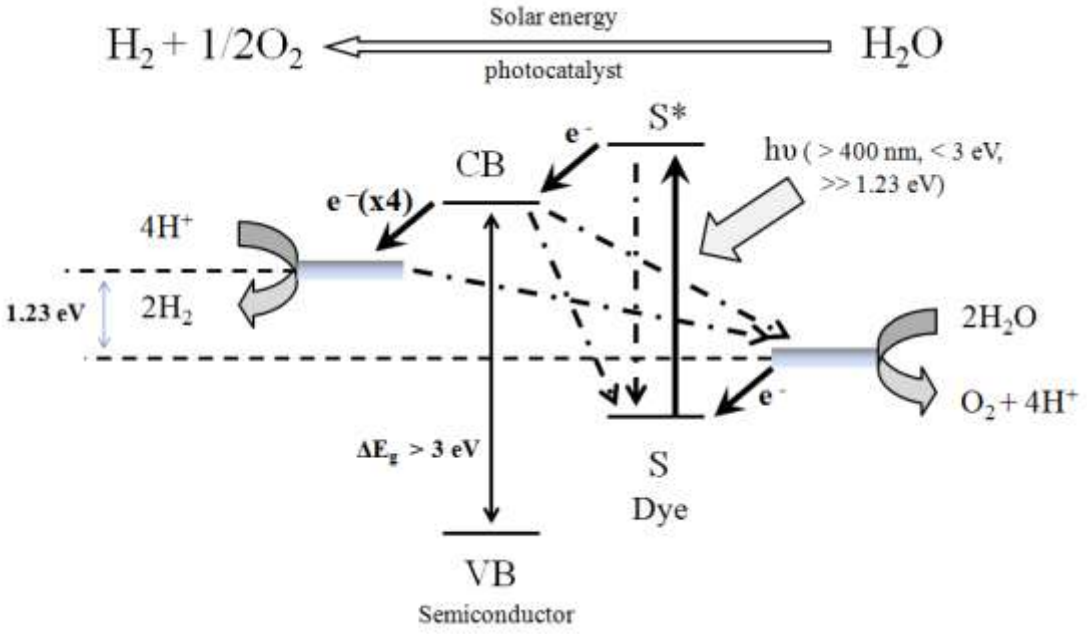

Figure 4.1 Energy level diagram for water-splitting. The solid arrows represent the forward electron transfer pathway, while the dashed arrows represent the competing back electron transfer steps. A dye molecule is adsorbed to a semiconductor. The ground state of the dye (S) absorbs light to promote an electron to the excited state (S*). H_2O donates an electron to the oxidized dye and forms the oxidation products O_2 and H^+. The excited state of the dye transfers its electron to the conduction band (CB) of the semiconductor. The CB of the semiconductor is sufficiently high in energy to donate electrons (4e-) to 4 H+ and form diatomic hydrogen (H_2). E_g defines the band gap energy of the semiconductor, which needs to be greater than 3 eV. The dye must have an E_g of at least 1.23 eV, but not larger than 3 eV.

to achieve quantum yields above 6% with visible light,[138] thus the power conversion efficiency has remained below 0.5%; much lower than the theoretical calculations.

Strategies have been implemented to promote the forward transfer of electrons and to slow the competitive back transfer. Electron transfer is strongly dependent on the thermodynamics as well as the distance between the donor and acceptor.[139] Creating an organized molecular assembly, utilizing polymer films or small molecules, can define the physical distance between the donor and acceptor species of the charge transfer reaction. A way to create multilayer constructions of thin films is with layer by layer (LbL) assembly, as described in Section 2.3.2. Figure 4.2A depicts the process of LbL deposition. As noted previously, when the polymer chains assemble, they mix with each other and the boundaries are described as "fuzzy".[63] When developing materials and molecules to investigate charge transfer, the distance between the donor and acceptor should be well-defined. To address this issue, researchers have used two-dimensional sheets, referred to as nanosheets, in order to create a stratified assembly.[136, 140-142] A general schematic of an LbL assembly incorporating a nanosheet is shown in Figure 4.2B.

4.1.2 Background to Nanosheets

The microscopic and macroscopic properties of inorganic aqueous clay suspensions were investigated in detail by J. D. F. Ramsay.[143] When microcrystalline powder of a cation-exchangeable metal oxide is added to water and stirred, the mineral

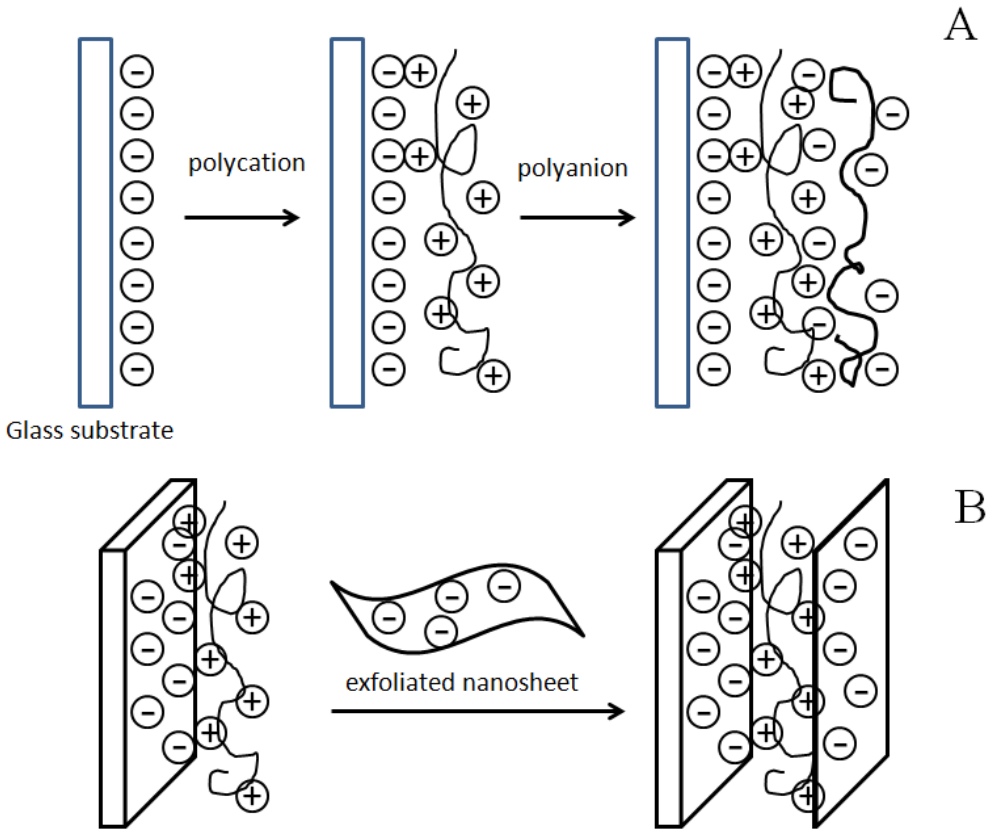

Figure 4.2 (A) Schematic of polyelectrolyte layer by layer (LbL) assembly of films. A positively charged polycation is adsorbed to a negatively charged glass substrate, followed by the adsorption of a negatively charged polyanion. This process is repeated to build multilayer films. (B) Schematic of LbL deposition with nanosheet incorporation. Nanosheets are exfoliated to create 2-D suspensions of a metal oxide. Negatively charged nanosheets are adsorbed onto a positively charged polycation and help to prevent intermixing between layers.

exfoliates into 2-dimensional, crystalline structures or nanosheets. A wide variety of inorganic layered compounds have been realized with appropriate combinations of interlayer cations and solvents, including metal chalcogenides, metal phosphates and phosphonates.[58] In particular, layered titanium oxide (titanate) has been of interest due to its semiconducting properties.[59] The nanosheets carry a negative charge, which is balanced by a counter ion such as tetrabutylammonium (TBA^+). During the deposition process, the positive counter ion is displaced by the positive charge of the surface.[140]

The two types of nanosheets that are used in this study are insulating alpha zirconium phosphate (α-ZrP) and a layered metal oxide semiconductor (LMOS), titanoniobate ($HTiNbO_5$). These nanosheets have been studied extensively in the Mallouk research group.[139, 144-145] α-ZrP nanosheets are 1 nm thick, with lateral dimensions of 1-2 μm and act as a passive interlayer (unable to accept electrons). They can, however, control the morphology of multilayer films by defining specific distances between the donor and acceptor layers.

The LMOS nanosheets are considered active spacers because they have been demonstrated the ability to accept electrons from donor molecules.[59] The $HTiNbO_5$ nanosheets are also 1 nm thick with lateral dimensions of about 2-5 μm. The estimated band gap energy of bulk $HTiNbO_5$ is 3.47 eV and the conduction band edge energy is -0.66 V vs. SCE.[144] These values are estimates calculated at the point of zero charge. The corresponding values of nanosheets incorporated into multilayer films may be different.

The Mallouk research group has used nanosheets as a way to control the 2-D construction of multilayer films. They demonstrated a distance dependence for

fluorescence energy transfer, determined by steady-state emission spectra, between fluorescein (Fl) (donor) and rhodamine B (RhB) (acceptor). α-ZrP nanosheets incorporated into the multilayer films served as a 'spectroscopic ruler'.[139] A general schematic for this multilayer assembly is shown in Figure 4.3A. The assemblies were designed such that the average interlayer distance between the donor and acceptor was either greater or smaller than the Förster radius, ca 40 Å.[139, 146] The energy transfer efficiencies match closely to the simulated theoretical efficiencies from Monte Carlo simulations.[139] Overall, they demonstrated that α-ZrP nanosheets could successfully control the interlayer distance and affect the energy transfer efficiency between the donor and acceptor molecules. Controlling the structure of the multilayers has the potential to be extended to a variety of charge and energy transfer systems.

The Mallouk group also investigated the use of semiconducting $HTiNbO_5$ nanosheets in the multilayer films.[59] They demonstrated, as with α-ZrP in the previous study, that energy transfer was dependent on the average interlayer distance between the donor and acceptor molecules. In order to study electron transfer, they also used a palladium porphyrin as an electron donor and a poly(viologen) as an electron acceptor. A schematic of the architecture of the film is shown in Figure 4.3B. To investigate electron transfer and charge separated state lifetimes, these films were constructed on silica colloids to perform transient diffuse reflectance spectroscopy. The presence of the reduced poly(viologen) species demonstrated that the electron transfer was successful between the Pd porphyrin and poly(viologen) with incorporation of either the α-ZrP or $HTiNbO_5$ nanosheets. The significant finding was that a charge separated state lifetime

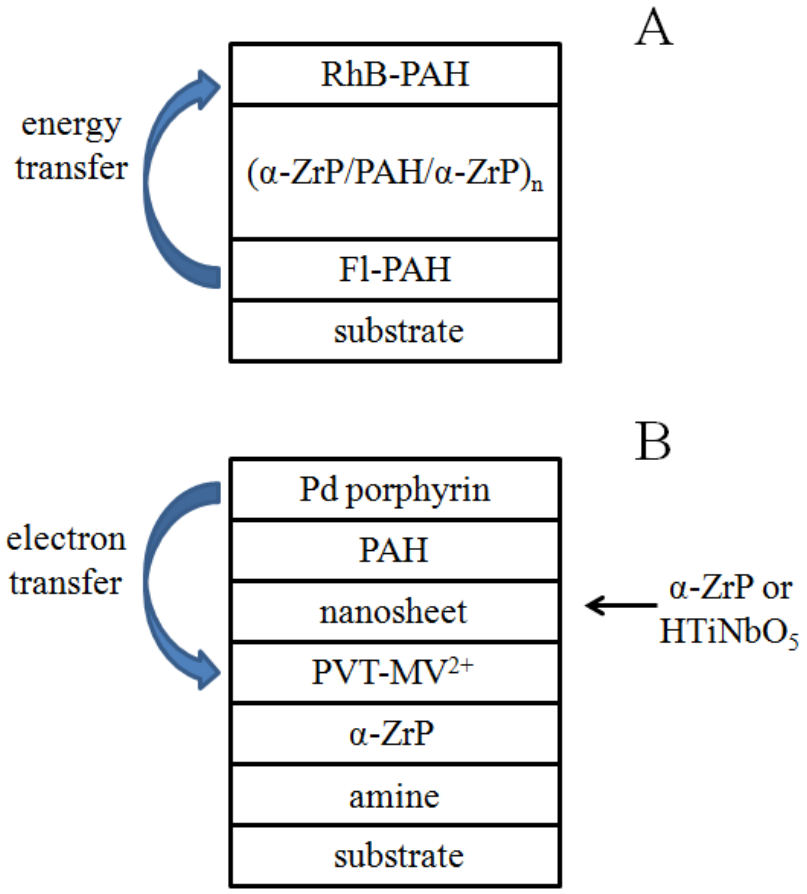

Figure 4.3 (A) Schematic of the multilayer construction on a glass substrate for energy transfer study.[139] Fluorescein and rhodamine B were covalently bound to positively charge PAH and are denoted as Fl-PAH and RhB-PAH. The layer in between the donor (Fl-PAH) and acceptor (RhB-PAH) was a series of α-ZrP nanosheets and PAH layers. To establish the average interlayer distance, the number of interlayers (n) ranged from 0-3. (B) Schematic of multilayer film construction for energy and electron transfer study.[59] The substrates for the electron transfer are silica colloids. A positively charged amine binds the initial α-ZrP nanosheet to the substrate. The purpose of this layer was to isolate each layer with distinct boundaries. A positively charged poly(viologen) ($PVT\text{-}MV^{2+}$) layer was adsorbed, followed by a nanosheet layer, PAH layer and, finally, a Pd porphyrin layer. $PVT\text{-}MV^{2+}$ accepts electrons from the photoexcited Pd porphyrin.

of 0.9 ms was achieved using $HTiNbO_5$, suggesting that $HTiNbO_5$ can readily accept electrons from the Pd porphyrin and plays an active role in charge transfer. This lifetime is significant because reducing the rate of charge recombination plays an important role in charge transfer efficiency not only in water-splitting, but also at interfaces in organic solar cells.[18, 22]

4.2 Motivation

The exceptionally long-lived charge separated state lifetimes show promise for inhibiting charge recombination and increasing efficiencies of water-splitting reactions. The studies of electron transfer by Mallouk and co-workers were performed on silica colloids with a diameter of ~50 nm, which is relatively small compared to lateral dimensions of the α-ZrP and $HTiNbO_5$ nanosheets (1-2 μm and 2-5 μm, respectively).[59] It is then expected that the planar morphology of these multilayer films would be different than on the colloids. The influence of this morphology on the charge separated state lifetimes is unknown.

In order to utilize charge separation in a device, access to each side of the reaction is imperative, therefore construction and investigation of multilayer films in a planar geometry is ideal as opposed to multilayer films on colloids. A complete circuit cannot be achieved without a connection to both electrodes or reactions. The effect of the passive and active nanosheets on the electron transfer from a donor to acceptor molecule in a planar geometry is yet to be determined. To understand the decay pathways contributing to the extended charge separated state lifetimes in a planar geometry,

transient ATR spectroscopy was employed for its proven sensitivity to interfaces and thin films, as demonstrated in Chapter 2. The planar geometry for these studies also allows for characterization with complementary techniques, such as AFM and ellipsometry.

Multilayer films were constructed with a light absorbing species as the donor molecule (Pd porphyrin) and an electron accepting species (poly(viologen)). α-ZrP and $HTiNbO_5$ nanosheets were incorporated into the films to study their effects on the kinetics of the photoinduced charge transfer reaction. The optical markers of these events are the absorbance of the reduced electron acceptor and the cation radical of the donor molecule, which are different from the neutral, ground state species. A significant challenge is to correctly assign absorbance bands to the molecules, as multiple species can contribute to the change in absorbance at a given wavelength. These studies will enhance the understanding of the charge transfer utilizing nanosheet interlayers, as well as move towards a planar architecture, which more closely represents the platform needed for water-splitting as well as other interfaces in multilayer devices.

4.3 Experimental

4.3.1 Nanosheet Exfoliation

Inorganic nanosheets composed of microcrystalline α-zirconium phosphate, α-$Zr(HPO_4)_2 \cdot H_2O$, (α-ZrP) or titanoniobate ($HTiNbO_5$) were first exfoliated to create individually suspended sheets prior to deposition as described by Mallouk and co-workers.[59] To prepare the α-ZrP exfoliated nanosheets or colloidal suspensions,

1.24 x 10^{-4} mol of tetra(*n*-butylammonium) hydroxide (TBA^+OH^-) was added to 1.66 x 10^{-4} mol of α-ZrP in 25 mL of water (HPLC grade) and allowed to stir overnight. This allowed for the acidic protons on the α-ZrP to be exchanged with TBA^+, a bulky cation, and separate layers were suspended in water. The colloid suspension should reach a pH of 8.4. In order to avoid base hydrolysis of the colloids, this reaction was carried out in an ice water bath. If needed, the pH of the suspension was adjusted with HCl or TBA-OH. The $HTiNbO_5$ nanosheets were prepared by combining 10 mg (4.5 x 10^{-5} mol) of $TiNbO_5$ with 25 mL of water (HPLC grade) and adding 40% TBA^+OH^- dropwise until the pH stabilized at 8.4 for one hour. The pH of this solution was adjusted as needed with HCl and NaOH. Structures of α-ZrP, $TiNbO_5$,[144] and TBA-OH are shown in Figure 4.4.

4.3.2 Preparation of Multilayer Films

The films were prepared on borosilicate glass coverslips (VWR) unless otherwise noted. A schematic of the full multilayer film structure is shown in Figure 4.5. The coverslips were cleaned first in piranha (7:3, sulfuric acid: 30% hydrogen peroxide) for 10 minutes. The coverslips were rinsed thoroughly with nanopure water and immediately immersed for at least one hour in a positively charged polymer solution, 10 mM poly(allylamine hydrochloride) (PAH) (Sigma, MW = 58,000), with the pH adjusted to 8.7 with HCl. The concentration of the PAH solution was determined by the molecular weight of the repeating polymer unit (93.5 g/mol). The PAH solution was filtered prior

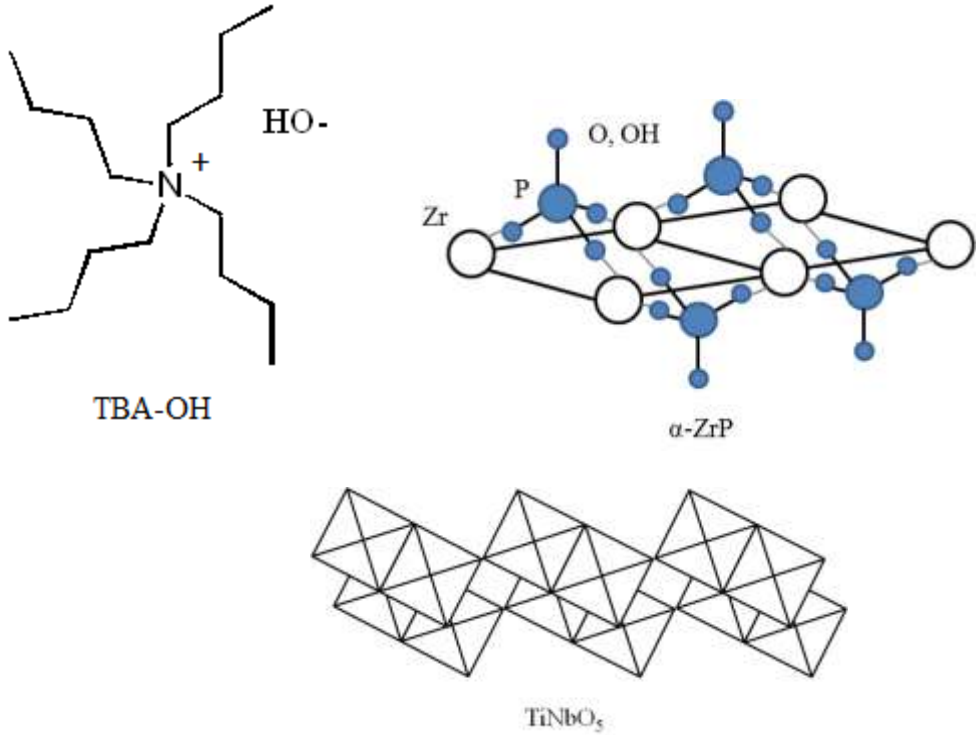

Figure 4.4 Structure of TBA-OH; α-zirconium phosphate (α-ZrP); and titanoniobate ($TiNbO_5$) nanosheets (hatched squares represent the MO_6 octahedra). Reprinted from ref. 144. Used with permission of the American Chemical Society.

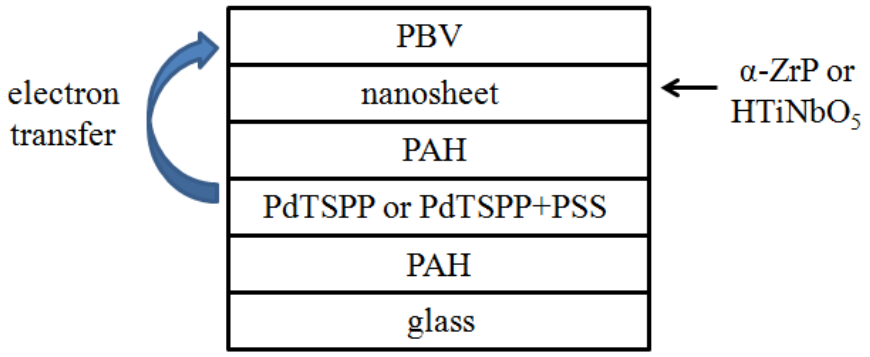

Figure 4.5 Schematic of the multilayer film used to investigate photoinduced charge transfer from the electron donor, PdTSPP, to the electron acceptor, poly(butyl viologen)(PBV). Positively charge poly(allylamine hydrochloride)(PAH) was adsorbed to the glass substrate. The porphyrin film was either deposited by itself or co-deposited with poly(sodium 4-styrenesulfonate)(PSS), followed by PAH. The nanosheets (α-ZrP or $HTiNbO_5$) were deposited on PAH followed by PBV.

to deposition. The coverslips coated with PAH were then rinsed and stored in water (HPLC grade).

Palladium(II)tetrakis(4-sulfonatophenyl) porphyrin (PdTSPP) (Frontier Scientific) was dissolved in water (HPLC grade) and carried four negative charges. Negatively charged poly(sodium 4-styrenesulfonate) (PSS) (Sigma) was dissolved in water and the pH was adjusted to 8.0 with HCl/NaOH. The concentration of the PSS solution was calculated using the molecular weight of the monomer unit (206 g/mol). The multilayer films were deposited by sequential adsorption of the oppositely charged molecules, with deposition times of 10 minutes unless otherwise noted. The films were rinsed thoroughly with water (HPLC grade) between deposition steps. PdTSPP was deposited with a concentration of 5 μM and co-deposited with 500 μM PSS. Co-deposition in this fashion creates a lower degree of porphyrin aggregation.[101] The films with porphyrin were deposited on a single side of the glass coverslip by balancing the coverslip on a watch-glass so that one side was facing up. The porphyrin solution was applied dropwise so that it spread over the entire face of the coverslip. The coverslip was covered with a glass water bath container to prevent significant evaporation of the PdTSPP solution in contact with the coverslip.

Structures of PAH, PdTSPP, and PSS are shown in Figure 4.6. A UV-Vis absorbance spectrum for 10 μM PdTSPP in water is shown in Figure 4.7. The molar absorptivity of PdTSPP in solution at 412 nm is 127,000 $M^{-1}cm^{-1}$ and at 520 nm is 10,700 $M^{-1}cm^{-1}$.[97]

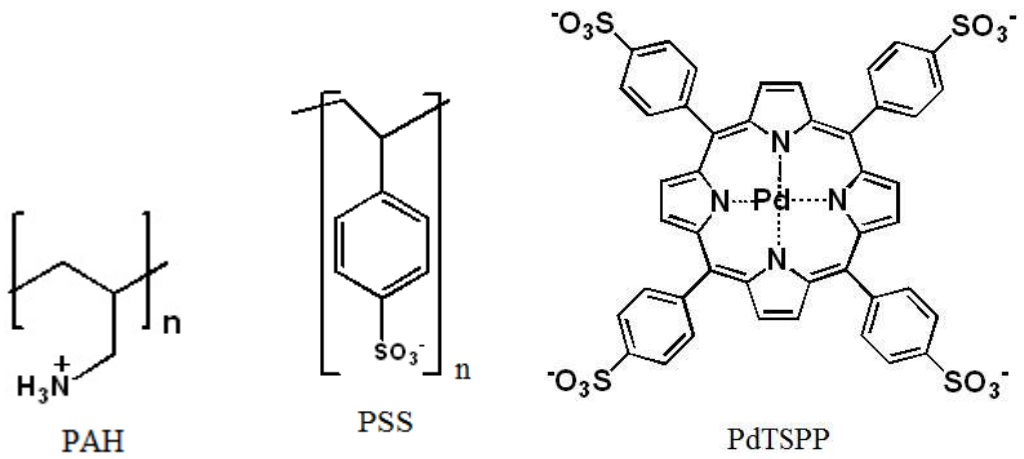

Figure 4.6 Structure of poly(allylamine hydrochloride) (PAH), poly(sodium 4-styrenesulfonate (PSS) and palladium(II)tetrakis(4-sulfonatophenyl) porphyrin (PdTSPP).

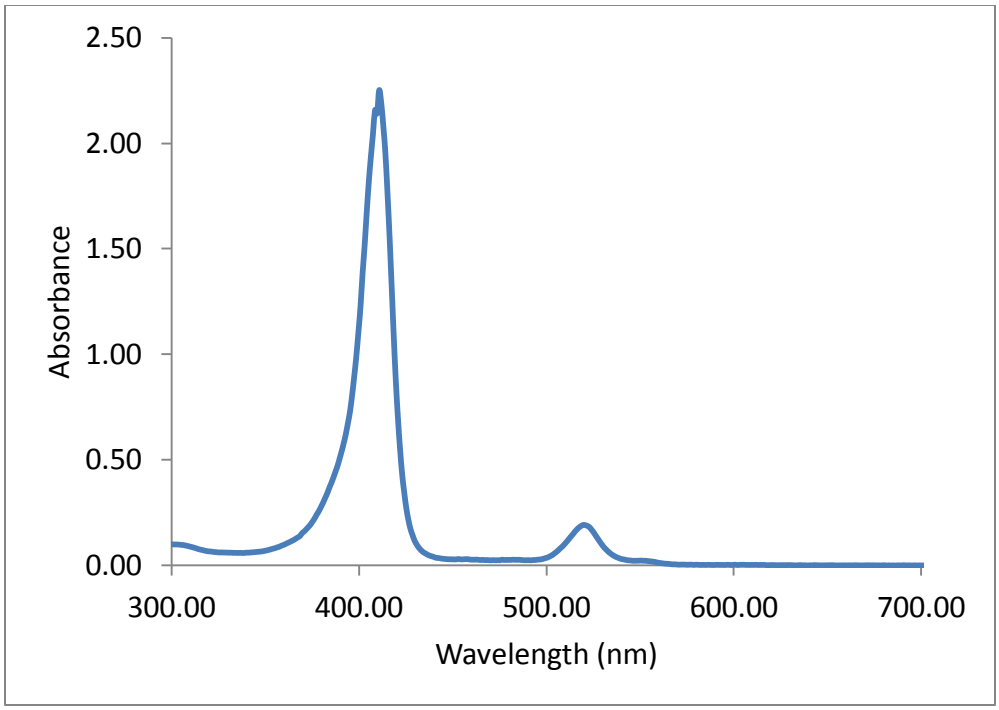

Figure 4.7 UV-Vis absorbance spectrum of 5 μM PdTSPP in water.

The nanosheets were either deposited out of solution or by using a Langmuir-Blodgett (LB) Nima model 611D Langmuir trough. The procedure for solution deposition of both α-ZrP and $HTiNbO_5$ was the same. Both α-ZrP and $HTiNbO_5$ suspensions were negatively charged and deposited on a layer of PAH. The suspensions were heated via a water bath to 35 - 40°C, to ensure close-packed, single layer films. Below 35°C the nanosheets create multilayers and above 40°C the surface coverage decreases.[147] The coverslips coated with PAH were immersed in the nanosheet solution for 15-20 min. Afterward the films were sonicated briefly in water (HPLC grade) with 1 drop of TBA-OH.

The LB films were prepared by filling the trough with water (HPLC grade), immersing the coverslip into the trough and adding 50 uL of the nanosheet suspension solution. The solution remained undisturbed in the trough for 1 hour to allow the nanosheets to spread over the air/water interface. The nanosheets on the surface were compressed until the surface pressure reached 12 mN/m. The film was deposited by raising the coverslip out of the trough at 48 mm/min, while maintaining constant surface pressure.

Poly(viologen) compounds were synthesized by John Swierk at Penn State and were incorporated into the multilayer films as the electron acceptors. The poly(viologen) molecular structures are depicted in Figure 4.8. Methyl viologen-functionalized poly(vinyltoluene) (PVT-MV^{2+}) was first used in the films with a deposition concentration of 10 mM in ethanol. Prior to deposition onto the negatively charged nanosheets, the films were immersed in dilute HCl and dried under a stream of N_2.

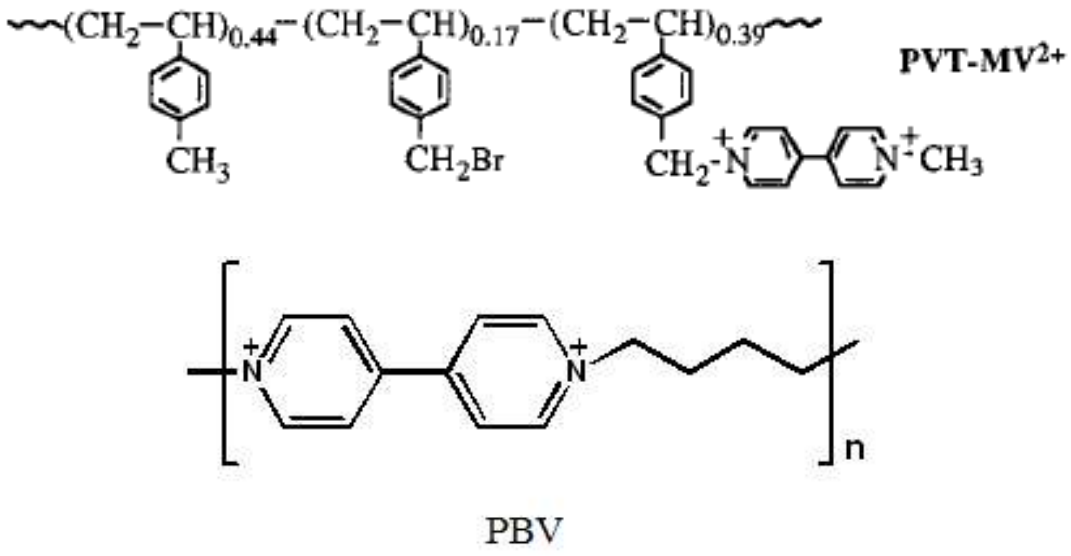

Figure 4.8 Structures of poly(viologen) molecules: methyl viologen-functionalized poly(vinyltoluene) (PVT-MV^{2+}) and poly(butyl viologen) (PBV). The values of 0.44, 0.17 and 0.39 on PVT-MV^{2+} denote the relative molar ratios of each species in the polymer. Reprinted from ref. 59. Used with permission from the American Chemical Society.

Poly(butyl viologen) (PBV), a water soluble polymer, was the electron acceptor used in the majority of the films due to the compatibility with the aqueous LbL technique and for the higher degree of coverage on the nanosheets. The multilayer films composed of a terminal nanosheet layer were rinsed with water (HPLC grade) and immersed in 10 mM PBV, 1 mM KBr solution for deposition times ranging from 30 min to overnight.

After the films were completely constructed, they were rinsed a final time in water (HPLC grade), dried under a stream of N_2 and a transmission UV-Vis spectrum was obtained immediately prior to conducting transient absorbance experiments.

4.3.3 Atomic Force Microscopy

The quality of the nanosheet surface coverage was determined from height images obtained with atomic force microscopy (Model Nanoscope, Dimension 3100 SPM, Digital Instruments, Santa Barbara, CA). Tapping mode was used to collect the images. The scan dimensions were 10 μm x 10 μm, 512 samples per line and a scan rate of 0.75 Hz. The samples terminated with the nanosheets were investigated.

4.3.4 Steady State ATR

The custom designed ATR instrument and flowcell are described in detail elsewhere.[73] A coverslip or microscope slide was coated with PAH and dried completely under a stream of N_2 and positioned in the flowcell. A background spectrum (the blank) was taken with the flowcell filled with deposition solvent, water (HPLC grade). A solution of PdTSPP was injected into the cell and the adsorption was monitored as a

function of time. The cell was then rinsed with water (HPLC grade), after which a spectrum of the porphyrin film was measured.

4.3.5 Transient Absorbance

The transient experiments of solution samples were conducted in a 1 cm x 1 cm pathlength quartz cuvet on the Proteus Instrument (Ultrafast Systems, Inc). The excitation and monitoring beams were aligned perpendicular to each other and the variable gain current amplifier was set to a gain of 10^4.

The transient ATR experiments were conducted with the commercial ATR instrument (SIS-5000, System Instruments, Japan) and the Delrin flowcell as detailed in Chapter 3. The multilayer films were constructed outside of the cell, measured with a UV-Vis spectrometer and then secured in the Delrin flowcell. BK-7 right angle prisms (Edmund Optics) were adhered to the coverslip with index matching fluid (Cargille, n_z = 1.515). A constant stream of Ar gas blew over the films during the transient ATR experiments. The films were excited with 532 nm light (~80 μJ, 5-7 ns pulse width) and monitored at 480 nm to observe the PdTSPP triplet state. The other wavelength monitored was 600 nm, although this was not ideal because several species absorb at this wavelength, including the reduced PBV,[148] the cation radical of PdTSPP and triplet state of the PdTSPP.[110]

4.4 Results and Discussion

4.4.1 Transient Absorbance of PdTSPP Solution

In this study the molecule used as the electron donor in the multilayer films is PdTSPP. As a control, the excited state lifetimes of PdTSPP were measured first in solution prior to constructing multilayer films. The transient decay curve was obtained of 50 μM PdTSPP in Ar-purged water and is depicted in Figure 4.9. The difference absorbance was monitored at 480 nm for the triplet state. The decay curve was fit to a 1st order exponential with a lifetime of 200 μsec and is reported in Table 4.1. This lifetime is consistent with previously reported triplet state lifetimes of PdTSPP in aqueous solution listed as 200 μsec[149] or 350 μsec.[97] These values are reported from the phosphorescence emission of the porphyrins in solution, rather than from transient absorbance. Despite argon purging the sample, some residual O_2 might still be present causing a shorter triplet state lifetime of the PdTSPP.

4.4.2 Surface Coverage of PdTSPP

The surface coverage of the PdTSPP was characterized to determine the absorption profile of PdTSPP adsorbed to the positively charged PAH film. Layer by layer (LbL) assembly was used to construct the films. To determine the surface coverage of the PdTSPP films, steady state ATR spectroscopy was performed. A blank was obtained with water (HPLC grade) in contact with a glass coverslip coated with one layer

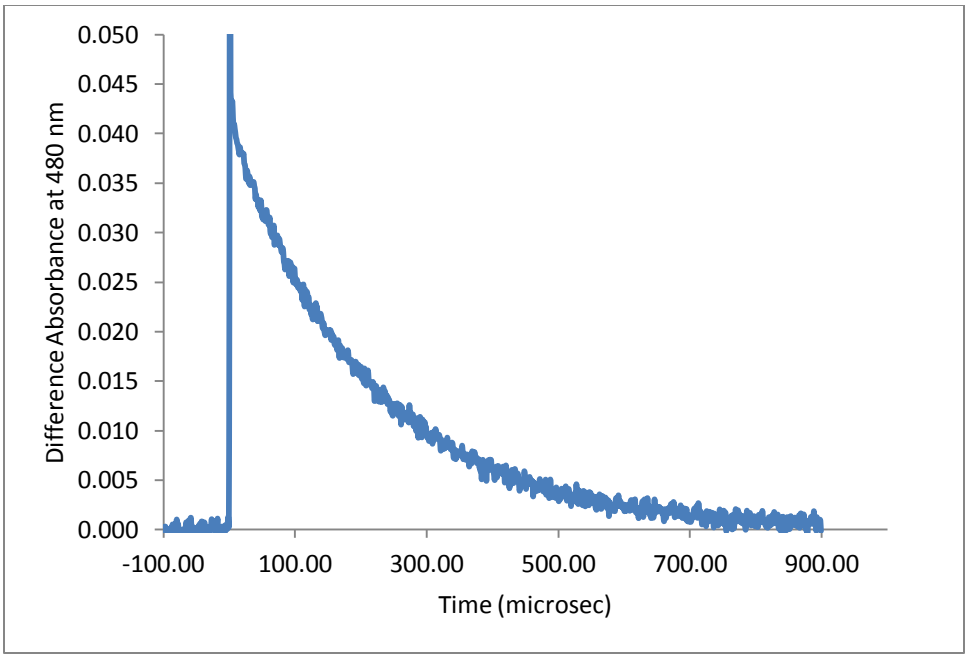

Figure 4.9 Solution transient curve of 50 μM PdTSPP in argon purged water at 480 nm, representing the triplet state. The decay curve was fit to a first order exponential with a lifetime of 200 μsec.

Table 4.1 Transient absorbance lifetimes and weighing factors for PdTSPP solution and multilayer films.

Sample	λ	Lifetime	Weighing factors	Onset amplitude	Ratio of onset amplitudes
50 μM PdTSPP, water (HPLC grade)	480 nm	200 μsec	1.0	N/A	N/A
glass/PAH/PdTSPP+PSS	480 nm	4 μsec, 49 μsec	0.82, 0.18	0.005	N/A
glass/PAH/PdTSPP+PSS/ PAH	480 nm	16.5 μsec, 250 μsec	0.78, 0.22	0.006	N/A
glass/PAH/PdTSPP+PSS/ PAH/α-ZrP	480 nm	28 μsec, 350 μsec	0.54, 0.46	0.016	5.3
	620 nm	N/A	N/A	0.003	
glass/PAH/PdTSPP+PSS/ PAH/α-ZrP/PBV	480 nm	1 μsec, 110 μsec, 650 μsec	0.91, 0.06, 0.03	0.005	5
	620 nm	N/A	N/A	0.001	
glass/PAH/PdTSPP+PSS/ PAH/$HTiNbO_5$	480 nm	35 μsec, 322 μsec	0.35, 0.65	0.018	4.5
	600 nm	N/A	N/A	0.004	
glass/PAH/PdTSPP+PSS/ PAH/$HTiNbO_5$/PBV	480 nm	5.8 μsec, 75 μsec, 480 μsec	0.56, 0.26, 0.18	0.009	3
	600 nm	N/A	N/A	0.003	
glass/PAH/PdTSPP+PSS/ PAH/$HTiNbO_5$ (no HCl exposure)	480 nm	35 μsec, 400 μsec	0.49, 0.51	0.018	N/A
glass/PAH/PdTSPP+PSS/ PAH/$HTiNbO_5$ (HCl exposure)	480 nm	5.6 μsec, 22 μsec, 220 μsec	0.33, 0.36, 0.29	0.009	N/A
glass/PAH/PdTSPP+PSS/ PAH/$HTiNbO_5$/PBV (no HCl exposure)	480 nm	5.8 μsec, 75 μsec, 480 μsec	0.56, 0.26, 0.18	0.009	N/A
glass/PAH/PdTSPP+PSS/ PAH/$HTiNbO_5$/PBV (HCl exposure)	480 nm	N/A	N/A	0.002	N/A

of PAH. 10 μM PdTSPP in water was injected into the flowcell and allowed to adsorb for 30 min. The cell was rinsed with 10 mL of water and spectra of the film were obtained for both the TE and TM polarizations. To ensure the film had reached full coverage, 25 μM PdTSPP in water was next injected into the flowcell and allowed to adsorb for 30 min. The cell was rinsed a final time with 10 mL of water and the ATR spectra were measured.

The ATR absorbance spectra of the films and the adsorption isotherm of 10 μM and 25 μM PdTSPP solutions are shown in Figure 4.10. The film had reached full coverage with the 10 μM PdTSPP so the 25 μM PdTSPP solution did not add an appreciable amount of molecules to the film. The peak for the Soret band had reached the stray light limit, thus the Q-band at 526 nm was monitored for the adsorption isotherm. The Q-band is slightly red shifted from the solution sample absorbance maximum of 520 nm. Galoppini and co-workers noted similar red shifts of the porphyrin Q-band when tethering zinc porphyrins to TiO_2 nanotubes and attributed these shifts to aggregation of porphyrin on the surface.[48, 150] PAH does not absorb in the visible region, so there was no interfering bands in the ATR spectra.

The calculations for surface coverage assumed a 2-phase system, ignoring the single layer of PAH (~ 0.5 nm)[141] and the values considered were the glass coverslip (n= 1.51, thickness = 150 μm) and the solvent, water (n=1.33). Equations 2.2, 2.3, and 3.2 were used to calculate the surface coverage of the PdTSPP thin film. The isotropic molar absorptivity of PdTSPP at 520 nm, 10,700 $M^{-1}cm^{-1}$,[97] was used to find the surface coverage. The overall surface coverage was determined to be 170 $pmol/cm^2$. Pd(II) 5-(4-

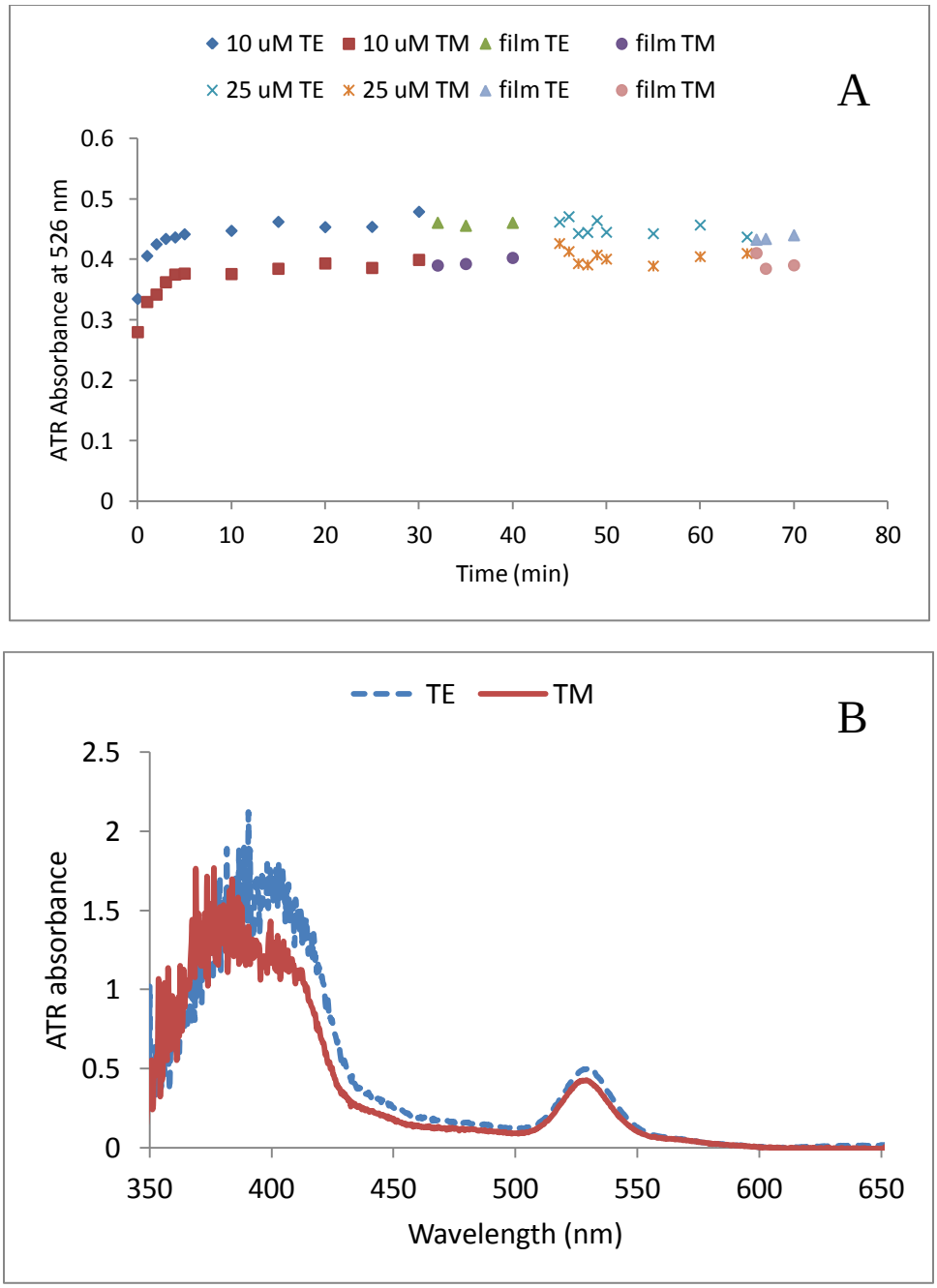

Figure 4.10 (A) ATR adsorption isotherm of 10 μM PdTSPP and 25 μM on PAH coated coverslip (B) ATR absorption spectra of PdTSPP film on PAH coated coverslip.

carboxyphenyl)-10,15,20-tris(4-methylphenyl) porphyrin in the edge-on geometry was determined to occupy a surface area of 90 $Å^2$/molecule.[108] Using this as an estimate, the coverage was calculated to be ~0.9 of a monolayer. This surface coverage seems reasonable as it is unlikely multilayer porphyrin films would form due to the electrostatic repulsion of the negatively charged PdTSPP molecules to one another.

In order to conduct a transient ATR experiment, the absorbance values at the excitation wavelength of the laser (532 nm) must be sufficient to promote a large fraction of molecules into the excited state. The absorbance values of the PdTSPP film at 532 nm are 0.46 and 0.4 for TE and TM polarizations, respectively. Therefore, the surface coverage of PdTSPP on PAH is sufficient to conduct transient ATR experiments.

4.4.3 Polyelectrolyte and Porphyrin Films

Before constructing the entire films as shown in Figure 4.5, LbL polyelectrolyte and porphyrin films were prepared as controls in order to measure the excited state lifetimes without the nanosheets or poly(viologen) electron acceptor present. The films were prepared as described and transmission UV-Vis spectra were taken prior to conducting transient experiments. The UV-Vis spectra are shown in Figure 4.11. The PAH and PSS did not absorb any visible light so the spectra are due to the PdTSPP absorbance. The first sample was a glass coverslip coated with a layer of PAH, followed by the co-adsorption of PdTSPP and PSS (glass/PAH/PdTSPP+PSS). The second sample was identical, but included a final layer of PAH, deposited for 10 min (glass/PAH/PdTSPP+PSS/PAH). The sample with the terminal layer of PAH had a

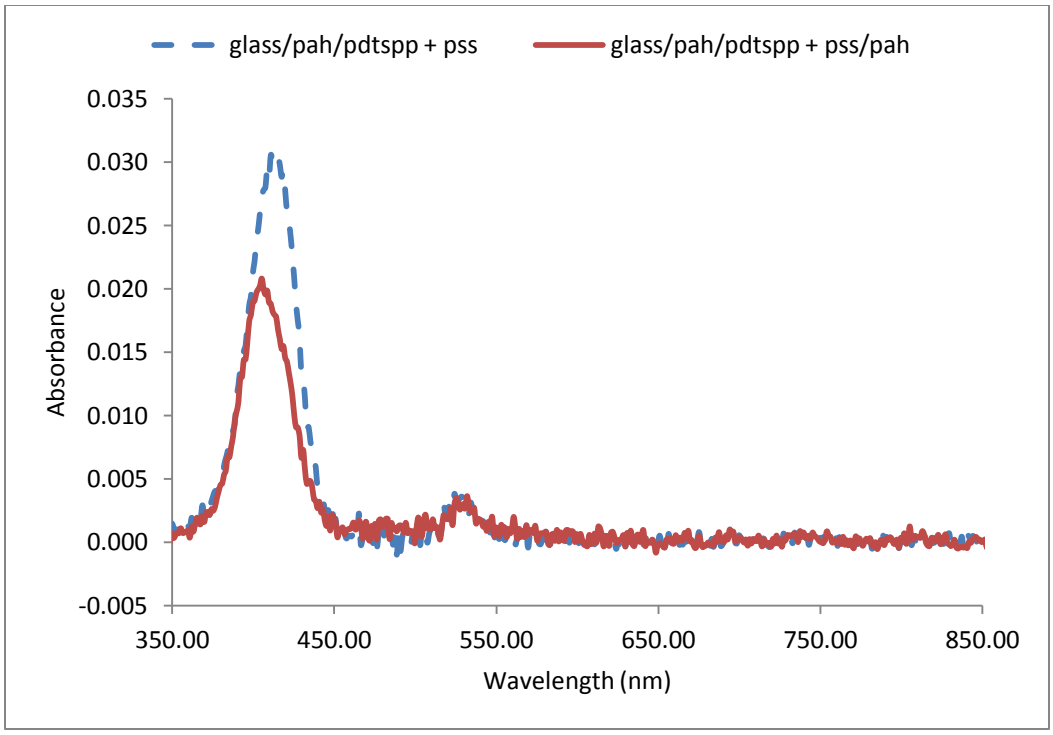

Figure 4.11 Transmission UV-Vis absorbance spectra of glass/PAH/PdTSPP + PSS (dashed line) and glass/PAH/PdTSPP + PSS/PAH (solid line).

decreased absorbance at the Soret band. This may indicate desorption of some PdTSPP during the PAH deposition procedure.

Transient ATR decay curves were taken of these films. The transient of the glass/PAH/PdTSPP+PSS sample is displayed in Figure 4.12. The difference absorbance was monitored at 480 nm, where the triplet state absorbs.[97] The amplitude of the transient is 0.005 absorbance units. By examination of the residuals, a first order fit was not satisfactory for the decay curve. A 2nd order exponential was then used to fit the decay curve with lifetimes of 4 μsec and 49 μsec, carrying a weighing factor of 0.82 and 0.18, respectively. The lifetimes are reported in Table 4.1.

The transient ATR of the glass/PAH/PdTSPP+PSS/PAH sample is shown in Figure 4.13. The amplitude of the difference absorbance at 480 nm is 0.006 absorbance units which is comparable to the first sample. The curve was fit to a 2nd order exponential with lifetimes of 16.5 μsec and 250 μsec, with weighing factors of 0.78 and 0.22, respectively. The lifetimes are reported in Table 4.1. Each of these samples has a two lifetimes, while the solution sample was fit to a first order exponential. The molecular environment of PdTSPP consists of positively and negatively charged polymers in addition to the sulfonate and amine functional groups. In addition, it is likely that there are aggregated populations of PdTSPP in the film.

It is unclear why the lifetimes of glass/PAH/PdTSPP+PSS/PAH are longer than the glass/PAH/PdTSPP+PSS sample. It is possible that the additional PAH layer change the electron density around the porphyrin macrocycle to stabilize the triplet state lifetime.

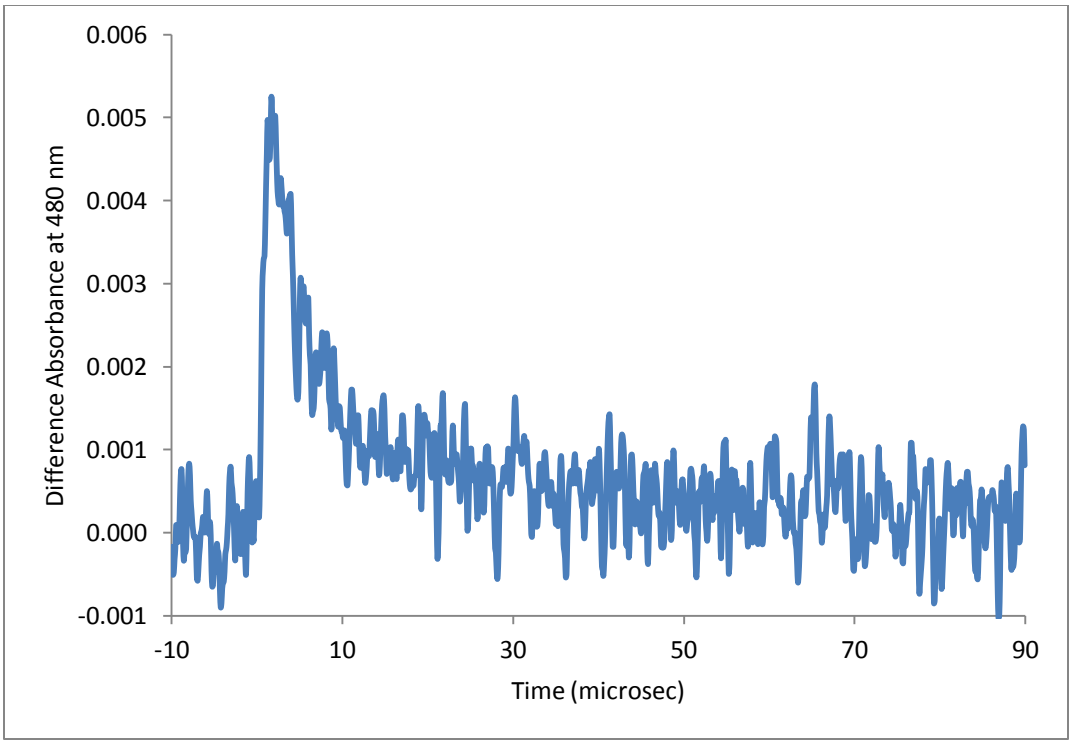

Figure 4.12 Transient ATR curve of glass/PAH/PdTSPP + PSS at 480 nm.

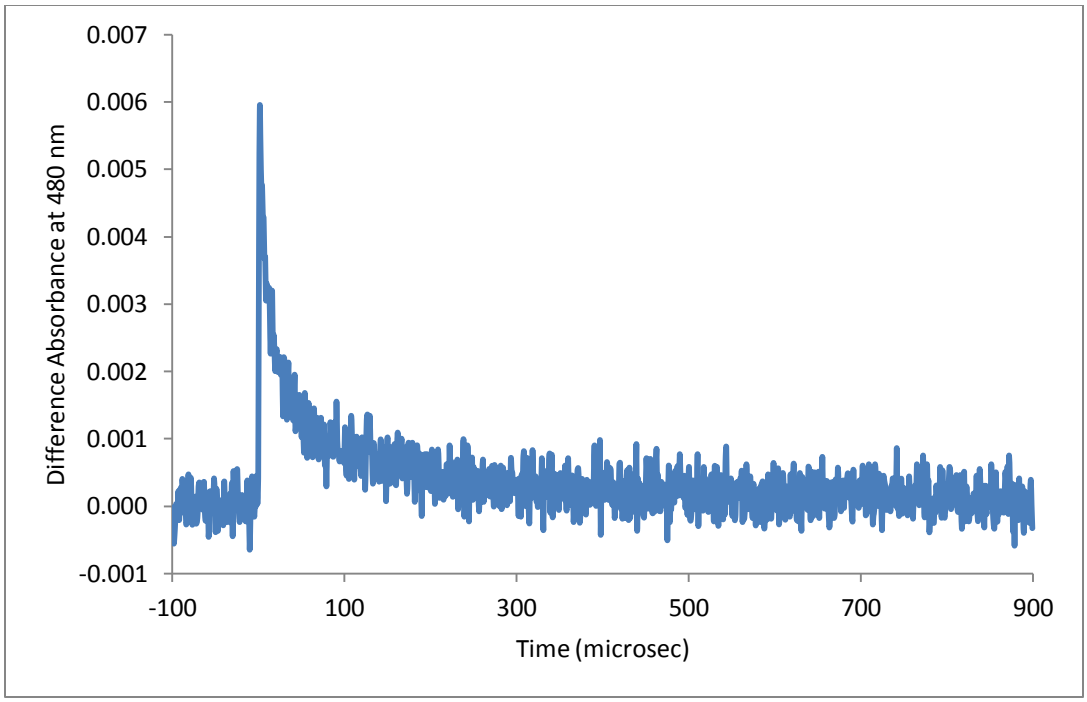

Figure 4.13 Transient ATR curve of glass/PAH/PdTSPP + PSS/PAH at 480 nm showing the triplet decay.

The longer lifetime of the glass/PAH/PdTSPP+PSS/PAH sample is still within the range of the triplet state decay of the PdTSPP reported in literature (200-350 μsec).[97]

Aggregation of PdTSPP within the films, which will cause triplet annihilation, may contribute to the shorter lifetimes of the triplet state.[100, 110] Although the co-deposition alleviates some aggregation of the porphyrin,[101, 119] it is known that chromophores associated with amine and other similar functional groups quench the emission via creation of charge separated states.[101]

4.4.4 Characterization of Films with Nanosheet Incorporation

There was clearly a difference in triplet excited state lifetime between the PdTSPP in solution and the PdTSPP incorporated into a solid state polymer film. It is not evident which forces dominate the triplet state decay. Some of forces involved are the intermolecular interactions of the functional groups of the individual molecules, the porphyrin forming aggregated species and electrostatic forces. Despite the shorter triplet state lifetimes as compared to solution samples, they are sufficiently long-lived to transfer a charge to the poly(viologen). In the studies with the silica colloids, the triplet state of the PdTSPP was shown to decay in ~2 μsec, by transferring its electron to poly(viologen).[59] Multilayer films without PBV were constructed and evaluated as controls to investigate the excited state lifetimes of PdTSPP, prior to study of the effects of the nanosheet incorporation on the charge transfer between PdTSPP and PBV.

Nanosheets can be deposited out of solution or via LB deposition. The main goal with these films is to achieve a closely packed film of these two dimensional spacers to

prevent further mixing associated with charged polymer in LbL films. The addition of nanosheets to the multilayers allows for segregation of electron donor and acceptor molecules.[136, 139]

The most consistent and reproducible coverage of the nanosheets was achieved with LB. The AFM height images of films terminated with the nanosheets (α-ZrP and $HTiNbO_5$) are shown in Figure 4.14. The glass coverslip was first coated with a layer of PAH, followed by co-adsorption of PdTSPP and PSS, then another layer of PAH, and finally the nanosheets. The sheets range from 1-2 μm for α-ZrP and 2-5 μm for $HTiNbO_5$ laterally with a thickness of 1 nm.[59] The estimated surface coverage from these images is about 80-90%. There is only a small degree of sheets overlapping as seen with the height image. It is important to have full coverage because direct donor-acceptor contact could occur in gaps between the sheets. It is also necessary to have single layers of the nanosheets so the distance the electrons travel between layers does not affect the electron transfer reaction. The thickness of the nanosheets are 8 Å and 10 Å, for α-ZrP and $HTiNbO_5$, respectively.[59] Adsorption of multilayers will affect the charge transfer because it is a function of intermolecular distance. Since electron tunneling distances range from ~1-3 nm,[151] electron transfer across multilayers of nanosheets may not be possible.

UV-Vis spectra were obtained of the films coated with LB nanosheets and are shown in Figure 4.15. The nanosheets did not absorb any visible light, so the spectra again are due to the PdTSPP absorbance. The absorbance of the Soret band is lower for both samples with nanosheets (0.015 a.u.) as compared to the spectrum of the

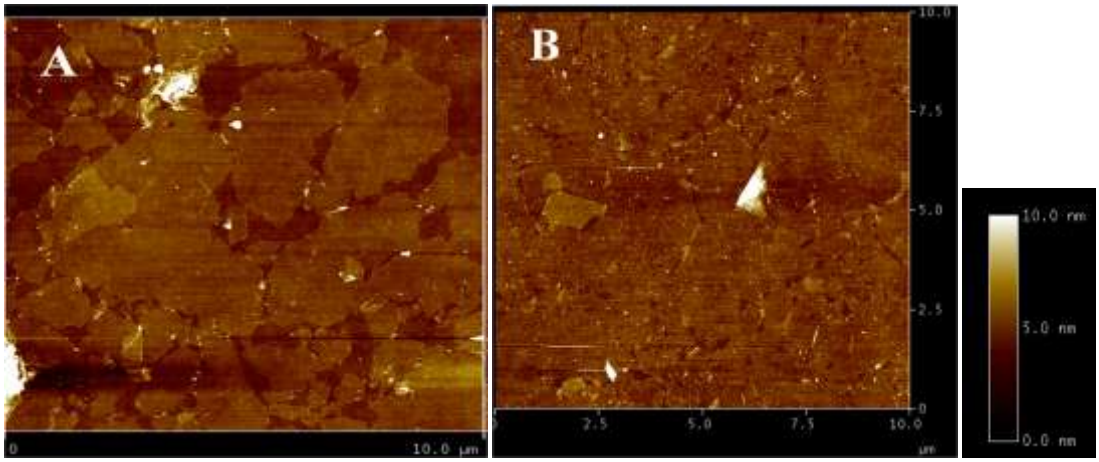

Figure 4.14 AFM height images of (A) α-ZrP and (B) $HTiNbO_5$ deposited onto glass/PAH/PdTSPP + PSS/PAH films.

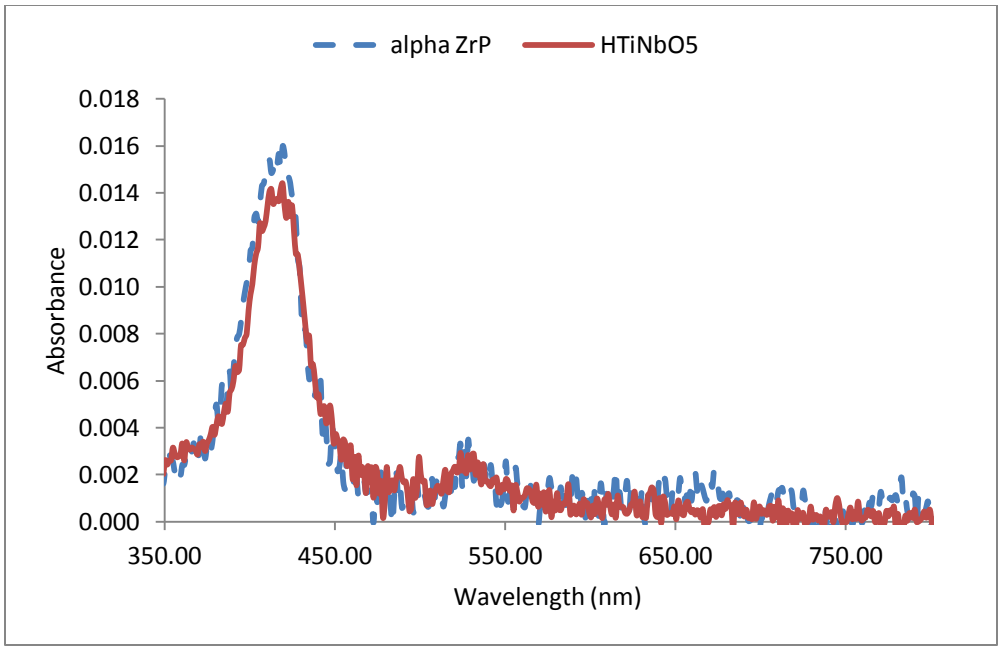

Figure 4.15 Transmission UV-Vis spectra of glass/PAH/PdTSPP+PSS/PAH/α-ZrP (dashed line) and glass/PAH/PdTSPP+PSS/PAH/$HTiNbO_5$ (solid line). The nanosheets were deposited via LB.

glass/PAH/PdTSPP+PSS/PAH in Figure 4.11 (0.02 a.u.). This could be due to slight desorption of PdTSPP in the LB trough prior to nanosheet deposition. Another possibility is the displacement of the PdTSPP at the surface by the nanosheets, since both are negatively charged.

The transient ATR curve of the glass/PAH/PdTSPP+PSS/PAH/α-ZrP sample is displayed in Figure 4.16. The difference absorbance was monitored at 480 nm and the curve was fit to a second order exponential with lifetimes of 28 μsec and 350 μsec with weighing factors of 0.54 and 0.46, respectively. The transient decay of the same film architecture, but with $HTiNbO_5$ nanosheets, is shown in Figure 4.17. This curve was also fit to a second order exponential with lifetimes of 35 μsec and 322 μsec with weighing factors of 0.35 and 0.65, respectively. The lifetimes are reported in Table 4.1.

The films with nanosheets have longer lived triplet state lifetimes, with a much larger contribution of the longest lived component as compared to samples without nanosheets. The negatively charged nanosheets are interacting with the positively charged PAH layer, possibly changing the overall net charge of the PdTSPP local environment. This effect could be stabilizing the triplet excited states. Since the LbL assembly of the film below the nanosheet has "fuzzy" boundaries,[63] it is possible that PdTSPP is in close proximity to the functional groups on the nanosheet. The nanosheet could also be providing a degree of order to the porphyrin aggregates that could affect the triplet state lifetime. In studies by Egawa et al., he determined that pH had an effect on the types of porphyrin aggregates (either H- or J-aggregates) formed in the multilayer polymer films.[119]

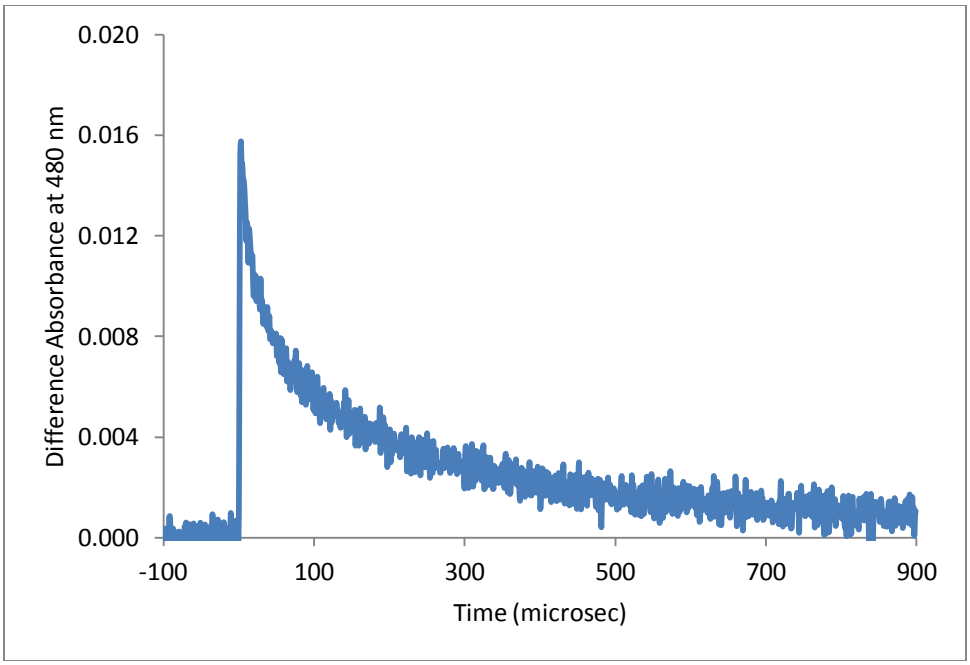

Figure 4.16 Transient ATR curve of glass/PAH/PdTSPP + PSS/PAH/α-ZrP at 480 nm representing the triplet state. The decay curve was fit to a 2nd order exponential with lifetimes of 28 μsec and 350 μsec.

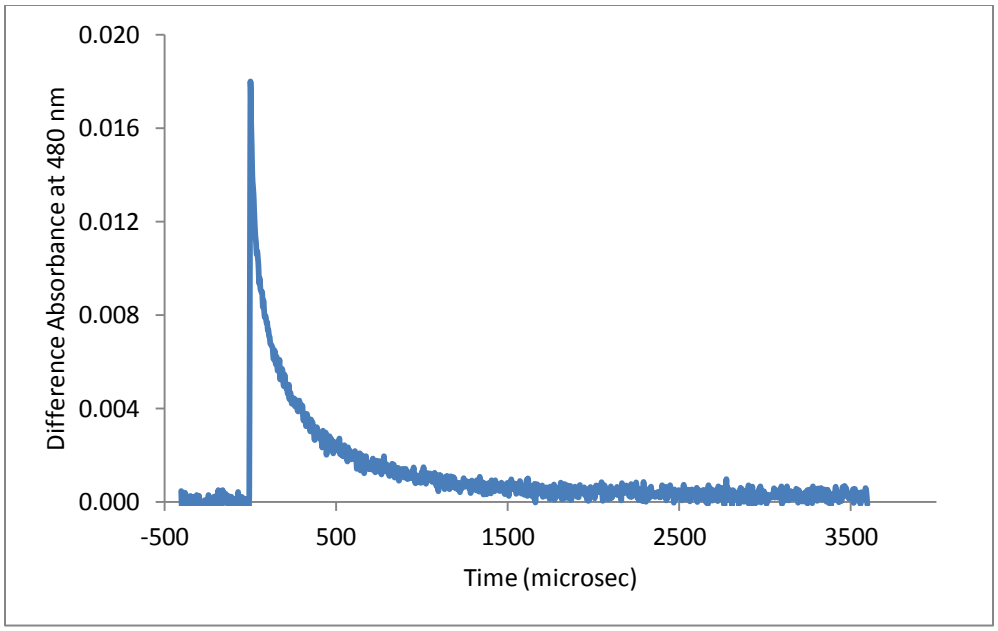

Figure 4.17 Transient ATR curve of glass/PAH/PdTSPP + PSS/PAH/HTiNbO$_5$ at 480 nm representing the triplet state. The decay curve was fit to a 2nd order exponential with lifetimes of 35 µsec and 322 µsec.

The onset difference absorbance at 480 nm is similar between the samples with nanosheets (0.016 a.u. for α-ZrP and 0.018 a. u. for $HTiNbO_5$), but both are higher than the samples without nanosheets (0.006 a.u.). These are reported in Table 4.1. A possibility is that the triplet molar absorptivity may be different between the samples with nanosheets and those without. The nanosheets may enhance the quantum efficiency of intersystem crossing (Q_{ISC}) as compared to the films without nanosheets. The Q_{ISC} has been reported for PdTSPP in solution (1.0),[97] but has not been reported for this particular molecule in a thin film or in the immediate presence of a network of polyanions and polycations. Extensive studies would have to be performed to test these hypotheses. For the purpose of this study, the long lived triplet state of the porphyrin is sufficient for charge transfer to an electron acceptor molecule.[59]

The results thus far have indicated that when PdTSPP is incorporated into a multilayer film the triplet state lifetime is altered as compared to the solution sample. Although the relationship between the local chemical environment and the triplet state lifetimes and yield are not fully understood, the lifetime of the triplet state is sufficiently long to donate an electron to the poly(viologen) electron acceptor molecule. This was demonstrated by the quenching of the PdTSPP triplet state in ~2 μsec due to electron donation to the poly(viologen) as shown in the studies by Mallouk and co-workers.[59]

4.4.5 Characterization of Polyelectrolyte Films with the Incorporation of Poly(viologen), an Electron Acceptor

The question this research aimed to address was the role of the nanosheets in an electron transfer reaction between an electron donor and acceptor. As discussed in detail previously, a significantly long-lived charge separated state lifetime (0.9 ms) was observed between an electron donor and acceptor after incorporation of $HTiNbO_5$.[59] The evidence suggested that $HTiNbO_5$ acted as an 'active' spacer in the film, with semiconducting properties that allowed it to accept electrons from the excited state of the donor. These experiments were performed on silica colloids, where the morphology would not reflect a planar geometry that would be used in a water-splitting device.[59]

The control experiments demonstrated that there are effects on the PdTSPP triplet state lifetime from the multilayer film as compared to a solution of PdTSPP. One of the most notable effects is the existence of a short-lived component, which may arise from quenching of the triplet state due to aggregation of PdTSPP within the film. The nanosheets alone have not significantly quenched the triplet state, which would be evidence of electron transfer.[59]

The electron acceptor chosen was PBV due to the positions of the VB and CB as compared to the $HTiNbO_5$ nanosheets and PdTSPP. In addition, PBV is water soluble so it can be easily incorporated into the LbL assembly. The band energy diagram of these molecules is shown in Figure 4.18. As discussed earlier, the band edge value for $HTiNbO_5$ is an estimate based on calculations of a bulk sample at the point of zero

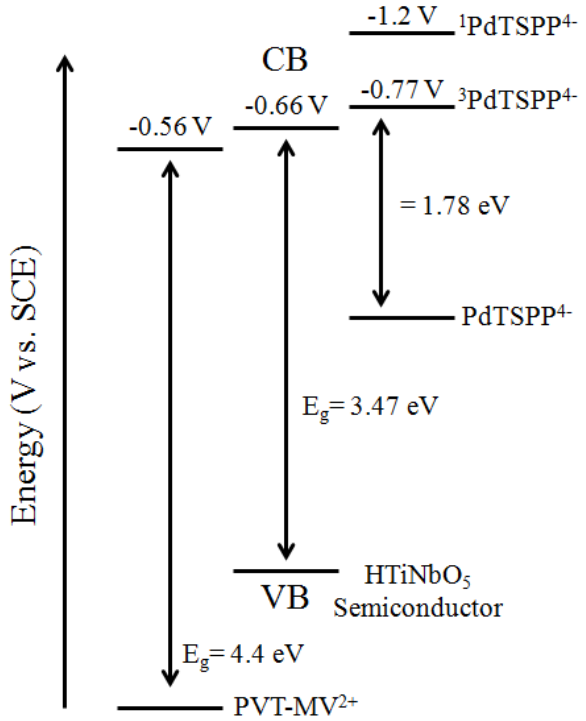

Figure 4.18: Band edge diagram of PdTSPP, $HTiNbO_5$ and PVT-MV^{2+}. E_g denotes the band gap energy of the semiconductors. The energy values are in V vs. SCE. The values for PVT-MV^{2+} shown here also apply to PBV.

charge, so the actual band edge of the nanosheets incorporated into a multilayer film is yet to be experimentally determined.[59, 144]

Poly(viologen) as a neutral molecule is transparent in the visible spectrum, but absorbs below 300 nm. After reduction, it absorbs around 380 nm and at 600 nm.[148] A UV-Vis absorbance spectrum of a quartz/PAH/PdTSPP/PAH/PSS/PVT-MV^{2+} is shown in Figure 4.19. The absorbance at 280 nm is due to poly(viologen). PVT-MV^{2+} in this film was deposited out of ethanol as compared to water soluble PBV used in the rest of the experiments, but the absorbance is similar.

The transient decay curves for multilayer films are shown in Figure 4.20: glass/PAH/PdTSPP+PSS/PAH/α-ZrP/PBV and glass/PAH/PdTSPP+PSS/PAH/$HTiNbO_5$/PBV. The difference absorbance was monitored at 480 nm. The transient curves with one and two component exponentials were statistically unsatisfactory upon examination of residuals, therefore the curves were fit with 3rd order exponentials. The lifetimes are reported in Table 4.1. The lifetimes for the glass/PAH/PdTSPP+PSS/PAH/α-ZrP/PBV sample were 1 μsec, 110 μsec and 650 μsec with weighing factors of 0.91, 0.06, and 0.03, respectively. The glass/PAH/PdTSPP+PSS/PAH/$HTiNbO_5$/PBV film had lifetimes of 5.8 μsec, 75 μsec, and 480 μsec with weighing factors of 0.56, 0.26, and 0.18, respectively. Due to the fact that these triplet decay curves had a much longer-lived third component as compared to solution samples of PdTSPP (200-350 μsec)[97], it can be inferred that there was another reaction pathway as a result of the presence of the poly(viologen). The long-lived component may arise from additional stabilization of the triplet state or a charge-

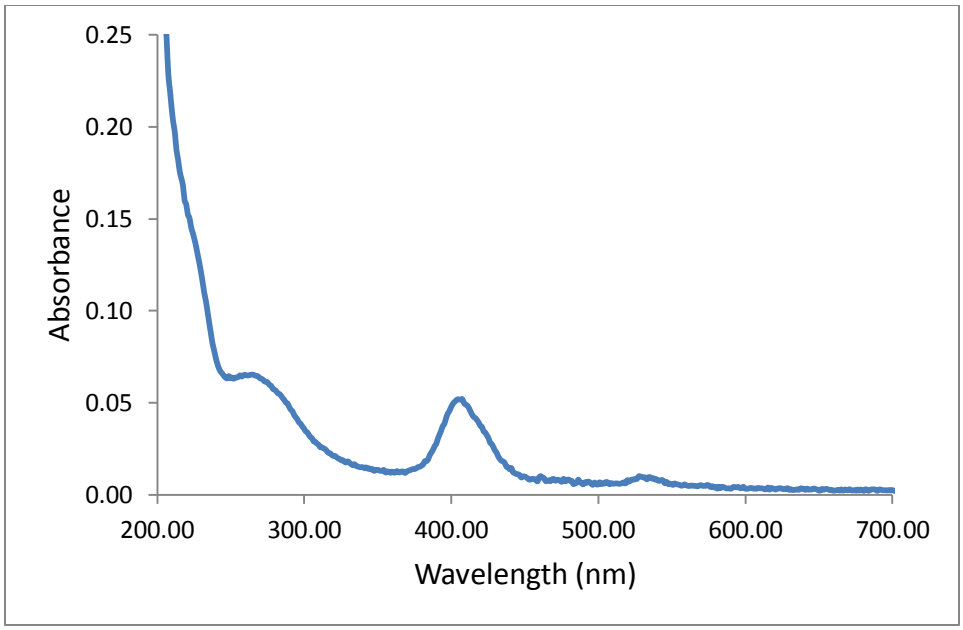

Figure 4.19 Absorbance UV-Vis spectrum of quartz/PAH/PdTSPP/PAH/PSS/PVT-MV^{2+}.

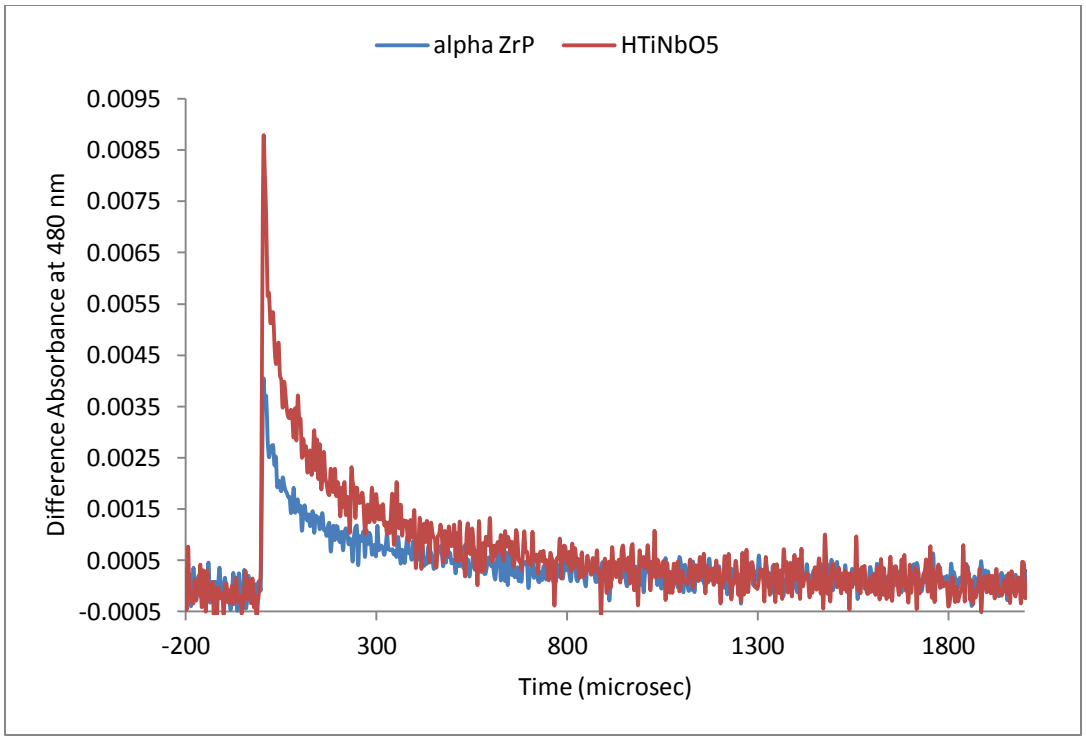

Figure 4.20 Transient ATR curves of glass/PAH/PdTSPP + PSS/PAH/nanosheets/PBV at 480 nm representing the triplet state; (blue) α-ZrP and (red) $HTiNbO_5$. Both decay curves were fit to a 3rd order exponential with lifetimes of 1 µsec, 100 µsec and 650 µsec for α-ZrP and 6 µsec, 75 µsec and 480 µsec for $HTiNbO_5$.

separated state. To our knowledge, the difference absorbance at 480 nm is only due to the triplet state of PdTSPP. An indication of charge transfer is the quenching of the PdTSPP triplet state. Although there is a long-lived component, the contributions from the shorter-lived components are much larger, especially in the glass/PAH/PdTSPP+PSS/PAH/α-ZrP/PBV sample. This data alone cannot verify charge transfer.

As discussed previously, the reduced PBV absorbs around 600 nm[148] and although there is a spectral overlap with the PdTSPP cation radical,[110] a difference in onset amplitudes or decay kinetics might provide evidence of charge transfer. The glass/PAH/PdTSPP+PSS/PAH/$HTiNbO_5$ and glass/PAH/PdTSPP+PSS/PAH/$HTiNbO_5$/PBV films were monitored at both 480 nm and 600 nm. Figure 4.21 shows the transient ATR decays of glass/PAH/PdTSPP+PSS/PAH/$HTiNbO_5$ with and without PBV at both 480 and 600 nm. There is clearly a difference in the onset amplitudes of the two samples at 480 nm; without PBV the initial difference absorbance is 0.018 a.u., while with PBV it is 0.009 a.u. These values are also reported in Table 4.1. A possibility for this difference could be that rapid quenching of the triplet state may be occurring before the time resolution of the transient ATR instrument (~3 μsec). Another value to note is the ratio between the onset potentials. For the sample without PBV, the ratio is around 4.5, whereas with the addition of PBV, the ratio is 3. Although this is not concrete evidence of formation of the reduced poly(viologen) species, there is clearly an effect from the addition of the PBV.

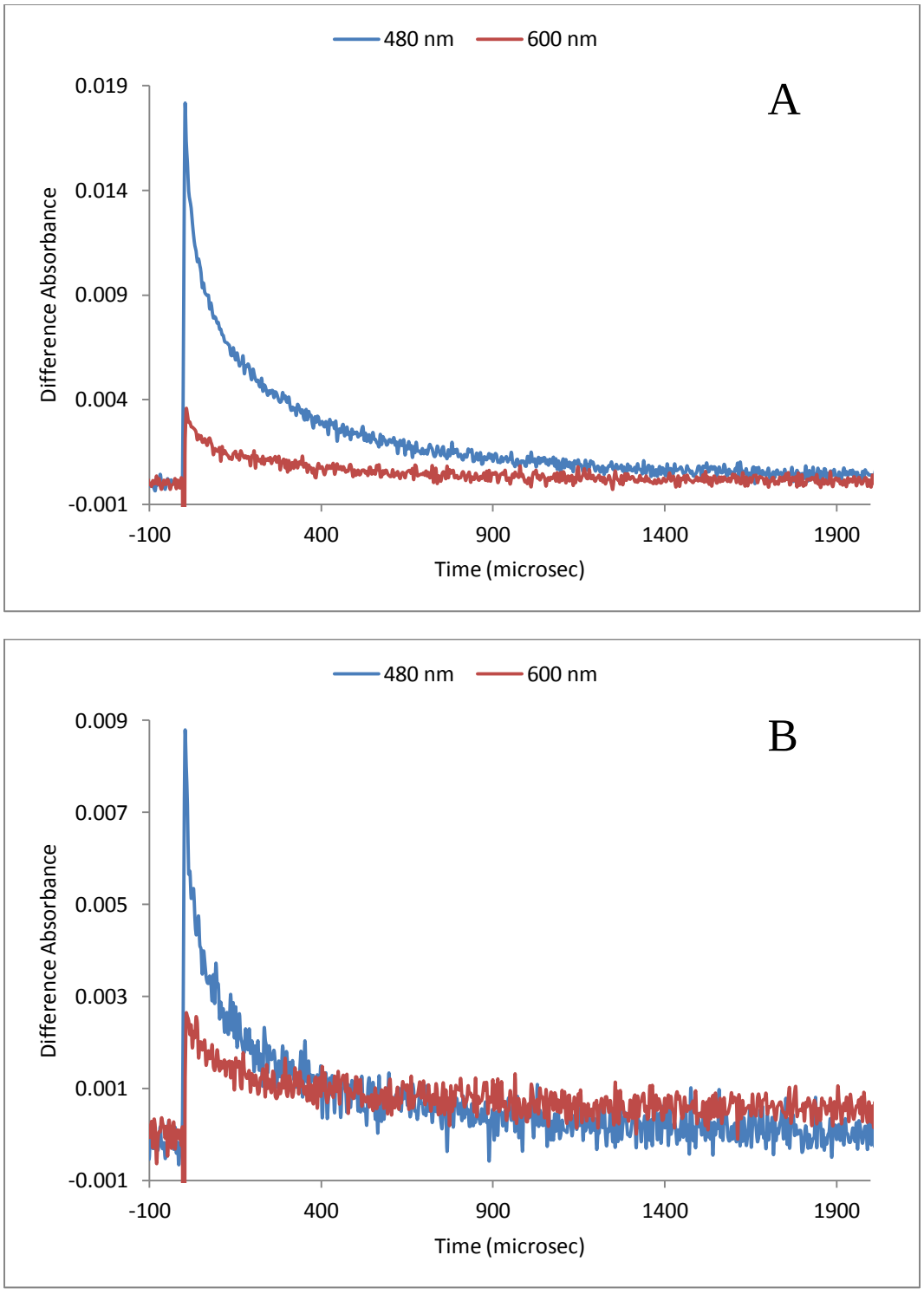

Figure 4.21 Transient ATR curves of (A) glass/PAH/PdTSPP+PSS/PAH/HTiNbO$_5$; (B) glass/PAH/PdTSPP+PSS/PAH/HTiNbO$_5$/PBV (blue - 480 nm; red - 600 nm).

The glass/PAH/PdTSPP+PSS/PAH/α-ZrP films, with and without PBV, were also monitored at 600 nm (data not shown). The ratios of the onset amplitudes between the triplet at 480 nm and the transient at 600 nm were ~5 for both samples. This is shown in Table 4.1. Although the triplet decay kinetics are altered by the adsorption of PBV, the nature of the quenching is unclear.

The addition of the electron acceptor, PBV, to the film did affect the triplet state lifetimes. A third component was introduced in order to fit the data, suggesting another decay pathway of the triplet state. This component was much longer-lived as compared to the films without PBV. The nature of this longer-lived species is unclear. It is longer than all of the films studied as well as PdTSPP in solution. The presence of the nanosheets in combination with PBV could provide higher stability for the triplet state, or it is possible that a charge separated or charge transfer state is formed that absorbs around 480 nm. Evidence suggesting charge transfer between the PdTSPP and PBV is the quenching of the triplet state, therefore the existence of the longer-lived species at 480 nm suggests that for at least a fraction of PdTSPP, the charge transfer is not occurring.

For the glass/PAH/PdTSPP+PSS/PAH/α-ZrP/PBV and glass/PAH/PdTSPP+PSS/PAH/$HTiNbO_5$/PBV samples, the largest contribution came from the shortest triplet state lifetime. This could be an indication of some charge transfer occurring since according to Mallouk and co-workers the PdTSPP quenching they observed occurred in ~2 μsec.[59] Although there is overlap of the reduced PBV absorbance band at 600 nm with the PdTSPP cation radical, the ratios between the onset amplitudes at 480 nm and 600 nm were compared. The ratio was similar for the α-ZrP

films with and without adding PBV (~5), while there was a difference in the ratio for the $HTiNbO_5$ films with (3) and without PBV (5). This difference could be an indication of charge transfer to the PBV, but this is clearly not conclusive.

4.4.6 Towards Understanding the Band-edge of the Layered Metal Oxide Semiconductor, $HTiNbO_5$

As discussed previously, the two types of spacers used in this investigation are inherently different. α-ZrP is an insulator and $HTiNbO_5$ is a semiconductor with its estimated conduction band edge just between the conduction band of the PdTSPP and poly(viologen), as shown in Figure 4.16. The preceding experiments displayed similar results after incorporating each type of nanosheet into the multilayer film architectures, which leads one to question the accuracy of the band diagram. $HTiNbO_5$ could be acting as a passive insulator instead of an active semiconductor.

One of the assumptions when calculating the $HTiNbO_5$ conduction band edge value was the point of zero charge. The effect of pH on semiconducting titanoniobates has been partially investigated as this is an important factor for incorporation into water-splitting systems.[144, 152-153] Kim et al. showed that several layered metal oxide sheets, including $KTiNbO_5$, showed a positive band edge shift upon proton exchange as well as a decrease in the band gap of these semiconducting nanoparticles, indicated by the red-shift in UV absorbance.[144]

To prepare the exfoliated nanosheets, the cation of the metal oxide (H^+ for $HTiNbO_5$) is exchanged with the bulky TBA^+ cation in order to separate the nanosheets

into a colloidal suspension. When the nanosheets are adsorbed to a positive surface, the TBA^+ cations are exchanged with the positive charges at the surface. If the nanosheets are not completely proton-exchanged, where all the metal oxide negative charges are not balanced by a proton, there is a shift in the value of the conduction band edge. The reported value used as the conduction band for $HTiNbO_5$ is for a fully proton-exchanged metal oxide. The conduction band of $HTiNbO_5$ of -0.66 V vs SCE, as described in Figure 4.16, would then sit at a more negative potential if the metal oxide was not completely proton exchanged; a position that would be less favorable for electron capture from the triplet state of PdTSPP. Fully exchanged metal oxides gave a pH value of 3-4 in water where the alkali metal forms ($KTiNbO_5$) gave a value of 8-9 in water.[144] It is highly unlikely that the band diagram as drawn in Figure 4.18 accurately represents this specific experiment, therefore it warrants further study of the pH effect on $HTiNbO_5$ in multilayer systems.

The effect of pH on the $HTiNbO_5$ layer was studied using transient ATR spectroscopy after exposing the nanosheets to HCl. A sample of glass/PAH/PdTSPP+PSS/PAH/$HTiNbO_5$ was made and secured into the ATR cell. The film was exposed to HCl vapor for 2 hours by injecting a low concentration of HCl into the flowcell.

Transient ATR curves of this sample at 480 nm without and with HCl vapor treatment are shown in Figure 4.22. The onset difference absorbance for the sample without HCl vapor treatment is almost 2 times higher than the sample with HCl vapor treatment. The film without HCl vapor treatment was fit to a 2^{nd} order exponential with

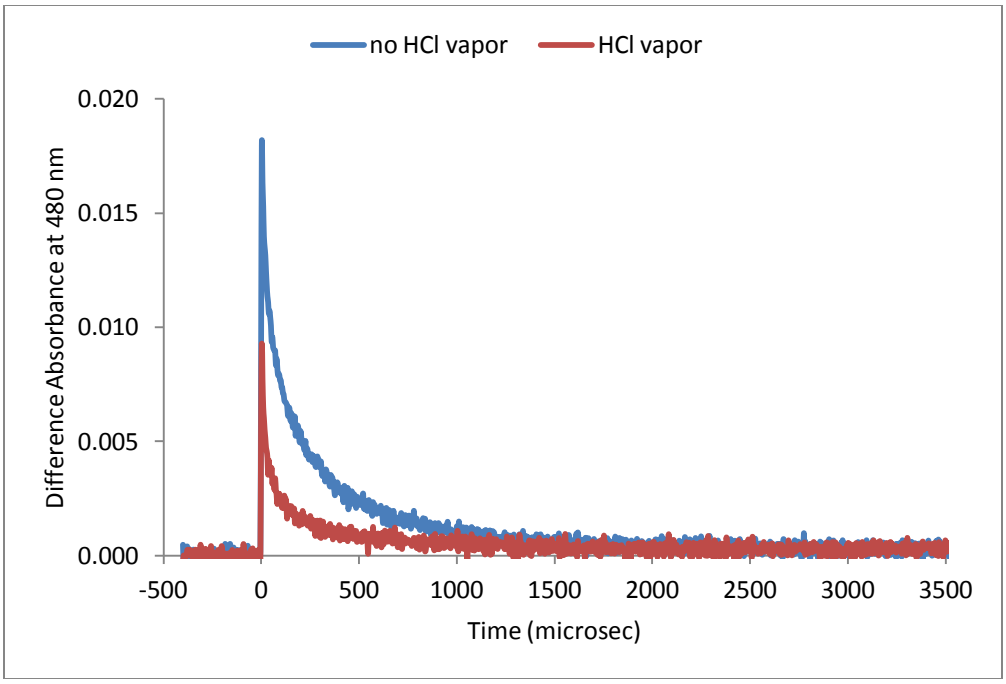

Figure 4.22 Transient ATR curves of glass/PAH/PdTSPP + PSS/PAH/HTiNbO$_5$ before (blue) and after exposure to HCl vapor (red). The difference absorbance was measured at 480 nm.

lifetimes of 35 μsec and 400 μsec with weighing factors of 0.49 and 0.51, respectively. The films with HCl vapor treatment were fit to a 3rd order exponential, with lifetimes of 5.6 μsec, 22 μsec, and 220 μsec with weighing factors of 0.33, 0.36, and 0.29, respectively. The additional component in the HCl treated films indicates another pathway for triplet decay, possibly as a result of charge injection to the $HTiNbO_5$. This long component is shorter than the glass/PAH/PdTSPP+PSS/PAH/$HTiNbO_5$ unexposed samples, where the longest components have been found to be 322 and 400 μsec. Clearly, there is a greater degree of quenching after exposure to HCl. Kaschak *et al.* reported the quenching of excited PdTSPP by a $HTiNbO_5$ layer in the absence of poly(viologen) since the semiconductor was aligned to accept electrons from the triplet state of the PdTSPP.[59] This, again, is not direct evidence of charge transfer, but it starts to define a more accurate view of the $HTiNbO_5$ role in the multilayer film.

A second series of films of glass/PAH/PdTSPP+PSS/PAH/$HTiNbO_5$/PBV were made and measured with transient ATR. One film was immersed in 100 mM HCl and rinsed with water (HPLC grade) prior to deposition of PBV. UV-Vis spectra were taken before soaking the film in 100 mM HCl and after immersion in 100 mM HCl and adsorption of PBV for 10 min. The spectra are displayed in Figure 4.23 and there is no evidence of appreciable desorption of the PdTSPP from the film.

Transient ATR decay curves at 480 nm were obtained for the film with and without HCl treatment and are shown in Figure 4.24. The onset difference absorbance of the HCl treated sample is 4.5 times lower than the sample that was not immersed in HCl. This is a significant amount of quenching of the triplet state. The untreated sample was

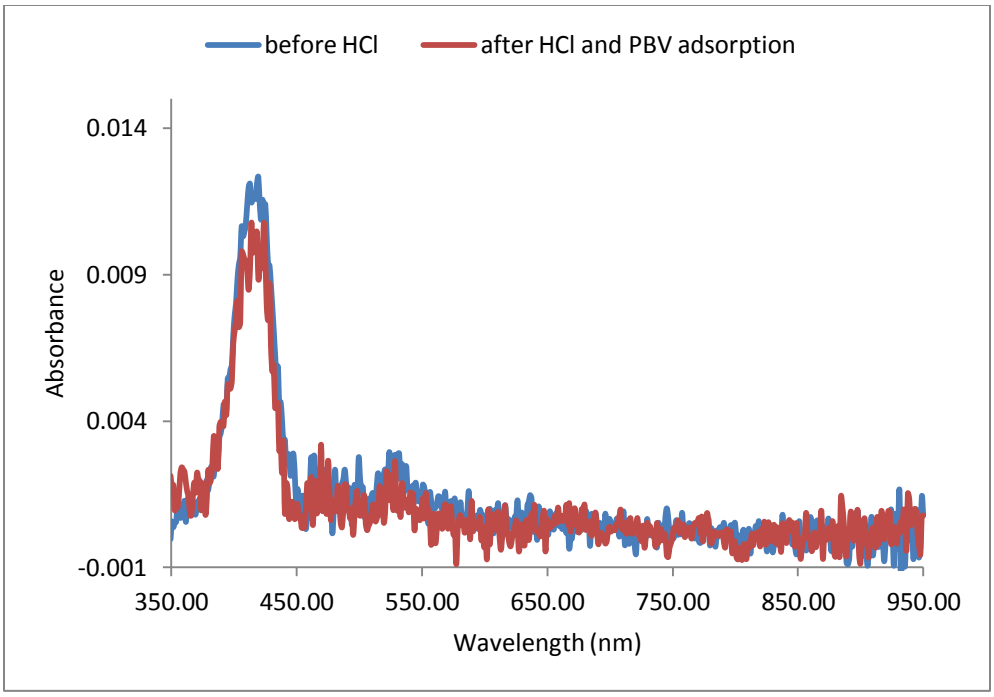

Figure 4.23 UV-Vis absorbance spectra of glass/PAH/PdTSPP + PSS/PAH/$HTiNbO_5$ (blue) and after (red) immersion in 100 mM HCl and deposition of PBV.

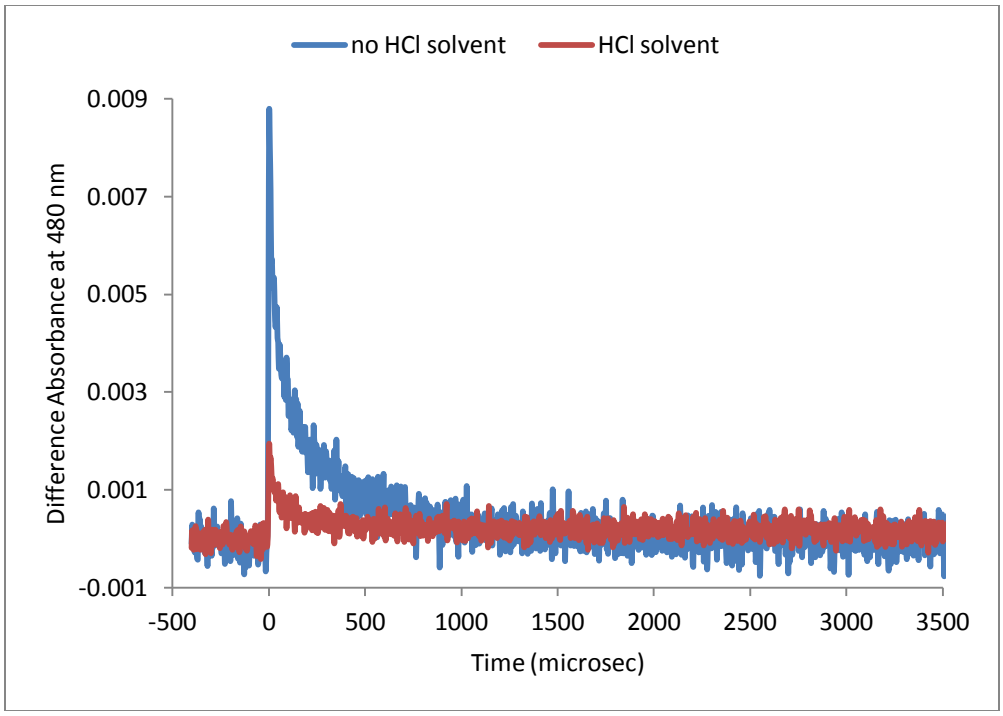

Figure 4.24 Transient ATR of glass/PAH/PdTSPP + PSS/PAH/HTiNbO$_5$/PBV before (blue) and after (red) exposure to 100 mM HCl. The difference absorbance was measured at 480 nm.

fit to a 3rd order exponential with lifetimes of 5.8 μsec, 75 μsec, and 480 μsec with weighing factors of 0.56, 0.26, and 0.18, respectively. The HCl treated sample was not fit, as the signal was too low. Qualitatively, there appears to be a long-lived component that does not decay back to zero. The difference in the onset amplitudes alone clearly shows that there is a quenching effect from the exposure to HCl.

In summary, in order to investigate the nature of the $HTiNbO_5$ and its effect on the electron transfer between PdTSPP and PBV, it was hypothesized from the previous experiments that the band edge diagram was not accurate. By increasing the pH of the film it was hypothesized that the $HTiNbO_5$ would align more favorably to the PdTSPP in order to accept electrons. Of course, the effect of changing the pH may also affect the other molecules in the multilayer, such as the PAH, PSS, and the PdTSPP. In order to improve our understanding of how semiconducting nanosheets can impact electron transfer, more studies would have to be performed to investigate the energy level alignments and the pH effects on the other molecules in the multilayer.

4.4.7 Conclusions

Although direct evidence of charge transfer was not obtained through these investigations, many important points about multilayer films were considered. The control experiments demonstrated that PdTSPP molecules incorporated into the multilayer films had different excited state lifetimes as compared to solution.[101] Alternative triplet decay pathways were introduced in the solid state thin film environment as evidenced by the multi-component exponential fits. Although it was

altered, the triplet state was sufficiently long lived to transfer a charge to the poly(viologen).[59]

The triplet state lifetime of the glass/PAH/PdTSPP + PSS sample was shorter-lived than the glass/PAH/PdTSPP + PSS/PAH sample indicating a stabilization of the triplet species, hypothesized to be caused by i) a lesser degree of aggregation of the PdTSPP in the film containing the terminal PAH; ii) increased intermolecular interactions between PdTSPP and PAH to aid in the triplet state stabilization; iii) a change in electron density around PdTSPP, from the additional PAH layer, stabilizing the triplet state. When the α-ZrP and $HTiNbO_5$ nanosheets were incorporated into the multilayer films (glass/PAH/PdTSPP + PSS/PAH/nanosheet), the triplet state lifetimes were further extended as compared to the glass/PAH/PdTSPP + PSS/PAH sample. Several reasons for this could be i) an even greater shift of the electron density around PdTSPP to stabilize the triplet state; ii) interaction of PdTSPP with the functional groups of the nanosheets, since the polymer layers are known to be "fuzzy"; iii) a degree of order within the film, favoring a longer-lived triplet state lifetime. In addition, the onset difference absorbance values with the nanosheets were larger than those with simply the terminal PAH group. The nanosheets may enhance the quantum efficiency of intersystem crossing, or even be changing the molar absorptivity of the PdTSPP triplet state.

Multilayer films were then constructed with the electron acceptor, PBV, and a longer-lived component of the PdTSPP triplet state was measured. In addition, the ratio between the onset amplitude of the triplet state and the cation radical for

glass/PAH/PdTSPP + PSS/PAH/$HTiNbO_5$ was higher than that for glass/PAH/PdTSPP + PSS/PAH/$HTiNbO_5$/PBV, which may be caused by charge transfer in the presence of PBV. The longer-lived component measured with the later films contradicts this charge transfer since the triplet state should be quenched, however this could be explained such that a fraction of PdTSPP triplet state may be unavailable for charge transfer, yet long-lived.

When the glass/PAH/PdTSPP + PSS/PAH/$HTiNbO_5$ sample was treated with HCl to alter the pH of the film, and compared to an untreated sample, a large decrease in the onset difference absorbance was observed, and an additional component was used to fit the HCl treated sample. Also, a large degree of triplet quenching was measured when HCl was used to alter the pH of glass/PAH/PdTSPP + PSS/PAH/$HTiNbO_5$/PBV. These are indications of an additional triplet decay pathway, possibly charge injection into $HTiNbO_5$, whose band edge may be favorably aligned between PdTSPP and PBV. This is not conclusive evidence since the HCl treatment could also alter other components in the multilayer film such as the PAH, PSS or PdTSPP.

Accurate values of semiconductor band edge positions are necessary when designing energy and electron transfer systems. The estimates from measurements on bulk samples and by calculation do not necessarily translate to multilayer thin films. The studies herein aimed to improve the understanding of the role nanosheets play in charge transfer. As with other solid-state molecular systems, the local molecular environment has an impact on the excited state species, and as a result, the charge transfer efficiency.

5. CONCLUSIONS AND FUTURE DIRECTIONS

5.1 Summary of Results

This research aimed to improve our fundamental understanding of charge and energy transfer across interfaces as a function of chemical and electronic properties. It has been shown that these properties play a role in the kinetics of charge transfer and ultimately affect efficiencies of organic solar cells such as OPVs and DSSCs.[18, 22, 55]

In order to investigate the photoinduced events in thin films and at interfaces, an innovative instrument was developed, coupling transient absorbance spectroscopy to attenuated total reflectance as described in Chapter 2. The photoinduced kinetics of bacteriorhodopsin thin films were measured. It was determined that a surface coverage of 1% of a monolayer could be detected with this geometry. The chemical nature of these films, containing positively charged polymers, did not significantly alter the kinetics of the conformational change of the chromophore in the protein.

The interface investigated in Chapter 3 was the molecular thin film/TCO interface which is relevant for organic devices, specifically organic based solar cells. Photoinduced excited state lifetimes of molecules in thin films directly affect charge transfer rates and are highly influenced by their molecular environment. Zinc porphyrins tethered to ITO were characterized and the excited states were investigated. The inability to observe excited state difference absorbance at these interfaces led to the study of zinc porphyrin monolayer and multilayer thin films to understand how the solid-state chemical environment may impact the lifetimes of the excited states. The control experiments,

conducted on solutions of ZnPA in the presence and absence charged polymers, led to the hypothesis that ZnPA in MES buffer (pH 5.5) was weakly aggregated in solution. In the absence of oxygen, these self-forming aggregates led to rapid triplet decay. The nature of this aggregation is not fully understood, but recent research by Kadish et al. have shown a interaction between the phosphoryl group and the zinc(II) ion (P=O···Zn) in zinc porphyrins with diethoxyphosphoryl ($P(O)(OEt)_2$)moieties.[118] The porphyrins are not identical nor is the solvent system, ZnPA is in MES buffer, pH 5.5, whereas zinc porphyrin with $P(O)(OEt)_2$ functional groups were in chloroform. The addition of positively charged PAH to the negatively charged ZnPA solution was hypothesized to disrupt this interaction. In the absence of oxygen, a longer-lived triplet state was observed. The chemical interaction between the amine functional group of the PAH and the phosphonic acid could also have led to stabilization of the triplet excited state in solution.

In solid state thin films, zinc porphyrin excited states were not observed with nanosecond resolution transient absorbance. Although the ground state recovery of a multilayer film was observed, from the UV-Vis spectrum a large population of porphyrin appears to be demetallated. Zinc porphyrin was then compared to palladium porphyrin (where the triplet state is observed in charged multilayer films) and it was hypothesized that singlet state quenching due to the aggregation is the dominant decay pathway for zinc porphyrins. The effects of aggregation and the local molecular environment are overriding factors for the excited state lifetimes of zinc porphyrins. This is relevant for

the efficiency of charge transfer at the molecular thin film/TCO interface and imperative for OPV and DSSC performance.

Excited state kinetics in multilayer films related to water splitting were studied in Chapter 4. The incorporation of 'passive' (α-ZrP) and 'active' ($HTiNbO_5$) spacers in the multilayer films was investigated to understand their role in the electron transfer from a photoexcited donor molecule (PdTSPP) to an electron acceptor (poly(viologen). The theoretical band edge diagram for the multilayer films proposed that $HTiNbO_5$ acts as an active spacer, with its conduction band edge positioned to accept an electron from PdTSPP and donate it to poly(viologen). The experimental evidence suggests that $HTiNbO_5$, as deposited, does not align energetically with the PdTSPP and poly(viologen). The position of the band-edge of $HTiNbO_5$ is dependent on the degree to which the negatively charged nanosheets are balanced by protons. The energetic alignment is assumed when $HTiNbO_5$ is fully protonated, but if the nanosheet is insufficiently protonated, the conduction band-edge would sit at a relatively more negative potential and injection from the PdTSPP triplet excited state would be unfavorable. The multilayer films were exposed to HCl vapor in order to lower the pH, upon which the PdTSPP triplet state was quenched, which would be expected for the representative band-edge diagram. This was inconclusive evidence of charge transfer, as an absorbance band assigned only to the reduced poly(viologen) was not observed.

As with the multilayer zinc porphyrin films studied in Chapter 3, the excited state lifetimes of PdTSPP were also affected by the electrostatics in the multilayer film. The

intersystem crossing efficiency (Q_{ISC}) of PdTSPP in solution is 1.0. The multilayer films may have decreased the Q_{ISC} as evidenced by quenching of the singlet state.

5.2 Future Directions

5.2.1 Charge Transfer from Palladium Porphyrin to ITO

As described in Chapter 3 the chemical question of interest was the role of properties such as molecular orientation, binding chemistries and electronic coupling in charge transfer at the molecular thin film/TCO interface. The model system constructed with zinc porphyrin films posed problems since the excited state lifetimes were significantly affected by molecular aggregation.

Palladium (Pd) porphyrin molecules incorporated into multilayer films, as described in Chapter 4, showed evidence of aggregation but retained relatively long-lived triplet state lifetimes from ~5 – 500 μsec, as detected by the Proteus transient ATR instrument. The sulfonate terminal groups of the Pd porphyrin molecules were negatively charged in water (HPLC grade). This allowed them to be readily deposited onto films of PAH, a positively charge polymer. The sulfonate groups do not bind strongly to metal oxides, therefore Pd(II)tetrakis(4-carboxyphenyl) porphyrin (PdTCPP) is proposed for the study of the molecular thin film/ITO interface. PdTCPP is commercially available from Frontier Scientific, Inc. (CAS: 94288-44-5). Pd porphyrins have been utilized as sensitive oxygen sensors since they have strong room temperature phosphorescence with a high quantum yield and long lifetime.[154] Amao *et al.* studied a

self-assembled film of PdTCPP prepared on an alumina plate. This film exhibited a high sensitivity to oxygen with little effects from aggregation.[155] Pd porphyrins have also been demonstrated as efficient triplet sensitizers in molecular motors due to their high quantum efficiency for intersystem crossing (~1.0) and long-lived triplet state lifetimes.[156] The band-edge diagram for the interface between ITO and a similar Pd porphyrin (Pd(II)5-(4-carboxyphenyl)-10,15,20-tris(4-methylphenyl) porphyrin) is shown in Figure 5.1.[108] The oxidation potential was taken from a cyclic voltammogram of Pd porphyrin in solution[108] and will likely be different in a thin film. These were converted from NHE to vacuum by adding 4.44 eV.[107] In order to achieve charge injection there must be a sufficiently large thermodynamic offset between the Pd porphyrin excited state and Fermi level of ITO. There is a ~0.7 eV difference between the singlet state and ITO, but only a ~0.25 eV difference for the triplet state. The thin film oxidation potentials should be determined for PdTCPP bound to ITO either with cyclic voltammetry or spectroelectrochemistry. This will provide a more accurate band-energy diagram at the PdTCPP/ITO interface. Spectroelectrochemical results will also provide the absorbance spectrum of the PdTCPP cation radical. The bands corresponding to the cation radical can then be monitored with transient absorbance to observe charge injection and recovery.

One of the difficulties in interpreting the results in Chapter 3 was the lack of control experiments to understand the effect of Zn porphyrin aggregation on the excited state species. PdTCPP is soluble in aprotic solvents such as dimethylformamide (DMF),

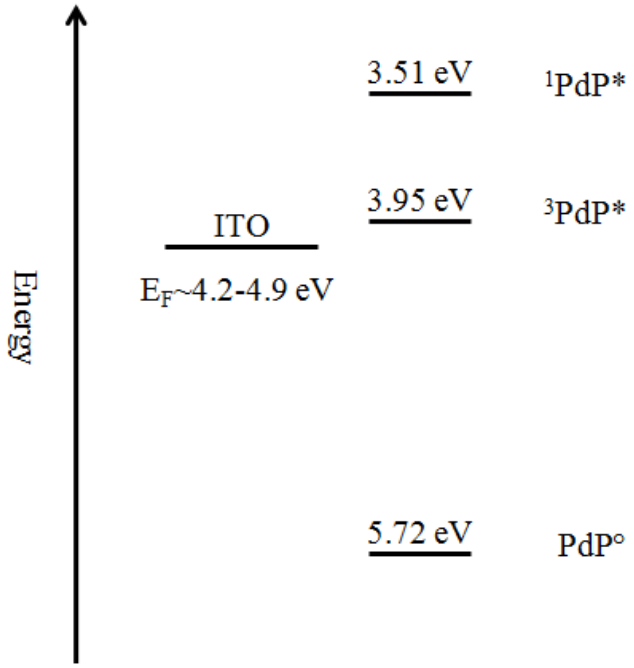

Figure 5.1 Band diagram of Pd porphyrin-ITO interface. Energy levels were converted from NHE to vacuum by 4.44 eV.[107]

and upon the addition of water has shown evidence of aggregation by the broadening of the Soret band and a decrease in the Soret peak intensities as compared to the Q bands.[97] For example, the ratio between the Soret band peak at 416 nm to the Q band peak at 522 nm, decreases by more than a factor of 2 in a 40:60 DMF:water solution.[97] When PdTCPP is incorporated into thin films, either adsorbed to positively charged polymers or bound to ITO, it will likely form aggregates. In order to investigate the effect of aggregation on the excited state species, control experiments should be conducted in solutions which exhibit varying degrees of PdTCPP aggregation. UV-Vis absorbance measurements can verify aggregation by the ratio of the Soret to Q band. Solution transient absorbance experiments can be conducted with the Proteus and the EOS/HELIOS transient instruments. In addition to the excited state lifetimes, the onset difference absorbance should be noted as it corresponds to the efficiency of populating the excited state. The EOS/HELIOS instrument can be used for these solutions to map the entire spectrum by monitoring the decay and recovery of the ground state and the triplet state on shorter timescales. The pathlength of the standard experiment in the EOS/HELIOS is 2 mm which would require a relatively high concentration of PdTCPP. Higher concentrations might add to the aggregation effects and should be considered when planning the experiments. The Proteus transient absorbance instrument typically operates with a pathlength of 1 cm for both the monitoring and excitation beams, but a 1-2 mm pathlength for the monitoring source while maintaining a 1 cm interaction path for the excitation beam, has yielded sufficient transient signals. PdTCPP in the ground state absorbs at 416 nm (Soret) and 522 nm (Q band),[97] so excitation at 532 nm with the

Nd:YAG Continuum laser should be adequate for the Proteus transient absorbance experiments. The samples should be deoxygenated either by purging with Ar or with the freeze-pump- thaw method, as the triplet state is sensitive to oxygen quenching. The triplet state of PdTCPP absorbs from 460-480 nm as well as at 720 and 850 nm.[97] In solutions of PdTCPP in DMF-water, where aggregation was observed, phosphorescence was significantly quenched.[97] Therefore it is expected that aggregation will alter the excited state lifetimes. Additionally, control experiments in solution should also be conducted of PdTCPP with PAH and PSS.

Films of PdTCPP adsorbed to PAH-coated glass slides should be investigated with transient absorbance prior to conducting transient absorbance experiments at the PdTCPP/ ITO interface. The construction of thin films of porphyrins on PAH is discussed in detail in Chapter 3 and 4. ATR spectroscopy can be used to determine the surface coverage and molecular orientation. The guidelines for sensitivity as described in Chapter 3 can be followed to obtain a high enough surface coverage of PdTCPP to conduct transient experiments in the ATR configuration. These films can also be used to test a second generation transient ATR instrument with the femtosecond EOS/HELIOS Ultrafast System.

The optimal surface coverage found for PdTCPP thin films on PAH should be used as a guideline for adsorption of PdTCPP on ITO. In addition, the band-energy diagram derived from thin film cyclic voltammetry or spectroelectrochemistry will provide insight to the thermodynamics of the interface. If the ITO Fermi level has a lower energy vs. vacuum as compared to the PdTCPP singlet and triplet states, electron

transfer from the excited states is highly unfavorable. Since ITO is a conductive metal oxide, it is possible that when ITO is at open circuit charge transfer from the PdTCPP excited states may occur on timescales too fast to observe with the Proteus instrument. Constructing an ATR transient configuration with the EOS/HELIOS instrument and testing with PdTCPP films will allow for detection of the short lived excited states as well as the full transient spectrum, as opposed to just the decay at a single wavelength with the Proteus instrument. Rapid intersystem crossing from the PdTCPP singlet to the triplet excited state will hopefully stabilize the excited state and aide in the ability to monitor charge injection into ITO. As with the solution experiments, the thin films of PdTCPP should be purged with Argon prior to conducting transient experiments, as the triplet state is sensitive to oxygen quenching. Controlling the potential of the ITO in these experiments is hypothesized to alter the driving force for charge transfer and recombination, as has been demonstrated with other porphyrin molecules bound to SnO_2 materials.[108] Positioning the energy of ITO at potentials where triplet state electron injection is favored or hindered may provide insight to the chemical nature of the interface.

After it has been confirmed that charge transfer is occurring, or that the triplet state plays a key role in the charge transfer, more geometries of Pd porphyrins can be investigated to understand the role of orientation or chemistry of the binding groups in the charge transfer to metal oxides.

5.2.2 Controlling the Architecture of Molecular Films

Although ATR spectroscopy has the ability to monitor changes in absorbance in both the TE and TM polarizations, ideally, molecular films with a narrow distribution of orientations should be created in order to understand the role of orientation in charge transfer and recombination kinetics. There have been many strategies used to control the molecular orientation, which as a result, can also influence the molecular aggregation properties.[44, 157-158] It is proposed that these approaches should be utilized to study the molecular thin film/TCO interface to understand the role on charge transfer kinetics.

Galoppini and co-workers studied several zinc porphyrin derivatives tethered metal oxide films and to TiO_2 nanorods.[48, 159-160] Aggregation was evident for the ZnTCPP bound to the metal oxide surface when the carboxylic acid functional groups were in the *para* position on the phenyl ring, denoted at *p*-ZnTCPP. However, when the carboxylic acid functional groups were in the *meta* position (*m*-ZnTCPP), allowing for a spider-like attachment to the metal oxide, aggregation was not detected.[160] The structures of the ZnTCPP molecules and their anticipated attachment chemistries are shown in Figure 5.2. The zinc porphyrins molecules with the geometry for spider-like binding were investigated tethered to TiO_2 nanorods and they exhibited a higher photoresponse, suggesting that the geometry plays a role in efficiency of charge injection.[48]

The synthesis of the porphyrin molecules is discussed in detail by Bonar-Law *et al.*[161] and Galoppini and co-workers.[160] To further investigate the charge injection and charge recombination rates at the molecular thin film/ITO interface, these spider-like porphyrins could be synthesized with palladium as the central metal and compared to the

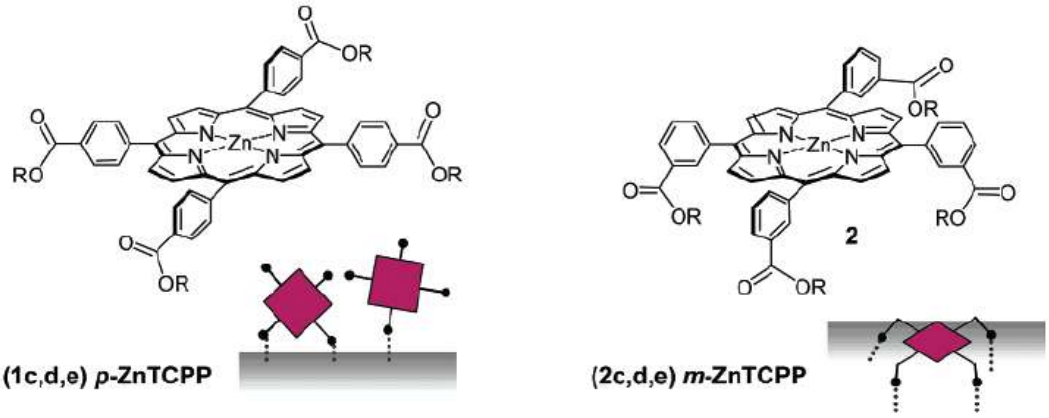

Figure 5.2 Molecular structures of *p*-ZnTCPP and *m*-ZnTCPP and their anticipated binding geometries to metal oxides. Reprinted from ref. 160. Used with permission from the American Chemical Society.

results obtained from the experiments outlined in 5.2.1. Steady state ATR measurements in TE and TM polarizations can verify the orientation and surface coverage of the molecular films on ITO. Spectroelectrochemistry and thin film cyclic voltammetry can be used to understand the band-edge diagram of the molecular thin film/ITO interface. The spectrum of the cation radical can be determined with spectroelectrochemistry. These can then be compared to the *p*-PdTCPP films described in 5.2.1.

Transient experiments can be conducted in solution and thin films, utilizing the ATR geometry. This has the potential to enhance our understanding of the role of orientation in charge transfer at the molecular thin film/TCO interface.

APPENDIX A: OPERATION OF TRANSIENT ATR INSTRUMENT

A brief description of the transient ATR instrument is provided in Chapter 2 and illustrated in Figure 2.1. This appendix serves as a reference for the components and the operation of the instrument.

A.1 Light Sources

The transient absorbance experiment utilizes two light sources, a high energy pulsed pump beam and a monitoring beam with a continuous output. The pump beam is a Nd:YAG (Continuum) laser with a wavelength output of 532 nm or 355 nm and a 5-7 ns pulse width at 10 Hz. Another option is to use the Nd:YAG as the excitation for the Dye Laser (Continuum), where the wavelengths of emission from a particular dye are utilized. The diffraction grating within the dye laser is fixed at ~565 nm and must be reconfigured for manual operation in order access different wavelengths. The monitoring beam is either a 150 W Xe lamp (Newport) coupled to a monochromator (Newport) or an Ar-Kr tunable continuous wave laser (CVI Mellos Griot).

A.1.1 Continuum Nd:YAG Laser

The main components of the Nd:YAG laser are the water circulator, power supply (Figure A.1), laser head including the operation pad (Figure A.2), the optics (Figure A.3) and flash lamp. The operational directions are listed below:

Starting the laser:

1) Make sure all electrical equipment in the area is turned off. Including computers, monitors, etc.
2) Plug in and turn on water circulator. It should be set to 14°C. Allow the water to get to that temperature. This water cools the power supply.
3) Plug in the Power supply, flip circuit breaker on power supply
4) Make sure the conductivity light is green. If this is not green it means that the DI water circulating in the laser head needs to be replaced. Allow for ~10 min for light to go from red to green.
5) Flip the red switch on power supply to "on"
6) Turn the key to "Laser On"
7) Put on laser goggles and make sure all the curtains are closed
8) The 532 nm laser line comes out of the middle of the 3 openings of the laser head, make sure the knob is in the down position so that it is closed. The covering of the laser head can be off or on at this point. The flash lamp covering must be in place before firing and warming up the laser

Figure A.1 Power supply and operation pad for Nd:YAG laser.

Warming up the Laser: Put on laser goggles

1) Press Auto/Manual, should display "Flash only – Prgm 1"
2) Press Start: The laser should charge up and begin flashing. Allow 30 minutes for flash lamp in the laser to arrive at the operating temperature
3) If testing the alignment continue to that section – otherwise proceed to directions for conducting a transient experiment

Testing the alignment of the laser:

1) It is very important to observe the spot quality using the burn paper at the exit of the flash lamp, after amplification, after leaving the laser head and after the beam has reflected off of the beam splitter. The beam dump should be in place at this time after the exit of the laser.
2) Put a piece of burn paper in a plastic Ziploc bag. Make sure to be wearing the laser goggles! Open the middle shutter by lifting the middle knob, at this point the covering on the laser head should be open.
3) Press Stop on the operation pad
4) In order to fire a single shot to make a burn: Use program up or program down button to select "program 2, single shot"; Press the **a**ctivate button; press the shutter button to open the shutter (should light up green); press the Q-switch button to turn on Q-switch (should light up red); press start to load program.
5) Place burn paper perpendicular to laser path (yellow slots below) and press fire. The burn spot should be symmetrical and circular: if it is not, double check to make sure the paper is perpendicular. Test first the output after the flashlamp

(right side of Figure A.3), both as a forward and back burn. Second, test after the beam has been amplified (left side of Figure A.3), again with a forward and back burn.

6) Take a burn after the laser beam has left the laser head
7) Take another burn after the beamsplitter
8) Log these burn spots in the log book.
9) If the burn spot after the amplification is not symmetrical/and the power is not high, the coupling prism can be rotated by using the 1 left rotation button or 1 right rotation button on the operation pad

Measuring the power of the laser and operating the transient instrument:

1) The continuous pulsing program should be activated
2) If the Q-switch is on, press the Q-switch button to disable. Press the The laser should still be charging and the flash lamp firing. Use program up or program down button to select "program 3, f/1"; press the activate button and start button. Press the Q-switch button to begin firing.
3) To turn off, press the Q-switch button again. This will keep the laser head and flash lamp at the proper temperature for uniform laser pulses. If the stop button is pressed instead, the start button should be pressed soon after to keep the laser firing
4) The power meter should be placed in the line of the reflection of the beamsplitter. The infrared portion of the laser beam will probably strip away any coatings and cause a crackling sound.

Figure A.2 Nd:YAG laser head optics and beamsplitter.

Operation of the laser for the Flash photolysis instrument:

1) Turn on the laser and warm up the flash lamp for 30 minutes as instructed previously. The beam quality should be checked at least once a week.
2) Set the program to "program 3/f/1"
3) Follow the Operation Instructions for the Ultrafast Flash Photolysis Instrument

The optimal operational output of the Nd:YAG at 532 nm is 350 mJ which is much more than is needed for these experiments. Once the laser pulse exits the laser head, it encounters a 1% beam splitter (CVI Mellos Griot) which directs the pump at 90° while the majority of the laser power passes through the beam splitter into a beam dump. The light is then directed with mirrors through an iris, followed by a slow shutter. The laser beam then interacts with a glass microscope slide to reflect a small portion of the beam into a diode to accurately monitor the timing of the pulse. The rest of the light is transmitted through the slide and passes through the cuvet sample holder.

For use of the instrument in the ATR geometry a flip mirror is engaged after the microscope slide to reflect the entire beam through a focusing lenses, (f/4) and into the end of a bifurcated optical fiber.

A.1.2 Continuum Dye Laser

The dye laser has two main components, the optical setup and the pump for circulating the dye into the laser head. The optical setup is mounted in front of the Nd:YAG laser. There are two reservoirs, the oscillator and amplifier, for the laser dye

solution and they require different concentrations. The manual provides the required concentrations. Rhodamine 590 was used in the experiments as it emits around the 565 nm wavelength corresponding to the fixed diffraction grating. Rhodamine 590 was dissolved in HPLC grade methanol at 50 ug/L for the oscillator and 100 ug/L for the amplifier. This dye is changed periodically in order to maintain the correct concentrations. If the dye is too concentrated flowing through laser optics, there is the potential to burn and damage the optics.

A.1.3 Xe Lamp

Operation of the Newport Xe lamp

SSS lab - Flash Photolysis Instrument; June 2010; AMS

Lamp – 150W Xe, Ozone Free, #6255

Housing – Single Element Fused Silica Asphere, F/1, Collimated, 50 – 500W, #67005

Power Supply – Universal Arc Lamp, 50 – 200W; #69907

Setup

Turn on the power supply

Press “SETUP” button

- SET MODE (option of CURRENT or POWER), choose POWER using the up or down arrows, press “SET/ENTER” to select, press “DISPLAY/SELECT” to move to next

- SET LIMIT – ranges are 40-300 WATTS or 1.5-12.0 AMPS; for Xe lamp #6522, the operating range is 120 -165 W. Set the limit to 165 W using the up and down arrows, press “SET/ENTER” to select, press “DISPLAY/SELECT” to move to next

- MEMORY – can ignore for now, press “DISPLAY/SELECT” to move to next

- HRS RESET – only need to change this when Xe lamp is replaced, press “DISPLAY/SELECT” to move back to SET MODE

- Press “SETUP” to exit

Operation if Setup is complete:

1) Turn on power supply (POWER mode light should be on)

2) Press and hold the “SET/ENTER” button, until display reads preset watts with the least significant digit blinking. Change the value with the up, down, right and left arrows to set to 150 W. Press “SET/ENTER” to save and exit

3) The display should read 0 W

4) Press the “LAMP START” button. The igniter will fire for ~ 5 sec. until the lamp reaches the pre-set value. Once reached, the “LAMP ON” light will be on. To scroll through and view current, voltage, watts or lamp operating time, press “DISPLAY/SELECT”.

5) To change the operating power with the lamp on, press “SET/ENTER” and use the up, down, right, and left arrows. The change will be immediate without pressing the “SET/ENTER” button to exit.

6) To shut down the lamp, press the “LAMP OFF” button. Once the output reaches 0 W, the “LAMP ON” light will turn off. Allow 20 minutes before turning off the power supply so the lamp can cool.

The lamp is positioned at the entrance of the monochromator. The light passes through a slow shutter and a fast shutter before reaching the monochromator. The shutters are not imperative for the experiment, but they do prevent excess light from

interacting and prematurely degrading the samples. The slit widths of the monochromator are set at the maximum, 3 mm, and they can be adjusted with the manual micromanipulator. The wavelength is selected through the Proteus computer program.

After exiting the monochromator the light interacts with a 4x objective telescope lenses attached to the exit slit. The light passes through a focusing lenses (f/#) and is focused into the center of the cuvet sample holder. The diverging light and is sent through a collimating lenses, followed by a focusing lenses to direct it into the end of an optical fiber. A core optical fiber is used to send the light to the silicon diode detector when conducting solution transient experiments. The light is coupled into a bifurcated optical fiber for the ATR geometry.

The end of the bifurcated optical fiber is coupled with an adaptor to a core fiber and is connected to the SMA connection in the commercial ATR instrument (SIS-5000). The light passes through a focusing lenses and a polarizer before coupling into the ATR element.

A.2 ATR Coupling and Operation of SIS-5000

The flowcells for this ATR instrument have been described in detail elsewhere (Chapter 2 and 3). For the initial testing of the instrument, the light was coupled into the waveguide via the polished edges of the 200 micron thick coverslip. Other experiments utilized prism coupling which can allow light to be coupled into microscope slides and coverslips.

The SIS-5000 is turned on first by switching on the circuit breaker on the back of the instrument and then turning on the switch on the front side. The computer program "SPR4000" is used to operate the translation stage, goniometers and to record the light intensities via the internal CCD camera. There are 2 lamps associated with the SIS-5000, a halogen lamp that sits outside of the instrument and a Xe lamp that is inside the body of the instrument. There are two CCD cameras in the instrument, one that operates from 180 – 750 nm and the other from 350 – 1000 nm. The light path through the instrument is from the lamp, through an optical fiber connected to an SMA connector that is mounted on the goniometer arm, through an aperature, focusing lens, and polarizer and then incident on the prism or polished slide edge. The light then is coupled down the waveguide, exits through the prism and is coupled into the end of an optical fiber via a focusing lens.

After the flowcell is mounted on the x-y translational stage the first step is to move the stage and prism in good alignment with the incident light by adjusting the translational stage and the angle of the input light goniometer arm. When good coupling is achieved by eye, then the output light goniometer arm is adjusted and the light intensity can be observed in real time with the CCD camera. The parameters for light collection and output are adjustable, typically I use 20 ms acquisition time and boxing of 1.

A.3 Transient Data Acquisition

When there is good alignment through the waveguide as determined by using the SIS-5000, the optical fibers are changed as indicated above. The wavelength is selected

on the Proteus software and the shutter is opened. The amount of light reaching the photodiode of the Proteus instrument can be current amplified with the variable gain current amplifier. For a transient ATR experiment with the Xe lamp a gain of 10^6 – 10^9 is needed, depending on the sample and wavelength. The cover on the SIS-5000 is closed. The shutter is closed by pressing Diode Align. Select the parameters of the experiment and press Data Acquisition. The signal will acquire on the oscilloscope and after the experiment is complete it will convert the data to a difference absorbance decay and transfer it to the computer interface.

Evaluating the data is discussed in Appendix B.2.

APPENDIX B: OPERATION OF HELIOS AND EOS TRANSIENT ABSORBANCE INSTRUMENT

B.1 Operation of Eos/Helios

1) Turn on the Mai-Tai laser and Topas as directed
2) Turn on the computer and open the EOS program & select VIS
3) Turn the key fully to the right on the light source (black box on shelf: labeled Ultrafast Systems). Wait until the yellow laser light stops blinking (if it doesn't blink at all, turn the key to off then back on) and press the laser start/stop button. Allow the laser to warm up for 5 min.
4) Turn on the timing box (pendulum). It should be set to monitor the interval between channel A (pump) and channel B (probe). The yellow lights above both of these channels inputs should be on. If channel B is not on – use a card to observe the white light coming out of the fiber output on the optical bench. If no light is coming out make sure the computer is turned on and the program is opened. Then observe the white light that is split off at the fiber output in the direction of another SMA /fiber connection. If the white light is not hitting the fiber properly the yellow light for channel B will not be illuminated. Also make sure the numbers are changing on the panel, if it is stuck press the decimal button [·] = HOLD button. Use the x-y-z adjustments to focus the beam into the fiber.

5) Fill the cuvette with sample, add stir bar and place in sample holder. Turn on the magnetic stirrer and make sure it is not in the path of the beam.

6) For the EOS system the interference filters need to be flipped down (not in the light path) – there are 2 of them located in the probe beam line (one in the reference beam path and one in the signal beam path)

7) There is an additional flip mirror that is used in the Helios system that should also be flipped down – this mirror is located to the right of the small sapphire white light continuum generator

8) On the EOS computer program, open the "Monitor Probe" tab. The red trace is the reference channel, the white trace is the signal channel. Adjust the neutral density filters in each of the light paths and the x-y-z stage of the SMA mounts (optical fiber inputs) to obtain the white light profile following the parameters:

   a. the signal be high without saturating the detector

   b. the shape of the white light to be uniform over the wavelength range

   c. the reference and signal overlap or look similar

9) Block the probe beam before the beam splitter, blocking both the reference and signal, and press "Correct Dark Noise"

10) Exit out of the "Monitor Probe" tab

11) Have a look at the pump laser beam – after it enters the optical box it goes through a neutral density filter and then a chopper. Hold up a card to the left of the chopper to observe the shape of the beam - it should look a normal laser

beam with the brightest point in the center. If it is brighter on the edges, the chopper is blocking the light path. Use a tool (twist-tie) to slide the panels of the chopper so the beam is not blocked.

12) Follow the pump laser beam and adjust the overlap of the pump and probe beam using the 2 tip-tilt mirrors in the laser beam path – one just before the beam passes over the beam-splitter and the other to the right. It might help to adjust the amount of laser light with the initial neutral density filter (in the far top right corner of the optical box where the laser beams enter)

    The goal of overlapping these beams is to have them converge in the center of the cuvet as shown in Figure B.2.

13) Press "Adjust Overlap" and select "continuous" in the top right corner of the screen to monitor the transient spectrum. There are several reasons why you might not see a transient.

    a. The delay time that is selected does not give a short enough time scale – look at the "pendulum" timing box – the actual delay time read off that screen should be in the 100s of nanoseconds. If it is not – change the delay time on the computer interface slightly so the number on the timing box is in the 100s of nanoseconds.

    b. The pump and probe beams might not be properly overlapping – try adjusting this with the directions from step #12 – again it will help to have the initial neutral density filter completely open

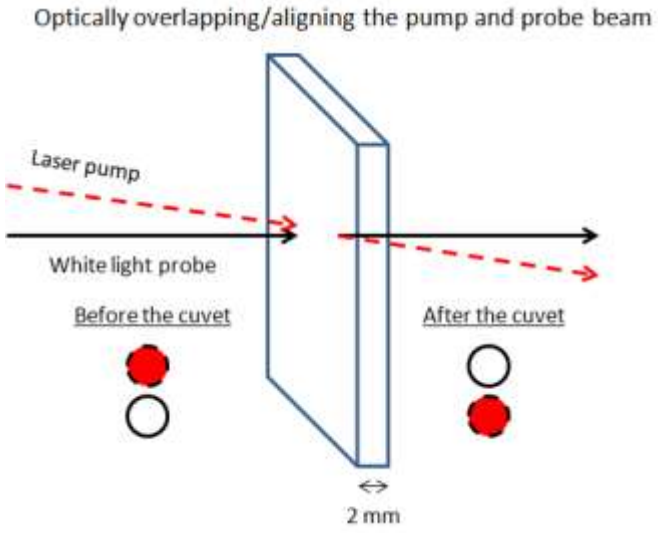

Figure B.1 Optical overlap/aligning the pump and probe beam.

c. For longer time scales (using 4 Hz rep rate of the laser, you might not see a transient spectrum)

d. The sample does not have a transient

14) Once a good preliminary transient spectrum is obtained – press the continuous button and exit the Adjust overlap screen.

15) Press the set time scale button. Select appropriate values for Time window, number of points and initial time resolution and press OK.

16) Press "Start DAQ" and name the file and click ok

a. The experiment will run for the defaulted amount of time, unless this is changed. You can always stop the collection of the data at any time.

b. In the ΔA spectrum window, you can move the red vertical cursor to the wavelength of interest and observe a transient curve in the ΔA kinetic profile window

c. In the ΔA kinetic profile window, you can move the red vertical cursor to see the different time points reflected in the ΔA spectrum

d. The Sample (log)/timepoint window is a histogram of each delay time that is being collected. The default setting is "Auto", if you would like to collect more points at a specific time range, set the delay control to "Manual" and drag the red cursor to the areas that you would like to collect more points. Make sure to switch this back to "Auto" if you step away from data collection.

17) When finished with data acquisition, press “Stop DAQ” and fill out the experimental details

18) When completely finished with all experiments

    a. Close the program

    b. Turn the key on the white light source all the way to the left

    c. Shut down the computer

    d. Place cover back on optical box

Moving to different time scales:

If you need to use a different time scale for the experiment – first change the rep rate of the Mai-Tai laser, and the EOS program must be turned off and re-opened to adjust to the new settings

B.2 Surface Xplorer (evaluation of data)

1) Open the Surface Xplorer program – allow it a couple seconds to load. From the “DynamicSurface (3D)” drop down menu select open new 3D data.
2) Make sure the correct time units are displayed in the top right window, if you need to change these, select the “Kinetics” drop down menu and select “Time Units..” select the right time unit using the down button and click ok.

3) You can drag the vertical and horizontal cursors around these windows as you could in the EOS program. Choose the wavelength you want to see the transient for in the top right window.
4) To fit this curve select the “Kinetics” drop down menu and choose “Fit Kinetic”
    a. Choose the number of exponentials and if you would like to use Ainf and press the button “Fit”
    b. To save this information press the “save” button
    c. Try other number of exps and selecting/deselecting Ainf
    d. Once the data is saved it will be converted to a CSV file that can be opened in Excel or other computer program. I recommend to save at least one fit – even if it looks like a improper fit, just to open it in another program

APPENDIX C: CHARACTERIZATION OF HEAD-GROUP POLYMERIZABLE LIPIDS

The evaluation of a new group of polymerizable lipids with the functional moieties in the head region is described herein.

C.1 Analytical Procedures

Preparation of lipid vesicles: The lipids were stored in chloroform and dried under flowing Ar, followed by vacuum drying for four hours. The lipids were then resuspended in nanopure water (obtained from a Barnstaed Nanopure system with measured of 18 MΩ·cm or higher) at a concentration of 0.5 mg/mL. The solution was vortexed several times and ultrasonicated (Branson Sonifier 450) for one minute. The solutions underwent 10 freeze thaw cycles (-78 ^{o}C, rt, 65 ^{o}C) and then were extruded through Millipore membrane filters three times each in decreasing succession: 600 nm, 400 nm, and 200 nm.

Polymerization conditions: The lipid vesicles were exposed to redox initiators (potassium persulfate and sodium bisulfate) for 8 hours under stirring and a steady flow of Ar.

Characterization of lipid vesicle stability: The distribution of vesicles sizes and stability to surfactant was determined with Viscotek Dynamic Light Scattering. Triton X-100 was added to the vesicle solution incrementally and the average sizes of the vesicles were recorded.

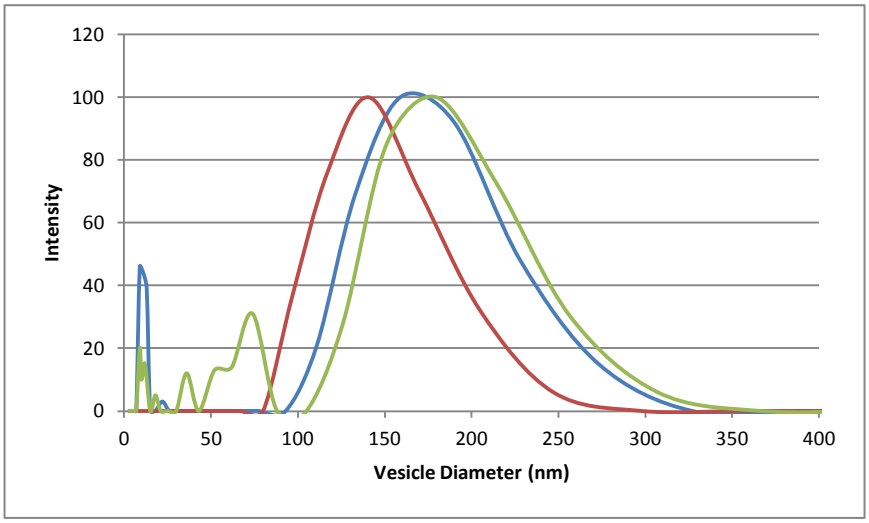

Figure C.1 Vesicle Size Shown by Light Scattering (blue = Sample #1, red = Sample #2, green = Sample #3)

Figure C.2 Stability of Vesicles to detergent Triton X-100 (Blue Circles = Unpolymerized Control Vesicles, Red Boxes = Redox Treated Vesicles)

C.3 Results

It was found that these lipids were unable form stable structure upon application of polymerization treatment conditions. The interactions between the lipid molecules were disrupted by the Triton X-100 surfactant.

REFERENCES

1. Graetzel, M.; Janssen, R. A. J.; Mitzi, D. B.; Sargent, E. H., Materials interface engineering for solution-processed photovoltaics. *Nature* **2012,** 488, (7411), 304-312.

2. www.eia.gov.

3. Hoffert, M. I.; Caldeira, K.; Jain, A. K.; Haites, E. F.; Harvey, L. D. D.; Potter, S. D.; Schlesinger, M. E.; Schneider, S. H.; Watts, R. G.; Wigley, T. M. L.; Wuebbles, D. J., Energy implications of future stabilization of atmospheric CO2 content. *Nature* **1998,** 395, (6705), 881-884.

4. Caldeira, K.; Jain, A. K.; Hoffert, M. I., Climate Sensitivity Uncertainty and the Need for Energy without CO2 Emission. *Science* **2003,** 299, (5615), 2052-2054.

5. Ardo, S.; Meyer, G. J., Photodriven heterogeneous charge transfer with transition-metal compounds anchored to TiO2 semiconductor surfaces. *Chemical Society Reviews* **2009,** 38, (1), 115-164.

6. Becquerel, E., Mémoire sur les effets électriques produits sous l'influence des rayons solaires. *Comptes rendus de l'Académie des sciences* **1839,** 9, 561-567.

7. Chapin, D. M.; Fuller, C. S.; Pearson, G. L., A New Silicon P-N Junction Photocell for Converting Solar Radiation into Electrical Power. *Journal of Applied Physics* **1954,** 25, (5), 676-677.

8. Gratzel, M., Photoelectrochemical cells. *Nature* **2001,** 414, (6861), 338-344.

9. Hegedus, S., Thin film solar modules: the low cost, high throughput and versatile alternative to Si wafers. *Progress in Photovoltaics: Research and Applications* **2006,** 14, (5), 393-411.

10. Ramanathan, K.; Contreras, M. A.; Perkins, C. L.; Asher, S.; Hasoon, F. S.; Keane, J.; Young, D.; Romero, M.; Metzger, W.; Noufi, R.; Ward, J.; Duda, A.,

Properties of 19.2% efficiency ZnO/CdS/CuInGaSe2 thin-film solar cells. *Progress in Photovoltaics: Research and Applications* **2003,** 11, (4), 225-230.

11. Tang, C. W., Two-layer organic photovoltaic cell. *Applied Physics Letters* **1986,** 48, (2), 183-185.

12. Kippelen, B.; Bredas, J.-L., Organic photovoltaics. *Energy & Environmental Science* **2009,** 2, (3), 251-261.

13. Green, M. A.; Emery, K.; Hishikawa, Y.; Warta, W., Solar cell efficiency tables (version 37). *Progress in Photovoltaics: Research and Applications* **2011,** 19, (1), 84-92.

14. Service, R. F., Outlook Brightens for Plastic Solar Cells. *Science* **2011,** 332, (6027), 293.

15. Nelson, J., Polymer:fullerene bulk heterojunction solar cells. *Materials Today* **2011,** 14, (10), 462-470.

16. Hwang, J.; Wan, A.; Kahn, A., Energetics of metal–organic interfaces: New experiments and assessment of the field. *Materials Science and Engineering: R: Reports* **2009,** 64, (1–2), 1-31.

17. Koch, N., Organic Electronic Devices and Their Functional Interfaces. *ChemPhysChem* **2007,** 8, (10), 1438-1455.

18. Ratcliff, E. L.; Zacher, B.; Armstrong, N. R., Selective Interlayers and Contacts in Organic Photovoltaic Cells. *The Journal of Physical Chemistry Letters* **2011,** 2, (11), 1337-1350.

19. O'Regan, B.; Gratzel, M., A low-cost, high-efficiency solar cell based on dye-sensitized colloidal TiO2 films. *Nature* **1991,** 353, (6346), 737-740.

20. Chiba, Y.; Islam, A.; Watanabe, Y.; Komiya, R.; Koide, N.; Han, L., Dye-Sensitized Solar Cells with Conversion Efficiency of 11.1%. *Japanese Journal of Applied Physics* **2006,** 45, (25), L638-L640.

21. Yella, A.; Lee, H.-W.; Tsao, H. N.; Yi, C.; Chandiran, A. K.; Nazeeruddin, M. K.; Diau, E. W.-G.; Yeh, C.-Y.; Zakeeruddin, S. M.; Grätzel, M., Porphyrin-Sensitized Solar Cells with Cobalt (II/III)–Based Redox Electrolyte Exceed 12 Percent Efficiency. *Science* **2011,** 334, (6056), 629-634.

22. Listorti, A.; O'Regan, B.; Durrant, J. R., Electron Transfer Dynamics in Dye-Sensitized Solar Cells. *Chemistry of Materials* **2011,** 23, (15), 3381-3399.

23. Nazeeruddin, M. K.; Baranoff, E.; Grätzel, M., Dye-sensitized solar cells: A brief overview. *Solar Energy* **2011,** 85, (6), 1172-1178.

24. Feldt, S. M.; Gibson, E. A.; Gabrielsson, E.; Sun, L.; Boschloo, G.; Hagfeldt, A., Design of Organic Dyes and Cobalt Polypyridine Redox Mediators for High-Efficiency Dye-Sensitized Solar Cells. *Journal of the American Chemical Society* **2010,** 132, (46), 16714-16724.

25. Yum, J.-H.; Baranoff, E.; Kessler, F.; Moehl, T.; Ahmad, S.; Bessho, T.; Marchioro, A.; Ghadiri, E.; Moser, J.-E.; Yi, C.; Nazeeruddin, M. K.; Grätzel, M., A cobalt complex redox shuttle for dye-sensitized solar cells with high open-circuit potentials. *Nat Commun* **2012,** 3, 631.

26. Nazeeruddin, M. K.; Kay, A.; Rodicio, I.; Humphry-Baker, R.; Mueller, E.; Liska, P.; Vlachopoulos, N.; Graetzel, M., Conversion of light to electricity by cis-X2bis(2,2'-bipyridyl-4,4'-dicarboxylate)ruthenium(II) charge-transfer sensitizers (X = Cl-, Br-, I-, CN-, and SCN-) on nanocrystalline titanium dioxide electrodes. *Journal of the American Chemical Society* **1993,** 115, (14), 6382-6390.

27. Brédas, J.-L.; Norton, J. E.; Cornil, J.; Coropceanu, V., Molecular Understanding of Organic Solar Cells: The Challenges. *Accounts of Chemical Research* **2009,** 42, (11), 1691-1699.

28. White, M. S.; Olson, D. C.; Kopidakis, N.; Nardes, A. M.; Ginley, D. S.; Berry, J. J., Control of charge separation by electric field manipulation in polymer-oxide hybrid organic photovoltaic bilayer devices. *physica status solidi (a)* **2010,** 207, (5), 1257-1265.

29. Rothenberger, G.; Fitzmaurice, D.; Graetzel, M., Spectroscopy of conduction band electrons in transparent metal oxide semiconductor films: optical determination of

the flatband potential of colloidal titanium dioxide films. *The Journal of Physical Chemistry* **1992,** 96, (14), 5983-5986.

30. Redmond, G.; O'Keeffe, A.; Burgess, C.; MacHale, C.; Fitzmaurice, D., Spectroscopic determination of the flatband potential of transparent nanocrystalline zinc oxide films. *The Journal of Physical Chemistry* **1993,** 97, (42), 11081-11086.

31. Hara, K.; Sato, T.; Katoh, R.; Furube, A.; Ohga, Y.; Shinpo, A.; Suga, S.; Sayama, K.; Sugihara, H.; Arakawa, H., Molecular Design of Coumarin Dyes for Efficient Dye-Sensitized Solar Cells. *The Journal of Physical Chemistry B* **2003,** 107, (2), 597-606.

32. Wang, P.; Wenger, B.; Humphry-Baker, R.; Moser, J.-E.; Teuscher, J.; Kantlehner, W.; Mezger, J.; Stoyanov, E. V.; Zakeeruddin, S. M.; Grätzel, M., Charge Separation and Efficient Light Energy Conversion in Sensitized Mesoscopic Solar Cells Based on Binary Ionic Liquids. *Journal of the American Chemical Society* **2005,** 127, (18), 6850-6856.

33. Montanari, I.; Nelson, J.; Durrant, J. R., Iodide Electron Transfer Kinetics in Dye-Sensitized Nanocrystalline TiO2 Films. *The Journal of Physical Chemistry B* **2002,** 106, (47), 12203-12210.

34. Nei de Freitas, J.; Nogueira, A. F.; De Paoli, M.-A., New insights into dye-sensitized solar cells with polymer electrolytes. *Journal of Materials Chemistry* **2009,** 19, (30), 5279-5294.

35. Pelet, S.; Moser, J.-E.; Grätzel, M., Cooperative Effect of Adsorbed Cations and Iodide on the Interception of Back Electron Transfer in the Dye Sensitization of Nanocrystalline TiO2. *The Journal of Physical Chemistry B* **2000,** 104, (8), 1791-1795.

36. Luis, A.; Nunes de Carvalho, C.; Lavareda, G.; Amaral, A.; Brogueira, P.; Godinho, M. H., ITO coated flexible transparent substrates for liquid crystal based devices. *Vacuum* **2002,** 64, (3–4), 475-479.

37. Lin, H.-C.; Polaske, N. W.; Oquendo, L. E.; Gliboff, M.; Knesting, K. M.; Nordlund, D.; Ginger, D. S.; Ratcliff, E. L.; Beam, B. M.; Armstrong, N. R.; McGrath, D. V.; Saavedra, S. S., Electron-Transfer Processes in Zinc Phthalocyanine–Phosphonic Acid Monolayers on ITO: Characterization of Orientation and Charge-Transfer Kinetics

by Waveguide Spectroelectrochemistry. *The Journal of Physical Chemistry Letters* **2012,** 3, (9), 1154-1158.

38. Chockalingam, M.; Darwish, N.; Le Saux, G.; Gooding, J. J., Importance of the Indium Tin Oxide Substrate on the Quality of Self-Assembled Monolayers Formed from Organophosphonic Acids. *Langmuir* **2011,** 27, (6), 2545-2552.

39. Hotchkiss, P. J.; Li, H.; Paramonov, P. B.; Paniagua, S. A.; Jones, S. C.; Armstrong, N. R.; Brédas, J.-L.; Marder, S. R., Modification of the Surface Properties of Indium Tin Oxide with Benzylphosphonic Acids: A Joint Experimental and Theoretical Study. *Advanced Materials* **2009,** 21, (44), 4496-4501.

40. Armstrong, N. R.; Carter, C.; Donley, C.; Simmonds, A.; Lee, P.; Brumbach, M.; Kippelen, B.; Domercq, B.; Yoo, S., Interface modification of ITO thin films: organic photovoltaic cells. *Thin Solid Films* **2003,** 445, (2), 342-352.

41. Bisquert, J.; Fabregat-Santiago, F.; Mora-Seró, I.; Garcia-Belmonte, G.; Barea, E. M.; Palomares, E., A review of recent results on electrochemical determination of the density of electronic states of nanostructured metal-oxide semiconductors and organic hole conductors. *Inorganica Chimica Acta* **2008,** 361, (3), 684-698.

42. Yu, G.; Gao, J.; Hummelen, J. C.; Wudl, F.; Heeger, A. J., Polymer Photovoltaic Cells: Enhanced Efficiencies via a Network of Internal Donor-Acceptor Heterojunctions. *Science* **1995,** 270, (5243), 1789-1791.

43. Paniagua, S. A.; Hotchkiss, P. J.; Jones, S. C.; Marder, S. R.; Mudalige, A.; Marrikar, F. S.; Pemberton, J. E.; Armstrong, N. R., Phosphonic Acid Modification of Indium−Tin Oxide Electrodes: Combined XPS/UPS/Contact Angle Studies†. *The Journal of Physical Chemistry C* **2008,** 112, (21), 7809-7817.

44. Mulhern, K. R.; Detty, M. R.; Watson, D. F., Aggregation-Induced Increase of the Quantum Yield of Electron Injection from Chalcogenorhodamine Dyes to TiO2. *The Journal of Physical Chemistry C* **2011,** 115, (13), 6010-6018.

45. Hiramoto, M.; Fujiwara, H.; Yokoyama, M., Three-layered organic solar cell with a photoactive interlayer of codeposited pigments. *Applied Physics Letters* **1991,** 58, (10), 1062-1064.

46. Maturová, K.; van Bavel, S. S.; Wienk, M. M.; Janssen, R. A. J.; Kemerink, M., Description of the Morphology Dependent Charge Transport and Performance of Polymer:Fullerene Bulk Heterojunction Solar Cells. *Advanced Functional Materials* **2011,** 21, (2), 261-269.

47. Oosterhout, S. D.; Wienk, M. M.; van Bavel, S. S.; Thiedmann, R.; Jan Anton Koster, L.; Gilot, J.; Loos, J.; Schmidt, V.; Janssen, R. A. J., The effect of three-dimensional morphology on the efficiency of hybrid polymer solar cells. *Nat Mater* **2009,** 8, (10), 818-824.

48. de Tacconi, N. R.; Chanmanee, W.; Rajeshwar, K.; Rochford, J.; Galoppini, E., Photoelectrochemical Behavior of Polychelate Porphyrin Chromophores and Titanium Dioxide Nanotube Arrays for Dye-Sensitized Solar Cells. *The Journal of Physical Chemistry C* **2009,** 113, (7), 2996-3006.

49. Santos, T. D.; Morandeira, A.; Koops, S.; Mozer, A. J.; Tsekouras, G.; Dong, Y.; Wagner, P.; Wallace, G.; Earles, J. C.; Gordon, K. C.; Officer, D.; Durrant, J. R., Injection Limitations in a Series of Porphyrin Dye-Sensitized Solar Cells. *The Journal of Physical Chemistry C* **2010,** 114, (7), 3276-3279.

50. Pechy, P.; Rotzinger, F. P.; Nazeeruddin, M. K.; Kohle, O.; Zakeeruddin, S. M.; Humphry-Baker, R.; Gratzel, M., Preparation of phosphonated polypyridyl ligands to anchor transition-metal complexes on oxide surfaces: application for the conversion of light to electricity with nanocrystalline TiO2 films. *Journal of the Chemical Society, Chemical Communications* **1995**, (1), 65-66.

51. Ernstorfer, R.; Gundlach, L.; Felber, S.; Storck, W.; Eichberger, R.; Willig, F., Role of Molecular Anchor Groups in Molecule-to-Semiconductor Electron Transfer†. *The Journal of Physical Chemistry B* **2006,** 110, (50), 25383-25391.

52. Persson, P.; Lundqvist, M. J.; Ernstorfer, R.; Goddard, W. A.; Willig, F., Quantum Chemical Calculations of the Influence of Anchor-Cum-Spacer Groups on Femtosecond Electron Transfer Times in Dye-Sensitized Semiconductor Nanocrystals. *Journal of Chemical Theory and Computation* **2006,** 2, (2), 441-451.

53. Anderson, N. A.; Ai, X.; Chen, D.; Mohler, D. L.; Lian, T., Bridge-Assisted Ultrafast Interfacial Electron Transfer to Nanocrystalline SnO2 Thin Films. *The Journal of Physical Chemistry B* **2003,** 107, (51), 14231-14239.

54. Ooyama, Y.; Inoue, S.; Asada, R.; Ito, G.; Kushimoto, K.; Komaguchi, K.; Imae, I.; Harima, Y., Dye-Sensitized Solar Cells Based on a Novel Fluorescent Dye with a Pyridine Ring and a Pyridinium Dye with the Pyridinium Ring Forming Strong Interactions with Nanocrystalline TiO2 Films. *European Journal of Organic Chemistry* **2010,** 2010, (1), 92-100.

55. Steim, R.; Kogler, F. R.; Brabec, C. J., Interface materials for organic solar cells. *Journal of Materials Chemistry* **2010,** 20, (13), 2499-2512.

56. Simon, A. M.; Marucci, N. E.; Saavedra, S. S., Measuring Photochemical Kinetics in Submonolayer Films by Transient ATR Spectroscopy on a Multimode Planar Waveguide. *Analytical Chemistry* **2011,** 83, (14), 5762-5766.

57. Saavedra, S. S.; Reichert, W. M., Integrated optical attenuated total reflection spectrometry of aqueous superstrates using prism-coupled polymer waveguides. *Analytical Chemistry* **1990,** 62, (20), 2251-2256.

58. Ma, R.; Sasaki, T., Nanosheets of Oxides and Hydroxides: Ultimate 2D Charge-Bearing Functional Crystallites. *Advanced Materials* **2010,** 22, (45), 5082-5104.

59. Kaschak, D. M.; Lean, J. T.; Waraksa, C. C.; Saupe, G. B.; Usami, H.; Mallouk, T. E., Photoinduced Energy and Electron Transfer Reactions in Lamellar Polyanion/Polycation Thin Films: Toward an Inorganic "Leaf". *Journal of the American Chemical Society* **1999,** 121, (14), 3435-3445.

60. Oesterhelt, D.; Stoeckenius, W., [69] Isolation of the cell membrane of Halobacterium halobium and its fractionation into red and purple membrane. In *Methods in Enzymology*, Sidney Fleischer, L. P., Ed. Academic Press: 1974; Vol. 31, pp 667-678.

61. He, J.-A.; Samuelson, L.; Li, L.; Kumar, J.; Tripathy, S. K., Oriented Bacteriorhodopsin/Polycation Multilayers by Electrostatic Layer-by-Layer Assembly. *Langmuir* **1998,** 14, (7), 1674-1679.

62. Decher, G.; Hong, J. D., Buildup of Ultrathin Multilayer Films by a Self-Assembly Process: II. Consecutive Adsorption of Anionic and Cationic Bipolar Amphiphiles and Polyelectrolytes on Charged Surfaces. *Berichte der Bunsengesellschaft für physikalische Chemie* **1991,** 95, (11), 1430-1434.

63. Decher, G., Fuzzy Nanoassemblies: Toward Layered Polymeric Multicomposites. *Science* **1997,** 277, (5330), 1232-1237.

64. Ormos, P.; Fabian, L.; Oroszi, L.; Wolff, E. K.; Ramsden, J. J.; Der, A., Protein-based integrated optical switching and modulation. *Applied Physics Letters* **2002,** 80, (21), 4060-4062.

65. Li, M.; Li, B.; Jiang, L.; Tussila, T.; Tkachenko, N.; Lemmetyinen, H., Long-Lived M-State in Multilayer Films Fabricated by Alternative Deposition of a Polycation and Bacteriorhodopsin. *Langmuir* **2000,** 16, (12), 5503-5505.

66. Lee, J. E.; Saavedra, S. S., Proteins at Interfaces II: Fundamentals and Applications. In *ACS Symposium Series 602*, T.A. Horbett, J. L. B., Ed. American Chemical Society: Washington, D.C, 1995; p 269.

67. Lee, J. E.; Saavedra, S. S., Molecular Orientation in Heme Protein Films Adsorbed to Hydrophilic and Hydrophobic Glass Surfaces. *Langmuir* **1996,** 12, (16), 4025-4032.

68. Edmiston, P. L.; Lee, J. E.; Wood, L. L.; Saavedra, S. S., Dipole Orientation Distributions in Langmuir−Blodgett Films by Planar Waveguide Linear Dichroism and Fluorescence Anisotropy. *The Journal of Physical Chemistry* **1996,** 100, (2), 775-784.

69. Cropek, D. M.; Bohn, P. W., Surface molecular orientations determined by electronic linear dichroism in optical waveguide structures. *The Journal of Physical Chemistry* **1990,** 94, (16), 6452-6457.

70. Luecke, H.; Schobert, B.; Richter, H.-T.; Cartailler, J.-P.; Lanyi, J. K., Structure of bacteriorhodopsin at 1.55 Å resolution. *Journal of Molecular Biology* **1999,** 291, (4), 899-911.

71. Earnest, T. N.; Roepe, P.; Braiman, M. S.; Gillespie, J.; Rothschild, K. J., Orientation of the bacteriorhodopsin chromophore probed by polarized Fourier transform infrared difference spectroscopy. *Biochemistry* **1986,** 25, (24), 7793-7798.

72. Reichert, W. M., Evanescent detection of adsorbed films: assessment of optical considerations for absorbance and fluorescence spectroscopy at the crystal/solution and polymer/solution interfaces. *Critical Reviews in Biocompatibility* **1989,** 5, (2), 173-205.

73. Doherty III, W. J.; Donley, C. A.; Armstrong, N. R.; Saavedra, S. S., Broadband Spectroelectrochemical Attenuated Total Reflectance Instrument for Molecular Adlayer Studies. *Applied Spectroscopy* **2002,** 56, (7), 920-927.

74. Niemi, H. E. M.; Ikonen, M.; Levlin, J. M.; Lemmetyinen, H., Bacteriorhodopsin in Langmuir-Blodgett films imaged with a scanning tunneling microscope. *Langmuir* **1993,** 9, (9), 2436-2447.

75. Baudry, J.; Tajkhorshid, E.; Molnar, F.; Phillips, J.; Schulten, K., Molecular dynamics study of bacteriorhodopsin and the purple membrane. *Journal of Physical Chemistry B* **2001,** 105, (5), 905-918.

76. Lanyi, J. K., Molecular Mechanism of Ion Transport in Bacteriorhodopsin: Insights from Crystallographic, Spectroscopic, Kinetic, and Mutational Studies. *Journal of Physical Chemistry B* **2000,** 104, (48), 11441-11448.

77. Saab, M.-b.; Estephan, E.; Cloitre, T.; Legros, R.; Cuisinier, F. d. r. J. G.; Zimányi, L. s.; Gergely, C., Assembly of Purple Membranes on Polyelectrolyte Films. *Langmuir* **2009,** 25, (9), 5159-5167.

78. Mukhopadhyay, A. K.; Dracheva, S.; Bose, S.; Hendler, R. W., Control of the Integral Membrane Proton Pump, Bacteriorhodopsin, by Purple Membrane Lipids of Halobacterium halobium. *Biochemistry* **1996,** 35, (28), 9245-9252.

79. Fruh, V.; Ijzerman, A. P.; Siegal, G., How to Catch a Membrane Protein in Action: A Review of Functional Membrane Protein Immobilization Strategies and Their Applications. *Chemical Reviews (Washington, D. C.)* **2011,** 111, (2), 640-656.

80. Jonkheijm, P.; Weinrich, D.; Schroder, H.; Niemeyer, C. M.; Waldmann, H., Chemical Strategies for Generating Protein Biochips. *Angewandte Chemie International Edition* **2008,** 47, (50), 9618-9647.

81. Wong, L. S.; Khan, F.; Micklefield, J., Selective Covalent Protein Immobilization: Strategies and Applications. *Chemical Reviews (Washington, D. C.)* **2009,** 109, (9), 4025-4053.

82. Li, M. L.; Li, B. F.; Jiang, L.; Tussila, T.; Tkachenko, N.; Lemmetyinen, H., Long-lived M-state in multilayer films fabricated by alternative deposition of a polycation and bacteriorhodopsin. *Langmuir* **2000,** 16, (12), 5503-5505.

83. Gergely, C.; Zimanyi, L.; Varo, G., Bacteriorhodopsin Intermediate Spectra Determined over a Wide pH Range. *The Journal of Physical Chemistry B* **1997,** 101, (45), 9390-9395.

84. Ryan, M. A.; Fitzgerald, E. C.; Spitler, M. T., Internal reflection flash photolysis study of the photochemistry of eosin at titania semiconductor electrodes. *Journal of Physical Chemistry* **1989,** 93, (16), 6150-6156.

85. omlc.ogi.edu/spectra/PhotochemCAD/abs_html/EosinY-JZL.html

86. Kaunisto, K.; Chukharev, V.; Tkachenko, N. V.; Lemmetyinen, H., Long-lived charge separated state in molecular films containing porphyrin-fullerene dyad. *Chemical Physics Letters* **2008,** 460, (1-3), 241-244.

87. Kawai, H.; Nakano, K.; Nagamura, T., White light optical waveguide detection of transient absorption spectra in ultrathin organic films upon pulsed laser excitation. *Chemistry Letters* **2001,** 12, 1300-1301.

88. Kalyanasundaram, K.; Neumannspallart, M., Photophysical and redox properties of water-soluble porphyrins in aqueous-media. *Journal of Physical Chemistry* **1982,** 86, (26), 5163-5169.

89. Nagamura, T.; Adachi, T.; Sasaki, K.; Kawai, H.; Chen, X.-M.; Itoh, K.; Murabayashi, M., Highly sensitive detection of transient absorption in dye-doped ultrathin polymer films by the TiO2/K+ composite optical waveguide method upon pulsed laser excitation. *Talanta* **2005,** 65, (5), 1071-1077.

90. Fissi, A.; Pieroni, O.; Ciardelli, F.; Fabbri, D.; Ruggeri, G.; Umezawa, K., Photoresponsive Polypeptides - Photochromism and conformation of poly(L-glutamic acid) containing spiropyran units. *Biopolymers* **1993,** 33, (10), 1505-1517.

91. Bradshaw, J. T.; Mendes, S. B.; Saavedra, S. S., New Dimensions in Planar Integrated Optical Waveguide Spectroscopy. *Analytical Chemistry* **2005,** 77, 28A-36A.

92. Bradshaw, J. T.; Mendes, S. B.; Saavedra, S. S., A Simplified Broadband Coupling Approach Applied to Chemically Robust Sol−Gel, Planar Integrated Optical Waveguides. *Analytical Chemistry* **2002,** 74, (8), 1751-1759.

93. Schnippering, M.; Neil, S. R. T.; Mackenzie, S. R.; Unwin, P. R., Evanescent wave cavity-based spectroscopic techniques as probes of interfacial processes. *Chemical Society Reviews* **2011,** 40, (1), 207-220.

94. Bradshaw, J. T.; Mendes, S. B.; Armstrong, N. R.; Saavedra, S. S., Broadband Coupling into a Single-Mode, Electroactive Integrated Optical Waveguide for Spectroelectrochemical Analysis of Surface-Confined Redox Couples. *Analytical Chemistry* **2003,** 75, (5), 1080-1088.

95. Araci, Z. O.; Runge, A. F.; Doherty, W. J.; Saavedra, S. S., Correlating Molecular Orientation Distributions and Electrochemical Kinetics in Subpopulations of an Immobilized Protein Film. *Journal of the American Chemical Society* **2008,** 130, (5), 1572-1573.

96. Mathew, S.; Iijima, H.; Toude, Y.; Umeyama, T.; Matano, Y.; Ito, S.; Tkachenko, N. V.; Lemmetyinen, H.; Imahori, H., Optical, Electrochemical, and Photovoltaic Effects of an Electron-Withdrawing Tetrafluorophenylene Bridge in a Push–Pull Porphyrin Sensitizer Used for Dye-Sensitized Solar Cells. *The Journal of Physical Chemistry C* **2011,** 115, (29), 14415-14424.

97. Kalyanasundaram, K.; Neumann-Spallart, M., Photophysical and redox properties of water-soluble porphyrins in aqueous media. *The Journal of Physical Chemistry* **1982,** 86, (26), 5163-5169.

98. Takagi, S.; Inoue, H., Molecular and Supramolecular Photochemistry of Porphyrins and Metalloporphyrins. In *Multimetallic and Macromolecular Inorganic*

Photochemistry, Ramamurthy, V.; Schanze, K. S., Eds. Marcel Dekker, Inc.: New York, NY, 1999; Vol. 4, pp 215-342.

99. Gonçalves, P. J.; Barbosa Neto, N. M.; Parra, G. G.; de Boni, L.; Aggarwal, L. P. F.; Siqueira, J. P.; Misoguti, L.; Borissevitch, I. E.; Zílio, S. C., Excited-state dynamics of meso-tetrakis(sulfonatophenyl) porphyrin J-aggregates. *Optical Materials* **2012,** 34, (4), 741-747.

100. Khairutdinov, R. F.; Serpone, N., Photoluminescence and Transient Spectroscopy of Free Base Porphyrin Aggregates. *The Journal of Physical Chemistry B* **1999,** 103, (5), 761-769.

101. Van Patten, P. G.; Shreve, A. P.; Donohoe, R. J., Structural and Photophysical Properties of a Water-Soluble Porphyrin Associated with Polycations in Solution and Electrostatically-Assembled Ultrathin Films. *The Journal of Physical Chemistry B* **2000,** 104, (25), 5986-5992.

102. Kalyanasundaram, K.; Vlachopoulos, N.; Krishnan, V.; Monnier, A.; Graetzel, M., Sensitization of titanium dioxide in the visible light region using zinc porphyrins. *The Journal of Physical Chemistry* **1987,** 91, (9), 2342-2347.

103. Imahori, H.; Kang, S.; Hayashi, H.; Haruta, M.; Kurata, H.; Isoda, S.; Canton, S. E.; Infahsaeng, Y.; Kathiravan, A.; Pascher, T. r.; Chábera, P.; Yartsev, A. P.; Sundström, V., Photoinduced Charge Carrier Dynamics of Zn−Porphyrin−TiO2 Electrodes: The Key Role of Charge Recombination for Solar Cell Performance. *The Journal of Physical Chemistry A* **2010,** 115, (16), 3679-3690.

104. Campbell, W. M.; Burrell, A. K.; Officer, D. L.; Jolley, K. W., Porphyrins as light harvesters in the dye-sensitised TiO2 solar cell. *Coordination Chemistry Reviews* **2004,** 248, (13–14), 1363-1379.

105. Bruner, E. L.; Koch, N.; Span, A. R.; Bernasek, S. L.; Kahn, A.; Schwartz, J., Controlling the Work Function of Indium Tin Oxide: Differentiating Dipolar from Local Surface Effects. *Journal of the American Chemical Society* **2002,** 124, (13), 3192-3193.

106. Neumann-Spallart, M.; Kalyanasundaram, K., On the One and Two-Electron Oxidations of Water-Soluble Zinc Porphyrins in Aqueous Media. *Zeitschrift fuer*

Naturforschung Teil B, Anorganische Chemie, organische chemie. **1981,** 36, (5), 596-600.

107. Trasatti, S., The Absolute Electrode Potential: An Explanatory Note. *International Union of Pure and Applied Chemistry* **1986,** 58, (7), 955-966.

108. Gervaldo, M.; Fungo, F.; Durantini, E. N.; Silber, J. J.; Sereno, L.; Otero, L., Carboxyphenyl Metalloporphyrins as Photosensitizers of Semiconductor Film Electrodes. A Study of the Effect of Different Central Metals. *The Journal of Physical Chemistry B* **2005,** 109, (44), 20953-20962.

109. Dabestani, R.; Bard, A. J.; Campion, A.; Fox, M. A.; Mallouk, T. E.; Webber, S. E.; White, J. M., Sensitization of titanium dioxide and strontium titanate electrodes by ruthenium(II) tris(2,2'-bipyridine-4,4'-dicarboxylic acid) and zinc tetrakis(4-carboxyphenyl)porphyrin: an evaluation of sensitization efficiency for component photoelectrodes in a multipanel device. *The Journal of Physical Chemistry* **1988,** 92, (7), 1872-1878.

110. Nahor, G. S.; Neta, P.; Hambright, P.; Thompson, A. N.; Harriman, A., Metalloporphyrin-sensitized photooxidation of water to oxygen on the surface of colloidal iridium oxides: photochemical and pulse radiolytic studies. *The Journal of Physical Chemistry* **1989,** 93, (16), 6181-6187.

111. Rowe, G. K.; Creager, S. E., Interfacial Solvation and Double-Layer Effects on Redox Reactions in Organized Assemblies. *The Journal of Physical Chemistry* **1994,** 98, (21), 5500-5507.

112. Sumner, J. J.; Creager, S. E., Redox Kinetics in Monolayers on Electrodes: Electron Transfer Is Sluggish for Ferrocene Groups Buried within the Monolayer Interior†. *The Journal of Physical Chemistry B* **2001,** 105, (37), 8739-8745.

113. Choudhury, B.; Weedon, A. C.; Bolton, J. R., Effects of Molecular Organization on Photophysical Behavior. 1. Steady-State Fluorescence and Fluorescence Quantum Yield Studies of Langmuir−Blodgett Monolayers of Some Surfactant Porphyrins. *Langmuir* **1998,** 14, (21), 6192-6198.

114. Harriman, A., Luminescence of porphyrins and metalloporphyrins. Part 3.-Heavy-atom effects. *Journal of the Chemical Society, Faraday Transactions 2: Molecular and Chemical Physics* **1981,** 77, (7), 1281-1291.

115. Crouch, A. M.; Langford, C. H., Photophysical behaviour of zinc tetraphenylporphyrins in solutions and polymer films. *Journal of Photochemistry and Photobiology A: Chemistry* **1990,** 52, (1), 55-64.

116. Lee, T. R.; Carey, R. I.; Biebuyck, H. A.; Whitesides, G. M., The Wetting of Monolayer Films Exposing Ionizable Acids and Bases. *Langmuir* **1994,** 10, (3), 741-749.

117. Harriman, A.; Porter, G.; Walters, P., Photo-oxidation of metalloporphyrins in aqueous solution. *Journal of the Chemical Society, Faraday Transactions 1: Physical Chemistry in Condensed Phases* **1983,** 79, (6), 1335-1350.

118. Kadish, K. M.; Chen, P.; Enakieva, Y. Y.; Nefedov, S. E.; Gorbunova, Y. G.; Tsivadze, A. Y.; Bessmertnykh-Lemeune, A.; Stern, C.; Guilard, R., Electrochemical and spectroscopic studies of poly(diethoxyphosphoryl)porphyrins. *Journal of Electroanalytical Chemistry* **2011,** 656, (1–2), 61-71.

119. Egawa, Y.; Hayashida, R.; Anzai, J.-i., pH-Induced Interconversion between J-Aggregates and H-Aggregates of 5,10,15,20-Tetrakis(4-sulfonatophenyl)porphyrin in Polyelectrolyte Multilayer Films. *Langmuir* **2007,** 23, (26), 13146-13150.

120. Gust, D.; Moore, T. A.; Moore, A. L., Solar Fuels via Artificial Photosynthesis. *Accounts of Chemical Research* **2009,** 42, (12), 1890-1898.

121. Gust, D.; Moore, T. A.; Moore, A. L., Molecular mimicry of photosynthetic energy and electron transfer. *Accounts of Chemical Research* **1993,** 26, (4), 198-205.

122. Gust, D.; Moore, T. A.; Moore, A. L.; Kang, H. K.; DeGraziano, J. M.; Liddell, P. A.; Seely, G. R., Effect of coordinated ligands on interporphyrin photoinduced-electron-transfer rates. *The Journal of Physical Chemistry* **1993,** 97, (51), 13637-13642.

123. Moore, T. A.; Moore, A. L.; Gust, D., The Design and Synthesis of Artificial Photosynthetic Antennas, Reaction Centres and Membranes. *Philosophical Transactions: Biological Sciences* **2002,** 357, (1426), 1481-1498.

124. Cho, H. S.; Rhee, H.; Song, J. K.; Min, C.-K.; Takase, M.; Aratani, N.; Cho, S.; Osuka, A.; Joo, T.; Kim, D., Excitation Energy Transport Processes of Porphyrin Monomer, Dimer, Cyclic Trimer, and Hexamer Probed by Ultrafast Fluorescence Anisotropy Decay. *Journal of the American Chemical Society* **2003,** 125, (19), 5849-5860.

125. Aoki, K.; Goshima, T.; Kozuka, Y.; Kawamori, Y.; Ono, N.; Hisaeda, Y.; Takagi, H. D.; Inamo, M., Electron transfer reaction of porphyrin and porphycene complexes of Cu(II) and Zn(II) in acetonitrile. *Dalton Transactions* **2009**, (1), 119-125.

126. Marcus, R. A., On the Theory of Oxidation-Reduction Reactions Involving Electron Transfer. I. *The Journal of Chemical Physics* **1956,** 24, (5), 966-978.

127. Inamo, M.; Aoki, K.; Ono, N.; Takagi, H. D., Electron transfer reaction of Cu(II) porphyrin complex: Effect of structural deformation on the electron self-exchange rate. *Inorganic Chemistry Communications* **2005,** 8, (11), 979-982.

128. Sun, H.; Smirnov, V. V.; DiMagno, S. G., Slow Electron Transfer Rates for Fluorinated Cobalt Porphyrins: Electronic and Conformational Factors Modulating Metalloporphyrin ET. *Inorganic Chemistry* **2003,** 42, (19), 6032-6040.

129. Sahoo, H., Förster resonance energy transfer – A spectroscopic nanoruler: Principle and applications. *Journal of Photochemistry and Photobiology C: Photochemistry Reviews* **2011,** 12, (1), 20-30.

130. Soler, M.; McCusker, J. K., Distinguishing between Dexter and Rapid Sequential Electron Transfer in Covalently Linked Donor−Acceptor Assemblies. *Journal of the American Chemical Society* **2008,** 130, (14), 4708-4724.

131. Kroeze, J. E.; Koehorst, R. B. M.; Savenije, T. J., Singlet and Triplet Exciton Diffusion in a Self-Organizing Porphyrin Antenna Layer. *Advanced Functional Materials* **2004,** 14, (10), 992-998.

132. Fujishima, A.; Honda, K., Electrochemical Photolysis of Water at a Semiconductor Electrode. *Nature* **1972,** 238, (5358), 37-38.

133. Abe, R., Recent progress on photocatalytic and photoelectrochemical water splitting under visible light irradiation. *Journal of Photochemistry and Photobiology C: Photochemistry Reviews* **2010,** 11, (4), 179-209.

134. Walter, M. G.; Warren, E. L.; McKone, J. R.; Boettcher, S. W.; Mi, Q.; Santori, E. A.; Lewis, N. S., Solar Water Splitting Cells. *Chemical Reviews* **2010,** 110, (11), 6446-6473.

135. Häussinger, P.; Lohmüller, R.; Watson, A. M., Hydrogen, 1. Properties and Occurence. In *Ullmann's Encyclopedia of Industrial Chemistry*, Wiley-VCH Verlag GmbH & Co. KGaA: 2000.

136. Youngblood, W. J.; Lee, S.-H. A.; Maeda, K.; Mallouk, T. E., Visible Light Water Splitting Using Dye-Sensitized Oxide Semiconductors. *Accounts of Chemical Research* **2009,** 42, (12), 1966-1973.

137. Bolton, J. R.; Strickler, S. J.; Connolly, J. S., Limiting and realizable efficiencies of solar photolysis of water. *Nature* **1985,** 316, (6028), 495-500.

138. Maeda, K.; Teramura, K.; Domen, K., Effect of post-calcination on photocatalytic activity of (Ga1−xZnx)(N1−xOx) solid solution for overall water splitting under visible light. *Journal of Catalysis* **2008,** 254, (2), 198-204.

139. Kaschak, D. M.; Mallouk, T. E., Inter- and Intralayer Energy Transfer in Zirconium Phosphate−Poly(allylamine hydrochloride) Multilayers: An Efficient Photon Antenna and a Spectroscopic Ruler for Self-Assembled Thin Films. *Journal of the American Chemical Society* **1996,** 118, (17), 4222-4223.

140. Kleinfeld, E. R.; Ferguson, G. S., Stepwise Formation of Multilayered Nanostructural Films from Macromolecular Precursors. *Science* **1994,** 265, (5170), 370-373.

141. Keller, S. W.; Kim, H.-N.; Mallouk, T. E., Layer-by-Layer Assembly of Intercalation Compounds and Heterostructures on Surfaces: Toward Molecular "Beaker" Epitaxy. *Journal of the American Chemical Society* **1994,** 116, (19), 8817-8818.

142. Fang, M.; Kaschak, D. M.; Sutorik, A. C.; Mallouk, T. E., A "Mix and Match" Ionic−Covalent Strategy for Self-Assembly of Inorganic Multilayer Films. *Journal of the American Chemical Society* **1997,** 119, (50), 12184-12191.

143. Ramsay, J. D. F., Colloidal properties of synthetic hectorite clay dispersions: I. Rheology. *Journal of Colloid and Interface Science* **1986,** 109, (2), 441-447.

144. Kim, Y. I.; Atherton, S. J.; Brigham, E. S.; Mallouk, T. E., Sensitized layered metal oxide semiconductor particles for photochemical hydrogen evolution from nonsacrificial electron donors. *The Journal of Physical Chemistry* **1993,** 97, (45), 11802-11810.

145. Kaschak, D. M.; Johnson, S. A.; Hooks, D. E.; Kim, H.-N.; Ward, M. D.; Mallouk, T. E., Chemistry on the Edge: A Microscopic Analysis of the Intercalation, Exfoliation, Edge Functionalization, and Monolayer Surface Tiling Reactions of α-Zirconium Phosphate. *Journal of the American Chemical Society* **1998,** 120, (42), 10887-10894.

146. Andrews, D. L., A unified theory of radiative and radiationless molecular energy transfer. *Chemical Physics* **1989,** 135, (2), 195-201.

147. Swierk, J.; Mallouk, T., Unpublished results. In.

148. Kuo, T.-H.; Hsu, C.-Y.; Lee, K.-M.; Ho, K.-C., All-solid-state electrochromic device based on poly(butyl viologen), Prussian blue, and succinonitrile. *Solar Energy Materials and Solar Cells* **2009,** 93, (10), 1755-1760.

149. Schmehl, R. H.; Whitten, D. G., Photoinduced redox reactions in aqueous micelles. Quenching, back-reaction, and competing processes for tetraanionic porphyrins with alkylviologens. *The Journal of Physical Chemistry* **1981,** 85, (23), 3473-3480.

150. Fleischer, E. B.; Shachter, A. M., Coordination oligomers and a coordination polymer of zinc tetraarylporphyrins. *Inorganic Chemistry* **1991,** 30, (19), 3763-3769.

151. McLendon, G., Long-distance electron transfer in proteins and model systems. *Accounts of Chemical Research* **1988,** 21, (4), 160-167.

152. Sekine, T.; Yoshimura, J.; Tanaka, A.; Domen, K.; Maruya, K.-i.; Onishi, T., Photocatalytic Reaction on Layered Cs-Nb-Ti Complex Oxide. *Bulletin of the Chemical Society of Japan* **1990,** 63, (7), 2107-2109.

153. Shibata, M.; Kudo, A.; Tanaka, A.; Domen, K.; Maruya, K.-i.; Onishi, T., Photocatalytic Activities of Layered Titanium Compounds and Their Derivatives for H_2 Evolution from Aqueous Methanol Solution. *Chemistry Letters* **1987,** 16, (6), 1017-1018.

154. Eastwood, D.; Gouterman, M., Porphyrins: XVIII. Luminescence of (Co), (Ni), Pd, Pt complexes. *Journal of Molecular Spectroscopy* **1970,** 35, (3), 359-375.

155. Amao, Y.; Asai, K.; Okura, I., Novel optical oxygen sensing by phosphorescence quenching of palladium porphyrin self-assembled film on alumina plate. *Journal of Porphyrins and Phthalocyanines* **2000,** 04, (02), 179-184.

156. Cnossen, A.; Hou, L.; Pollard, M. M.; Wesenhagen, P. V.; Browne, W. R.; Feringa, B. L., Driving Unidirectional Molecular Rotary Motors with Visible Light by Intra- And Intermolecular Energy Transfer from Palladium Porphyrin. *Journal of the American Chemical Society* **2012,** 134, (42), 17613-17619.

157. Gervaldo, M.; Funes, M.; Durantini, J.; Fernandez, L.; Fungo, F.; Otero, L., Electrochemical polymerization of palladium (II) and free base 5,10,15,20-tetrakis(4-N,N-diphenylaminophenyl)porphyrins: Its applications as electrochromic and photoelectric materials. *Electrochimica Acta* **2010,** 55, (6), 1948-1957.

158. Wang, Z.; Al-Raqa, S. Y.; Chambrier, I.; Russell, D. A.; Cook, M. J., Evanescent wave excitation of palladium metalated porphyrins as self-assembled monolayers and phosphorescence quenching by oxygen. *Journal of Porphyrins and Phthalocyanines* **2012,** 16, (11), 1186-1195.

159. Galoppini, E.; Rochford, J.; Chen, H.; Saraf, G.; Lu, Y.; Hagfeldt, A.; Boschloo, G., Fast Electron Transport in Metal Organic Vapor Deposition Grown Dye-sensitized ZnO Nanorod Solar Cells. *The Journal of Physical Chemistry B* **2006,** 110, (33), 16159-16161.

160. Rochford, J.; Chu, D.; Hagfeldt, A.; Galoppini, E., Tetrachelate Porphyrin Chromophores for Metal Oxide Semiconductor Sensitization: Effect of the Spacer

Length and Anchoring Group Position. *Journal of the American Chemical Society* **2007,** 129, (15), 4655-4665.

161. Bonar-Law, R. P.; Sanders, J. K. M., Synthesis, binding properties and self-functionalization of a steroid-capped porphyrin. *Journal of the Chemical Society, Chemical Communications* **1991,** 0, (8), 574-577.